SAPIENZA
UNIVERSITÀ DI ROMA

Dynamic interaction and control of an indoor blimp inside the CERN FCC-hh magnetic environment

Facoltà di Ingegneria Civile e Industriale

Corso di Laurea Magistrale in Ingegneria Spaziale e Astronautica

Candidate

Francesco Mazzei
ID number 1747447

Thesis Advisor

Prof. Fabio Curti

Co-Advisor

Dr. Ing. Lorenzo Teofili

Academic Year 2020/2021

Thesis defended on 24 January 2022
in front of a Board of Examiners composed by:

Prof. Francesco Nasuti (chairman)
Prof. Mauro Pontani
Prof. Pasquale Tommasino
Prof. Alessandro Zavoli
Prof. Renato Paciorri
Prof. Roberto Seu

Dynamic interaction and control of an indoor blimp inside the CERN FCC-hh magnetic environment
Master's thesis. Sapienza – University of Rome

This thesis has been typeset by LaTeX and the Sapthesis class.

Author's email: fmazzei97@gmail.com

To my family

Abstract

The purpose of this thesis is to study the dynamic interaction and control of an indoor airship robot, also called blimp, inside the new generation of CERN FCC-hh detector cavern. The problem falls in the field of robotics in harsh environment due to the presence of high magnetic fields and radiation. This work is part of an R&D program of the Experimental Physics department at CERN which deals with the development of new robotic technologies for automated and robotized services and interfaces for the maintenance and disposal of the detector. After studying and deriving the 6 DOF nonlinear dynamic model of an indoor blimp, the work focused on the estimation of magnetic disturbances acting on the brushless electric motors with which the blimp is equipped. Through electromagnetic simulations with FEM modeling software such as FEMM and CST it was possible to characterize the magnetic behavior of an electric motor by associating it with a magnetic dipole moment and calculating the interaction in terms of forces and torques of this within the simulated nonuniform magnetic field of the detector. Then, the control problem was analyzed using linear control techniques such as PID and LQR for the trajectory tracking control of the linearized and decoupled longitudinal and lateral dynamics simulated in MATLAB. The last part concerns the practical tests that were carried out during the internship period at CERN. The activities involved the assembly of a real COTS blimp like Blimpduino from jjrobots and its identification dynamic parameters with the creation of a CAD model on CATIA. The tests has been done inside a cleanroom of a CERN laboratory without the presence of disturbances in which the PhaseSpace motion capture system was installed. Before doing the test was necessary to setup the motion caputure system which required cameras calibration, reference frame alignment and tracking rigid body triad definition. After implementing and updating the PID controller in the Arduino board, the station keeping test was carried out with two blimp of different sizes for altitude and yaw control. The blimp is followed with the telemetry of the on board sensors and with the tracking data of the motion capture system and the results were finally compared with a MATLAB simulation in which the same scenario was reproduced and the state was generated with the numerical integration of the dynamics model.

Keywords: Indoor blimp robot, harsh environment, magnetic field, electric brushless motors, magnetic dipole moment, control, motion capture system.

Contents

List of Figures

List of Tables

Acronyms

ANN Artificial Neural Network

API Application Programming Interface

ATLAS A Toroidal LHC ApparatuS

BEM Boundary Element Method

BEMF Back ElectroMotive Force

BLDC BrushLess Direct Current

CAD Computer Aided Design

CATIA Computer Aided Three dimensional Interactive Application

CB Center of Buoyancy

CDR Conceptual Design Report

CERN Conseil Européen pour la Recherche Nucléaire

CG Center of Gravity

CLIC Compact LInear Collider

COTS Commercial Off The Shelf

CTC Computed Torque Control

CV Center of Volume

DC Direct Current

DCM Direction Cosine Matrix

DOF Degree of Freedom

DT Detector Technologies

DXF Drawing Exchange Format

ECM Electronically Commutated Motor

EO Engineering Office

EP Experimental Physics

EPPSU European Particle Physics Strategy Update

FCC Future Circular Collider

FDM Finite Difference Method

FEM Finite Element Method

FEMM Finite Element Method Magnetics

FOC Field Oriented Control

GPS Global Positioning System

ICRP International Commission on Radiological Protection

IDE Integrated Development Environment

IMU Inertial Mass Unit

IP Internet Protocol

IPS Indoor Positioning System

LHC Large Hadron Collider

LIDAR Laser Imaging Detection and Ranging

Linac Linear accelerator

LIPO Lithium-Ion POlymer

LQR Linear Quadratic Regulator

LTA Lighter-Than-Air

MEMS Micro Electro-Mechanical Systems

MIMO Multi-Input Multi-Output

MMF MagnetoMotive Force

MPU Motion Processing Unit

NED North East Down

PD Proportional Derivative

PID Proportional Integral Derivative

PM Permanent Magnet

PMSM Permanent Magnet Synchronous Machine

PP Pole Placement

R&D Research and Development

RAS Robotics and Autonomous Systems

RB Rigid Body

RF Radio Frequency

SISO Single-Input Single-Output

STL Standard Triangulation Language

UAV Unmanned Aerial Vehicles

UDP User Data Protocol

USB Universal Serial Bus

VTOL Vertical Take-Off and Landing

WP Work Packages

Chapter 1

Introduction

1.1 Background and motivation

Robotics and autonomous systems (RAS) have been increasingly used in human and industrial activities for two decades; they were initially predominant in the context of factory processes and today their use has expanded successfully to all aspects of human life. This is also thanks to the constant decrease in costs and the parallel growth of capacity and flexibility [91]. Today there are many types of robotic systems, each characterized by a large number of functions and which can be used in many circumstances. Some common classifications that can be done on RAS include wheeled mobile vehicles, Unmanned Aerial Vehicles (UAV), humanoid robots, serial-link manipulators, snake robots and legged robots. Once the robotic system suitable for the user's needs has been identified, the control allows the use of that particular system according to the chosen objectives. The challenge today in robot control lies in the variability and unpredictability of the environments in which these robots have to work. One way to ensure proper control of RAS by managing the characteristics of the surrounding environment is to manually control the robots or let them perform semi-autonomous operations. This approach combines human cognitive decision-making processes with robot capabilities and therefore it guarantees the reliability of the operations and the avoidance of problems that can be presented to the system. However, this modality has a very low efficiency but above all it remains an asset that always keeps the presence of human active, which involves additional efforts and resources. For these and many other reasons, today there is a great interest in autonomous robotics which is capable of developing a higher level of intelligence and autonomy. This need is even more corroborated by the applications of robotics in so-called *harsh environments*.

The term harsh environment has two main meanings. Primarily it can constitute a dangerous and hazardous environment for the agents present inside it (such as humans or robots) and this because it could be characterized by high levels of radiation, high magnetic fields, high explosive risk, extreme temperatures or pressures, and lack of oxygen. Secondly it can represent an environment that is challenging for agents to operate in, such as remote, unknown, cluttered, dynamic, unstructured and limited in visibility environments. A classic example of a harsh environment is space and universe but there are many other activities on Earth that equally involve interactions with harsh environments.

One example of harsh environment is the Conseil Européen pour la Recherche Nucléaire (CERN) particles accelerator complex and experiments. The CERN environments can be considered as harsh

environments in both meanings of the term. Particle accelerator facilities like detectors present harsh environments as they are characterized by radiations and high magnetic fields. Furthermore, the underground accelerator complex consists in several kilometres of semi-structured areas with thousands of different items of equipment which needs to be inspected and maintained. An environment is called *semi-structured* when the topological navigation through segmentation of the environments and categorization of local areas is difficult to carry out. In particular, the semi-structured environments of particle accelerators in CERN have peculiar characteristics such as long distances, accessibility and occlusion areas. In addition to this, it must be considered that the machines equipment's are delicate and expensive. In this environment, therefore, the use of intelligent robotic systems is essential for both maintenance, inspection and intervention, all this reduces operational costs, mitigates accidents during operations and decreases human exposure to hazards and intervention time.

In this type of environments, the use of RAS is therefore essential. They can work in areas inaccessible to humans, assess safety conditions prior to human entry, carry out inspections and map unfamiliar environments. The features that robotic systems for harsh environments must have to ensure sufficient flexibility and robustness are associated with intelligence and autonomy. The autonomous capability greatly improves the efficiency of the operations and control of robots compared to the manual operations. The intelligence feature will certainly improve the performance of robotic systems in dealing with environmental variations, uncertainty and unpredictability of the environment in which they work.

1.2 Problem statement

The new generation of particle accelerators on which the particle physics community of CERN is working are: the Future Circular Collider (FCC) in its two configurations *ee* [16] and *hh* [17] and the Linac CLIC [86].

The work of this thesis is part of the Research & Development (R&D) of the future detectors robotics interfaces program of the Engineering Office (EO) section in the Detector Technologies (DT) group of the Experimental Physics (EP) department at CERN [21].

In 2017, the head of CERN's Experimental Physics department conceived a strategic R&D program on technologies for future experiments, also called the EP R&D program, aimed at developing key detector technologies essential for the next generation of experiments planned at CERN. During 2018 and 2019, with a series of public meetings, the foundations were laid for the definition of the work plan which was organized into 8 Work Packages (WP) addressing well-defined technological challenges that were documented in a detailed report [22]. The EP R&D program was presented in 2019 to the CERN Enlarged Directorate and was approved for an initial period of five years (2020-2024).

My thesis was the result of a collaboration with the WP4 of the EP R&D program, which is the work group of *Detector Mechanics*. The WP4 is related to challenges that are based on very stringed requirements such as confined space, thermal constraint, high accuracy, low mass and radiation hardness. Its development have repercussions on the design and operation of the detector itself which then affects the performance of the physical experiment. One of the main subgroups of Detector Mechanics (WP4) is that of *Robotics* in which new robotics solutions for the detectors

interfaces and services are studied.

The main problem for these new particle accelerators, especially for FCC-hh, is the radiation which comes from the beam activated material. Indeed, beam-matter interaction simulations performed on a FCC-hh reference detector design [17] using Fluka [12, 34] revealed that the detectors parts closer to the beam chamber were activated and capable of delivering a dose up to 1 mSv/h. An operator working in an environment with a radiation rate of 1 mSv/h would reach the annual dose limits fixed by the French [7] and Swiss authorities (that follows the limits recommended by the International Commission on Radiological Protection (ICRP) [46]) in a very short time. This example shows that working in such an environment would be a threat for the human health, thus the operations to perform on the detector after the activation of its materials (i.e. maintenance and disposal) should be automated and robotized to a large extent with the use of RAS. Robotic solutions will minimize the personnel dose exposure, the maintenance time and the need to send personnel in radioactive environment.

Therefore, the use of robotics within the structures of the particle accelerator complex, such as the detector cavern, would help not only to avoid radiation exposure for human operators in the moments of maintenance and disposal of the detector but would even allow for use these systems while the accelerator is running. However, a major problem in the use of robotics in a harsh environment does not only concern radiation but also the high magnetic field present. Indeed robotic systems are typically equipped with electric motors for their movement which can be strongly influenced by the field and this can induce malfunctions that affect uncontrolled movements of the robot.

For this reason, the WP4 of the EP R&D program has started a research activity to develop a mechanical design of a robotic and automation friendly particle detector in which ideally the maintenance and disposal operations should be performed by robotic and automated systems without operators in the detectors cavern. Therefore, the main scope of the R&D is to define new detector interfaces and services architectures for automated installation, maintainability and disposal. In this context, robotic platforms can be used for regular inspections and fault detection and the greatest difficulty will be to operate in confined, inaccessible spaces with a high content of radiation and magnetic fields.

The WP4 identified three systems that would perform operations with the particle accelerator detector components which are listed below:

1. **Motion Of Volumetric-massive Equipment System (MOVES)**. This is a system that moves volumetric and massive objects in the detector cavern.

2. **HANDling and Survey ON detector (HANDS-ON)**. This system performs operations and survey on the detector.

3. **Mechanism for AuTomatic service Connection Handling (MATCH)**. It is a part of the detector itself and concerns the service interfaces of the detector.

My contribution is part of the HANDS-ON system which will perform different crucial operations like mounting/dismounting parts, repairing and substitution of damaged equipment. The other important operations of this kind of system is based on environmental information perception that is: acquiring 3D maps of the radiation and of the magnetic field, performing visual inspections to

the equipment, precise location of detector components, areas inspection in case of alarm. This is where the thesis project is born; it represents a feasibility study of one of the latest applications belonging to the HANDS-ON system, that is the concept of environmental inspection. Indeed, to be able to carry out robotic inspection the optimal choice falls on flying machines.

In this work, we will focus on the blimp, which is a small non-rigid airship. Different from semi-rigid and rigid airships, it maintains the shape by the pressure of the lifting gas inside the envelope [27]. As a Vertical Take-Off and Landing (VTOL) system, blimps have the ability for vertical, stationary and low speed flight. Moreover, in contrast to other VTOL system like helicopters and multirotors, the static lift produced by lifting gas (usually helium) makes it possible for blimp to stay in air for a long time without much fuel consumption, in the case of flying machines that use electric motors to fly (like drones), the blimp have a lower battery consumption for the same flight time thanks to the buoyancy force. This key advantage makes the blimp an ideal platform for applications where high speeds are not needed like surveillance and exploration.

The most important reason that led to the choice of blimp as a robotic solution in the detector cavern is related to safety issues. In fact, if the blimp suddenly stopped working due to the discharge of the batteries or any other problem, it would not fall violently to the ground but would begin to drop slightly thanks to the contribution of the buoyancy force which, being slightly lower than the force of gravity, allows the blimp not to crash into delicate and expensive instrumentation, avoiding severe damage that would lead to consequent huge losses of money and repercussions on the physical experiment. Summing up, as an Unmanned Aircraft Vehicle (UAV), the blimp is an ideal platform for scientific research and below we report its advantages:

- Ability to VTOL,
- Low speed flight;
- Long endurance in air;
- Low battery consumption;
- Low acoustic noise level;
- Safe Human-Robot interaction.
- Long-term surveillance and monitoring;
- Unknown environment exploration and mapping

However, indoor blimp also have disadvantages when compared with analogous outdoor large scale airships. Indoor blimps are limited in size and payload, this means that it is possible to mount small and light sensors and actuators on board and therefore the measurement of on-board sensors can not be very accurate, and the capacity of actuator is constrained. Another problem is the workspace of indoor blimp that is more cluttered and filled with obstacles. Thus, it demands a higher accuracy of blimp motion control to achieve indoor operations [89]. For us the complexity of the environment in which the blimp will fly both from a topographical and a dynamic point of view represents the challenge of the thesis project.

1.3 Contribution

This thesis deals with the study of the control of an indoor blimp within a harsh environment such as the FCC-hh detector cavern. The interaction that makes the mission challenging is that between the electric motors of the robotic system and the magnetic field present in the cavern. The main contribution lies in the study of the magnetism of the DC motors with the characterization of their external magnetic field and the representation of their behavior through an associated dipole moment. The work contains both theoretical and practical parts.

The first theoretical activity concerned the development of the kinematic and dynamic model of the blimp with the writing of its equations of motion.

The second theoretical activity concerned the study of the operating principle of Brushless Direct Current (BLDC) motors trying to represent them from the magnetic point of view. The main contribution was to demonstrate that it is possible to associate a magnetic dipole moment with an electric motor that comes from the contribute of its internal ferromagnetic components. Once an analytical method has been developed through software simulations, in order to calculate the magnitude and direction of the dipole moments vector, it is possible to estimate the forces and torques to which it is subject when immersed in an external magnetic field to verify the feasibility of the blimp flight in relation to the ability of its actuators to control the platform despite the presence of magnetic disturbances.

The third theoretical activity concerned the study of the physical environment with the characterization of the magnetic field and its gradient that led to the calculation of magnetic interactions with the magnetic dipole moment.

After having estimated the disturbances on the system coming from the external environment, we moved on to the control part, to ensure that the blimp follows a desired trajectory and rejects the disturbances.

Regarding the practical part, this work is an experimental thesis and part of it has been done in the CERN headquarters. As an intern for a period of two months I had the opportunity to build a real blimp and carry out a flight experiment to test the designed control. This activity also concerned the setting of the system monitoring environment and in particular the implementation of a motion capture system that allowed us follow the motion of the system.

1.4 Thesis structure and content

This thesis is structured as follows:

In this chapter the topic in which the thesis is placed is introduced and the motivation for its development is given. In addition, the definition of the problem and the contribution that this work intends to solve is specified.

In Chapter 2 the mathematical model of an indoor blimp is obtained and the hypotheses that lead us to the writing of the equations of motion are specified. In particular, the model starts from the definition of the reference systems in which the motion of the robot is represented and then moves on to the development of the kinematics and dynamics of the blimp system.

In Chapter 3 we want to determine the magnetic interaction of a blimp with an external magnetic field. For this reason the operating principle of brushless electric motors is analyzed. After studying

its structure, simulations are carried out which tend to model an electric motor and calculate the magnetic field external to it. Then from the torque that acts on it, if immersed in a uniform magnetic field, a method is introduced to derive its magnetic moment.

In Chapter 4, after having characterized the motors magnetically, we move on to characterize the environment in which the blimps will have to fly. In particular, the environment of the future CERN detector is described and its magnetic field simulated. Then the expressions for the calculation of the forces and torques that a magnetic moment undergoes when immersed in an external magnetic field are obtained and through these we pass to the estimate of the magnetic disturbances calculated by inserting a magnetic dipole inside the environment of the detector. Finally, from the description of the structural environment of the detector, a method is introduced to generate a reference trajectory based on the knowledge of via points through which the blimp must pass.

In Chapter 5, after an introduction on the most used techniques to control an airship, the linearization method of the equations of motion is introduced for the creation of two simplified models which are the longitudinal and lateral model. With linear equations, two feedback control techniques are implemented which are the PID and LQR controllers. After specifying the disturbance estimation method, the results of the simulations performed on the two techniques are shown.

Chapter 6 reports the results that refer to the practical part of the thesis, i.e. the one that took place at the EO of the EP-DT department of CERN. In particular, in this internship activity, real tests and experiments are carried out to control a real blimp. The activity involved the assembly phase of the system, the study and modeling aimed at determining the parameters useful for comparing the tests with the simulation, the setting of an environment in which to perform the experiment with the installation of a sophisticated motion capturing system. Finally, the results of the station keeping tests carried out with the real system are shown.

In Chapter 7 the conclusions of this thesis work that have led to satisfactory results are presented and all the still open questions of the problem are discussed, thus delineating the future developments that lie ahead for this work linked to an interesting R&D activity of the EP-DT department of CERN.

Appendix A presents the mathematical method of Newton-Euler in order to derive the dynamic model of the equations of motion with the explanation of all the terms that appear in them.

Appendix B concerns an in-depth study in the field of the theory of electromagnetism in which the essential tools of magnetostatics are provided to be able to understand the magnetic phenomena that are the basis of the functioning of electric motors, to understand the meaning of magnetic moment and to explain the phenomenon of magnetization.

Appendix C concerns the study of nonlinear stability according to Lyapunov's theory and the application of a nonlinear control technique called feedback linearization with the presentation of the results of a simulation on the control of the blimp.

Chapter 2

Mathematical Modelling

2.1 Introduction

This chapter discusses the mathematical modelling of the blimp which has six degree of freedom (DOF). The goal is to obtain the kinematic and dynamic model of the mini airship in order to be able to carry out the necessary simulations through its equations of motion. The details on the mathematical derivation of the various terms that appear in the dynamic model are given in Appendix A.

In section 2.2 some general assumptions are introduced that allow to frame the model and simplify some concepts concerning the flight mechanics of LTA systems. In section 2.3 we introduce the fundamental reference systems in which we choose to represent the motion of the system. In section 2.4 the kinematic model are reported and finally, in section 2.5, the 6 DOF dynamic model of the rigid body are derived.

2.2 General hypotheses

The general assumptions that will be applied to the dynamic model of the blimp are listed below:

- The blimp is able to stay aloft with a small action of the actuators and this is guaranteed by the fact that its equivalent density is almost equal to that of the surrounding air.
- The hull is considered a rigid body, this implies that its surface does not show folds, wrinkles or deformations and therefore the aeroelastic phenomena on the balloon are neglected [19].
- It is assumed that the shape of the balloon is maintained during flight by the internal pressure of the helium gas which does not change.
- The hull of the blimp is an ellipsoid.
- The masses and volumes of the blimp are constant over time, this is true for indoor blimp but not for traditional airships which are equipped with ballonet inside the hull to adjust inner pressure and buoyancy.
- The helium molecules that inflate the balloon are considered to be stationary and this leads to the neglect of the phenomenon of internal added fluid [45].

- The center of volume (CV) and the center of buoyancy (CB) of the hull are considered coincident, while the center of gravity (CG) is lower on the vertical axis due to the presence of the gondola.
- The motion of blimp does not modify locally the density of air whose viscosity is considered constant.
- Given the low speeds of motion in the indoor environment, the control surfaces such as rudder and elevator have poor efficiency for changing the yaw and pitch angle [41]. So the system is controlled only by the action of the thrusters.

2.3 Reference frames

To study the motion of blimps in 6 DOF it is very important to define the correct reference frames through which the equations of motion are written. For our model it is necessary to define two coordinate frames which are reported in Figure 2.1. The first one is the moving reference frame fixed to the body F_b. The direction of F_b is forward-right-down and the origin can be chosen either in the CG of the body or in another point (we will choose the CV coinciding with the CB as the center of the body-fixed reference frame). The second reference frame is the inertial one in which we chooses to represent the motion of the body-fixed reference frame. The direction of the inertial frame F_n, also called *navigation frame*, is North-East-Down (NED) and it is considered inertial because the operation of blimp robot in indoor environment ignores the movement of the Earth.

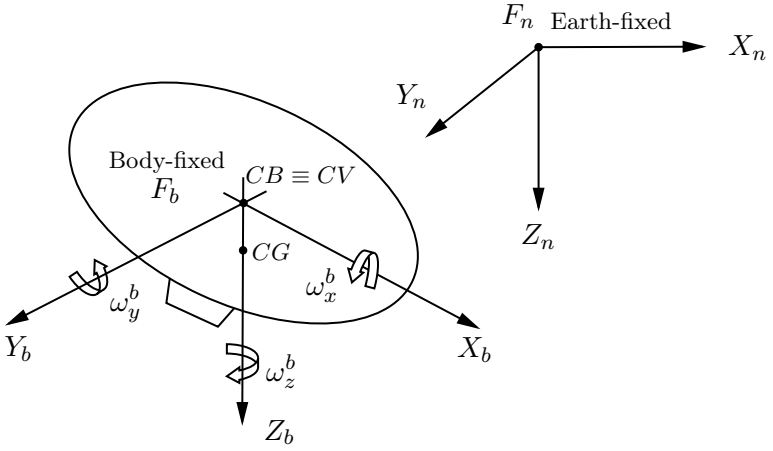

Figure 2.1: Reference frames for indoor blimp robot.

2.4 Kinematic model

The instantaneous linear and angular velocities of the blimp are described in F_b as

$$\boldsymbol{\xi}^b = \begin{bmatrix} (\boldsymbol{v}^b)^T & (\boldsymbol{\omega}^b)^T \end{bmatrix}^T = \begin{bmatrix} v_x^b & v_y^b & v_z^b & \omega_x^b & \omega_y^b & \omega_z^b \end{bmatrix}^T \tag{2.1}$$

whereas the position and orientation of the blimp with respect to F_n are expressed as

$$\boldsymbol{\eta}^n = \begin{bmatrix} (\boldsymbol{\eta}_1^n)^T & (\boldsymbol{\eta}_2^n)^T \end{bmatrix}^T = \begin{bmatrix} x^n & y^n & z^n & \phi & \theta & \psi \end{bmatrix}^T \tag{2.2}$$

where ϕ, θ and ψ are roll, pitch and yaw angle, respectively. To describe the orientation of the body with respect to some fixed reference frame, a 3×3 direction cosine matrix (DCM) is used [82]. Adopting this formulation, the DCM, also called rotation matrix $\boldsymbol{R}$, is constructed by three successive rotation written as a function of $\boldsymbol{\eta}_2 = [\phi, \theta, \psi]^T$.

$$\boldsymbol{R}(\boldsymbol{\eta}_2^n) = \boldsymbol{R}_z(\psi)\boldsymbol{R}_y(\theta)\boldsymbol{R}_x(\phi) \tag{2.3}$$

with

$$\boldsymbol{R}(\boldsymbol{\eta}_2^n) = \begin{bmatrix} 1 & 0 & 0 \\ 0 & \cos\phi & -\sin\phi \\ 0 & \sin\phi & \cos\phi \end{bmatrix} \begin{bmatrix} \cos\theta & 0 & \sin\theta \\ 0 & 1 & 0 \\ -\sin\theta & 0 & \cos\theta \end{bmatrix} \begin{bmatrix} \cos\psi & -\sin\psi & 0 \\ \sin\psi & \cos\psi & 0 \\ 0 & 0 & 1 \end{bmatrix} \tag{2.4}$$

Taking the product of the three successive rotation matrices, we obtain the global transformation matrix which allows us to represent a vector from one reference to another, this is written as

$$\boldsymbol{R}_n^b(\boldsymbol{\eta}_2^n) = \begin{bmatrix} \cos\psi\cos\theta & -\sin\psi\cos\phi + \cos\psi\sin\theta\sin\phi & \sin\psi\sin\phi + \cos\psi\sin\theta\cos\phi \\ \sin\psi\cos\theta & \cos\psi\cos\phi + \sin\psi\sin\theta\sin\phi & -\cos\psi\sin\phi + \sin\psi\sin\theta\cos\phi \\ -\sin\theta & \cos\theta\sin\phi & \cos\theta\cos\phi \end{bmatrix} \tag{2.5}$$

The rotation matrix $\boldsymbol{R}$ belongs to the special orthogonal matrix group $SO(3)$ defined as:

$$SO(3) = \{\boldsymbol{R} \in \mathbb{R}^{3\times3},\ \boldsymbol{R}^T\boldsymbol{R} = I_{3\times3},\ det(\boldsymbol{R}) = 1\} \tag{2.6}$$

To complete the kinematics equation we need the relationship between the body angular velocity vector $\boldsymbol{\omega}^b = [\omega_x, \omega_y, \omega_z]^T$ and the rate of change of the Euler angles $\dot{\boldsymbol{\eta}}_2^n = [\dot{\phi}, \dot{\theta}, \dot{\psi}]^T$ that can be determined by resolving the Euler rates into the body-fixed coordinate frame.

$$\begin{bmatrix} \omega_x^b \\ \omega_y^b \\ \omega_z^b \end{bmatrix} = \begin{bmatrix} \dot{\phi} \\ 0 \\ 0 \end{bmatrix} + \begin{bmatrix} 1 & 0 & 0 \\ 0 & \cos\phi & -\sin\phi \\ 0 & \sin\phi & \cos\phi \end{bmatrix} \begin{bmatrix} 0 \\ \dot{\theta} \\ 0 \end{bmatrix} + \begin{bmatrix} 1 & 0 & 0 \\ 0 & \cos\phi & -\sin\phi \\ 0 & \sin\phi & \cos\phi \end{bmatrix} \begin{bmatrix} \cos\theta & 0 & \sin\theta \\ 0 & 1 & 0 \\ -\sin\theta & 0 & \cos\theta \end{bmatrix} \begin{bmatrix} 0 \\ 0 \\ \dot{\psi} \end{bmatrix} \tag{2.7}$$

Combining together gives

$$\begin{bmatrix} \omega_x^b \\ \omega_y^b \\ \omega_z^b \end{bmatrix} = \begin{bmatrix} 1 & 0 & -\sin\theta \\ 0 & \cos\phi & \cos\theta\sin\phi \\ 0 & -\sin\phi & \cos\theta\cos\phi \end{bmatrix} \begin{bmatrix} \dot{\phi} \\ \dot{\theta} \\ \dot{\psi} \end{bmatrix} \tag{2.8}$$

From the inverse of (2.8) it can be found that

$$\dot{\boldsymbol{\eta}}_2^n = \boldsymbol{T}_n^b(\boldsymbol{\eta}_2^n)\boldsymbol{\omega}^b = \begin{bmatrix} 1 & \sin\phi\tan\theta & \cos\phi\tan\theta \\ 0 & \cos\phi & -\sin\phi \\ 0 & \sin\phi/\cos\theta & \cos\phi/\cos\theta \end{bmatrix} \boldsymbol{\omega}^b \tag{2.9}$$

It is easy to note that $\boldsymbol{T}_n^b$ has singularities at $\theta = (2k+1)\frac{\pi}{2},\ k \in \mathbb{Z}$, this is one of the disadvantages using Euler angles to represent the orientation. This problem can be avoided by using a different representation of the attitude, i.e. that of the Euler parameters, also called *quaternions*, which constitute a set of four parameters that are able to describe all the possible orientations without

having singularity problems. However, the motion of blimp is considered to be mild, thus the pitch angle will never reach the singularity condition.

Finally, from (2.5) and (2.9) the kinematic equation relating the linear and angular velocities is given by:

$$\begin{bmatrix} \dot{\boldsymbol{\eta}}_1^n \\ \dot{\boldsymbol{\eta}}_2^n \end{bmatrix} = \begin{bmatrix} \boldsymbol{R}_n^b(\eta_2^n) & \mathbf{0}_{3\times3} \\ \mathbf{0}_{3\times3} & \boldsymbol{T}_n^b(\boldsymbol{\eta}_2^n) \end{bmatrix} \begin{bmatrix} \boldsymbol{v}^b \\ \boldsymbol{\omega}^b \end{bmatrix} \tag{2.10}$$

or

$$\dot{\boldsymbol{\eta}}^n = \boldsymbol{J}(\boldsymbol{\eta}^n)\boldsymbol{\xi}^b \tag{2.11}$$

2.5 Dynamic model

This section presents the typical dynamics design of indoor blimp robots. The approach used in literature is to assimilate the design of the airship to that of an underwater vehicle and it is for this reason that we were inspired by the following works to derive the equations of motion of the blimp: [35], [41],[80] and [97].

Appendix A reports the complete development of the 6 DOF nonlinear dynamic equations of the system based on the Newton-Euler method. From this procedure we finally reach the equations of the dynamic model written in the body-fixed reference frame F_b. In our case the location of F_b is at the CB of the blimp, which is also the CV of the balloon. Then, due to the fact that the gondola with actuators and other electrical components are mounted on the bottom of the hull, CG is located on the $\boldsymbol{Z}_b$ axis of body-fixed frame.

$$\boldsymbol{r}_G^b = \begin{bmatrix} 0 & 0 & z_G \end{bmatrix}^T \tag{2.12}$$

As reported in the Appendix A, the 6 DOF nonlinear dynamic equation of the blimp motion expressed in the body-fixed frame is:

$$\boldsymbol{M}\dot{\boldsymbol{\xi}}^b + \boldsymbol{C}(\boldsymbol{\xi}^b)\boldsymbol{\xi}^b + \boldsymbol{D}(\boldsymbol{\xi}^b)\boldsymbol{\xi}^b + \boldsymbol{g}(\boldsymbol{\eta}^n) = \boldsymbol{\tau}^b \tag{2.13}$$

where the terms are:

- $\boldsymbol{M}$: inertia matrix including added mass terms;
- $\boldsymbol{C}(\boldsymbol{\xi}^b)$: matrix of the Coriolis and centripetal terms including added mass terms;
- $\boldsymbol{D}(\boldsymbol{\xi}^b)$: damping matrix;
- $\boldsymbol{g}(\boldsymbol{\eta}^n)$: vector of restoring forces and moments;
- $\boldsymbol{\tau}^b$: vector of control inputs.

These terms are presented below.

2.5.1 Inertia matrix

As we have seen in Appendix A, the inertia matrix $\boldsymbol{M}$ consists of the sum of the rigid body (RB) inertia $\boldsymbol{M}_{RB}$ and the added inertia $\boldsymbol{M}_{Added}$. The RB inertia matrix is defined in (A.32) and

considering that the blimp has two planes of symmetry (xy- and yz- planes), thus the RB matrix of inertia is simplified as

$$\boldsymbol{M}_{RB} = \begin{bmatrix} m & 0 & 0 & 0 & mz_G & 0 \\ 0 & m & 0 & -mz_G & 0 & 0 \\ 0 & 0 & m & 0 & 0 & 0 \\ 0 & -mz_G & 0 & I_x & 0 & 0 \\ mz_G & 0 & 0 & 0 & I_y & 0 \\ 0 & 0 & 0 & 0 & 0 & I_z \end{bmatrix} \tag{2.14}$$

As for the identification of the parameters, in order to know $\boldsymbol{M}_{RB}$ matrix, one must know the static mass m, the distance $\boldsymbol{r}_G^b$ defined in (2.12) and the diagonal elements of the inertia tensor that can be calculated based on the distribution of the masses on the blimps (obviously including the inertia of the helium in the balloon).

As we explained in the Appendix A, the moving body displaces a large number of air particles and this effect generates a resistance to motion that is not quantified in the RB model but is added to the mass matrix. These added terms are calculated through the Lamb's k-factors [58] (see Appendix A for derivation). Putting together the added mass matrix which is defined in (A.43) and the RB inertia matrix (2.14) we then derive the global inertia matrix $\boldsymbol{M}$ as the sum of the two.

$$\boldsymbol{M} = \boldsymbol{M}_{RB} + \boldsymbol{M}_A = \begin{bmatrix} m'_x & 0 & 0 & 0 & mz_G & 0 \\ 0 & m'_y & 0 & -mz_G & 0 & 0 \\ 0 & 0 & m'_z & 0 & 0 & 0 \\ 0 & -mz_G & 0 & I'_x & 0 & 0 \\ mz_G & 0 & 0 & 0 & I'_y & 0 \\ 0 & 0 & 0 & 0 & 0 & I'_z \end{bmatrix} \tag{2.15}$$

where

$$\begin{cases} m'_x = m + m_{A_x} \\ m'_y = m + m_{A_y} \\ m'_z = m + m_{A_z} \\ I'_x = I_x + I_{A_x} \\ I'_y = I_y + I_{A_y} \\ I'_z = I_z + I_{A_z} \end{cases}$$

2.5.2 Coriolis and centripetal matrix

Since we have derived the equations of motion in a non-inertial reference frame such as the body-fixed one F_b, then the effects of the fictitious forces are present, these are the Coriolis and centripetal forces. The first one occurs when the motion is composed of linear and rotational velocities and it is expressed as $\boldsymbol{\omega} \times \boldsymbol{v}$. This fictitious force acts perpendicularly to the linear velocity vector and to the axis of rotation of the body and tends to maintain the initial direction of the motion without looking at the rotation of the body. The centripetal force is given by $\boldsymbol{\omega} \times (\boldsymbol{\omega} \times \boldsymbol{r})$ and it is present when a rotating body is not seen from its CG, which is the case of F_b. Both fictitious forces are

function of the velocity $\boldsymbol{v}$ and therefore they are merged into a single vector in the form:

$$\boldsymbol{F}_c = \boldsymbol{C}(\boldsymbol{\xi}^b)\boldsymbol{\xi}^b \tag{2.16}$$

where $\boldsymbol{C}(\boldsymbol{\xi}^b)$ is called Coriolis and centripetal matrix. We have seen in Appendix A that from the result of [80], the Coriolis matrix can be derived directly from the inertia matrix

$$\boldsymbol{C}(\boldsymbol{\xi}^b) = \begin{bmatrix} \boldsymbol{0}_{3\times3} & -S(\boldsymbol{M}_{11}\boldsymbol{v}^b + \boldsymbol{M}_{12}\boldsymbol{\omega}^b) \\ -S(\boldsymbol{M}_{11}\boldsymbol{v}^b + \boldsymbol{M}_{12}\boldsymbol{\omega}^b) & -S(\boldsymbol{M}_{21}\boldsymbol{v}^b + \boldsymbol{M}_{22}\boldsymbol{\omega}^b) \end{bmatrix} \tag{2.17}$$

where $\boldsymbol{M}_{ij}\,(i,j=1,2)$ are the four 3×3 sub-matrices of the global inertia matrix $\boldsymbol{M}$. Applying the definition of inertia matrix (2.15), the explicit form of $\boldsymbol{C}(\boldsymbol{\xi}^b)$ is

$$\boldsymbol{C}(\boldsymbol{\xi}^b) = -\begin{bmatrix} 0 & 0 & 0 \\ 0 & 0 & 0 \\ 0 & 0 & 0 \\ 0 & -m'_z v_z & m'_y v_y - m z_G \omega_x \\ m'_z v_z & 0 & -m'_x v_x - m z_G \omega_y \\ -m'_y v_y - m z_G \omega_x & m'_x v_x + m z_G \omega_y & 0 \end{bmatrix}$$

$$\begin{bmatrix} 0 & -m'_z v_z & m'_y v_y - m z_G \omega_x \\ m'_z v_z & 0 & -m'_x v_x - m z_G \omega_y \\ -m'_y v_y - m z_G \omega_x & m'_x v_x + m z_G \omega_y & 0 \\ 0 & -I'_z \omega_z & m z_G v_x + I'_y \omega_y \\ I'_z \omega_z & 0 & m z_G v_y - I'_x \omega_x \\ -m z_G v_x - I'_y \omega_y & -m z_G v_y + I'_x \omega_x & 0 \end{bmatrix}$$

As stated by [97], an axial motion of the blimp is intrinsically unstable. This is evident from the Coriolis and centripetal forces vector $\boldsymbol{C}(\boldsymbol{\xi}^b)\boldsymbol{\xi}^b$ because if we look at the yaw moment we notice the difference between m'_x and m'_y. Therefore any small angle between the $\boldsymbol{X}_b$-axis and the direction of motion will tend to increase [68]. This unstable moment is proportional to the difference of lateral and longitudinal Lamb's k-factors $(k_2 - k_1)$ defined in equation (A.46) and in some literature is referred to as Munk moment [61]. Hence the phenomenon of additional masses also explain why there may be an unstable yaw moment during forward motion, as well as explain why the apparent inertia of the hull shaped blimp is higher than that predicted by $\boldsymbol{M}_{RB}$. The Coriolis and centripetal matrix also explains other phenomena due to the presence of these fictitious forces, for example the slight inclination of the roll that appears during the curved trajectories and due to the centripetal force.

2.5.3 Dumping matrix

As regards the dumping matrix, this has already been discussed in the section A.5 in which we made the hypothesis that the vehicle carries out an uncoupled motion, has three planes of symmetry and that the second order terms are negligible. This suggests a diagonal structure of $\boldsymbol{D}(\boldsymbol{\xi}^b)$ with only the linear and quadratic damping terms on the diagonal. In addition, for small indoor blimps which are characterized by low speed, laminar boundary layer conditions can be assumed, considering only

linear skin friction coefficient. Thus, the expression of $\boldsymbol{D}(\boldsymbol{\xi}^b)$ is simply diagonal

$$\boldsymbol{D}(\boldsymbol{\xi}^b) = -diag \begin{bmatrix} D_{v_x} \\ D_{v_y} \\ D_{v_z} \\ D_{\omega_x} \\ D_{\omega_y} \\ D_{\omega_z} \end{bmatrix} \tag{2.18}$$

The elements of $\boldsymbol{D}(\boldsymbol{\xi}^b)$ can be estimated either from wind-tunnel testing or system identification tools.

2.5.4 Restoring vector

As shown in section A.6, vector $\boldsymbol{g(\eta)^n}$ contains gravitational and buoyancy forces. The gravitational force $\boldsymbol{f}_G$ acts on the CG which is at $\boldsymbol{r}_G^b$ from the CV of the blimp, and the buoyancy force $\boldsymbol{f}_B$ acts at the CB, which is the origin of F_b, i.e. $\boldsymbol{r}_B^b = \boldsymbol{0}_{3\times1}$. Taking up the expression (A.52) and replacing the components of $\boldsymbol{r}_G^b$ and $\boldsymbol{r}_B^b$ we obtain:

$$\boldsymbol{g(\eta)^n} = - \begin{bmatrix} -(f_G - f_B)\sin\theta \\ (f_G - f_B)\cos\theta\sin\phi \\ (f_G - f_B)\cos\theta\cos\phi \\ -z_G f_G \cos\theta\sin\phi \\ -z_G f_G \sin\theta \\ 0 \end{bmatrix} \tag{2.19}$$

2.5.5 Propulsion forces and moments

As mentioned above, applications of small indoor blimps are characterized by low flight speeds, therefore in laminar boundary conditions, the control surfaces (such as rudder and elevator) are not included because they are not efficient. Propulsive forces are generated by propeller electric motors. However, the number of thrusters and their mounting positions and orientations may vary from different applications. As a consequence, the propulsion forces $\boldsymbol{\tau}^b$ depends only on the installation of motors. The general notation brings to the following expression of $\boldsymbol{\tau}^b$:

$$\boldsymbol{\tau}^b = \begin{bmatrix} f_{px} & f_{py} & f_{pz} & \tau_{px} & \tau_{py} & \tau_{pz} \end{bmatrix}^T \tag{2.20}$$

In our case the vector $\boldsymbol{\tau}^b$ will be a function of the geometrical arrangement of the propulsive units around the body axes:

$$\boldsymbol{\tau}^b = \begin{bmatrix} T_{cmn} & 0 & T_v & 0 & d_z T_{cmn} & d_y T_{diff} \end{bmatrix}^T$$

where $T_{cmn} = (T_s + T_p)$ in the common mode component of thrust coming from the starboard and port side propellers, in analogy to naval terminology. T_v is the thrust resulting from the vertical propeller, $T_{diff} = T_s - T_p$ is the difference between starboard and port side propeller thrust, d_y is the horizontal offset from the CV of the horizontal propellers and d_z is the vertical offset of the vertical propeller from the CV. Figure 2.2 shows the geometrical arrangements of the thrusters with

their positions with respect to the body-fixed frame.

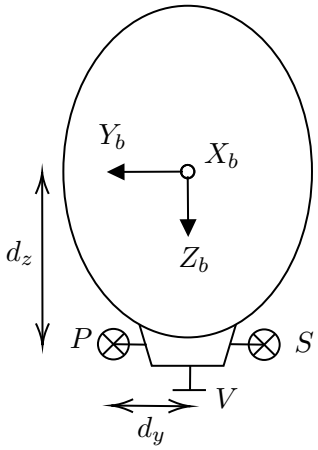

Figure 2.2: Frontal view of the blimp showing the positions of the three thrusters indicated by the letters S, P and V and their relative distances d_y and d_z with respect to the reference F_b.

2.6 Equation of Motion

At this point, we have presented the indoor blimp robot dynamic model (2.13) in the body-fixed reference frame. This model contains all the components including inertia matrix (2.15), Coriolis and centripetal matrix (2.17), damping matrix (2.18), restoring forces (2.19) and propulsion forces (2.20). We can report the 6 DOF body-fixed vector representation (2.13) in which we omit the superscript ^{b} and ^{n} because we know that $\boldsymbol{\xi}$ and $\boldsymbol{\eta}$ are defined in the body-fixed and earth-fixed reference frames respectively:

$$\boldsymbol{M}\dot{\boldsymbol{\xi}} + \boldsymbol{C}(\boldsymbol{\xi})\boldsymbol{\xi} + \boldsymbol{D}(\boldsymbol{\xi})\boldsymbol{\xi} + \boldsymbol{g}(\boldsymbol{\eta}) = \boldsymbol{\tau} \tag{2.21}$$

In addition to this we have also derived the kinematics equation:

$$\dot{\boldsymbol{\eta}} = \boldsymbol{J}(\boldsymbol{\eta})\boldsymbol{\xi}$$

If we write in components the 6 DOF dynamic model of the blimp (2.21) we obtain:

$$\begin{aligned}
m'_x\dot{v}^b_x + m\dot{\omega}^b_y z_G - \omega^b_z(m'_y v^b_y - m\omega^b_x z_G) + m'_z\omega^b_y v^b_z - v^b_x(D_{v_x} + D_{v^2_x}|v^b_x|) + (f_G - f_B)\sin\theta &= f_{px} \\
m'_y\dot{v}^b_y - m\dot{\omega}^b_x z_G + \omega^b_z(m'_x v^b_x + m\omega^b_y z_G) - m'_z\omega^b_x v^b_z - v^b_y(D_{v_y} + D_{v^2_y}|v^b_y|) - (f_G - f_B)\cos\theta\sin\phi &= f_{py} \\
m'_z\dot{v}^b_z + \omega^b_x(m'_y v^b_y - m\omega^b_x z_G) - \omega^b_y(m'_x v^b_x + m\omega^b_y z_G) - v^b_z(D_{v_z} + D_{v^2_z}|v^b_z|) - (f_G - f_B)\cos\theta\cos\phi &= f_{pz} \\
I'_x\dot{\omega}^b_x - m\dot{v}^b_y z_G + I'_z\omega^b_y\omega^b_z - v^b_z(m'_y v^b_y - m\omega^b_x z_G) - \omega^b_z(I'_y\omega^b_y + m v^b_x z_G) + m'_z v^b_y v^b_z & \\
-\omega^b_x(D_{\omega_x} + D_{\omega^2_x}|\omega^b_x|) + z_G f_G\cos\theta\sin\phi &= \tau_{px} \\
I'_y\dot{\omega}^b_y + m\dot{v}^b_x z_G - I'_z\omega^b_x\omega^b_z + v^b_z(m'_x v^b_x + m\omega^b_y z_G) + \omega^b_z(I'_x\omega^b_x - m v^b_y z_G) - m'_z v^b_x v^b_z & \\
-\omega^b_y(D_{\omega_y} + D_{\omega^2_y}|\omega^b_y|) + z_G f_G\sin\theta &= \tau_{py} \\
I'_z\dot{\omega}^b_z + v^b_x(m'_y v^b_y - m\omega^b_x z_G) - v^b_y(m'_x v^b_x + m\omega^b_y z_G) + \omega^b_x(I'_y\omega^b_y + m v^b_x z_G) - \omega^b_y(I'_x\omega^b_x - m v^b_y z_G) & \\
-\omega^b_z(D_{\omega_z} + D_{\omega^2_z}|\omega^b_z|) &= \tau_{pz}
\end{aligned} \tag{2.22}$$

2.7 Conclusion

In this chapter we have obtained the kinematic model of the indoor blimp using the representation of the Euler angles. Then we moved on to the dynamic model which is more complicated to derive. In Appendix A all the steps for the derivation of the equations of motion using the Newton-Euler formalism are reported. It is good to mention that the resulting mathematical model does not include the contribution of the environmental disturbances which are present inside the detector. Environmental modeling will be discussed in Chapter 4 after studying in detail what is the magnetic interaction between a Direct Current (DC) motor and an external magnetic field in Chapter 3.

Despite the general simplifying assumptions presented in section 2.2, the complexity of the 6 DOF model can be noted. The first difficulty come from the identification of parameters. However, for our application, we use an already existing blimp model which is the Blimpduino robot [51] with which it was possible to estimate the parameters that appear in the dynamics. The second difficulty comes from the nonlinear and coupled nature of the indoor blimp dynamic model that we recall have been simplified with respect to the general case. Even though this model tries as much as possible to represent the real situation, there are still many terms that cannot be modeled precisely or that are not really considered in the equations. Furthermore, many assumptions made to construct this model are far from reality when compared with the real situation.

For instance, the assumption of a prolate ellipsoid in which the lateral and vertical semi-axes are equal and less than the longitudinal one is not true for our prototype used. Thus the Lamb's k-factors for added-inertia calculation should be determined for this specific geometric shape of the hull. This could be very complex and may require expensive equipment like the wind tunnel to make real tests and acquire reliable data.

Another example of a simplifying assumption made for the dynamic model was to neglect the airflow generated by the propellers of electric motors. This hypothesis is not a correct approximation especially for our case in which the vertical thruster positioned under the hull is close to the surface of the balloon itself. The airflow generated by the propellers that skims the surface of the balloon influences aerodynamic effects such as drag forces.

As a last example we have assumed that the temperature, pressure and density of the air are constant during the experiment. In an indoor environment the thermodynamic properties of the air could change and this would have a greater influence on the buoyancy force, for example if the density of the air decreases then there is a loss of buoyancy force. However, we have solved these problems as we carried out our experiments in a cleanroom in the CERN laboratories and this guaranteed us that the ambient air conditions were controlled and constant.

Chapter 3

Magnetic Interaction

3.1 Introduction

To better understand the blimp's interaction with the external magnetic field, first of all we need to find what are the mechanical parts that can interact magnetically. This problem recalls the concept of magnetism that refers to magnetic fields and their effects on matter. Magnetism is caused by electric currents, i.e. motion of electric charges and the main part of the blimp in which there are electric currents and materials that can interact magnetically are the electric motors, in particular the most used for UAV applications are the Brushless Direct Current motors (BLDC motors).

The problem here is to characterize the magnetism of BLDC motors. This type of problem has never been addressed until now; indeed, research in the field of electromagnetic devices has always focused on the magnetic interactions that act inside the motor (between stator and rotor) that lead to the generation of torque. Examples of BLDC motor simulations and modeling that calculate the torque through magnetic interactions are reported in [57] and [30]. We are instead interested in characterizing the magnetic field of a BLDC motor outside its structure, and studying the effect of an external magnetic field on its materials.

As it will be reported in Section 3.2, the BLDC motor is composed by different materials like permanent magnets, ferromagnetic materials and windings in which current flows, this means that seen from the outside, it behaves like a magnetic material that is characterized by its own magnetic field that interacts with another external field, if present. In addition to this, it must be considered that BLDC motors are made up of ferromagnetic materials that can be hard (like the permanent magnets of the rotor) or soft (like the slotted structure of the stator). Soft materials are characterized by a high permeability and a low coercivity ($H < 1000$ A/m), which makes them easy to magnetize and demagnetize. Hard materials have a relatively low permeability and a high coercivity ($H > 10,000$ A/m), which makes them more difficult to magnetize and demagnetize. For this reason it is necessary to analyze also the magnetization effect that the external magnetic field exerts on this kind of motors.

At the end of this study we want to demonstrate that the sum of the two effects (permanent internal magnetization of the rotor and magnetization of the stator due to the external magnetic field) will give rise to a magnetic field distribution of the motor that resembles that of a magnetic dipole with an offset angle with respect to the axis of rotation of the motor. This allows us to make a simplifying assumption: at a certain distance, the motor, can be imagined as a magnetic dipole

moving inside an external magnetic field. This type of assumption greatly simplifies the calculation of the magnetic interaction of the blimp with the external field. Hence the problem boils down to calculating the forces and torques acting on a dipole moment immersed in a non-uniform magnetic field.

This chapter begins with the recall of the operating principle of BLDC motors (section 3.2) in which the internal structure of a brushless motor is described and the modality in which the motor torque is generated is specified. Also the control techniques for the stator currents are analyzed.

Then, in section 3.3 the various typologies of methods for simulating an electric motor given a certain geometry are explained. The *Finite Element Method Magnetics* (FEMM) simulation software is introduced, which solves magnetostatic problems with the finite element method (FEM).

In section 3.4, a 2D FEM simulation of a BLDC motor is carried out with the FEMM electromagnetic simulation software, this is done in order to characterize the external residual magnetic field of a inrunner BLDC motor. These simulations show that the electric motor has a magnetic field distribution that approaches that of a magnetic dipole, and this is due to the presence of the internal permanent magnet (PM) that generates a dipole moment perpendicular to the axis of rotation of the motor and to the contribution of the stator windings where current flows. All this is done in order to be able to magnetically model the motor and to treat it ideally as a magnetic dipole.

In this regard, in section 3.5 we study the behaviour of the motor immersed in an external uniform magnetic field. As mentioned before, the motor has soft magnetic materials that are able to magnetize themselves in the presence of an external magnetic field. This study was conducted through CST simulation software and the results show that there is another dipole moment due to the magnetization of the motor cover material. Hence, the total magnetic dipole moment of the motor is the sum of the dipole moment of the rotor, which is perpendicular to the axis of rotation, and the magnetic moment due to the magnetization of the ferromagnetic shell of the motor in the presence of the external field. In these simulations we will show the torques acting separately on the PM, on the cover and then the sum of the two. From these simulations, arguments and calculations will then be carried out that lead to the deduction of the magnetic moment of the two components and also the trend of the torques will be studied as the geometric parameters of the internal magnet and the external field vary.

3.2 Brushless DC motor

Before being able to magentically characterize a BLDC motor, it is appropriate to understand the operating principle of it. A BLDC motor also known as an *Electronically Commutated Motor* (ECM) or synchronous DC motor, is a synchronous motor using a direct current (DC) electric power supply. The windings of the motor that make up the stator part produce a rotating magnetic field that the permanent magnets of the rotor follow in space and this is guaranteed by a closed-loop electronic controller that changes the DC of the windings to generate this effect. The speed and the torque of the motor are controlled thanks to the electronic controller which monitors the phase and the amplitude of the DC current pulses. This electronic control system takes the place of brushes in the so called *brushes electric motors* where control takes place thanks to these mechanical commutators.

As regards the topology, being an electric motor, the BLDC motor consists of a stationary

component which is the stator and a rotary part which is the rotor. In particular, the rotor is made from PM and it is excited to spin with help of magnetic coupling. As shown in the Figure 3.1, the rotor can spin both inside or outside the stator. The first configuration is called *inrunner* in which the rotor rotates inside and the stator is external, while the opposite configuration in which the stator is internal and rotor external is called *outrunner*.

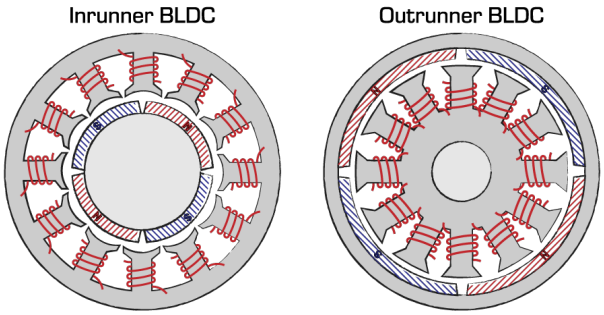

Figure 3.1: Comparison between inner (left) and outer (right) rotor configurations. From [88].

The stator is made out of laminated steel stacked up to carry the windings which are powered by electric current; this process produces the magnetic field thanks to the law of Biot-Savart[1] which is then rotated by the action of the electronic controller that switches from one winding to another. The stator arrangement can be of two patterns: a star (Y) or delta pattern (Δ), represented in Figure 3.2. Depending on the type of winding arrangement, the torque-speed function changes. In particular, the Y pattern gives high torque at low speed; on the contrary, the Δ pattern gives high torque at high speed.

Typically the windings are organized in three phases which are wound to the slots of the stator in the case in which this is constituted by a *slotted lamination steel*. There is actually an alternative to this configuration which is what is called *slotless lamination steel*. The slotless configuration has a drawback because it leaves more air-gap between rotor and stator armature which produces an unwelcome high reluctance in the magnetic circuit. This problem can be compensated by increasing the number of windings which decreases the space left free but at the same time it increases the cost of the motor due to the presence of more windings. The advantage instead of choosing the slotless configuration rather than the slotted one is that the latter has higher frictional drag and higher acoustic noise if compared to the slotless one.

To interpret the generation of the magnetic flux density B we must consider the stator as a magnetic circuit in which similarities can be made with electrical circuits. The expression of the magnetic flux is given by

$$\Phi = \frac{N \cdot I}{R} \tag{3.1}$$

where Φ is the magnetic flux, N is the number of windings, I is the current and R is the magnetic reluctance. In analogy with electrical circuits, the magnetic flux Φ [Wb] is the equivalent of the current, the magnetic reluctance R is the equivalent of ohmic resistance, the product of current and number of windings is the equivalent of the electric voltage and is called magnetomotive force (MMF). The reluctance is, just like resistance, a material parameter. Here we understand the presence of an iron core because it has a low reluctance and guarantees a greater magnetic flux.

[1] See Appendix B for the definition.

The magnetic circuit is closed by the air gap that allows the magnetic flux to pass from one part of the stator slots to the other. Depending on the cross section of the slotting teeth, the produced flux makes a given flux density measured in Tesla which is

$$B = \frac{\Phi}{A} \tag{3.2}$$

where A is the cross section of the flux conductor.

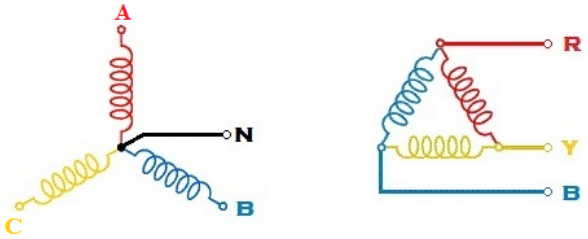

Figure 3.2: Comparison between star pattern (left) and delta pattern (right).

In a BLDC motor the rotor is made up of PM. Indeed in literature the abbreviation PM BLDC is often found which refers precisely to the nature of the rotor. PM can have multiple poles and the higher the number of the poles, the smaller the ripple in the magnetic torque at the cost of reducing the maximum speed. Therefore, if we fix the same rotor speed, increasing the number of poles, the electrical frequency of the windings will consequently increase, which however is limited by the speed of the microprocessor of the electronic controller. Usually, the rotor has an even number of poles: two or four in most of the applications [59].

The choice of rotor greatly affects the performance of the motor such as the maximum torque. A crucial factor is the choice of material and the manufacturing process which is essential to make the PM motor as efficient as possible. A fundamental physical value that indicates the quality of the magnet is the magnetic flux density B_r present in the datasheets of permanent magnets where the r stands for *retentivity*. Retentivity corresponds to the ability of a material to maintain a residual magnetic field value after reaching the saturation in a magnetization process; it is a characteristic that can be obtained from the hysteresis curve[2]. Nowadays, the most performing and most used PM are the Neodymium-Iron-Boron (NdFeB) magnets which provide the highest energy and residual flux density. Other types of magnets used are Alnico and ceramic magnets. Alnico is a family of iron alloys which in addition to iron are composed primarily of Aluminium (Al), Nickel (Ni) and Cobalt (Co), hence acronym Al-Ni-Co. Considering NdFeB magnets, they are simpler to produce compared to Alnico magents but more expensive than ceramic magnets. Typical B_r values for NdFeB magnets are in the range of 1 T to 1.35 T, as shown in the NdFeB Magnets /Neodymium Iron Boron Magnets datasheet [63].

3.2.1 Torque generation

To continue the knowledge of the operating principle of BLDC motors, let's see how the torque is generated once a magnetic field is built. The torque is generated through the magnetic interaction forces that exchange the rotor and the stator with each other. From the Faraday's law, a wire that

[2]See section B.2.7 in Appendix B for more details.

carries current, placed in a magnetic field, experiences a mechanical force which is the vectorial product of the current $\boldsymbol{i}$ [A] and the magnetic flux density $\boldsymbol{B}$ [T].

$$\boldsymbol{F} = l \cdot \boldsymbol{B} \times \boldsymbol{i} \tag{3.3}$$

where l [m] is the length of the wire. From the vector product in (3.3) it is possible to obtain the maximum electromagnetic force when the stator and rotor fields are in quadrature. This condition is what the designer will always have to try to achieve to maximize efficiency of the motor. To ensure a quadrature condition that lasts over time despite the rotor will try to cancel the phase shift, the stator currents must be constantly commuted in order to guarantee that there is a perennial tracking of the rotor around the stator currents. The resultant electromagnetic torque of this process is

$$\boldsymbol{T} = \boldsymbol{F} \times \boldsymbol{r} \tag{3.4}$$

where $\boldsymbol{r}$ is the lever arm of the force and corresponds to the vector which goes form the centre of the rotor to the air gap surrounding it. Therefore the torque depends on the size of the motor. In a PM BLDC motor once the geometry of the motor, the air gap, the constant magnitude of the rotating magnetic field $\boldsymbol{B}$ and the length of the wires have been fixed, the only parameter that can cause the torque to vary is the stator current. Hence it is possible to rewrite the expression (3.4) in a more compact form assuming that the current is perpendicular to the field

$$T = k_t I \tag{3.5}$$

where the k_t [Nm·A] is the motor torque constant and for a given motor it represents how much torque is produced per unit armature current.

3.2.2 Back Electromotive Force

Another important concept that is part of the principle of operation of the BLDC motor is the Back Electromotive Force (BEMF). The concept of BEMF comes from Faraday's law of induction which explains the formation of a counter electromotive force when there is a time-variant flux linkage in a coil. In particular this happens when the windings of the BLDC motor are energized and as soon as the motor starts rotating, the flux linkage in the coils changes. The BEMF is given by

$$BEMF = -\frac{d\varphi(\boldsymbol{B})}{dt} \tag{3.6}$$

Also in this case, as for the torque, the expression can be rewritten in a more useful form which is obtained by developing the derivative of the flux in equation (3.6)

$$BEMF = k_e \omega \tag{3.7}$$

where ω [rad/s] is the speed of the rotating $\boldsymbol{B}$ which is also the rotor speed, the constant k_e tells how much BEMF is produced per unit rotational speed. It can be seen that the electromagnetic force constant is equal to the torque constant $k_t = k_e = k$ [32]. The distribution of the magnetic flux in the air gap which depends on the arrangement of the stator windings determines the particular

waveform of the BEMF voltage [56]. Then the arrangement of the stator windings causes the BEMF to change the waveform, for a PM BLDC the arrangement produces a trapezoidal waveform. Another example is the sinusoidal BEMF waveform which is generated by the Permanent Magnet Synchronous Machine (PMSM) which is another kind of motor.

3.2.3 Motors control techniques

To conclude this section we briefly explain the electronic control techniques that are used to produce the torque resulting from the attraction and repulsion between the magnetic field of the stator and that of the rotor. The controller has the objective of changing the current flowing in the stator windings in order to generate a magnetic field that has a precise direction and amplitude, the direction is constantly changed in such a way that the rotor is attracted and repelled at the same time by the action of the rotating magnetic field and this guarantees the generation of torque. To have a constant torque, the electronic controller must ensure that the space vector of the current must be synchronous with the rotor and always maintain the direction in quadrature. To do this there are many control techniques that can be Trapezoidal, Sinusoidal and Field Oriented Control (FOC).

3.3 Electromagnetic simulation software

In order to study and analyze the interaction between an electric motor immersed in a magnetic field we have two ways to approach the problem: the simulation and the experiment. In reality the two compensate and one needs the other in order to deeply understand the phenomenon and arrive at predicting what happens in a given situation. In this work, as far as the magnetic disturbance part on electric motors is concerned, we focused on the simulation but we foresee as a future work that of putting into practice the results of the simulations that we have obtained through the electromagnetic simulation software.

The simulation, analysis and prediction of the magnetic characteristics of a PM BLDC motor are very difficult to obtain because of the complex geometries used and due to the presence of nonlinear magnetic materials associated with the motor. The nonlinear behavior of magnetic materials refers to the magnetization curve which is represented by the phenomenon of hysteresis (see Appendix B). Despite this complexity, many methods have been developed over the years that attempt to solve the problem of electromagnetic simulation of electric motors. They are the Finite Difference Method (FDM), the Boundary Element Method (BEM) and the Finite Element Method (FEM). Among these the most used is the FEM method, this is because it is able to represent geometrically complex structures such as that of an electric motor and to represent nonlinear magnetic materials that characterize it. The finite element method (FEM) has proved to be particularly flexible, reliable, and effective in the analysis and synthesis of power-frequency electromagnetic and electromechanical devices [44], [69], [9], [24].

In this thesis we have used two different magnetic simulation software which are FEMM and CST Studio Suite. FEMM is a suite of programs that solves linear/nonlinear magnetostatic problems, linear/nonlinear time harmonic magnetic problems, linear electrostatic problems and steady-state heat flow problems. For our purposes we have used the suite of the nonlinear magnetostatics problem. The advantage of FEMM package lies in being an open source, user friendly, accurate

and low computational cost freeware product. For these reasons it is widely used in science and engineering especially at the didactic level. Its applications range from electromagnetism, materials science, industry, medicine, experimental particle physics, robotics, astronomy and space. In the proposed model, FEMM software package has been used to investigate the external magnetic field produced by PM BLDC motor. Another important aspect is that it contains a CAD-like interface to draw the geometry of interest and for defining material properties and boundary conditions. It also has the ability to import AutoCAD DXF files to facilitate the analysis of existing geometries [10]. Then it has a post processing part in which it can be possible to extract the values of the magnetic field in certain areas or contours and contains the Lua scripting language integrated into the interactive shell which can be used to program processing functions automatically [66].

On the other hand CST Studio Suite is a computational electromagnetism tool developed by Dassault Systèmes Simulia. It contains several simulation methods, including FEM and it is a high performance 3D electromagnetic analysis software package for the design, analysis and optimization of electromagnetic components and systems. Typically the electromagnetic analysis simulated with CST is aimed at calculating the performance and efficiency of antennas and filters, electromagnetic compatibility and interference, exposure of the human body to electromagnetic fields, electromechanical effects in motors and generators and thermal effects in high-power devices. CST Studio Suite is employed in the main technology and engineering companies all over the world and in fact I had the opportunity to use it during my internship at CERN.

3.4 Simulation of PM BLDC Motor

In this section a 2D static FEM simulation is carried out with the FEMM software. This simulation is inspired to the electronically commutated Maxon EC motors shown in Figure 3.3 [65]. It analyzes the external magnetic field of a BLDC motor and compares this with the field distribution of a magnetic dipole moment. The results obtained show that the external magnetic field of an electric motor is given by two contributions, one coming from the permanent magnet of the internal rotor and the other from the stator current windings. This simulation being magnetostatic does not take into account the effect of the magnetization of the stator as only the field emitted by the motor is evaluated and the external applied one is not yet considered.

Figure 3.3: Maxon EC 32. From [65].

3.4.1 Magnetostatic problem

To perform this simulation the FEMM software solves the magnetostatic problem that we briefly report in this paragraph (see Appendix B for more details). Magnetostatic means that the field is

time-invariant. In this case, the field intensity $\boldsymbol{H}$ and flux density $\boldsymbol{B}$ must obey Maxwell equations [49]:

$$\boldsymbol{\nabla} \times \boldsymbol{H} = \boldsymbol{J} \tag{3.8}$$

$$\boldsymbol{\nabla} \cdot \boldsymbol{B} = 0 \tag{3.9}$$

where $\boldsymbol{J}$ is the density current. The relationship between B and H is called constitutive relationship and is given by:

$$B = \mu H \tag{3.10}$$

where μ is the magnetic permeability of the material, a physical quantity that expresses the ability of the material to become magnetized in the presence of a magnetic field. The magnetic permeability generally depends on the position inside the material and on the direction of the magnetic field: it is therefore described with a second order tensor. If the medium is isotropic and homogeneous it is reduced to a scalar. If a material is nonlinear (e.g. alnico magnets), the permeability μ is a function of B:

$$\mu = \frac{B}{H(B)} \tag{3.11}$$

FEMM software solves the equations (3.8), (3.9) and (3.10) through the vector potential $\boldsymbol{A}$ which can be used to write the flux density

$$\boldsymbol{B} = \boldsymbol{\nabla} \times \boldsymbol{A} \tag{3.12}$$

This definition of $\boldsymbol{B}$ satisfies (3.9). Then, (3.8) can be rewritten as

$$\boldsymbol{\nabla} \times \left(\frac{1}{\mu(B)} \boldsymbol{\nabla} \times \boldsymbol{A} \right) = \boldsymbol{J} \tag{3.13}$$

If we assume that the material is isotropic and linear (so that μ is constant) and we apply the Coulomb gauge $\boldsymbol{\nabla} \cdot \boldsymbol{A} = 0$, equation (3.13) reduces to

$$-\frac{1}{\mu} \boldsymbol{\nabla}^2 A = \boldsymbol{J} \tag{3.14}$$

To solve magnetostatics problems where the $B - H$ relationship is nonlinear, FEMM uses the equation (3.13). These are elliptic partial differential equations, a form that appears in many engineering phenomena and to solve them there are a large number of tools that have been developed over the years.

3.4.2 Modeling of PM BLDC

The specifications of the motor used for FEMM simulation are given in Table 3.1. Here the permanent magnets of inner rotor are chosen as N42 (Neodymium Magnet) while the material chosen for the stator is M-22-Steel (Silicon Steel). Material properties chosen for various components and electromagnetic properties of the three phase windings are detailed in Table 3.2. The material chosen as the stator, silicon steel M22, is a nonlinear material, i.e. its $B-H$ characteristic is not a straight line because the magnetic permeability is not constant. While the material chosen for the rotor, a sintered NdFeB PM, is a linear magnetic material with constant magnetic permeability. The two

characteristics are shown in Figure 3.4. The developed PM BLDC motor model has been shown in Figure 3.5a. Stator windings are made of plain stranded copper wire, the numeber of strand is 8 and the strand diameter is 0.34 mm. The windings turns per stator' slot are 100 and each winding is excited by three phases current, namely A, B, and C of 3 A. The simulation is carried out in an instant in which the rotor has the north pole in the vertical direction and the maximum current flows in phases B and C and zero current in phase A to make the rotor rotate in an anti-clockwise direction. The motor has been modeled with 909109 nodes and 1817655 elements, the meshed 2D model is shown in Figure 3.5b. Flux lines established at a distance of 1 meter from the motor, for the given excitation of the three phases is shown in Figures 3.6.

Inner rotor radius	8 mm
Stator radius	20 mm
Rotor pole	2
Stator slots	6

Table 3.1: Motor specifications.

Stator	M-22-Steel (Silicon Steel) Nonlinear B-H Relationship Electrical Conductivity $\sigma = 1.9$ MS/m
Rotor	N42 (Sintered NdFeB) Linear B-H Relationship Relative $\mu_x = 1.05$ Relative $\mu_y = 1.05$ Coercitivity $H_c = 994529$ A/m Electrical Conductivity $\sigma = 0.667$ MS/m
Air	Linear B-H Relationship Relative $\mu_x = 1$ Relative $\mu_x = 1$
Stator Windings	Copper Linear B-H relationship Relative $\mu_x = 1$ Relative $\mu_x = 1$ Electrical Conductivity $\sigma = 58$ MS/m Plain stranded wire Number or strand 8 Strand diameter 0.34 mm Number of turns used 100 Current in each phases 3 A

Table 3.2: Material properties.

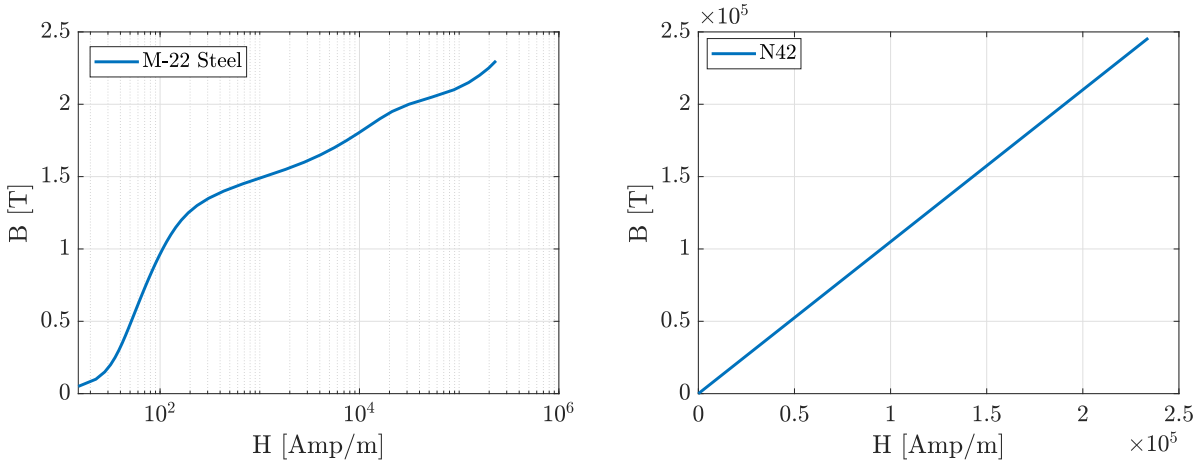

(a) **(b)**

Figure 3.4: M22-steel (a) and N42 (b) $B - H$ curve.

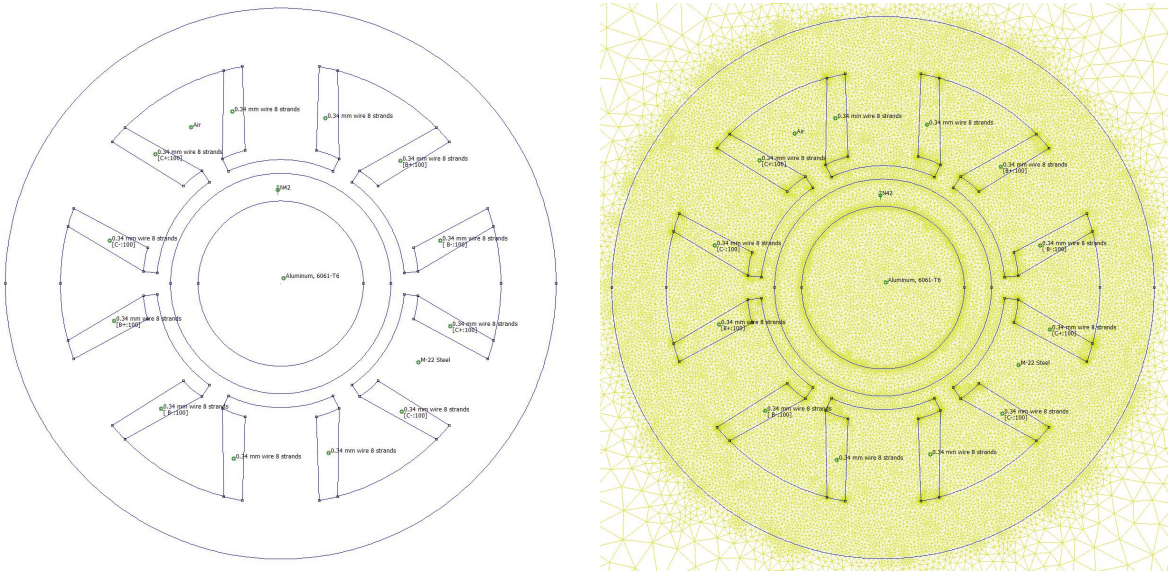

(a) **(b)**

Figure 3.5: FEMM BLDC motor model (a). FEMM BLDC FEM meshed 2D model (b).

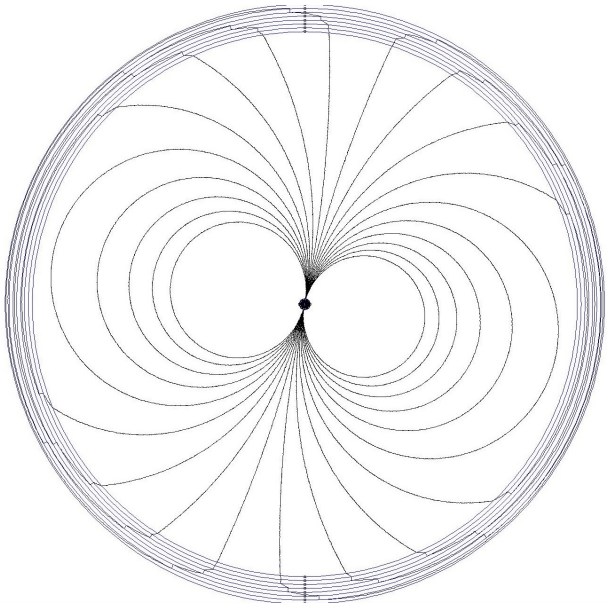

Figure 3.6: BLDC magnetic field lines obtained with FEMM simulation software.

3.4.3 Results and discussions

From Figure 3.6 it is evident that the distribution of the external magnetic field is comparable with that of a magnetic dipole, which from section B.1.4 in Appendix B is equal to equation (B.27) that we reported here in spherical components.

$$\begin{cases} B_r = \dfrac{\mu_0 m}{4\pi r^3} 2\cos(\theta - \theta^*) \\ B_\theta = \dfrac{\mu_0 m}{4\pi r^3} \sin(\theta - \theta^*) \\ B_\phi = 0 \end{cases} \tag{3.15}$$

This is the magnetic field distribution of a dipole moment in spherical coordinates where m is the magnitude of the moment vector, r is the distance between the measuring point of the field and the origin of the reference system, θ is the polar angle and ϕ is the azimuthal angle. In this case the dipole is not aligned with the z-axis (see Figure B.4) but has an offset angle equal to θ^*. From the FEMM simulation, the tangential and normal components of the magnetic field along a circumference that is 1 meter from the motor are obtained, Figure 3.7 shows these components and their module. We can compare the single spherical components of the magnetic field with those of a dipole placed at the same distance of 1 meter and with an offset angle from z-axis equal to θ^*. In particular, it is possible to derive the value of m from the motor curve. Considering the zero crossing angle for the radial component $B_r(\theta^*)$ we obtain

$$m = \frac{2B_r(\theta^*)\pi r^3}{\mu_0}$$

With this value of m, the radial and tangential magnetic field curves are drawn using the dipole model (3.15) and finally compared with those obtained from the software simulation (Figures 3.7). Then the errors on the single components are calculated as the difference between the values taken

from the dipole model and those of the simulation (Figure 3.8).

$$\begin{cases} \epsilon_r = B_{r,dip} - B_{r,sim} \\ \epsilon_r = B_{\theta,dip} - B_{\theta,sim} \end{cases}$$

This 2D FEMM simulation shows us that the magnetic field external to a BLDC motor can be well represented by the field of a magnetic dipole at a distance of 1 m. In particular, the magnetic field of the BLDC motor is the superposition of the magnetic field of the permanent magnet of the internal rotor and the magnetic field of the 3 phases of the currents flowing in the windings of the stator slots. The following study shows that the contribution of the latter on the total field is weaker. Two other FEMM simulations are presented in which the same motor is simulated but once without internal rotor and once without currents in the windings to compare the contribution these make to the total external field of the motor.

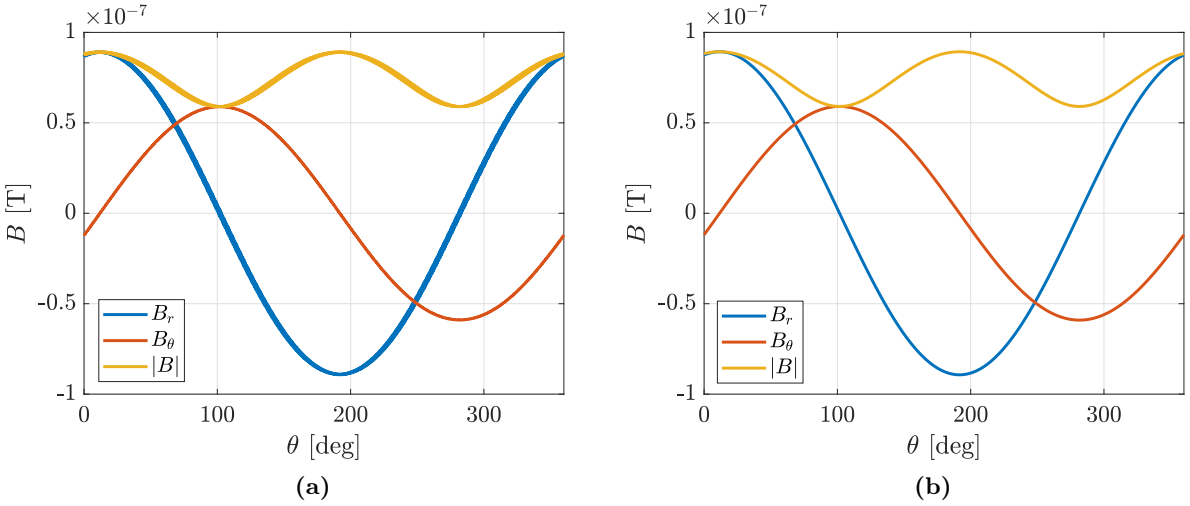

Figure 3.7: Spherical components of the magnetic field for a BLDC motor simulated in FEMM (a) and for a magnetic dipole with $\theta = 11.6\,deg$ and $m = 0.4465\,Am^2$ at $r = 1$ m.

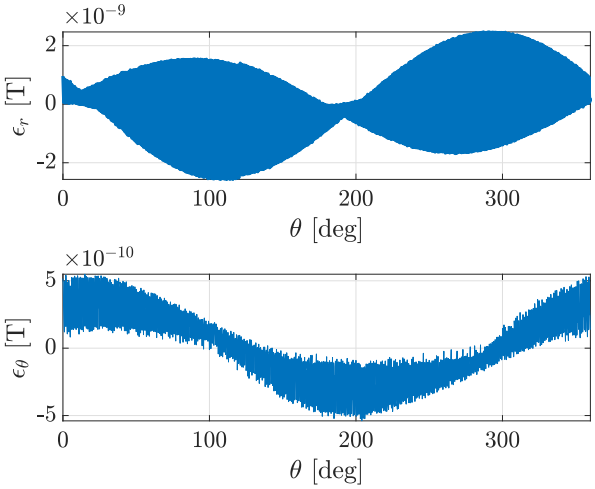

Figure 3.8: Errors of the magnetic field as the difference of the radial and tangential components between the dipole values and simulation values for the BLDC motor.

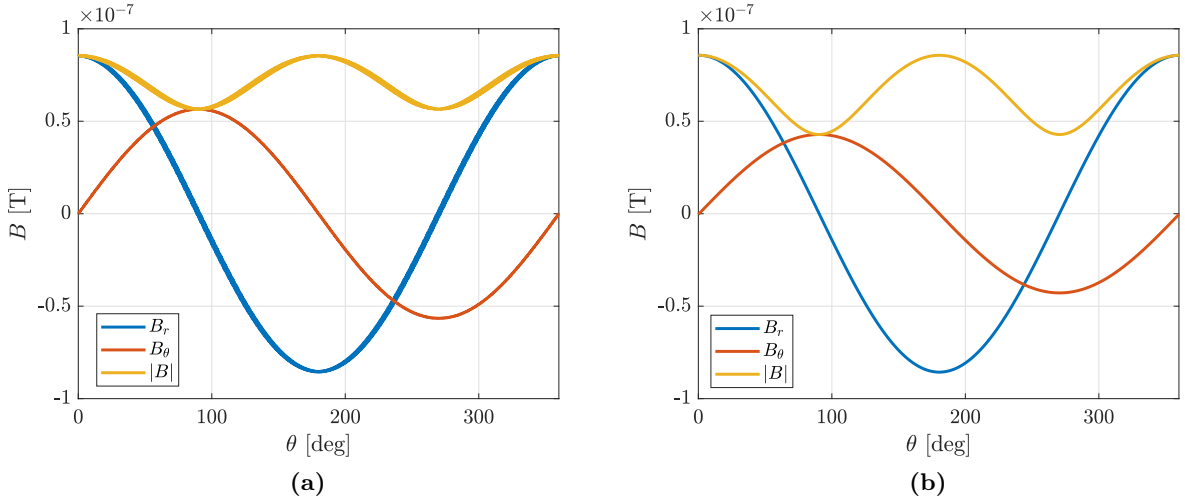

Figure 3.9: Spherical components of the magnetic field for a BLDC motor in which zero current flows in the windings simulated in FEMM (a) and for a magnetic dipole with $\theta = 0.5\,deg$ and $m = 0.4283\,Am^2$ at $r = 1$ m.

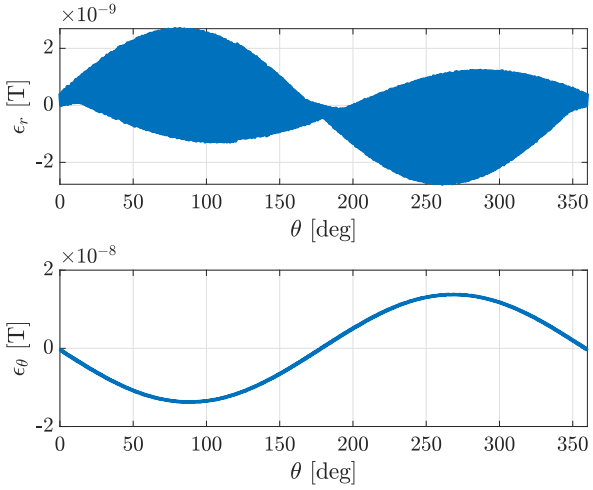

Figure 3.10: Errors of the magnetic field as the difference of the radial and tangential components between the dipole values and simulation values for the BLDC motor with zero current in the windings.

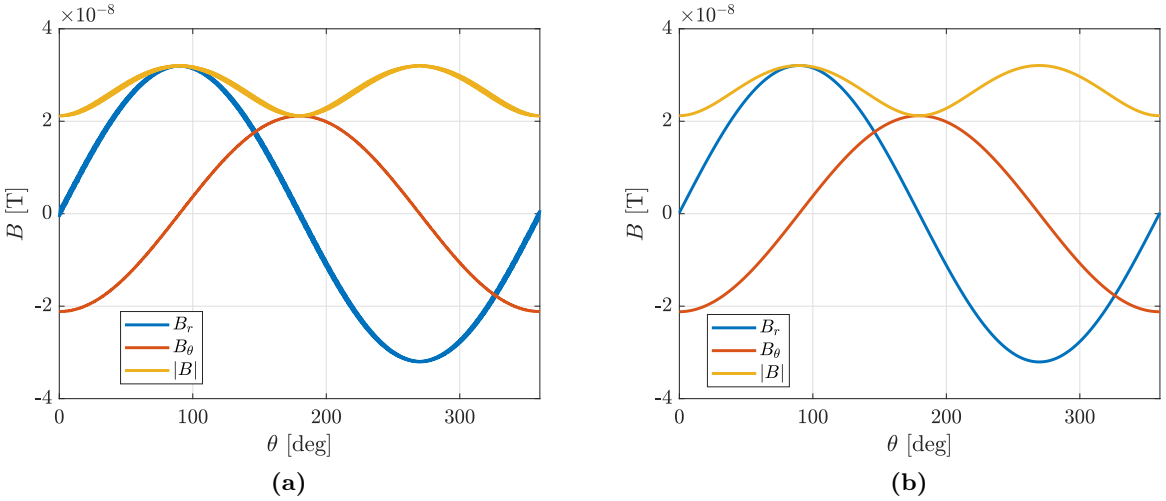

Figure 3.11: Spherical components of the magnetic field for a BLDC motor in which there is no internal rotor simulated in FEMM (a) and for a magnetic dipole with $\theta = 89.63\,deg$ and $m = 0.1603\,Am^2$ at $r = 1$ m.

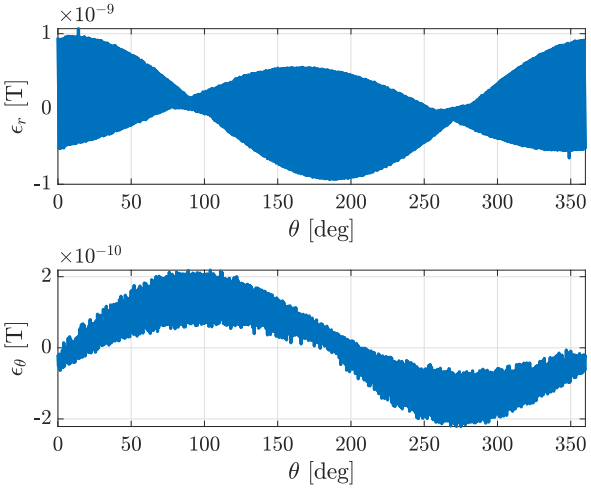

Figure 3.12: Errors of the magnetic field as the difference of the radial and tangential components between the dipole values and simulation values for the BLDC motor in which there is no internal rotor.

Figures 3.7 and 3.8 refer to the case in which the BLDC motor is on, Figures 3.9 and 3.10 refer to the case in which there is no current in the windings (there is only the contribute of the internal rotor), Figures 3.11 and 3.12 refer to the case where current flows in the stator windings but the internal rotor is not present. Figure 3.10 and 3.12 show the magnetic field errors calculated as the difference of the radial and tangential components between the dipole values and the simulation values for the two cases in which the current windings are off and the internal rotor is not present. By looking at Figures 3.9 and 3.11 and comparing the obtained equivalent dipole moments, it can be assumed that the magnetic field generated by the stator currents alone is one order of magnitude lower than the field generated by the internal rotor alone.

In conclusion, from this study we can deduce that the magnetic characterization of the motor outside it sees a distribution of the magnetic field rotating with the direction of the rotor and disturbed by the effect of the stator current phases that they too generate magnetic fields that follow the trend of the currents themselves over time and which, when added together, contribute to the field of the internal rotor but in a weak way. The result obtained in these simulations simply shows that a PM is characterized by a magnetic moment per unit of volume which therefore generates its own magnetic field distribution. The same applies to the stator currents which are simply coils wound around a ferromagnetic material and which are characterized by their own magnetic moment. These simulations are static, i.e. they are representations in a precise instant of time. Therefore, we are not taking into account that the magnetic field distribution (formed by the overlap of the rotor field and the coils field) is rotating over time because of the rotation of the rotor and the spatial distribution of the three phases of the stator.

An effect that we are not considering in this study is that, being the stator made of an easily magnetizable ferromagnetic material, there will be a magnetization effect of the stator due to the magnetic field of the internal permanent magnet and this in turn will generate an external magnetic field that will contribute to the whole field. The expected effect is that the external field that for now is being considered only that of the rotor and the currents will be disturbed by the effect of the stator material that has become magnetized.

3.5 Simulation of PM BLDC motor in external field

This section analyzes the behavior of a BLDC motor within a uniform external magnetic field through a CST software simulation with the aim of calculating the torques that act on its components. This simulation is fundamental to extract information about the total magnetic moment of the motor through the characterization of its internal components that interact individually with the field. This is done in view of a practical test in which it is possible to reproduce the simulation experiment by testing a true DC motor within a constant magnetic field generated by a magnet and consequently measuring the torques acting on it. From the analyzes carried out in the previous section 3.4 it has been demonstrated that the motor seen from the outside can be represented as a magnetic dipole moment perpendicular to the axis of rotation of the motor which is due to the contribution of the permanent magnet of the rotor and the stator windings, we call this $\boldsymbol{m}_1$.

If we insert a dipole inside an external field, we would expect the dipole to align with the magnetic field lines so that the motor axis should be positioned perpendicular to the field lines. However, this is not what really happens. In fact, it is noted that the motor assumes a position of

equilibrium with an angle between the axis and the field lines of less than 90 degrees. This means that the dipole moment that characterizes the motor is not actually perpendicular to the rotation axis but has a certain offset angle with respect to the axis. Hence, at the dipole moment of the permanent magnet, another moment must be added, whose vector sum gives this offset angle. This total magnetic moment then aligns itself with the field lines making the motor assume an inclined position with respect to the vertical position. The second moment to be added is inevitably that coming from the ferromagnetic material of the external structure which is strongly influenced by the external field.

As reported in section B.2, in the presence of an external magnetic field, a ferromagnetic material becomes magnetized and generates a certain distribution of magnetic field which is the same as would be produced by a volume current throughout the material and a surface current on the boundary. The motor seen from the outside can be considered as a hollow cylinder of soft ferromagnetic material. If this is inserted in a constant distribution of magnetic field, the lines of $\boldsymbol{B}$ thicken inside the material because they meet a higher permeability than that of air, this thickening effect of the lines of $\boldsymbol{B}$ generates an alignment of all the small atomic magnetic dipoles that characterize the material, the alignment generates a global magnetization of the object $\boldsymbol{M}$, consequently this effect can be represented as a magnetic dipole moment $\boldsymbol{m}_2 = \boldsymbol{M}V$, with V the volume of the solid. This modeling of the motor is shown in Figure 3.13, where the hollow cylinder representing the outer cover of the motor and the inner permanent magnet representing the rotor are shown. Moreover, the two moments of magnetic dipole are represented with which the magnetism of the entire system is modeled. Therefore the vector sum of the two then aligns itself with the lines of $\boldsymbol{B}$, making the motor assume a certain equilibrium configuration.

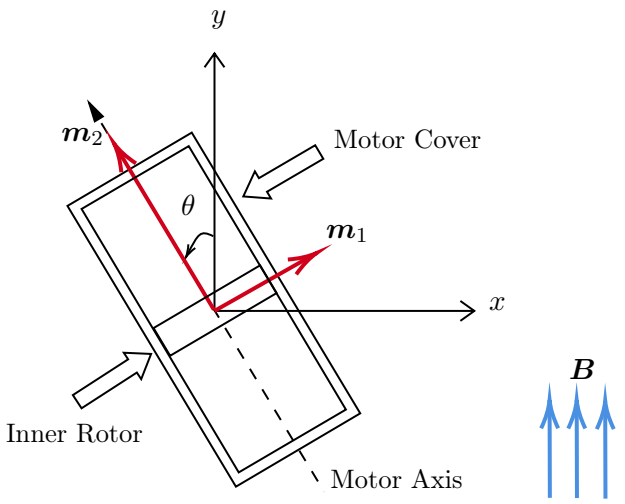

Figure 3.13: Modeling of the motor immersed in a uniform magnetic field $B = 0.3$ T.

3.5.1 Calculation of the torques on the motor

The geometry shown in the Figure 3.13 is simulated within the CST software and it is reported in Figure 3.14. This is done in order to calculate the magnetic torques acting on the motor cover and on the internal magnet for different motor configurations with the θ angle in Figure 3.13 varying from 0 to 2π and for a uniform magnetic field along the y-axis of 0.3 T. Then the sum is made to obtain the torque on the entire system. The result of the simulation are shown in the Figure 3.15

where the magnetic torque values on the magnet, on the cover and the sum of the two are reported as θ angle varies.

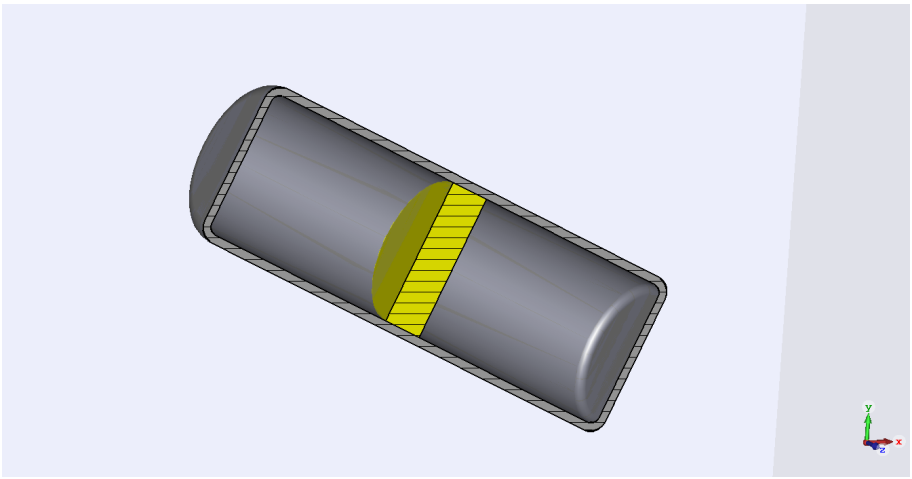

Figure 3.14: Modeling of the BLDC motor with the CST software.

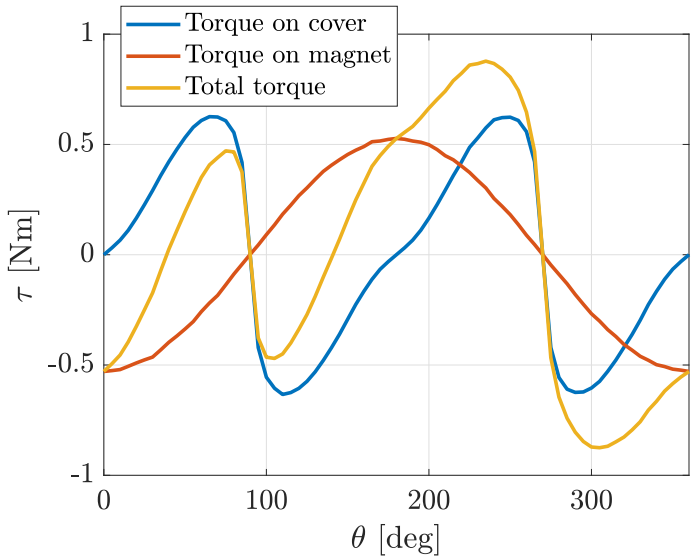

Figure 3.15: Magnetic torque on the motor as the sum of the torque on the motor cover and on the internal permanent magnet, obtained with the CST simulation with a uniform magnetic field $B = 0.3$ T along the y direction as the rotation angle of the motor axis θ varies.

As shown in section B.2 the torque on a dipole $\boldsymbol{m}$ in a field $\boldsymbol{B}$ is given by

$$\boldsymbol{T} = \boldsymbol{m} \times \boldsymbol{B} = mB \sin\theta \, \hat{z}$$

From this type of curves the goal is to extract the information of m (both for the magnet and for the cover). This information will be useful later in order to calculate the torque and force acting on the motor if immersed in a non-uniform magnetic field. Let's start by analyzing the rotor torque curve.

- **Permanent magnet of the inner rotor**

The inner rotor of the BLDC motor is a PM (like the neodymium magnet), so it behaves like a

magnetic dipole which is 90 degrees from the cylinder axis. A torque equal to

$$\tau_1(\theta) = Bm_1 \sin(\theta - 90) \tag{3.16}$$

acts on it. There is a shift of 90 degrees because the magnetization direction of the PM is perpendicular to the axis of the cylinder from which the θ angles are calculated. To extract m_1 from the torque curve on the magnet obtained with CST in Figure 3.15, we calculate the angle θ at which the torque is maximum, and this angle is 180 degrees, therefore

$$\tau_1(180) = Bm_1 \Rightarrow m_1 = \frac{\tau_1(180)}{B} = 1.7574\, Am^2$$

with this value of m_1 we can calculate the magnetic torques acting on an equivalent dipole of intensity m_1 which therefore represents the internal rotor of an electric motor. In Figure 3.16 we compare the two torque curves: the one obtained with the CST simulation (the red one in Figure 3.15) and the one obtained with the hypothesis of a perfect magnetic dipole given by equation (3.16). Then, in Figure 3.17 the error between the two curves is calculated, i.e. the difference between the torques calculated in the two different methods divided by the maximum value of the torque obtained with the CST simulation. From Figure 3.17 it can be seen that passing from the real model to the dipole model, for the inner magnet, there is a relative error with respect to the maximum value of the torque of about 1%. The error is low, indeed the perfect dipole approximation for the permanent magnet is sufficiently adequate.

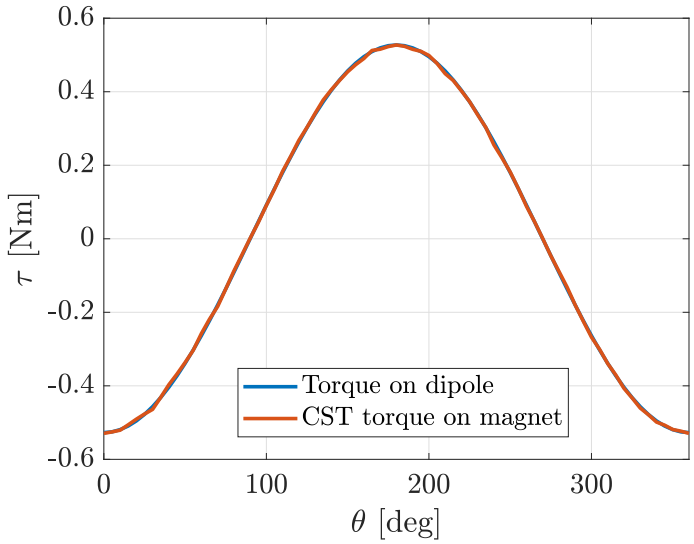

Figure 3.16: Magnetic torque on the permanent magnet obtained with the CST simulation compared to the magnetic torque acting on a dipole moment $m_1 = 1.7574$ Am^2 as the rotation angle of the motor axis θ varies.

- **Ferromagnetic cover of the motor**

Let us now consider the contribution of the torque given by the motor cover. In the presence of the external magnetic field, this becomes magnetized and generates a magnetic dipole per unit volume which is aligned with the cylinder axis because it follows the flow of the magnetic field lines that

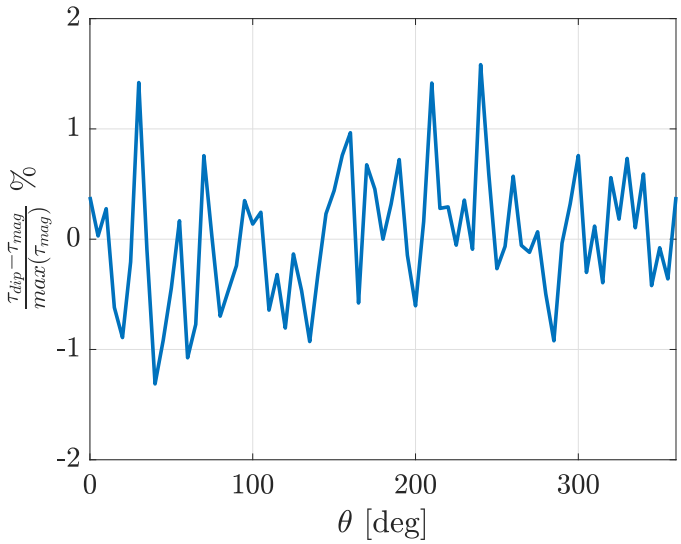

Figure 3.17: Magnetic torque relative error obtained as the difference between the torque calculated with the dipole model and the torque obtained with the CST simulation divided by the maximum value of the simulation torque on the permanent magnet of the rotor as the rotation angle of the motor axis θ varies.

enter the structure from the bottom up. However, the direction of magnetization reverses when θ exceeds 90 degrees even if from the magnetic field point of view, the lines continue to go from the bottom up. In practice, when the axis motor is at 90 degrees from the y-axis, in that instant the $\boldsymbol{B}$ field lines follow the thickness of the motor cover both to the right and to the left, thus there exists a magnetic moment in both directions giving a null effect. This situation is represented in Figure 3.15 where it can be seen that at $\theta = 90$ degrees the torque on the cover change sign. As the motor axis exceeds the 90 degree angle from the y-axis, the field lines follow again the direction of the cylinder axis and in this case the magnetization of the cover is in the opposite direction compared to the case in which $\theta < 90$ degrees. The situation in which $\theta = 90$ degrees is shown in the Figure 3.18. In this situation, the lines of $\boldsymbol{B}$ which magnetize the hollow cylinder do not have a preferential direction to enter, therefore they contribute both in the positive direction of the cylinder axis and in the negative direction. When the axis of the motor exceeds $\theta = 90$ degrees, in that case the lines of $\boldsymbol{B}$ flow preferentially in the direction of the axis always from the bottom to the top, therefore the dipole moment has overturned compared to the previous case.

Again from the torque curve obtained with the CST simulation we want to extract the information of m_2 and therefore find an analytical expression for the curve. Looking at Figure 3.15 for the torque curve on the motor cover (the blue one), it can be deduced that for $0 < \theta < 90$ degrees the law is a classic sine curve with an amplitude equal to Bm_2. At $\theta = 90$ degrees the moment resets and starts overturned therefore a torque will always act on it that follows the sinusoidal law but in this case translated by 180 degrees, this is followed until the motor reaches an orientation of 270 degrees. The analytical expression of the torque curve will be given by the following expression.

$$\tau_2(\theta) = \begin{cases} Bm_2 \sin\theta & \text{for } 0° < \theta < 90° \\ Bm_2 \sin(\theta + 180) = -\sin\theta & \text{for } 90° < \theta < 270° \\ Bm_2 \sin\theta & \text{for } 270° < \theta < 360° \end{cases} \tag{3.17}$$

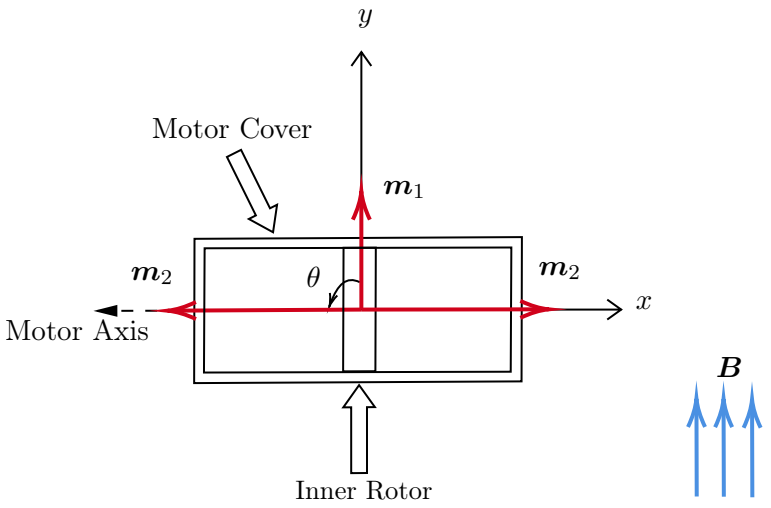

Figure 3.18: Modeling of the motor immersed in a uniform magnetic field $B = 0.3$ T in the case in which $\theta = 90$ degrees and there are two opposite magnetizations of the cover which give a null contribution.

To obtain the analytic expression from this case function, we have to multiply each parts by the angle window. We want to filter the piece of function in that interval and ignore the remaining parts. To do this we use the rectangular function that is a combination of the step function which is defined as

$$\delta_{-1}(t) = \begin{cases} 1 & \text{if } t > 0 \\ 0 & \text{if } t \leq 0 \end{cases}$$

This is the general definition but our domain of interest is the θ angle. Let's filter the equation (3.17) through the different angular windows defined as a combination of step function.

$$\tau_2(\theta) = Bm_2 \Big\{ \big[\delta_{-1}(\theta) - \delta_{-1}(\theta - 90)\big] \sin\theta + \big[\delta_{-1}(\theta - 90) - \delta_{-1}(\theta - 270)\big](-\sin\theta) + \big[\delta_{-1}(\theta - 270) - \delta_{-1}(\theta - 360)\big] \sin\theta \Big\}$$

Rearranging the terms we get

$$\tau_2(\theta) = Bm_2 \sin\theta \Big\{ \delta_{-1}(\theta) - 2\delta_{-1}(\theta - 90) + 2\delta_{-1}(\theta - 270) - \delta_{-1}(\theta - 360) \Big\} \tag{3.18}$$

To calculate m_2 we consider the torque curve on the cover obtained with CST, we obtain the θ angle at which the torque is maximum, and this angle is 65 degrees, therefore:

$$\tau_2(65) = Bm_2 \Rightarrow m_2 = \frac{\tau_2(65)}{B} = 2.0866\, Am^2$$

In Figure 3.19 we compare the two torque curves: the one obtained with the simulation (the blue one in Figure 3.15) and the one obtained with the hypothesis of a perfect magnetic dipole given by equation (3.18). Then, in Figure 3.20 the error between the two curves is calculated, i.e. the difference between the torques calculated in the two different methods divided by the maximum value of the torque obtained with the simulation.

Comparing the two curves in Figure 3.19 it can be immediately seen that the magnetic dipole

model approximates quite well the real torque curve obtained with the simulation. The relative errors in Figure 3.20 are less than 10% except in two instants in which they reach the value of 30%, this is due to the fact that in the dipole model it was assumed that when the θ angle is 90 degrees, the vector m_2 resets and then reverses immediately its direction. However, in the real process this phenomenon will be slower and more gradual and this is underlined by the real curve in Figure 3.19 in which at 90 degrees it drops more smoothly and not abruptly as a perfect dipole would do.

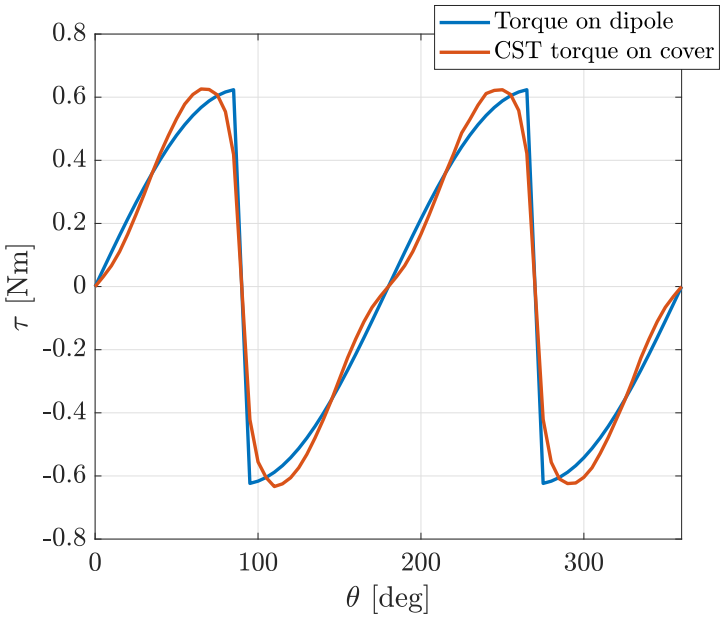

Figure 3.19: Magnetic torque on the motor cover obtained with the CST simulation compared to the magnetic torque acting on a dipole moment $m_2 = 2.0866$ Am^2 as the rotation angle of the motor axis θ varies.

- **Total torque on motor**

We have previously calculated the values of m_1 and m_2 starting from the torque curves obtained with the simulation in Figure 3.15. With these values and together with the known value of $\boldsymbol{B}$ we have obtained an analytical expression for the torque that best approximates the real behavior of the two components (cover and magnet). At this point we can add the two effects and obtain the torque curve that acts on the complete system and then compare it with the real one. Figure 3.21 compares the two torque curves while Figure 3.22 shows the relative errors calculated as the difference between the total torque obtained with the dipole method and that obtained with the CST simulation divided by the maximum torque value obtained with the simulation. Also in this case it is possible to notice that with the magnetic dipole approximation the overturning of the magnetization moment of the cover is more abrupt than the smoother variation of the real motor. Relative errors are always kept at a value of less than 10% except in the two critical situations in which the inversion of the magnetization occurs.

3.5.2 From total torques to magnetic dipoles

Now let's consider the problem in which we only know the total torque curve as it will be the curve obtained by carrying out an experiment which can be the yellow one shown in Figure 3.15. From

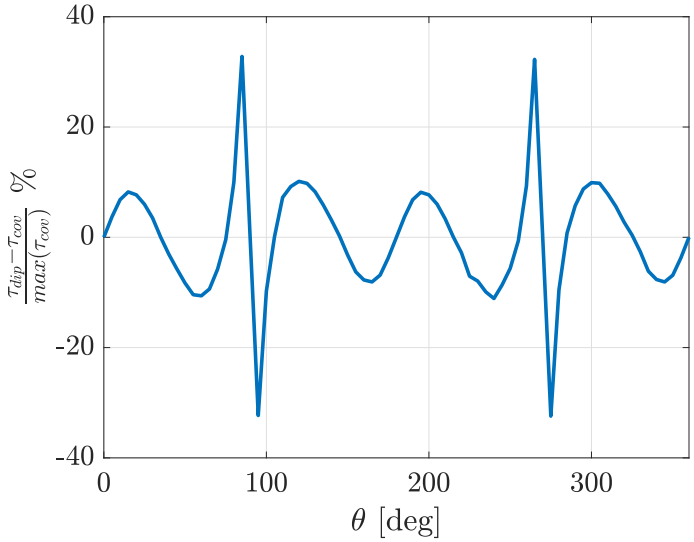

Figure 3.20: Magnetic torque relative error obtained as the difference between the torque calculated with the dipole model and the torque obtained with the CST simulation divided by the maximum value of the simulation torque on the cover as the rotation angle of the motor axis θ varies.

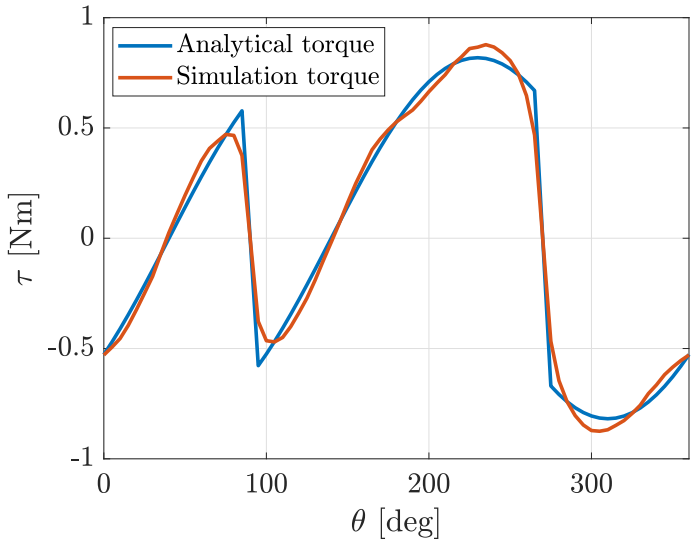

Figure 3.21: Comparison of the magnetic torque acting on the motor between the analytical method and the CST simulation method as the rotation angle of the motor axis θ varies.

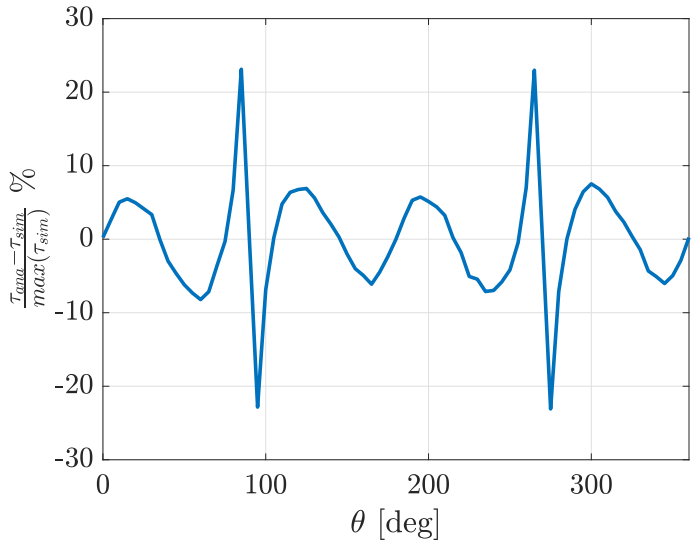

Figure 3.22: Magnetic torque relative errors calculated as the difference between the total torque obtained with the dipole method and that obtained with the CST simulation, divided by the maximum torque value obtained with the simulation for the entire total motor as the rotation angle of the motor axis θ varies.

this curve we should be able to extrapolate information about the two magnetic dipole moments which constitute the motor. Knowing that the rotor is perpendicular to the motor axis, if we align the axis of the motor to the y-axis (direction of $\boldsymbol{B}$), we know that no torque acts on the dipole of the cover because it is aligned with the field while the rotor is subjected to a maximum torque in magnitude. Therefore if we take the value of the total torque for $\theta = 0$ degrees, at that point the torque is given only by the contribution of the rotor.

$$\tau_{tot}(\theta) = \tau_1(\theta) + \tau_2(\theta)$$

with $\tau_1(\theta)$ and $\tau_2(\theta)$ given by equations (3.16) and (3.18). For $\theta = 0$ degrees we have

$$\tau_{tot}(0) = \tau_1(0) + \tau_2(0) = Bm_1 \sin(-90) = -Bm_1$$

from which we can calculate m_1

$$m_1 = \frac{\tau_{tot}(0)}{-B} = 1.7642 Am^2$$

Once we have obtained m_1 we can plot the torque curve of the rotor $\tau_1(\theta)$ and by difference with the total simulation one, the torque curve of the cover is obtained. From the plot of the cover torque, we can then extract the magnetic dipole of the cover m_2: we calculate the angle θ at which the torque is maximum, and this angle is 65 degrees, therefore

$$\tau_2(65) = Bm_2 \Rightarrow m_2 = \frac{\tau_2(65)}{B} = 2.1031\ Am^2$$

Figure 3.23 shows the three torque curves: the total one is obtained from the CST simulation which we now imagine to be the one obtained from an experiment, the torque curve that acts on the permanent magnet of the internal rotor is obtained with the magnetic dipole model while the

torque curve on the motor cover is obtained as the difference between the previous two (motor and magnet). Figure 3.24 shows the relative errors obtained with this method with respect to the torques of the simulation.

Looking at Figure 3.23 and comparing this with Figure 3.15 we can see a perfect agreement and this is also demonstrated by the errors reported in Figure 3.24 which are always kept below 2%. Therefore, summarizing, from the information of the total torque on the system, without having any information regarding the magnet and the cover, the torques for the two components were obtained and these do not differ by more than 2% from those obtained with the simulation software. In particular, it should be noted that in the previous discussion we had obtained errors of 10% (and 30% in the critical points) for the cover of the motor; while in this case, knowing well the behavior of the internal magnet (which is approximate to that of a prefect dipole), its torque curve is extracted from the total torque curve and consequently by difference one can obtain that of the cover, gaining now an error much smaller than in the previous case in which an analytic expression for the cover torque was obtained.

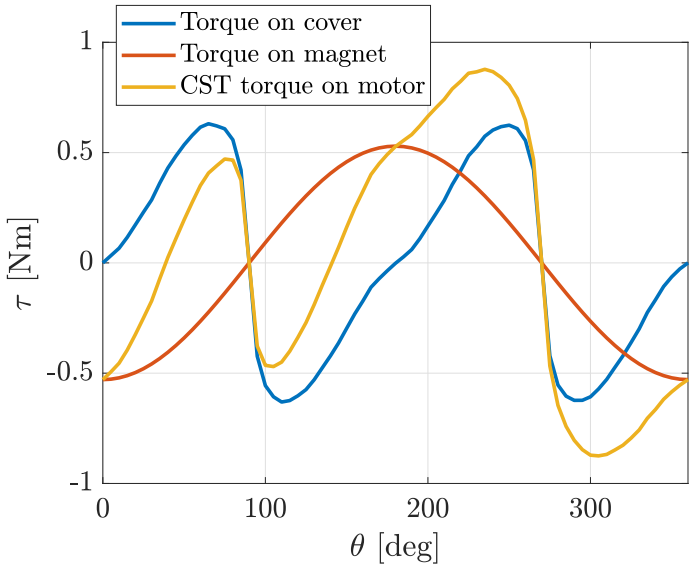

Figure 3.23: Magnetic torque on the motor obtained with the CST simulation, magnetic torque on magnet obtained with the dipole model and magnetic torque on motor cover obtained as the difference between the two as the rotation angle of the motor axis θ varies.

Once magnetic moments m_1 and m_2 have been calculated, the total motor moment can be obtained as

$$m_{tot} = \sqrt{m_1^2 + m_2^2} = 2.7451 \ Am^2$$

From the total torque curve, it is also possible to calculate the zero crossing θ angle which indicates one of the motor equilibrium points within the magnetic field, this indicates that the vector sum of the two dipole moments aligns with the lines of $\boldsymbol{B}$, this angle in this case is 40 degrees. To obtain the two components m_1 and m_2 again, we can project m_{tot} in the two directions x and y.

$$\begin{cases} m_1 = m_{tot} \sin 40 = 1.7645 \ Am^2 \\ m_2 = m_{tot} \cos 40 = 2.1029 \ Am^2 \end{cases}$$

Therefore, seen from the outside, the motor appears as a magnetic object that can be represented

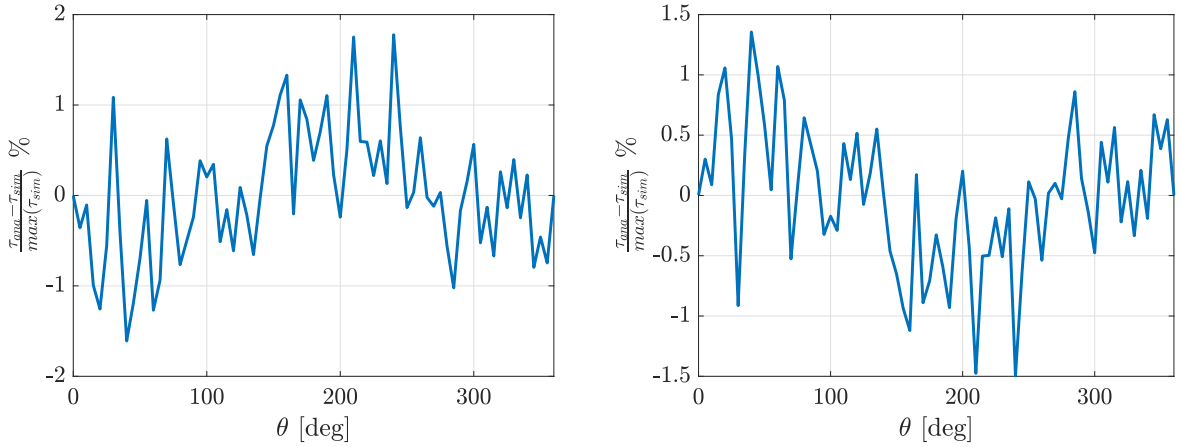

Figure 3.24: Relative errors of the magnetic torque acting on the permanent magnet obtained as the difference between the torque calculated with the dipole model and the CST simulation divided by the maximum torque value of the simulation as the rotation angle of the motor axis θ varies (a). Relative errors of the magnetic torque acting on the motor cover obtained as the difference between the torque obtained as the difference between the total torque of the simulation and the dipole torque of the magnet divided by the maximum value of the simulated cover torque as the rotation angle of the motor axis θ varies (b).

by a magnetic dipole m_{tot} that forms an angle equal to 40 degrees from the y-axis.

In conclusion, the goal of this simulation was to assign to the electric motor a total magnetic dipole which is the combination of two effect: the dipole of the internal PM and that resulting from the magnetization of the external cover. This was done through a software simulation that calculated the torques that act on the two main components of the motor. What happens is that the ferromagnetic cover magnetizes itself, so a torque acts both on the internal PM and on the magnetized cover. By summing the contributions of the torque on the two components, the torque acting on the entire system was obtained. From this result, a method has been proposed to derive the magnetic dipole moments which represent the magnetism of the entire structure as a first approximation. This method can therefore be used for any motor and any value of $\boldsymbol{B}$-field. However, some comments are needed: the simulation was carried out with a uniform magnetic field, this field value corresponds to a certain magnetization of the cover and a consequent magnetic torque on it. If the field value changes, then the magnetization will be stronger or weaker depending on the applied field and this will determine a certain torque value. Therefore, if the motor moves in areas where the value of $\boldsymbol{B}$ varies in magnitude and direction, the contribution of the magnetization of the motor and with it the magnetic interaction of the motor will vary accordingly. Another important comment is that in a BLDC motor the dipole of the permanent magnet rotates following the rotation movement of the rotor itself and the trend of the phases of the stator windings. However, if we consider instead of a brushless motor, a brushed motor, in which the rotor is fixed and with it also its dipole, what rotates is the stator. In that case the rotor would make a constant and fixed contribution. Another effect that we are not yet considering is the magnetization of the cover due to the internal PM.

3.5.3 Parametric total torques

In this section we analyze the behavior of the torques acting individually on the permanent magnet, on the cover and the sum of the two as the rotation angle of the motor axis varies but this time we want to analyze them by varying the three parameters that we have so far considered fixed which are the radius r_m and the length l_m of the internal permanent magnet and the value of the external magnetic field B_{ext}. The varying parameters can assume the following values:

$$
\begin{aligned}
r_m &= \begin{bmatrix} 5 & 6.5 & 8 & 8.9 & 9 \end{bmatrix} \text{ mm} \\
l_m &= \begin{bmatrix} 2.5 & 10 & 20 \end{bmatrix} \text{ mm} \\
B_{ext} &= \begin{bmatrix} 0 & 0.5 & 0.1 & 0.15 & 0.2 & 0.25 & 0.3 & 0.35 & 0.4 \end{bmatrix} \text{ T}
\end{aligned}
$$

Since showing all the possible combinations with the graphs would be inconvenient, here are some more important cases on which it is useful to give comments.

- **Varying B_{ext}**

We want to show how the magnetic torque curves vary with the uniform magnetic field as parameter. In the next figures we will show two different cases: the first case is the one in which the permanent magnet has a length of $l_m = 2.5$ mm and a radius of $r_m = 5$ mm. This case coincides with a motor in which the internal magnet is very small compared to the radius of the motor cover, as the maximum value of the radius that the permanent magnet can take is $r_m = 9$ mm which coincides with the internal radius of the motor cover. The second case is the one in which the permanent magnet has dimensions comparable to those of the motor cover as length and radius values are equal to $l_m = 20$ mm and $r_m = 8.9$ mm.

In Figures 3.25, 3.26 and 3.27 we analyze the magnetic torques acting on the permanent magnet, on the motor cover and the total torque as the sum of the two, respectively. We have fully discussed the trend of the curves in the previous sections where we have also shown a method for obtaining the value of the magnetic moment that undergoes the same torque under the effect of the magnetic field and with this dipole we can approximate the behavior of the electric motor inside an external uniform magnetic field. What we want to emphasize in these figures is the change in torque if the motor is in a magnetic field that has a different intensity.

In Figure 3.25 we can see that if the value of the magnitude of B_{ext} increases, the value of the torque acting on the permanent magnet also increases since the magnetic torque is the vector product between the dipole moment and the magnetic field. Also in Figure 3.26, as the value of B_{ext} increases, the module of the torque that the motor cover undergoes increases, we remind that the cover is made up of a soft ferromagnetic material that is magnetized in the presence of the field. The result of the sum of the two is shown in Figure 3.27. In this case, as we mentioned before, the radius and length of the magnet are small in comparison to the size of the motor cover so we can say that the magnetic torque contribution of the magnet, even if it has a permanent magnetization, is lower than the torque contribution of the cover. Indeed, in the case of a magnetic field with an intensity equal to 0.4 T, the maximum torque that the magnet undergoes, which as we know is found for $\theta = 180$ degrees, is equal to 0.25 Nm while, with the same field, the maximum torque that the cover undergoes is 0.8 Nm (i.e. more than three times greater). This is the reason why

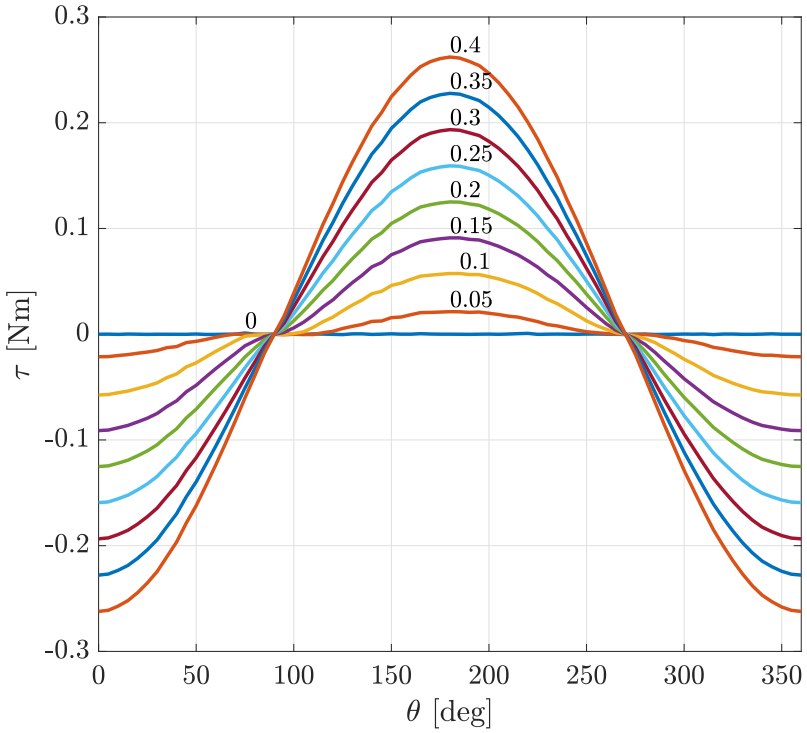

Figure 3.25: Magnetic torque on the permanent magnet obtained with the CST simulation as the rotation angle of the motor axis θ varies with the magnetic field in Tesla as a parameter and with l_m=2.5 mm and r_m=5 mm.

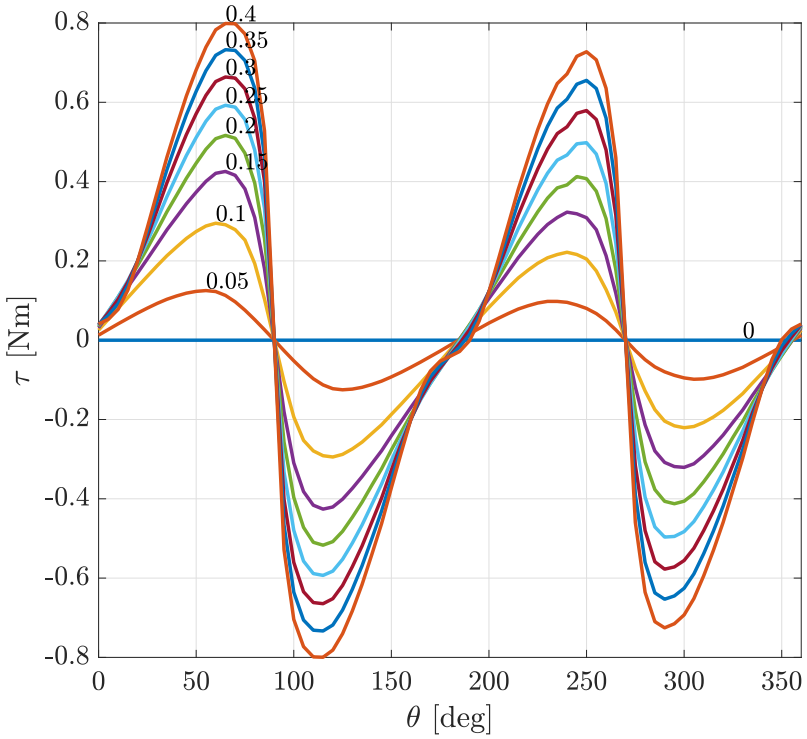

Figure 3.26: Magnetic torque on the motor cover obtained with the CST simulation as the rotation angle of the motor axis θ varies with the magnetic field in Tesla as a parameter and with l_m=2.5 mm and r_m=5 mm.

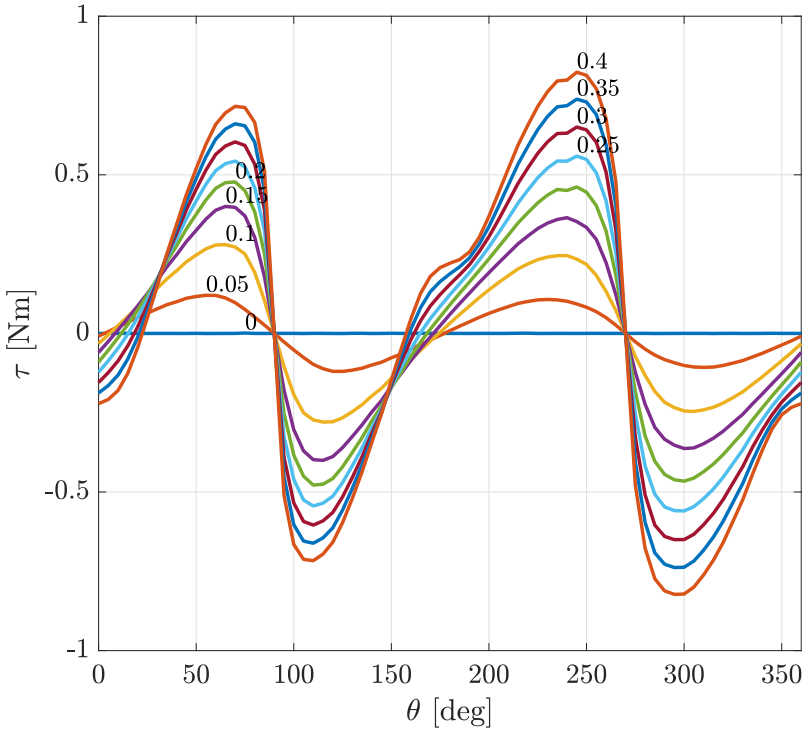

Figure 3.27: Total magnetic torque on the motor obtained with the CST simulation as the rotation angle of the motor axis θ varies with the magnetic field in Tesla as a parameter and with l_m=2.5 mm and r_m=5 mm.

in Figure 3.27 the trend of the sum of the two previous contributions is more similar to the torque received by the cover because the contribution of the cover with the same field is greater than the contribution of the torque on the magnet. These figures show us that the greater the magnetic field, the greater the magnetization of the motor cover which could even turn into a permanent magnet if it reached the saturation point in the hysteresis curve.

In the next simulation instead we will show the opposite case, that is the one in which the permanent magnet assumes maximum dimensions, that is $l_m = 20$ mm and $r_m = 8.9$ mm. In this case we will see that the contribution of the torque that the permanent magnet component undergoes is predominant with respect to the torque contribution of the cover in the calculation of the total interaction on the motor. This will be reflected in the total torque curve in which its shape will resemble that of the magnet rather than that of the cover because, with the same magnetic field applied, the permanent magnet interacts more than the cover. In the following Figures 3.28, 3.29 and 3.30 we show, as in the previous case, the torque on the magnet, on the cover and the sum of the two, respectively, as a function of the rotation angle of the motor axis with the magnetic field intensity as a variable parameter.

Figure 3.28 shows the magnetic torques that act on the internal PM as a function of the rotation angle of the motor axis with the magnetic field as a parameter. From this figure we can see that the torque values are very high and can reach a maximum of 6 Nm for the case where the magnet is 180 degrees to the field lines. These high values are due to the large dimensions of the magnet which here assumes a length $l_m = 20$ mm and a radius equal to $r_m = 8.9$ mm which is one millimeter smaller than the internal radius of the cover.

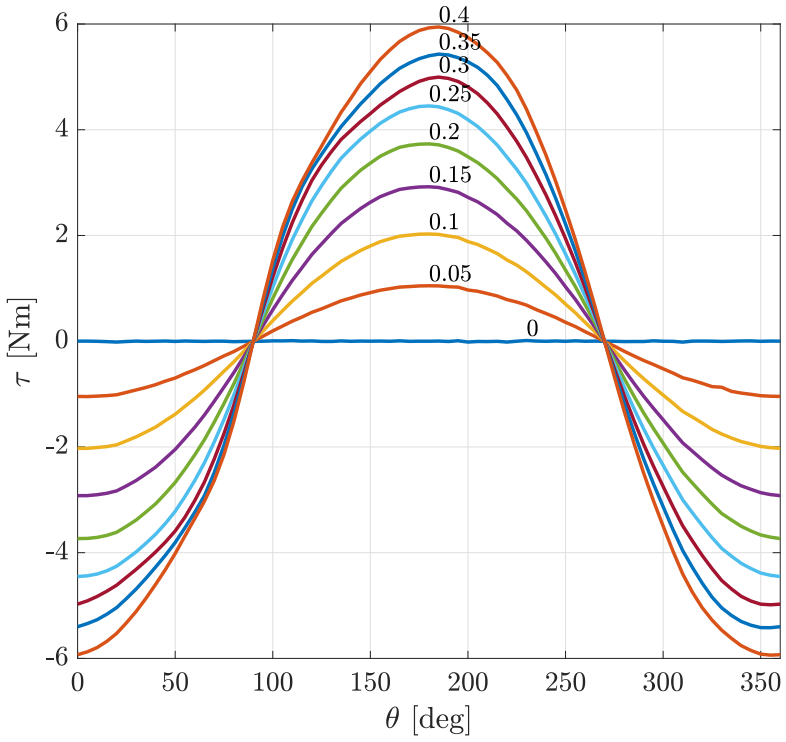

Figure 3.28: Magnetic torque on the permanent magnet obtained with the CST simulation as the rotation angle of the motor axis θ varies with the magnetic field in Tesla as a parameter and with l_m=20 mm and r_m=8.9 mm.

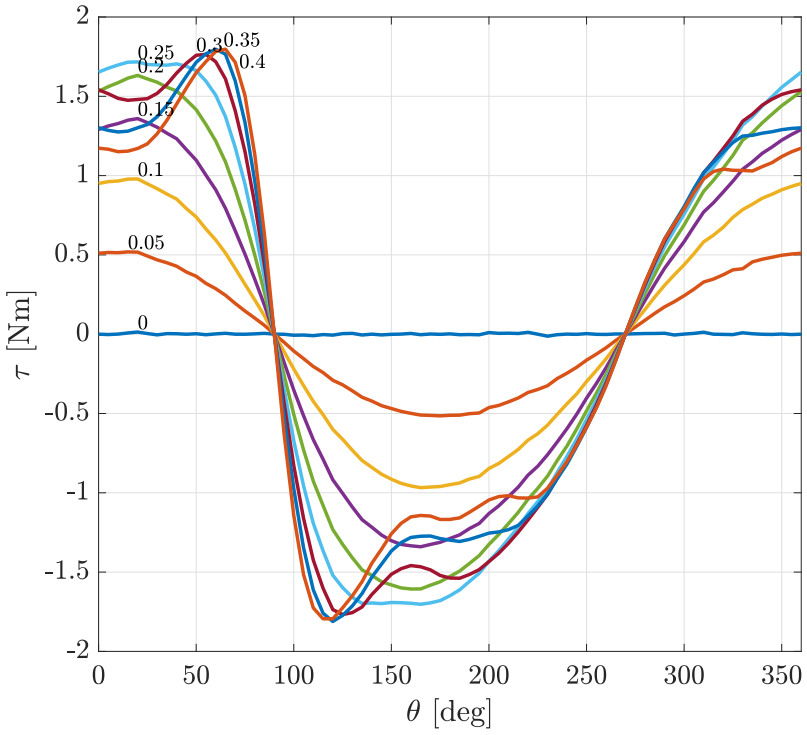

Figure 3.29: Magnetic torque on the motor cover obtained with the CST simulation as the rotation angle of the motor axis θ varies with the magnetic field in Tesla as a parameter and with l_m=20 mm and r_m=8.9 mm.

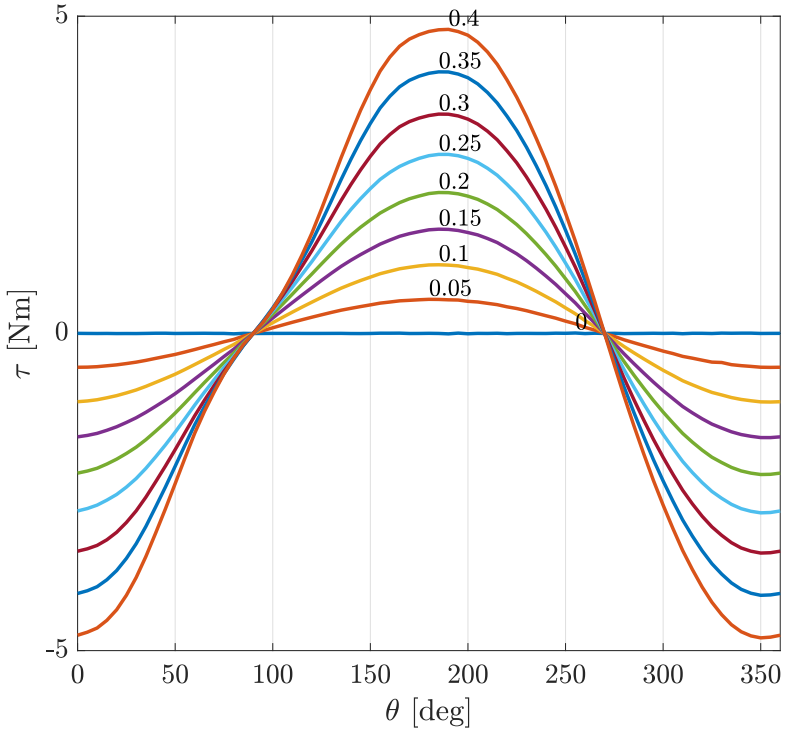

Figure 3.30: Total magnetic torque on the motor obtained with the CST simulation as the rotation angle of the motor axis θ varies with the magnetic field in Tesla as a parameter and with l_m=20 mm and r_m=8.9 mm.

Figure 3.29 shows the magnetic torques that the external ferromagnetic cover of the motor experiences when immersed in the magnetic field, as the rotation angle of the motor axis varies. From this figure we can deduce very significant results beyond the comment that the torque values are in modulus lower than those of the permanent magnet given the large size of the latter. What can be seen is that the shape of the curve no longer resembles the shape it had in the case in which the magnet was smaller and this therefore makes us understand that the behavior of the ferromagnetic material of the external case is strongly influenced by two factors: the external field and the internal magnet. When the magnetic moment of the magnet is very high given its large dimensions, then the behavior of the cover is strongly influenced by the internal magnet. This is also evident as we no longer notice that the torque curve is zero for θ equal to zero. This means that if the motor axis is aligned with the lines of $\boldsymbol{B}$ the cover experiences a certain torque greater than zero and therefore its magnetic moment is no longer aligned with the lines of $\boldsymbol{B}$ but forms a certain angle with the motor axis. In this case is just 90 degrees which means that also the moment $\boldsymbol{m}_2$ is perpendicular to the motor axis as $\boldsymbol{m}_1$ of the permanent magnet. Looking at the behaviour of the curve we can see a torque trend like the perfect sinusoidal one. This shows that the huge internal magnet has magnetized the cover generating a magnetic dipole which remains frozen and does not vary with the rotation of the motor. This effect is especially evident at low external magnetic fields where it is the internal magnet that determines the magnetization of the cover and not the external field. This behavior can be seen in the torque curves which correspond to a magnetic field value from 0.05 T to 0.25 T. For higher magnetic field values (0.3 T, 0.35 T and 0.4 T) we notice a clear change in the shape of the torque curves that looks more like the

previous case where the magnetization of the cover was dominated exclusively by the external field. In conclusion, Figure 3.29 provides important deductions that demonstrate how much the behavior of the cover is dictated by two magnetization mechanisms from the internal magnet and from the external field. We have seen that when the first is very large then the magnetization of the cover is given exclusively to the magnet and this has the effect of generating a fixed and frozen dipole inside the cover which will then undergo a sinusoidal torque when immersed in the external field; we can deduce that the cover has turned into a permanent magnet. On the contrary, from the results of section 3.5.1 we have seen that if the magnetization of the cover is due to the external field this generates a dipole which is not frozen but which undergoes overturning when the motor rotates in the field.

Figure 3.29 shows the sum of the two torques acting on the two components. The trend is similar to the permanent magnet but with slightly lower values. This is because the torque on the cover is that of a sine translated by 90 degrees with respect to that of the magnet (the dipole moment of the magnet and the magnetization dipole moment of the cover are perpendicular to each other). The two sines are therefore in phase opposition so they would tend to cancel each other out, this does not happen as the values of the first are much greater than the second and in fact the sum of the two results as the sine of the magnet but with slightly lower values. So if an electric motor is characterized by a large internal permanent magnet then its behavior within an external magnetic field is that experienced by the same with slightly lower values given by the contribution of the cover which, when magnetized, generates a dipole moment perpendicular to that of the magnet.

- **Varying l_m**

We want to show the curves of the magnetic torques with the variation of another parameter which is the length of the internal magnet l_m. Hence, this time fixing the value of the radius r_m and the external field B_{ext}. As always we will show three graphs which are the torques on the magnet, on the cover and the sum of the two. We will do this for one case: the one in which the radius is $r_m = 5$ mm and the magnetic field is $B_{ext} = 0.05$ T.

Figure 3.31 shows the magnetic torques that act on the motor magnet as a function of the rotation of the motor axis as the parameter l_m varies with $r_m = 5$ mm and $B_{ext} = 0.05$ T. From this figure we can see that since the external magnetic field is low, the torque acting on the magnet is consequently low, but increases as the axial dimension increases until it assumes the classic translated sinusoidal shape for $l_m = 20$ mm.

In Figure 3.32 we find the same results seen previously for Figure 3.29. Here we show the magnetic torques that act on the cover as the rotation angle of the motor axis varies. The magnetic field is always 0.05 T and $r_m = 5$ mm. In this case it can be seen that when the length of the magnet is also small ($l_m = 2.5$ mm) then the cover is affected by the magnetization from the external field and not by the magnet, as the magnet length increases, the contribution of magnetization on the cover due to the magnet increases as well, up to the curve of a perfect dipole that is fixed and does not vary, its direction is reversed with respect to that of the magnet. In this figure this behavior is also very evident in the central curve ($l_m = 10$ mm) in which there is the transition between the magnetization dictated by the external field and that dictated by the internal magnet.

In Figure 3.33 the sum of the two previous curves is simply carried out and it can be seen that for small lengths and radii of the magnet the torque curve on the motor is dictated by the cover,

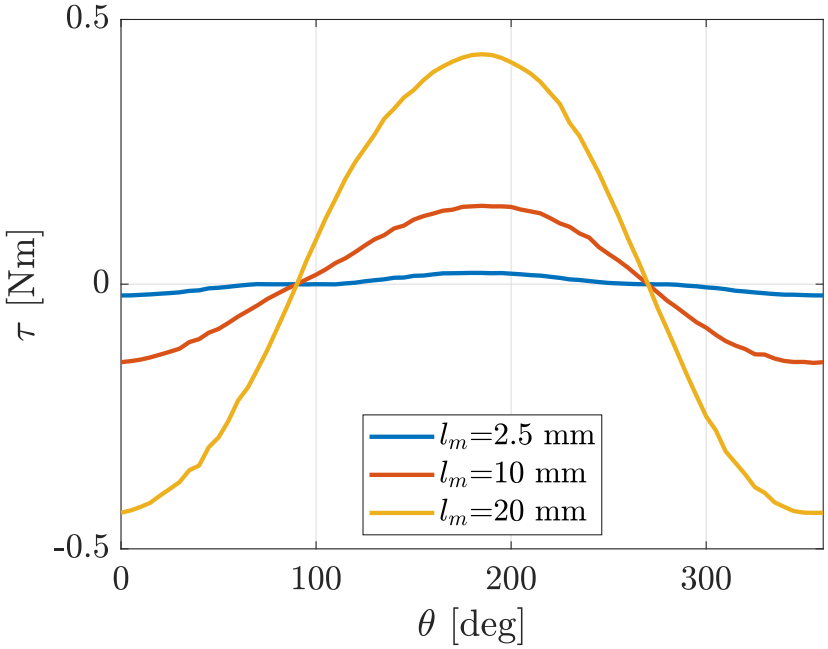

Figure 3.31: Magnetic torque on the permanent magnet obtained with the CST simulation as the rotation angle of the motor axis θ varies with the length of the magnet as a parameter and with r_m=5 mm and B_{ext}=0.05 T.

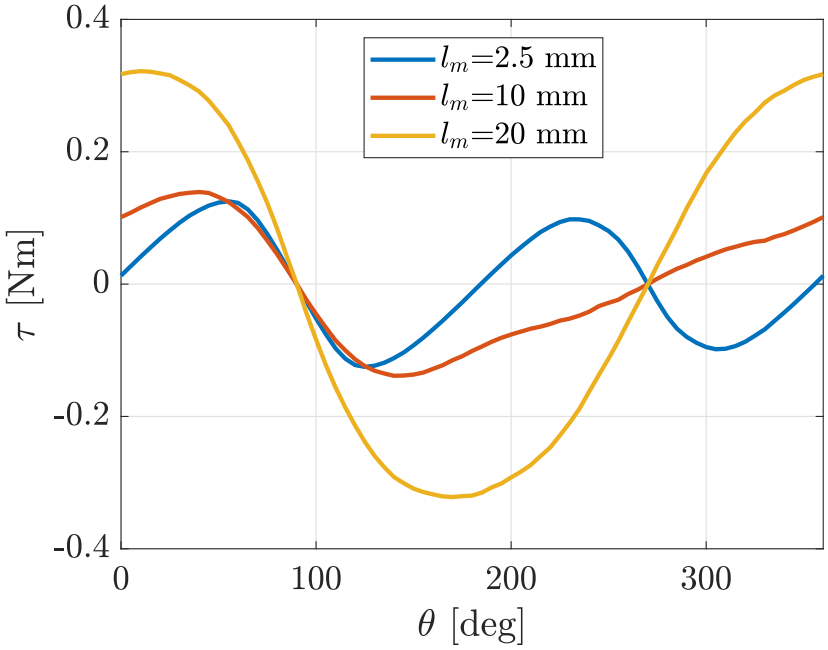

Figure 3.32: Magnetic torque on the cover obtained with the CST simulation as the rotation angle of the motor axis θ varies with the length of the magnet as a parameter and with r_m=5 mm and B_{ext}=0.05 T.

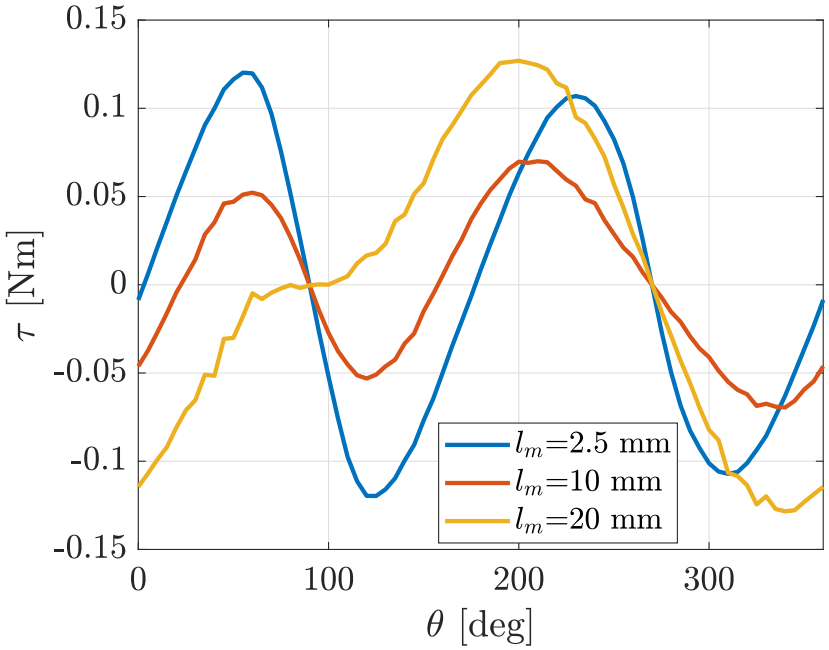

Figure 3.33: Total magnetic torque on the motor obtained with the CST simulation as the rotation angle of the motor axis θ varies with the length of the magnet as a parameter and with r_m=5 mm and B_{ext}=0.05 T.

on the contrary if the size of the magnet increases the total torque on the motor is affected mostly by the behavior of the magnet.

- **Varying r_m**

In the last simulation we want to show, we represent the torque curves in the three cases (magnet, cover, total) by varying the radius of the internal magnet r_m and keeping the values of length l_m and magnetic field B_{ext} fixed. The simulation is performed in the case where the length $l_m = 2.5$ mm and the magnetic field is $B_{ext} = 0.25$ T while the radius r_m is left free to vary.

Figure 3.34 shows the magnetic torques that act on the internal magnet with a radius of $r_m = 2.5$ mm as a function of the angle θ of the axis of the motor immersed in an external magnetic field equal to $B_{ext} = 0.25$ T. We recognize the shape of the sinusoidal which shows that the permanent magnet behaves like a perfect dipole that undergoes a torque that tends to align it with the field lines. The larger the radius of the magnet, the greater the torque acting on it.

Figure 3.35 shows the torques acting on the cover of the motor which, being a soft ferromagnetic material in the presence of a magnetic field, undergoes a magnetization that generates the alignment of all the internal atomic dipoles that lead to the creation of a magnetic dipole moment, which in turn is influenced by the external field applied. In this example the radius of the magnet is small and consequently the magnetization of the cover is due exclusively to the external field, but as the radius of the magnet increases, the magnetization due to magnet begins to have an effect on the cover.

Figure 3.36 shows the sum of the magnetic torques acting separately on the two components and it can be seen that the torque trend of the motor has a similar shape to that of the cover, this is because the magnetization of the cover feels more the effect of the external magnetic field and therefore generates a greater magnetic moment than that of the internal magnet.

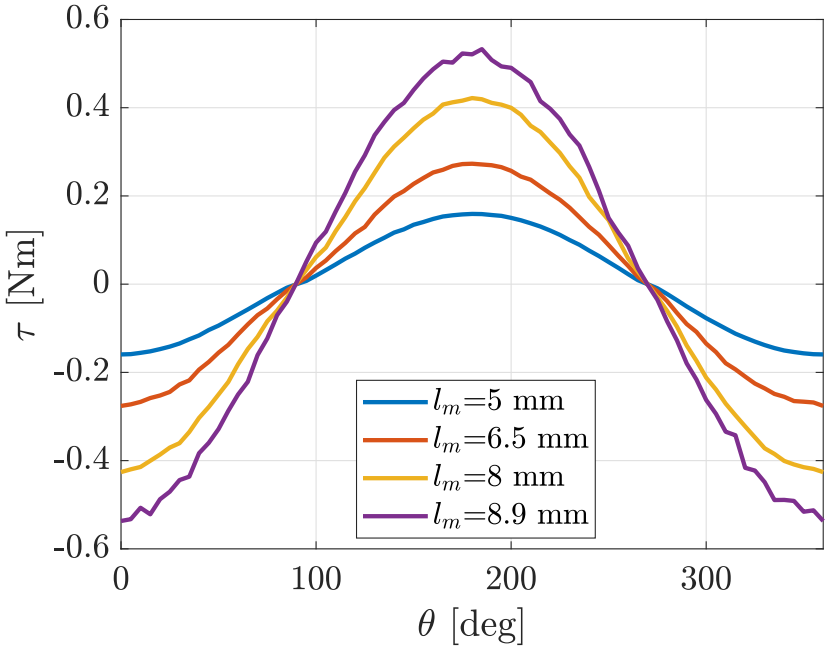

Figure 3.34: Magnetic torque on the permanent magnet obtained with the CST simulation as the rotation angle of the motor axis θ varies with the radius of the magnet as a parameter and with l_m=2.5 mm and B_{ext}=0.25 T.

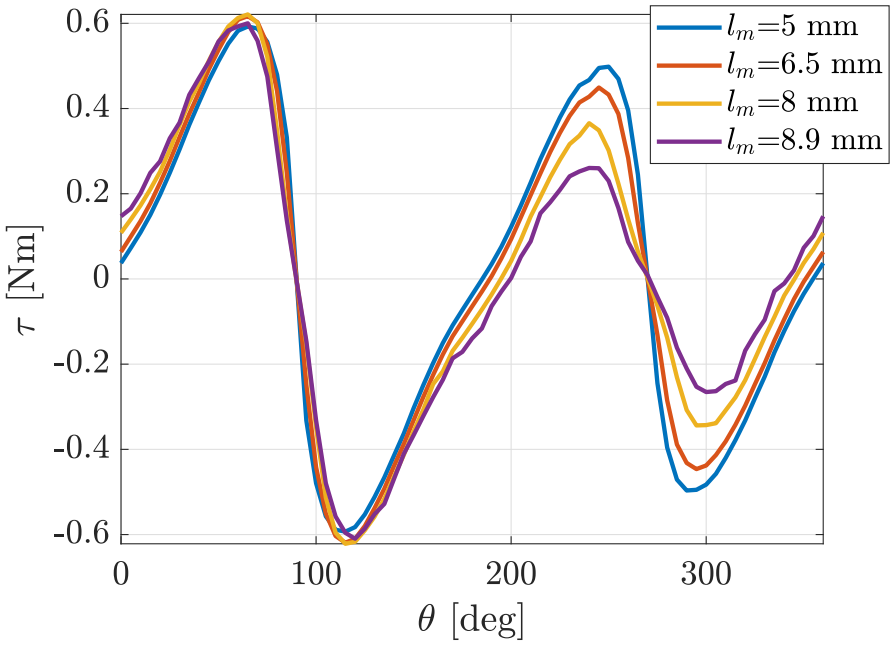

Figure 3.35: Magnetic torque on the cover obtained with the CST simulation as the rotation angle of the motor axis θ varies with the radius of the magnet as a parameter and with l_m=2.5 mm and B_{ext}=0.25 T.

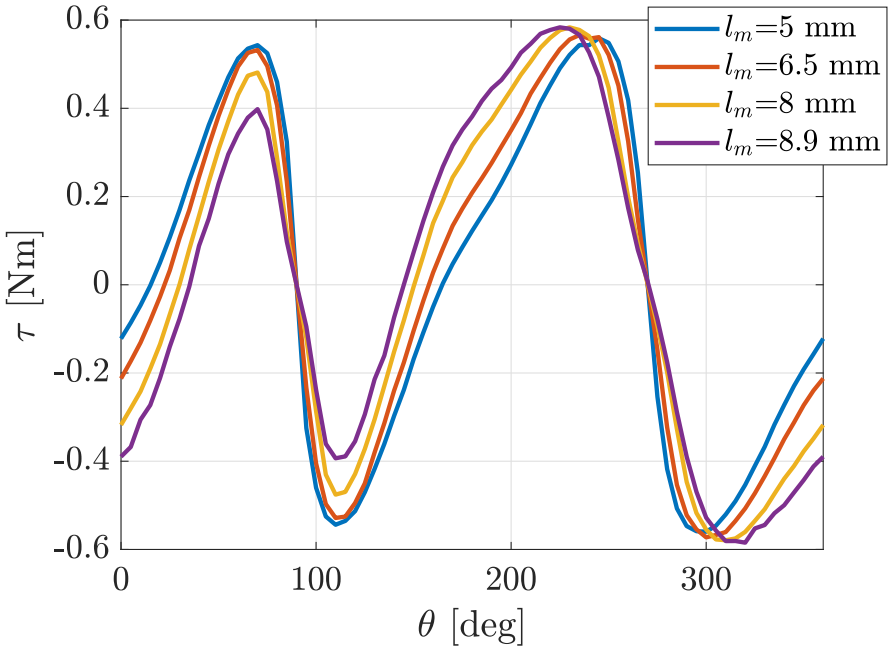

Figure 3.36: Total magnetic torque on the motor obtained with the CST simulation as the rotation angle of the motor axis θ varies with the radius of the magnet as a parameter and with l_m=2.5 mm and B_{ext}=0.25 T.

3.6 Conclusion

We conclude this chapter by briefly reviewing the results obtained. After recalling the operating principle of brushless motors, we have defined the problem of their magnetic simulation. First of all, we made use of a magnetostatic simulation to be able to determine the residual external magnetic field generated by the motor. With these simulations we have noticed that the field lines seen at a certain distance from the motor are very close to those of a magnetic dipole, so we can treat the electric motor as a dipole moment. However, these first magnetostatic simulations did not take into account a fundamental component of the motor which is the external cover and in particular its contribution due to the phenomenon of magnetization for the presence of two fields which are the external one and the internal one generated by the PM. These two have the result of generating a second magnetic moment for the motor inside the cover structure, which is strongly influenced by the geometric dimensions of the PM and by the value of the external field. So we are left with the presence of two dipole moments that characterize a BLDC motor. These two can be combined with each other to create a single moment that will have an offset angle with respect to the motor axis. An important factor that we are not considering is the rotation of the PM around the motor axis. This results in a similar rotation of the dipole moment which we have called $\boldsymbol{m}_1$. However what remains unchanged is the angle of the moment $\boldsymbol{m}_1$ with respect to the axis of the motor, the two are perpendicular. This will effect generate a total moment seen as the sum of $\boldsymbol{m}_1$ and $\boldsymbol{m}_2$ (magnetization moment of the cover) which will have the same offset angle from the axis of the motor but this time, the total moment is not fixed in space but rotates describing a cone around the motor axis (if the moment $\boldsymbol{m}_2$ is aligned to the motor axis).

Chapter 4

Physical Environment

4.1 Introduction

In this chapter we are going to characterize what will be the working physical environment of the blimp, i.e. its *flight environment*. This is crucial both for the definition of the mission belonging to the CERN project and for the purpose of this thesis because as we have already said, the environment in which the robotic system will have to fly was the main reason that led to the choice of blimps as flying robotic platforms that meet the requirements and constraints of the mission. The main discussion topic of this chapter is the magnetic field inside the detector cavern. The blimp must be able to measure the magnetic field but at the same time must prevent it from affecting its motion.

In section 4.2, we will characterize the environment of the FCC-hh detector not only from the magnetic point of view, but we will also show its architecture in terms of dimensions and components. Once the value of the magnetic vector field and its intensity have been characterized, through software simulations and graphical plots, we moved on to the study of the interaction of a magnetic moment (which represents the DC motor) with a non-uniform magnetic field. In particular, in section 4.3 the formulas leading to the expression of the forces and torques, to which the motors will be subjected if inserted in that environment, will be demonstrated. Once the topology of the environment is known, the system must be able to navigate within it, avoiding collisions with obstacles, Therefore in 4.4, the choice of the particular trajectory that the blimp will have to perform within that environment will be shown.

4.2 The FCC-hh

The Future Circular Collider (FCC) is a next-generation particle accelerator which is a CERN project in collaboration with the international scientific community around all over the world in response to the 2013 Update of the European Strategy for Particle Physics (EPPSU). The FCC is intended to accompany by 2035 the Large Hadron Collider (LHC) with which the knowledge of the *standard model* theory[1] of particle physics has been deepened. In particular, the confirmation of the existence of the Higgs boson announced in 2012, thanks to one of the many LHC experiments, will remain one of the most important discoveries of the new millennium. However, these experiments

[1]It is the physical theory that describes three of the four known fundamental interactions: the strong, electromagnetic and weak interactions and all the elementary particles connected to them.

never went above 8 TeV energies. Hence, the current knowledge of the standard model through the observation of particles describes only 5% of the universe. Questions still open today concern the presence of dark matter, the zero mass of the neutrino and any fundamental questions still unknown today. The length of LHC is 27 km and the energy is 14 TeV while the project of the new FCC-hh accelerator will consist of a 100 TeV maximum collider inserted in a 100 km long tunnel (Figure 4.1) and the project foresees the existence of three new accelerators based on the same infrastructure that are

- FCC-hh proton-proton collider;
- FCC-ee lepton-lepton machine;
- FCC-he lepton-proton.

The design of the new FCC particle accelerator is something groundbreaking that will push research in particle physics to horizons never achieved today. What has been done so far since the day of its presentation is an intense work and growth in international collaborations that have led to the Conceptual Design Report (CDR), consisting of four volumes covering the physics opportunities, technical challenges, cost and schedule of different circular colliders, some of which could be part of an integrated programme extending until the end of the 21st century [2].

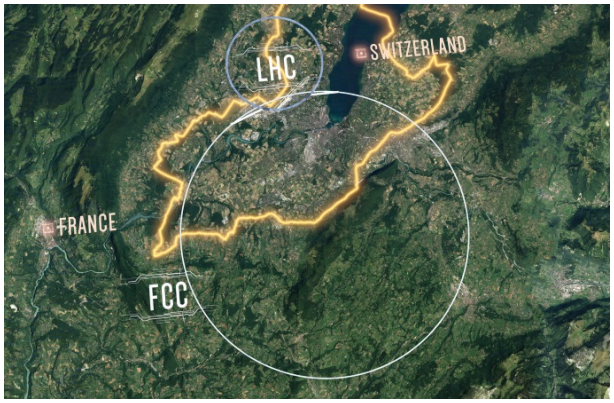

Figure 4.1: Outline of the 100 km circumference of the FCC compared to the dimensions of the 27 km circumference of LHC. From [92].

4.2.1 FCC-hh detector

Detectors are the physical place where the particles collide, they are fundamental parts of the particle accelerator complex at CERN. In short, accelerators bring the particles to high energies before making them collide inside the detectors in which it can be deduced various properties of particles such as their velocity, mass and charge from which physicists can derive the identity of a particle. The process requires accelerators, powerful electromagnets, and layers of sub-detectors each designed to look for particular properties of particles. Others important detector parts are tracking devices that detect the path of a particle; calorimeters which stop, absorb and measure the energy of a particle and particle identification detectors that use a variety of techniques to define the identity of a particle. We focus on the FCC-hh detector which to date is still a project and has not yet been implemented.

In the CDR mentioned above there is the three-dimensional representation of the FCC-hh reference detector which is reported in Figure 4.2. As can be seen from the representation, the detector has a diameter of 20 m and a length of 50 m, which are comparable to the dimensions of the ATLAS detector at the LHC. In the complex mechanism of components that form a detector of accelerator particles, the part we are interested in is the source of the magnetic field, which is fundamental for the functioning of a detector to be able to curve the particle trajectory following the impact and therefore determine the identity of the particle itself. This crucial components are the solenoids contained in the detector. For the FCC-hh detector, the magnetic field is generated together by three distinct solenoids. The first is the *main solenoid* which generates a 4 T field and has a free bore diameter of 10 m. The other two are the *forwards solenoids*. They have been designed at the two ends of the detector from the point of interaction along the axis of the beam. This is done to achieve better performance in terms of the magnetic field. These forward solenoids have an inner bore of 5 m (Figure 4.3a) and these also generate a magnetic field of 4 T. Finally, the assembled system forms a total solenoid volume of 32 m length. There is also an alternative to this three solenoid system which consists in replacing the two forward solenoids with two magnetic dipoles placed in the forward regions with a field integral along the z-axis of about 4 Tm (Figure 4.3b). The first configuration is preferred to the second because although dipole system shows better tracking performance in the very forward region, the fact of losing the rotational symmetry and the requirement of a compensation system for the hadron beam are seen as drawbacks.

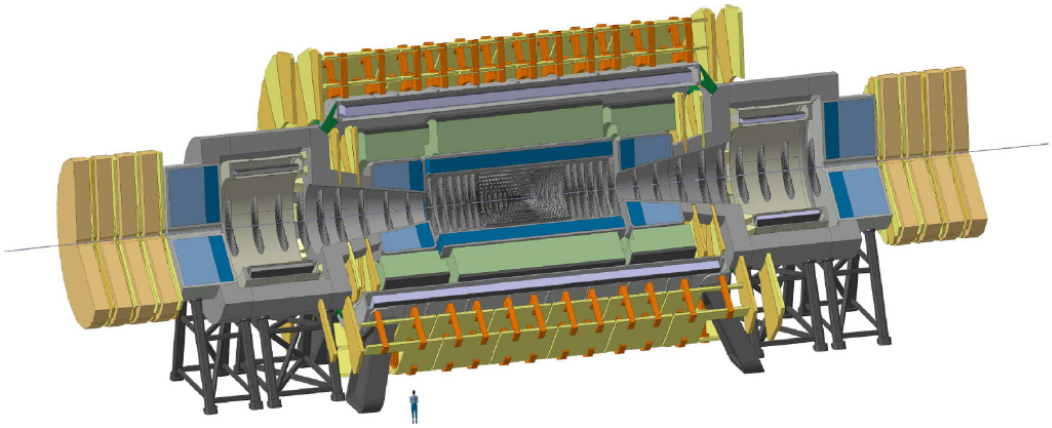

Figure 4.2: Three-dimensional model of the FCC-hh reference detector. A central solenoid with 10 m diameter bore and two forward solenoids with 5 m diameter bore provide a 4 T field. From [2].

Another interesting representation of the detector environment present in the CDR [2] document is a section of the three-dimensional model of the FCC underground system reported in Figure 4.4. This view shows the presence of two environments: the detector cavern on the left and the service cavern on the right. The former hosts the detector and the latter hosts services for the detector. From this figure it can be deduced that the detector installation needs a longitudinal dimension of 66 m. It should be noted that the harsh environment, i.e. the presence of a high residual magnetic field and a background of radiation are present only inside the detector cavern. Still in the same Figure 4.4, on the left, where the detector cavern is represented, two detectors of different sizes are shown. The FCC-hh detector is the larger one on the right.

Also in the CDR [2] document there is the longitudinal cross-section of the FCC-hh reference detector (Figure 4.5). In this representation we see the detector in section and all the fundamental

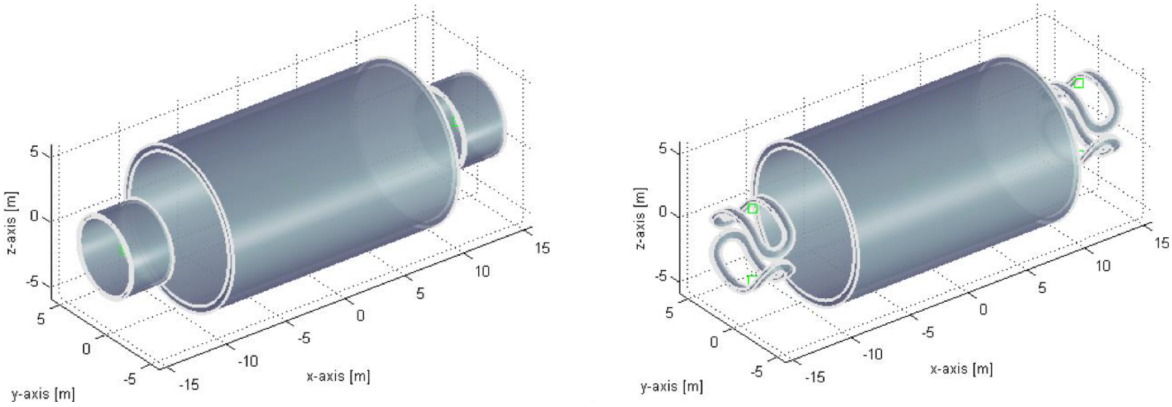

(a) **(b)**

Figure 4.3: Magnet system of the FCC-hh detector: main solenoid + 2 forward solenoids (a), main solenoid + 2 forward dipoles (b). From [78].

components for its use are specified with precise positions. In particular, this figure is fundamental not only because it shows us the precise position in space of the main solenoid and the forward solenoids but also provides us information about the areas in which the blimp can fly and the areas that instead represent obstacles for it.

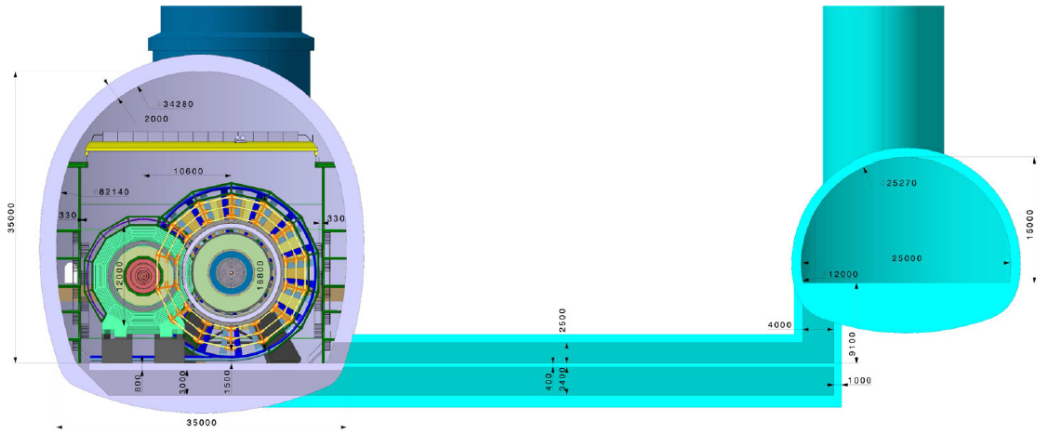

Figure 4.4: Section view of a 3D model of the FCC underground system. The provided dimensions are in millimeters. From [78].

4.2.2 The magnetic field in the FCC-hh detector cavern

Once the three-dimensional structure of the FCC-hh detector have been studied and analyzed, a fundamental element for our simulations is that of the magnetic field both inside and outside the solenoids system. In order to estimate the disturbance acting on the blimp, it is necessary to know the magnetic field generated by the FCC-hh detector in which the flying system will have to move. Obviously we will be interested in the residual field values outside the solenoids system rather than the internal one.

As already done for the BLDC motors in Chapter 3, we have carried out two types of simulations with the two software already presented which are FEMM and CST. The first FEMM simulation is

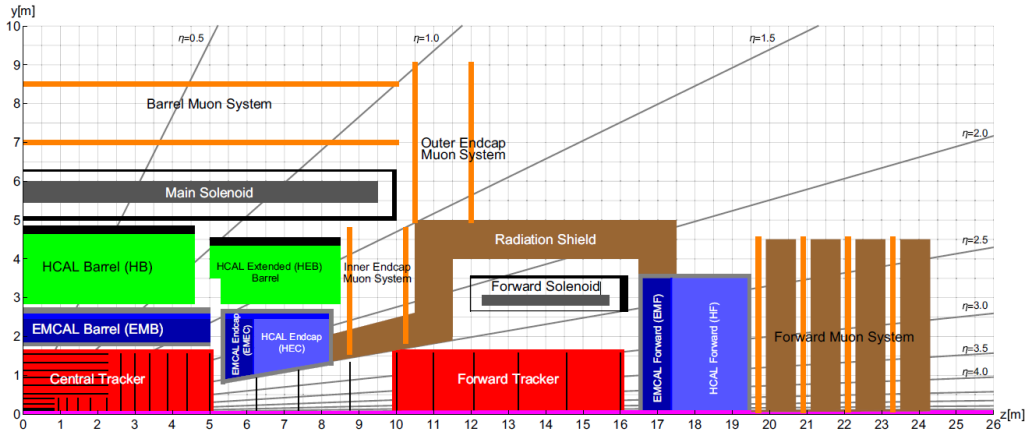

Figure 4.5: Longitudinal cross-section of the FCC-hh reference detector. From [2].

the one at a lower level in terms of results, while the CST simulation is more accurate and provides greater details. The big difference between the two, is that with FEMM software we can only perform two-dimensional and static electromagnetic simulations while with the CST software it is possible to carry out three-dimensional electromagnetic analyzes. Despite this, for a first approach to the problem, the FEMM software is preferred as it is faster and easier to use. Then as soon as we became more familiar with the problem we moved on to a CST simulation whose results were kindly given to me by the EP-DT-EO team at CERN.

4.2.3 FEMM FCC-hh magnetic field simulation

To simulate the magnetic field of the FCC-hh solenoids system through the FEMM software, we first created the model by defining the problem as magnetic and axisymmetric. Then we moved on to the design of the solenoids with the definition of nodes that delimit their real dimensions. As soon as the design phase was completed, the properties of the materials of each structure were assigned. Solenoids were defined as copper coils with a diameter of 1.6 mm each. For the two forward solenoids 300 windings have been set while for the main solenoid 1800. Furthermore, it has been chosen that the system is surrounded by ambient air. After assigning the correct materials to the various structures we set the boundary conditions. The simulation we want to do is an *open boundary* problem, i.e., we want to solve the field in a space without boundary conditions, therefore not affected by neighboring boundary constraints. However the finite element problem with FEMM needs the definition of boundary conditions to be solved so we used the *Open Boundary Builder* button on the toolbar, which creates a boundary structure that simulates the impedance of an open domain. The complete geometry is reported in Figure 4.6, where it is present the axisymmetric structure of the solenoids system of and the multilayer structure of the open domain.

After having designed the two-dimensional model, we proceed with the definition of the mesh. This action generates a triangular mesh based on the definition made of each object. In our case 282797 nodes and 564368 elements was generated. After generating the mesh and run the process we can analyze the results in a post-processor window. As a first result we show the color magnetic flux density in Figure 4.7 and then the magnetic field in magnitude along the axial direction of the solenoids system as reported in Figure 4.8. This gives us an order of magnitude of the value of $|\boldsymbol{B}|$ running along the entire axis of the cylinders.

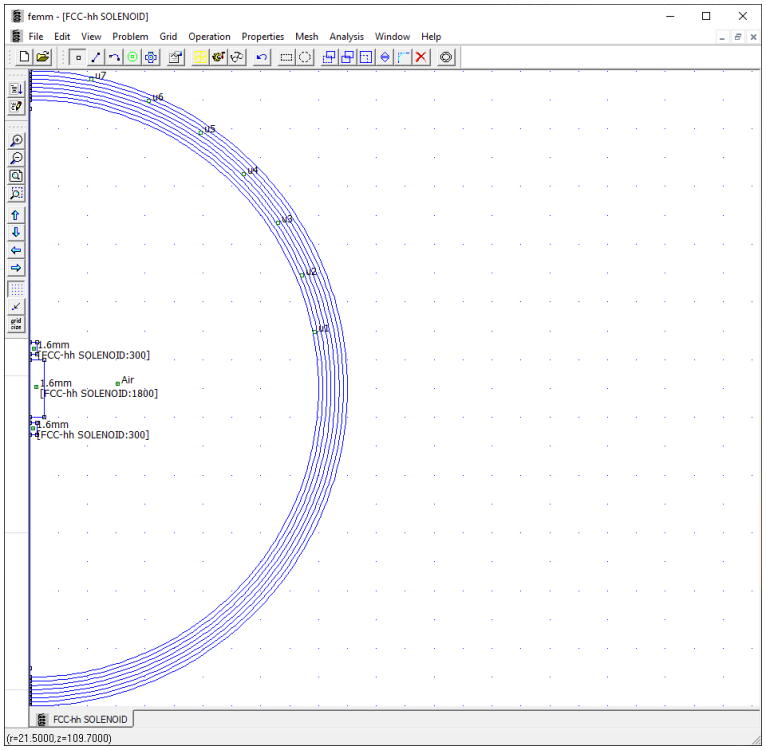

Figure 4.6: Complete model of FCC-hh solenoids system on FEMM software ready to be analyzed.

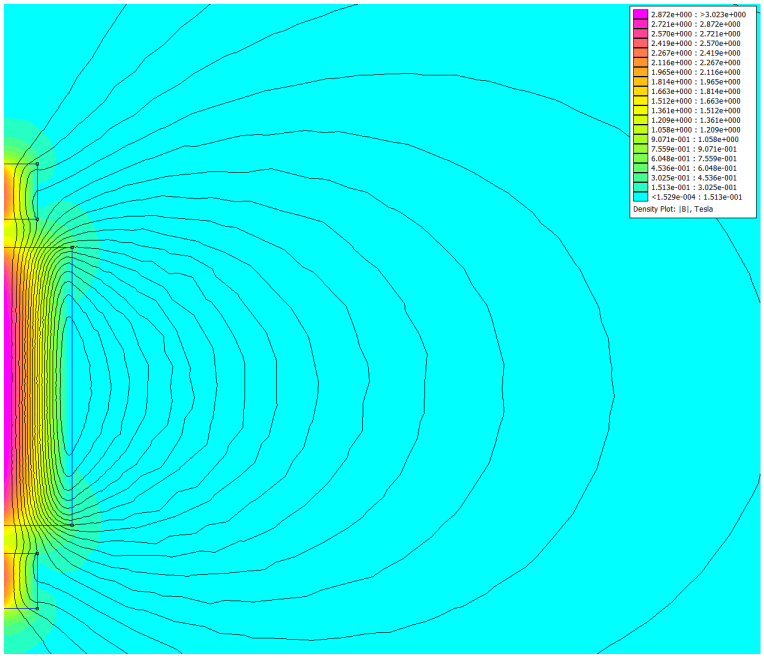

Figure 4.7: Color flux density plot of the magnetostatic solution of the solenoids system of FCC-hh obtained with FEMM software.

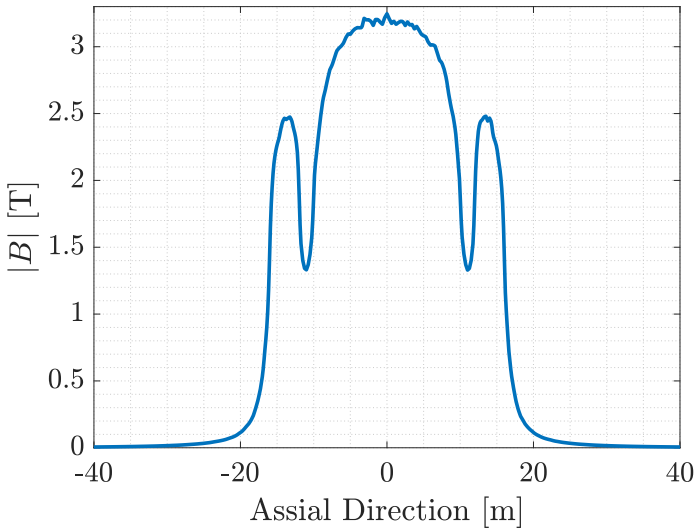

Figure 4.8: Plot of the magnitude of the magnetic field generated by the solenoids system of FCC-hh along the axis of the cylinder system obtained with FEMM software.

Figure 4.7 shows the magnetic field color flux density plot in two-dimensional space. In the thickening regions of the lines, higher magnetic field values are present. This can be observed in the inner area near the axis of the main solenoid and the two forward solenoids. In the table at the top right in the same figure there are the values of the module of the field reported in Tesla according to the coloring of the map.

Figure 4.8 shows the magnitude of the magnetic field along a particular direction in space, which is the axis of the cylindrical system. This graph was obtained with MATLAB through the data provided by the FEMM simulation and shows how in the central region of the field, which coincides with the presence of the main solenoid, values around 3 T are reached. In the transition from the main solenoid to the side solenoid there is a sharp drop in the magnetic field module which then goes up inside the forward solenoid. However, this is not exactly what happens in reality, in fact, as we will see in the subsequent CST simulation of the field, the transition between the central solenoid and the forward solenoid, which coincides with a connection area for the field lines, is softer and less abrupt than that shown in this Figure 4.8. The value of the field inside the forward solenoid is in any case high and equal to about 2.5 T. The result we are interested in, looking at Figure 4.8 is to see how the magnetic field drops sharply as we move away from the solenoids system. It can be seen that there is a clear decrease of the field from the value above 2 T of the forward solenoid to values below 0.5 T. This is very important because the blimp will have to fly outside this structure and with these simulations we can therefore realize the orders of magnitude of the magnetic field to which the robotic system will be subject.

4.2.4 CST FCC-hh magnetic field simulation

After having carried out a first design of the two-dimensional and axisymmetric system, we now move on to a more accurate simulation, based on the three-dimensional definition of the system. The solenoids system was simulated at the beam pipe level trough the CST software. The three solenoids that generate the high magnetic field are shown in the Figure 4.9. As input for the

simulation, the material of the coils was chosen iron which has a relative permeability[2] of $\mu_r = 1000$. The transparent solids represent the envelope of the FCC-hh detector, outside those there is the detector cavern of interest of us. The material of the other detector components and the cavern was set to air which has a relative permeability of $\mu_r = 1$.

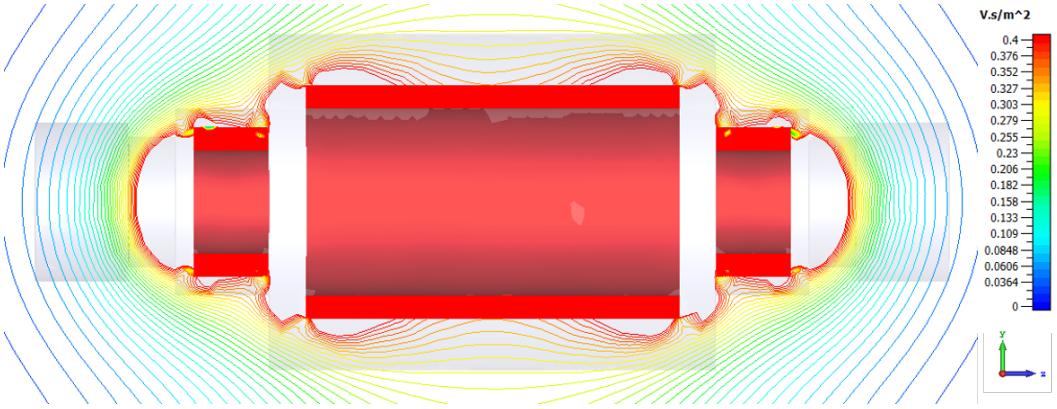

Figure 4.9: Map of the magnetic field in the future detector of the FCC-hh as a cut at the beam pipe level obtained with CST. From [78].

In Figure 4.9, obtained with the CST simulation, it is possible to notice the reference system chosen in which the detector solenoids have been placed. We can call this reference *FCC reference frame*. In particular, the $\boldsymbol{Z}_{FCC}$-axis is the one that runs longitudinally along the axis of the main solenoid, the $\boldsymbol{Y}_{FCC}$-axis is instead the vertical axis and the $\boldsymbol{X}_{FCC}$-axis comes out of Figure 4.9 so as to form a right-hand triad. This reference frame will be very important in Chapter 5 because through the knowledge of the magnetic field in the FCC frame it is possible to estimate the magnetic disturbance that must be written with respect to the body-fixed reference F_b, that is the reference chosen for the integration of the equations of motion.

With the data provided by the CST simulation it is possible to represent the magnetic field in space, with respect to the FCC reference through MATLAB. However, having the value of the three components of the magnetic field in space, it is still difficult to be able to visualize the value of a vector field with graphs. Therefore in the following figures we will show the field and its gradient in cutting planes and particular directions.

Figure 4.10 depicts the components of the magnetic field vector in three shear planes of the FCC reference frame. The color coding is given by the magnitudes of the component vectors and the color scale goes from 0 to 1 as the vector magnitude has been normalized with respect to the maximum magnitude which is 3.2 T. From Figure 4.10b and 4.10c it is possible to note that if we put $x = 0$ m or $y = 0$ m the component where the field is greater is obviously inside the solenoid and in the direction of the axis, this in analogy to the distribution of lines of $\boldsymbol{B}$ generated by an ideal solenoid in which the internal field is as direct as the axis. Consequently, if we look at the solenoid of FCC-hh for $z = 0$ m we see some field components in the x and y direction which are almost zero as we are looking in the plane normal to the magnetic field flux lines inside a solenoid.

Now instead of plotting the two-dimensional vectors in the three particular cutting planes, let's try to graph the single three components always showing colored scales which this time indicate the true and not dimensionless module. We report this type of graph only for the zy plane at $x = 0$ m.

[2]See relation B.43 for the definition of relative permeability.

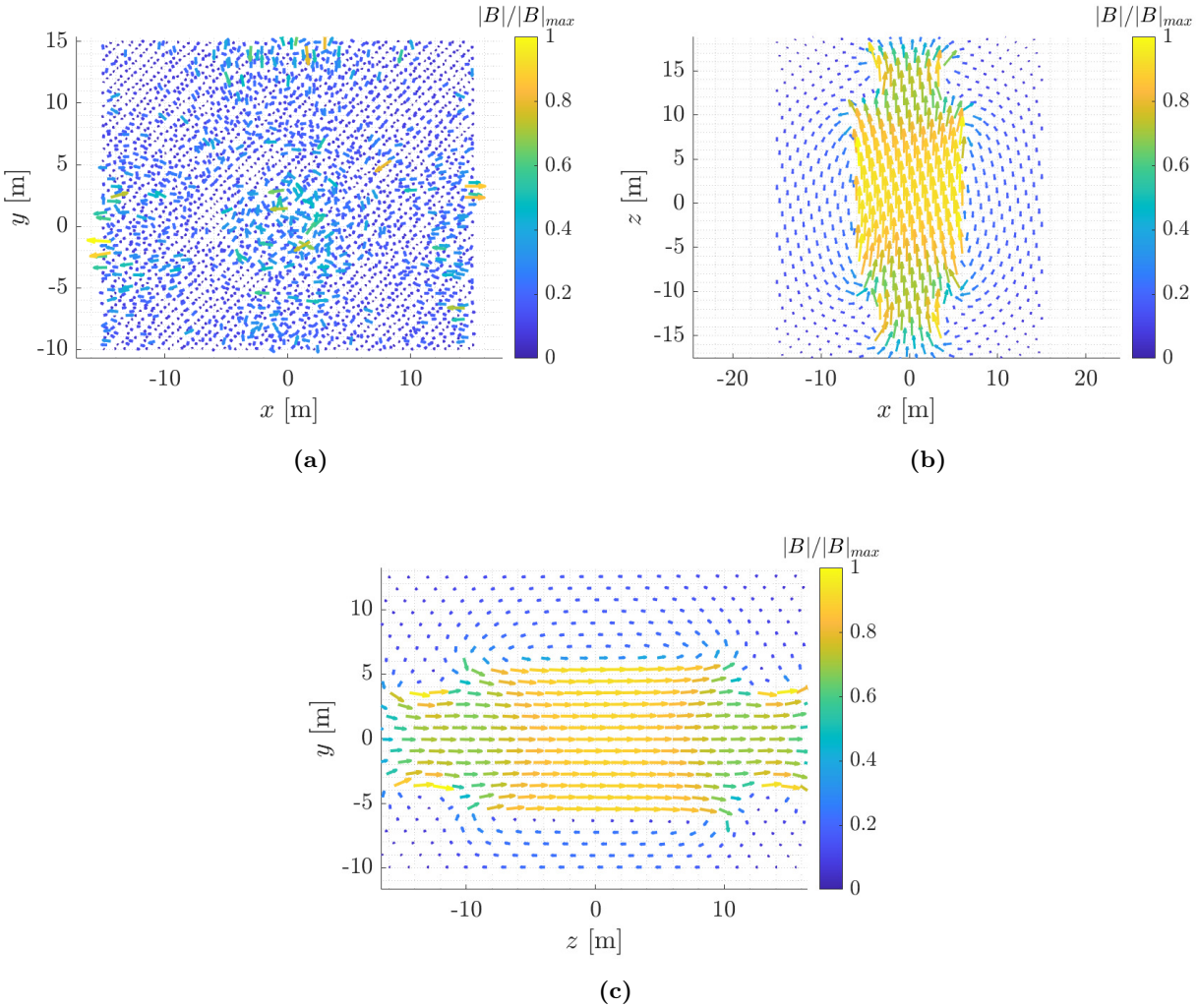

Figure 4.10: Components of the vector space of the magnetic field inside the FCC-hh detector cavern reported in three shear planes: xy @ $z = 0$ m (a), xz @ $y = 0$ m (b), yz @ $x = 0$ m (c). The color scale reports the magnitude of the vectors scaled with respect to the maximum magnitude value.

Figure 4.11 shows the B_x (a), B_y (b) and B_z (c) components of the magnetic field in the zy plane for $x = 0$ m in three separate graphs. From the third figure (c) we can see that inside the solenoid the B_z component is the preponderant one and reaches magnitudes of 3 T, which is what we had predicted with the FEMM simulation shown in Figure 4.7.

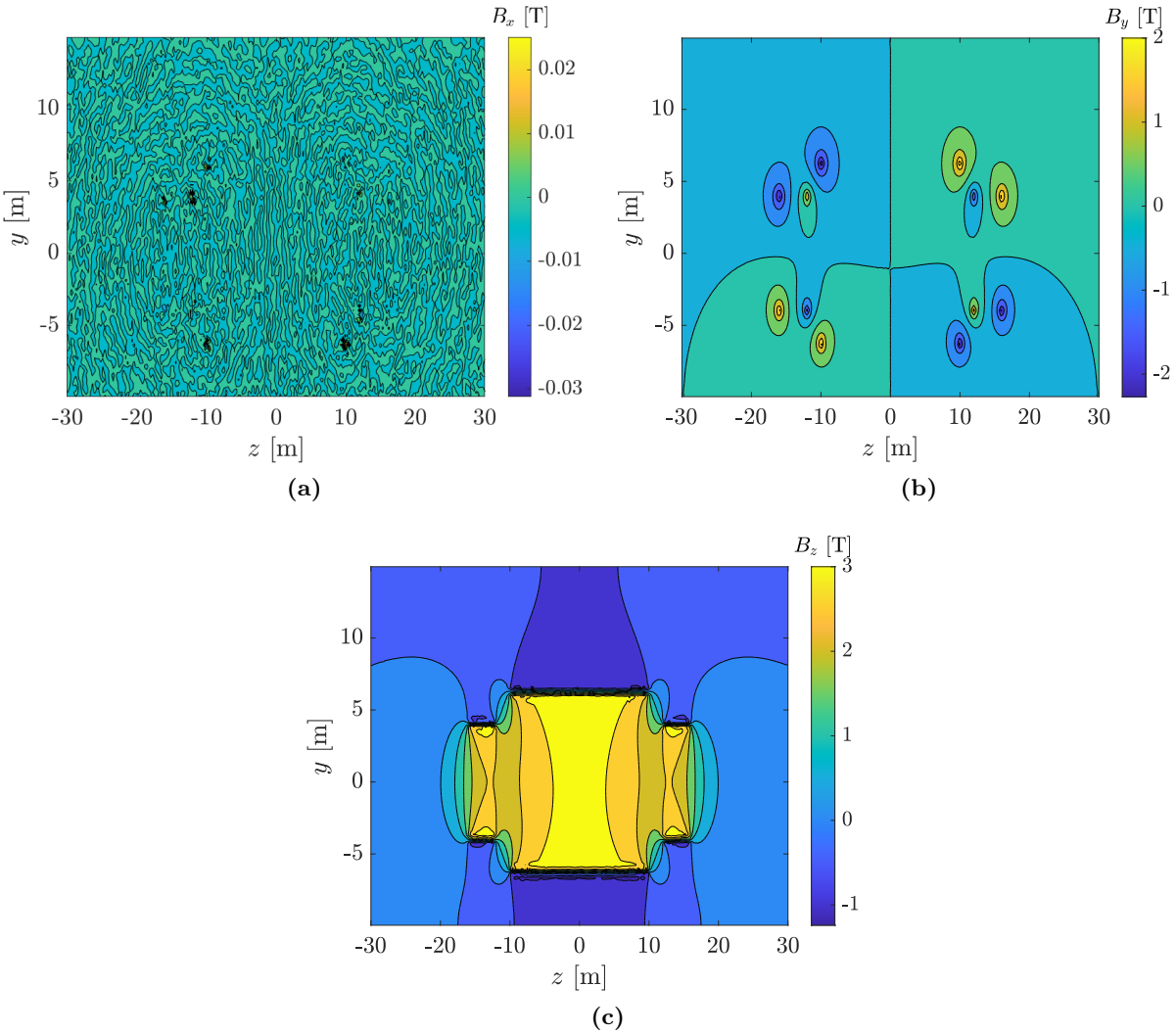

Figure 4.11: B_x (a), B_y (b) and B_z (c) components of the magnetic field inside the FCC-hh detector cavern reported in yz plane @ $x = 0$ m. The color scale reports the magnitude of the components in Tesla.

Since it is not very easy to grasp the characteristics of the magnetic field from Figures 4.10 and 4.11, we now want to report the components of the magnetic field vector along a particular direction which are not only that belonging to the area that can be flown by the blimp, but we will also consider other directions that are not actually feasible in reality and we do it to become familiar with the orders of magnitude of the field.

Figure 4.12a shows the trend of the components of $\boldsymbol{B}$ along the x direction of the FCC reference frame with y and z set at 0 m. In particular, it can be noted that the greater component of the three is B_z. In this case, moving in the direction perpendicular to the axis of symmetry of the solenoid, the axial component B_z remains almost constant inside the solenoid and above 3 T while, on the other hand, when it comes out of the solenoid, it sees a sharp decrease in intensity.

Figure 4.12b instead shows the trend of the $\boldsymbol{B}$ components with x and y fixed at 0 m, so the

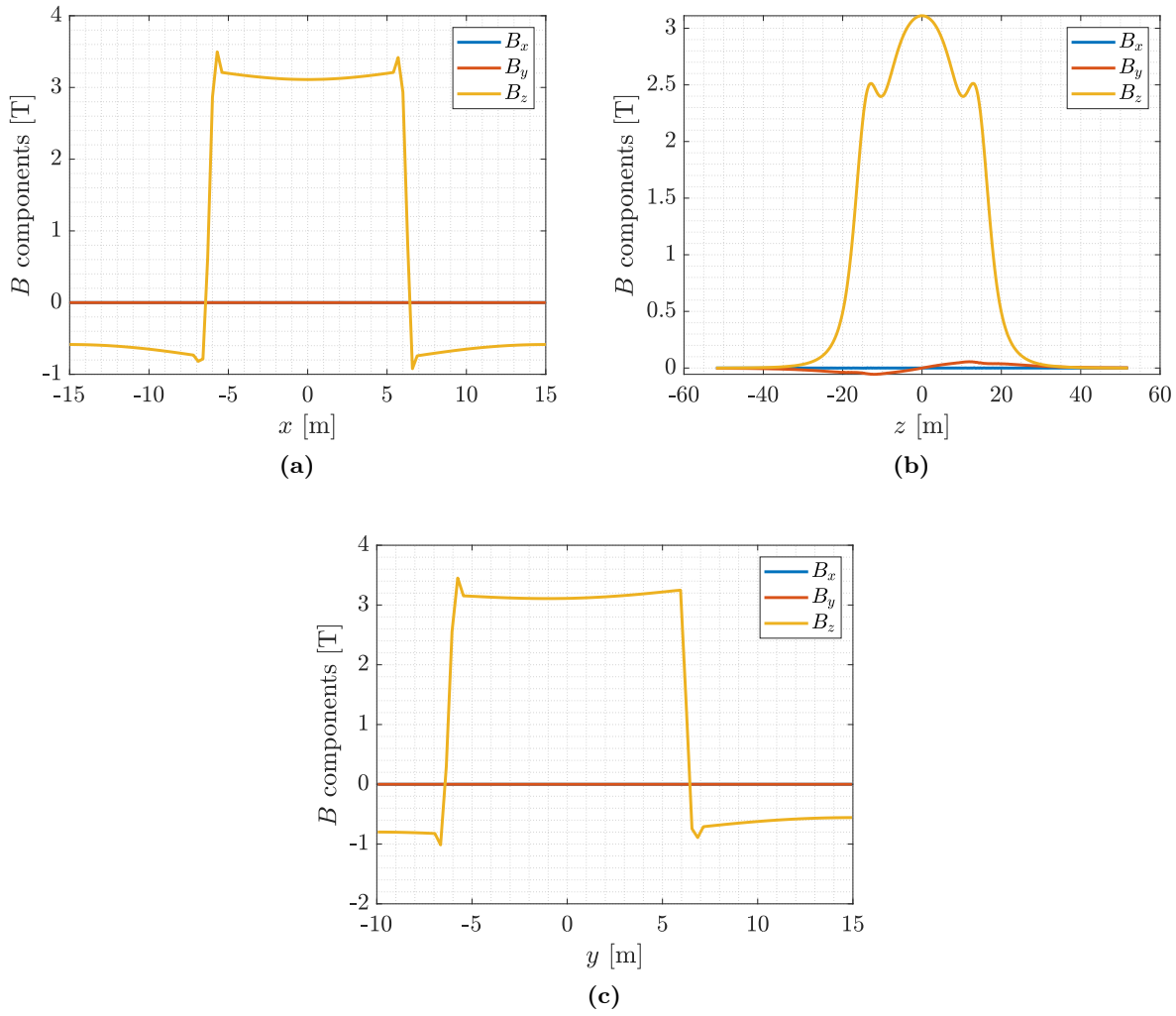

Figure 4.12: Magnetic fields components inside the FCC-hh detector cavern along specific directions: along x @ $y = 0$ m and $z = 0$ m (a), along y @ $x = 0$ m and $z = 0$ m (b), along z @ $x = 0$ m and $y = 0$ m (c).

direction in which we see the change of the components of the field this time is z and we are moving precisely along the symmetry axis of the solenoid. Also in this case we note that the main component among the three is always B_z which has a peak at the center of the reference system which coincides with the center of the solenoid and then drops abruptly to zero going to the right and to the left i.e., exiting the solenoid. This figure can be compared with Figure 4.8 obtained with the FEMM software in which we simulated the magnitude of the magnetic field along the axis of the cylinder. In that case, as we had pointed out, there was a more evident decrease in the transition from the main to the lateral solenoid because of the less detailed simulation of FEMM software compared to CST.

Figure 4.12c shows the trends of the components of $\boldsymbol{B}$ in the y direction for x and z fixed at 0 m. In this case again the greater component of the magnetic field is the B_z which remains constant as long as we move perpendicular to the axis of the solenoid within its radius, if we go outside the value of the field drops abruptly.

These three graphs show the variation of the three components of the field along one of the three axes of the FCC reference frame by setting the other two to zero. These results are therefore useful for seeing what happens in the transition from inside the solenoid to the outside. However, these graphs are not of particular interest as regards the magnetic field that the blimp experiences in its flight, rather they are useful for understanding the whole physical magnetic environment generated by the presence of the detector. The blimp must be able to fly over the areas near the detector and obviously will not be able to enter the solenoid. For this reason we will show representative graphs on the trends of the magnetic field components along the direction that do not intersect the solenoid but surround it from the outside. These will be fundamental for the study of magnetic disturbances on the system.

Therefore we have simulated two scenarios that are represented in the Figure 4.14 where the geometric system of the solenoids is reported to scale and two directions of movement are represented, along y and along z. The first scenario is to fix the coordinate $z = -25$ m and $x = 0$ m and move in the y direction. It can be seen from Figure 4.14a which is the trend of the components of the magnetic field along the y direction. These values, in particular B_z fluctuate up to a maximum of 0.1 T. In the next Figure 4.14b, on the other hand, the scenario imagined is that in which the blimp flies over the solenoid along its entire length in the z direction at $x = 0$ m and at an altitude of $y = 10$ m. Here the magnetic field values that the blimp can hypothetically feel are even higher. We can see a bell-shaped trend of the B_z component with a maximum in modulus of 0.6 T and also the B_y component in this case passes from -0.3 T to +0.3 T.

These two simulated directions of movement are not randomly chosen; later in Chapter 5 we will simulate a trajectory that will have a similar trend, i.e. that of climbing to a certain altitude and then traveling the entire length of the solenoid maintaining that altitude and finally descending at ground level on the other side. The choice of z and y values is dictated by the fact that as can be seen from Figure 4.5, these are the first possible directions where the blimp can fly avoiding obstacles.

An important quantity which is useful to analyze is the gradient of the magnetic field. Since the magnetic field is non-uniform, is essential to understand how it varies in space in order to know the forces and torques it exerts on a magnetic dipole. We briefly recall that the gradient of a function

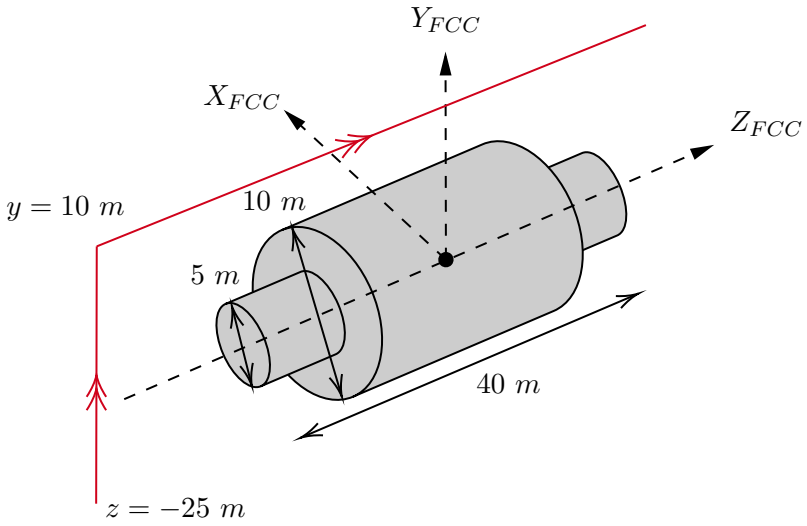

Figure 4.13: Geometric representation of the solenoid system of FCC-hh and directions of movement of the blimp with respect to the FCC frame.

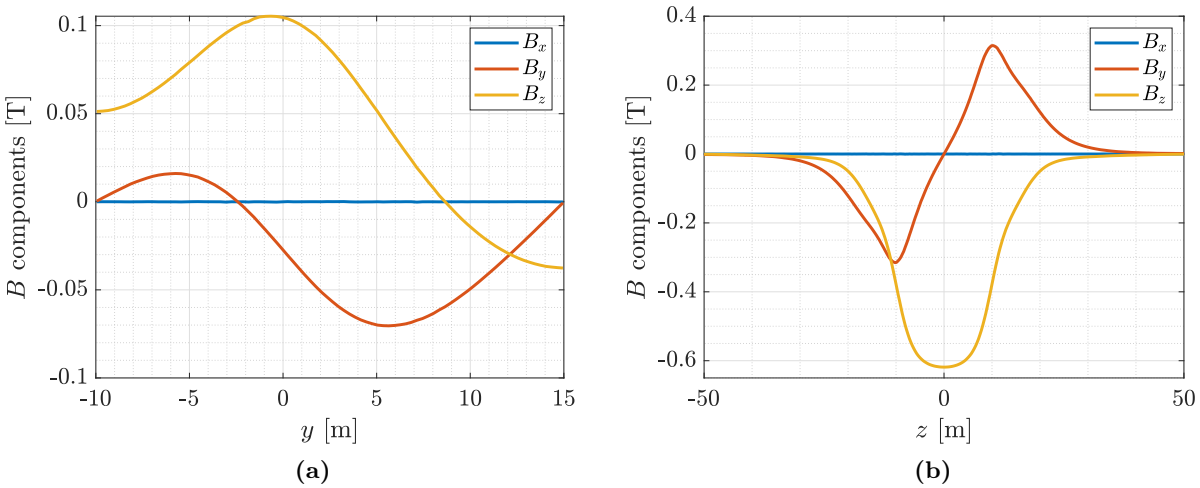

Figure 4.14: Magnetic fields components inside the FCC-hh detector cavern along y @ $x = 0$ m and $z = -25$ m (a), along z @ $x = 0$ m and $y = 10$ m (b).

$f : \mathbb{R}^n \to \mathbb{R}$ at a point P in $\mathbb{R}^n$ is the vector

$$\boldsymbol{\nabla} f = \begin{bmatrix} \dfrac{\partial f}{\partial x_1}(P) & \dfrac{\partial f}{\partial x_2}(P) & \cdots & \dfrac{\partial f}{\partial x_n}(P) \end{bmatrix}^T$$

We also remember that the so-called *gradient formula* applies to the gradient, if the function f is differentiable at a point P, then:

$$\frac{\partial f}{\partial v}(P) = \boldsymbol{\nabla} f \cdot \boldsymbol{v} = \sum_{i=1}^{n} \frac{\partial f}{\partial x_i} v_i$$

where $\boldsymbol{v}$ is any vector and $\frac{\partial f}{\partial v}(P)$ is the directional derivative in P with respect to the direction of $\boldsymbol{v}$. Starting from these notions of mathematical analysis we must calculate the gradient of a vector field[3] in which the definition of a gradient vector extends to that of a *Jacobian matrix*. If we consider a function of the type $f : \mathbb{R}^n \to \mathbb{R}^m$, starting from this function we can define m functions, which we call f_i (with $1 \leq i \leq m$) ranging from $\mathbb{R}^n$ to $\mathbb{R}$, these functions are such that

$$f(x) = \begin{bmatrix} f_1(x) & f_2(x) & \cdots & f_m(x) \end{bmatrix}^T$$

and each f_i admits its corresponding gradient $\boldsymbol{\nabla} f_i$, where it exists. So if we define the Jacobian matrix, the matrix obtained by juxtaposing the m gradients of the f_i in P as rows of the matrix we obtain

$$Jf(P) = \begin{bmatrix} \boldsymbol{\nabla}^T f_1(P) \\ \boldsymbol{\nabla}^T f_2(P) \\ \vdots \\ \boldsymbol{\nabla}^T f_m(P) \end{bmatrix} = \begin{bmatrix} \dfrac{\partial f_1}{\partial x_1} & \cdots & \dfrac{\partial f_1}{\partial x_n} \\ \vdots & \ddots & \vdots \\ \dfrac{\partial f_m}{\partial x_1} & \cdots & \dfrac{\partial f_m}{\partial x_n} \end{bmatrix}$$

In our case the magnetic field is a vector field of three components defined for three independent variables $\boldsymbol{B} : \mathbb{R}^3 \to \mathbb{R}^3$:

$$\boldsymbol{B} = \begin{bmatrix} B_x(x, y, z) \\ B_y(x, y, z) \\ B_z(x, y, z) \end{bmatrix}$$

Hence the Jacobian matrix is a square matrix of order three.

$$J\boldsymbol{B} = \begin{bmatrix} \boldsymbol{\nabla}^T B_x \\ \boldsymbol{\nabla}^T B_y \\ \boldsymbol{\nabla}^T B_z \end{bmatrix} = \begin{bmatrix} \dfrac{\partial B_x}{\partial x} & \dfrac{\partial B_x}{\partial y} & \dfrac{\partial B_x}{\partial z} \\ \dfrac{\partial B_y}{\partial x} & \dfrac{\partial B_y}{\partial y} & \dfrac{\partial B_y}{\partial z} \\ \dfrac{\partial B_x}{\partial x} & \dfrac{\partial B_x}{\partial y} & \dfrac{\partial B_x}{\partial z} \end{bmatrix}$$

As we have already done for the magnetic field, we take some cutting plane and graph the two-dimensional components of the gradient vectors in this plane. In particular, the planes are xy at $z = 0$ m, xz at $y = 0$ m and yz at $x = 0$ m. The results are shown in Figure 4.15.

As we know the gradient represents the direction along which the function grows fastest and in this case it is possible to notice in the three graph in Figure 4.15 that the greater values of the

[3]The vector field associates a vector of the same space to every point of a region of a Euclidean space.

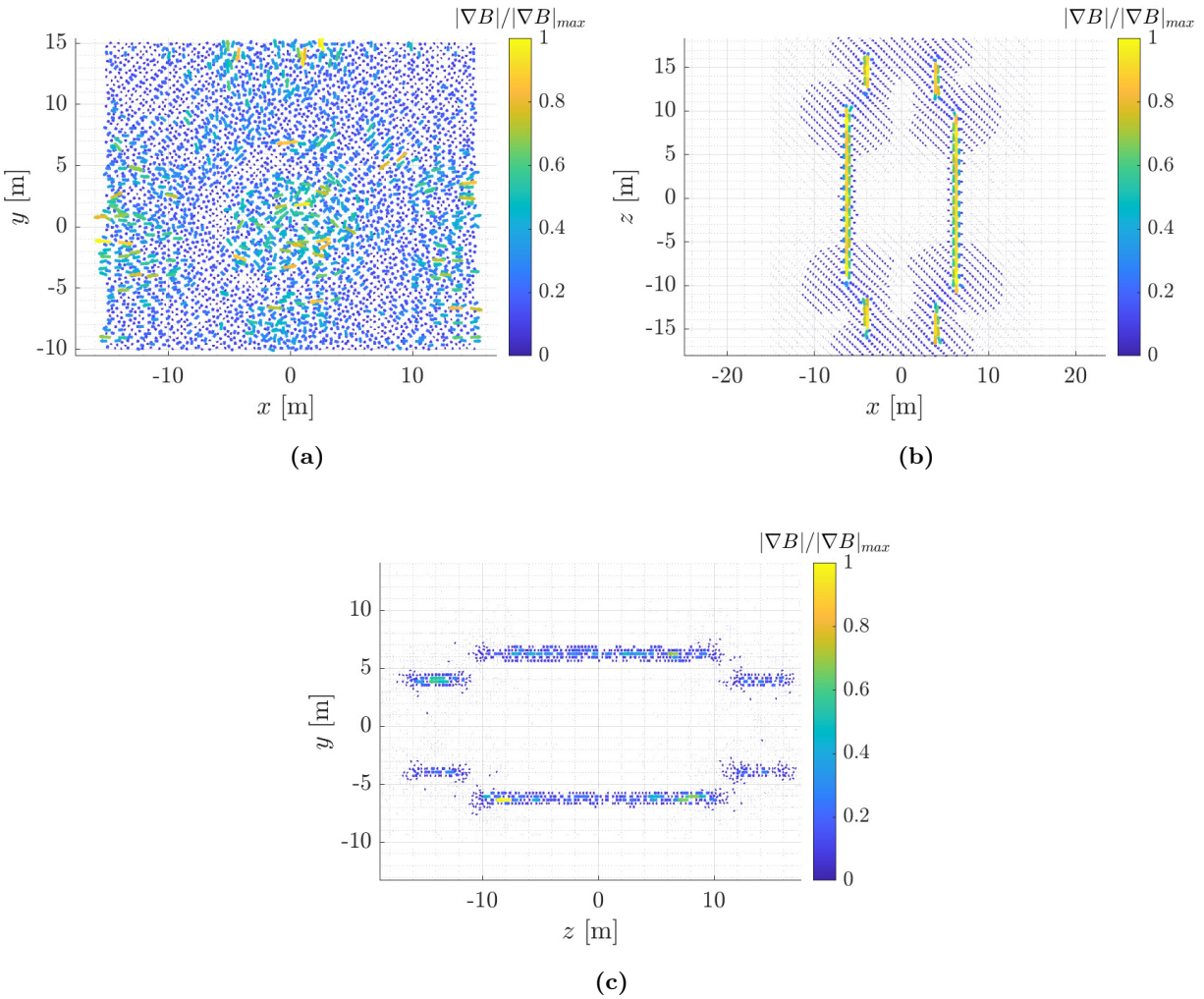

Figure 4.15: Components of the vector space of the magnetic field gradient inside the FCC-hh detector cavern reported in three planes: xy @ $z = 0$ m (a), xz (b) @ y=0 m and yz (c) @ $x = 0$ m. The color scale reports the magnitude of the vectors scaled with respect to the maximum magnitude value.

gradient we have in the passage from inside to outside the solenoid. This is reasonable as the goal of a particle detector would be to obtain a uniform magnetic field within the solenoid structure and then a low field outside. The knowledge of the value of the external residual magnetic field is fundamental for our application as it is precisely the environment in which the mini airship system should fly and knowing its value allows us to estimate the disturbance. The mission of the blimp system will actually be to measure the magnetic field in the detector cavern through inspections. But an initial estimate of the field can be useful to understand the feasibility of the flight of the system itself.

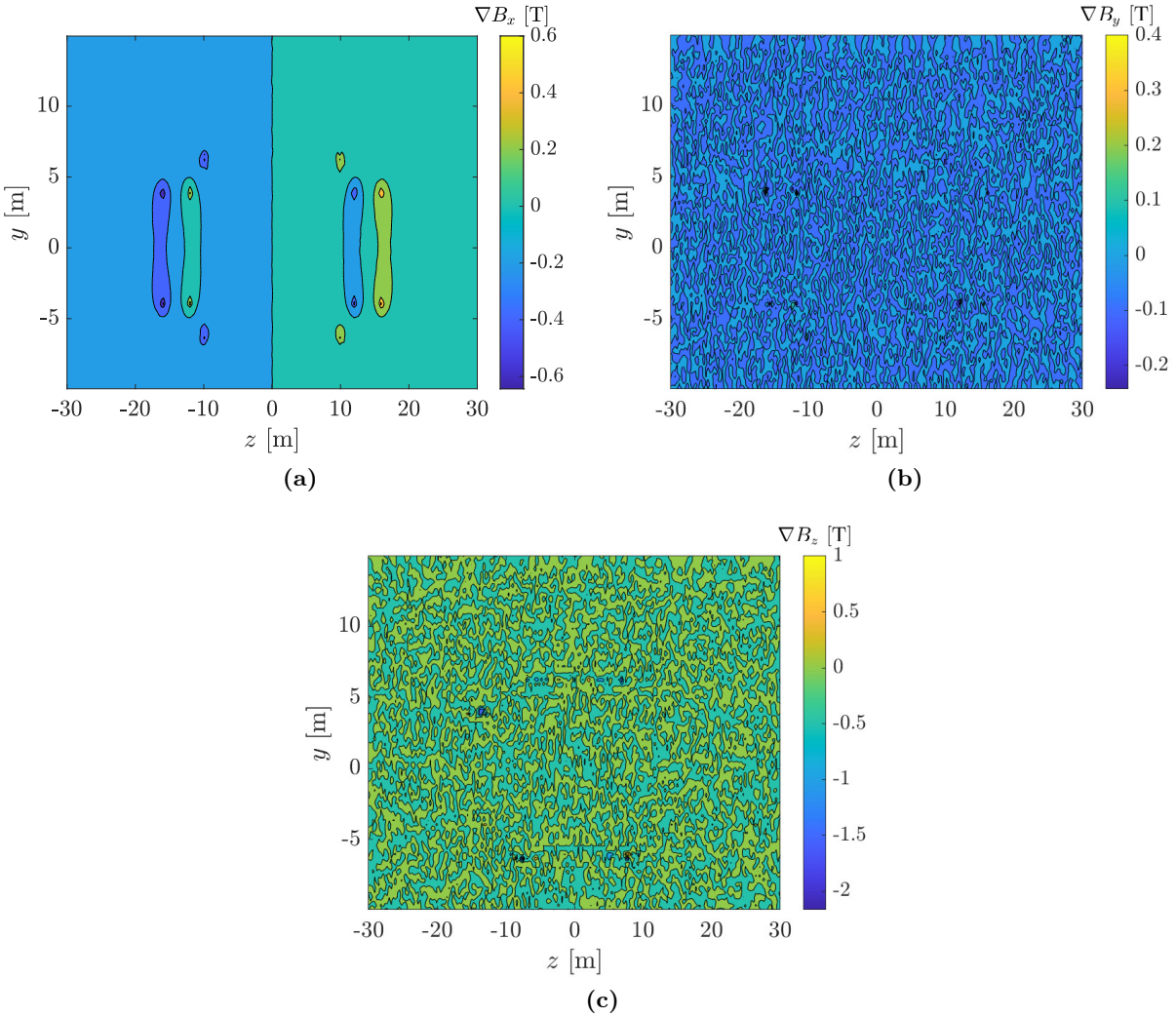

Figure 4.16: ∇B_x (a), ∇B_y (b) and ∇B_z (c) components of the magnetic field gradient inside the FCC-hh detector cavern reported in zy plane @ $x = 0$ m. The color scale reports the magnitude of the components in Tesla.

In Figure 4.16 we report ∇B_x, ∇B_y and ∇B_z components for the ZY plane at $x = 0$ m in three separate graphs. The areas in which the color tone does not change indicate areas in which the gradient is constant, i.e. there are no sensitive variations in the magnetic field, this is clear in Figure 4.16a which shows the ∇B_x vector in the zy plane.

4.3 Magnetic dipole moments in an external magnetic field

In this section we want to recall what a magnetic dipole moment is and calculate the energy, the force, and the torque that it experiences in a non-uniform magnetic field such as that of the FCC-hh detector. As we have shown in Chapter 3, the electric motors of the blimp can be represented from the magnetic point of view as magnetic dipoles. Therefore to quantify the disturbance, in terms of forces and torques, it is necessary to study the interactions of magnetic dipoles with $\boldsymbol{B}$-fields. A more detailed discussion on magnetic moments and the magnetic field generated by them or by magnetized objects is present in Appendix B.

4.3.1 Magnetic moments

The general definition of the magnetic dipole moment $\boldsymbol{m}$ is that of an axial vector constructed to describe the interaction of current loops with the magnetic field [52]. In analogy with an electric dipole, we can imagine that magnetic dipole is formed by a fictitious positive magnetic charge $p^+ = +p$ and a negative magnetic charge $p^- = -p$ of equal magnitude separated by a distance d, as shown in Figure 4.17. By definition, the dipole moment $\boldsymbol{m} = p\boldsymbol{d}$ points from the negative to the positive magnetic pole while the magnetic field $\boldsymbol{B}$ points in the opposite direction so from the positive or north pole to the negative or south pole.

The magnetic dipole moment is used to represent any magnetic field at a great distance. Indeed any non-homogeneous magnetic field can be described by the superposition of the magnetic fields generated by an even number of magnetic poles (see section B.1.4). The higher poles are called quadrupoles, sextupoles, octopoles, etc. The field strength of the higher multipoles naturally decreases even faster with distance r than for the dipole, namely r^{-5}, r^{-7}, r^{-9}, etc. Consequently, at large distances, the field from the dipole is the dominant contribution to the total magnetic field [52].

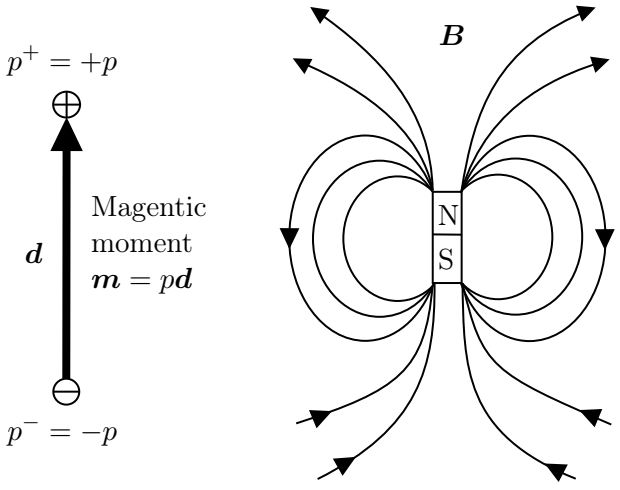

Figure 4.17: Definition of the magnetic moment $\boldsymbol{m}$ and the direction of the $\boldsymbol{B}$ field lines.

4.3.2 The energy of a magnetic dipole

To derive the force that a magnetic dipole undergoes if immersed in an external magnetic field, we must first introduce the concept of energy of a magnetic dipole. The energy of a dipole $\boldsymbol{m}$ in a field

$\boldsymbol{B}$ is given by:

$$E = -\boldsymbol{m} \cdot \boldsymbol{B} \tag{4.1}$$

We see that the energy is a true scalar obtained by multiplying two axial vectors. Equation (4.1) shows that magnetic moments tend to align themselves parallel to the magnetic field [52].

To derive the equation (4.1) it is necessary to consider a dipole as shown in Figure 4.17 which, however, starts from a position perpendicular to the field $\boldsymbol{B}$, therefore it starts to rotate in the direction of $\boldsymbol{B}$ as reported in Figure 4.18. The energy gained by the magnetic dipole which rotates in this way is given by the force times length of the path travelled by the magnetic poles in the direction of the magnetic field. In analogy to what happens in electrostatics, the force can be calculated as the product between the magnetic field and the charge which in the magnetostatic case is the fictitious magnetic charge that makes up a magnetic dipole.

$$\boldsymbol{F}^+ = p^+ \boldsymbol{B} = p\boldsymbol{B}$$

and

$$\boldsymbol{F}^- = p^- \boldsymbol{B} = -p\boldsymbol{B}$$

The energy gain is given by

$$E = \int (\boldsymbol{F}^+ - \boldsymbol{F}^-) \cdot d\boldsymbol{l} = 2p \int \boldsymbol{B} \cdot d\boldsymbol{l} \tag{4.2}$$

Looking at Figure 4.18 we see that $\boldsymbol{B} \cdot d\boldsymbol{l} = B(d/2)\cos\phi d\phi$, therefore we can rewrite equation (4.2) as follows

$$E = pdB \int_{\pi/2}^{0} \cos\phi d\phi = -\boldsymbol{m} \cdot \boldsymbol{B}$$

where we have used the definition $p\boldsymbol{d} = \boldsymbol{m}$ from Figure 4.17.

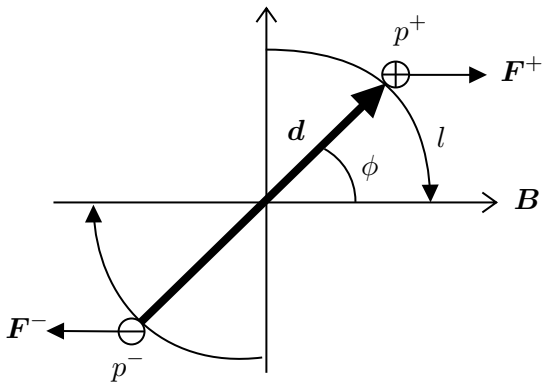

Figure 4.18: A magnetic dipole $\boldsymbol{m} = p\boldsymbol{d}$ initially perpendicular to the magnetic field direction is turned into its stable state parallel to the magnetic field.

4.3.3 The force on a magnetic dipole

To derive the force $\boldsymbol{F}$ of a magnetic dipole $\boldsymbol{m}$ in an non-homogeneous static magnetic field $\boldsymbol{B}(x, y, z)$, we calculate the negative gradient of the energy.

$$\boldsymbol{F} = \boldsymbol{\nabla}(\boldsymbol{m} \cdot \boldsymbol{B}) \tag{4.3}$$

We can write (4.3) component by component obtaining

$$\begin{aligned} F_x &= \frac{\partial}{\partial x}(\boldsymbol{m}\cdot\boldsymbol{B}) = \frac{\partial \boldsymbol{B}}{\partial x}\cdot\boldsymbol{m} = \frac{\partial B_x}{\partial x}m_x + \frac{\partial B_y}{\partial x}m_y + \frac{\partial B_z}{\partial x}m_z \\ F_y &= \frac{\partial}{\partial y}(\boldsymbol{m}\cdot\boldsymbol{B}) = \frac{\partial \boldsymbol{B}}{\partial y}\cdot\boldsymbol{m} = \frac{\partial B_x}{\partial y}m_x + \frac{\partial B_y}{\partial y}m_y + \frac{\partial B_z}{\partial y}m_z \\ F_z &= \frac{\partial}{\partial z}(\boldsymbol{m}\cdot\boldsymbol{B}) = \frac{\partial \boldsymbol{B}}{\partial z}\cdot\boldsymbol{m} = \frac{\partial B_x}{\partial z}m_x + \frac{\partial B_y}{\partial z}m_y + \frac{\partial B_z}{\partial z}m_z \end{aligned} \tag{4.4}$$

We can expand the right-hand side of (4.3) according to the gradient operator rules and by assuming that the dipole is small we obtain

$$\boldsymbol{F} = (\boldsymbol{m}\cdot\boldsymbol{\nabla})\boldsymbol{B} \tag{4.5}$$

4.3.4 The torque on a magnetic dipole

In Figure 4.18 we can see that the magnetic field is homogeneous therefore it has the same magnitude at the location of the poles p^+ and p^- of a magnetic dipole. Hence it exerts an equal but opposite force $\boldsymbol{F} = p\boldsymbol{B}$ on each magnetic pole with a net force equal to zero. However, the dipole experiences a torque $\boldsymbol{T}$. The torque on a dipole $\boldsymbol{m}$ in a field $\boldsymbol{B}$ is given by

$$\boldsymbol{T} = \boldsymbol{m}\times\boldsymbol{B} \tag{4.6}$$

4.3.5 Magnetic interactions inside the FCC-hh detector cavern

From the formulas for calculating the force (4.5) and the torque (4.6) that a magnetic dipole moment undergoes if immersed in a non-uniform external magnetic field, it is clear that these depend not only on the value of the magnetic field but also on the value of the magnetic moment. From what we have just seen, the value of the magnetic field at least through the CST simulation is known. Obviously this is a first starting point and let us remember once again that the objective of the blimp mission in the future will be precisely to be able to map the magnetic field inside the cavern.

The other parameter that determines the order of magnitude of the magnetic interactions fall on the value of $\boldsymbol{m}$. As we have seen in Chapter 3, it is possible to represent an electric motor with a magnetic moment vector whose magnitude and orientation in space will strongly depend on the characteristics of the motor itself even if in reality it will also depend on the value of the magnetic field (for the magnetization of materials). In this section we want to obtain the orders of magnitude of forces and torques with the value of the field calculated before with the CST simulation and the value of $\boldsymbol{m}$ as parameter.

Let's imagine we have a magnetic dipole moment immersed inside the detector cavern. Based on its orientation in space and its magnitude, it will experience forces and torques. We assume that the magnetic moment has a general orientation in space. We can therefore represent the vector in space through its spherical coordinates[4] (Figure 4.19) . The three Cartesian coordinates of a point, with respect of the FCC frame, are obtained from the three spherical coordinates of that point

[4]Spherical coordinates are an extension of the polar coordinates in three-dimensional space.

with the following relationship:

$$\begin{cases} x = \rho \sin\theta \cos\varphi \\ y = \rho \sin\theta \sin\varphi \\ z = \rho \cos\theta \end{cases} \tag{4.7}$$

where ρ is the distance from the pole, θ is the angle formed with the z-axis and φ is the angle formed by the projection onto the xy plane with the x-axis as shown in Figure 4.19.

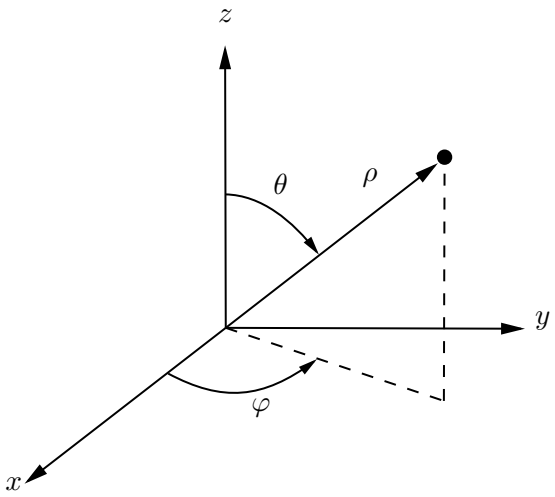

Figure 4.19: Spherical coordinate system.

At this point, we imagine to freeze its orientation and we begin to move the vector in space with the purpose of calculating at each point in space the pair of force and torque vectors that the magnetic moment with that orientation and with that magnitude would experience. We actually create a vector space where we associate a force vector and a torque vector to each point of the FCC reference space. We are going to graph the value of the force field and the torque field in different directions keeping the orientation fixed and changing the module instead.

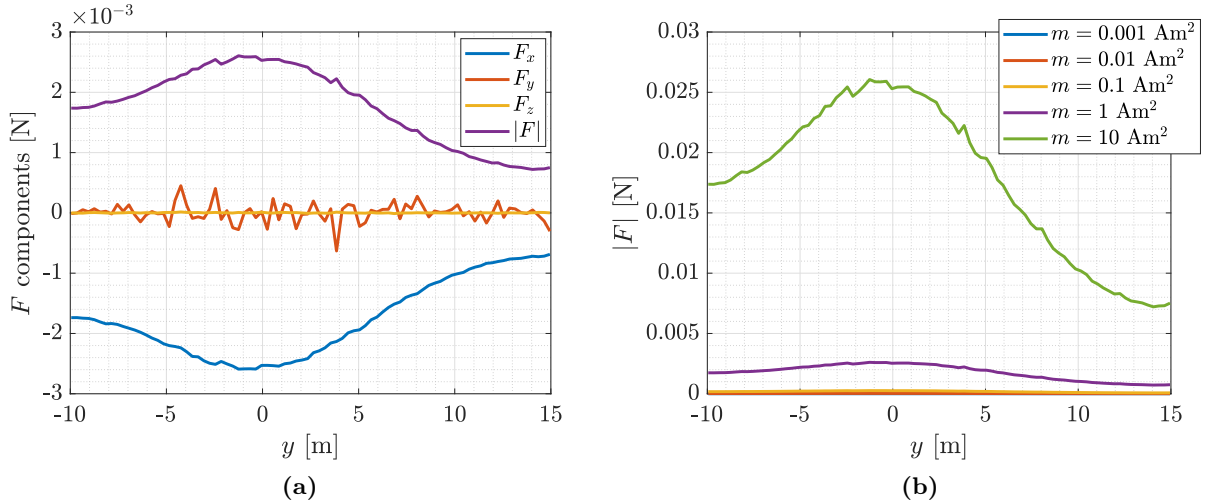

(a) **(b)**

Figure 4.20: Magnetic force vector inside the FCC-hh detector cavern along y with $x = 0$ m and $z = -25$ m with $\theta = \phi = 10$ deg: force components with $m = 1$ Am^2 (a) and magnitude of the magnetic force vector with m varying from 0.001 to 10 Am^2 (b).

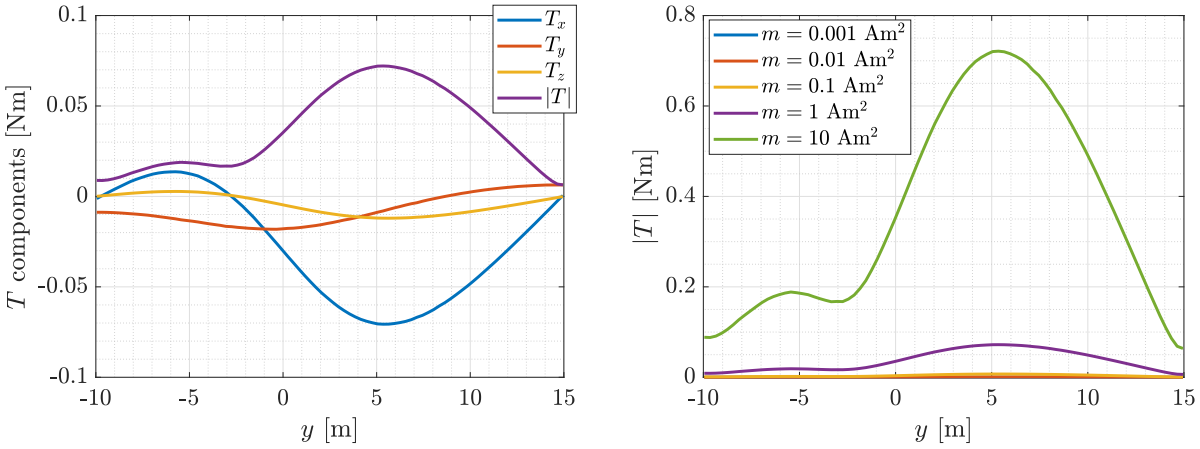

Figure 4.21: Magnetic torque vector inside the FCC-hh detector cavern along y with $x = 0$ m and $z = -25$ m with $\theta = \phi = 10$ deg: torque components with $m = 1$ Am^2 (a) and magnitude of the magnetic torque vector with m varying from 0.001 to 10 Am^2 (b).

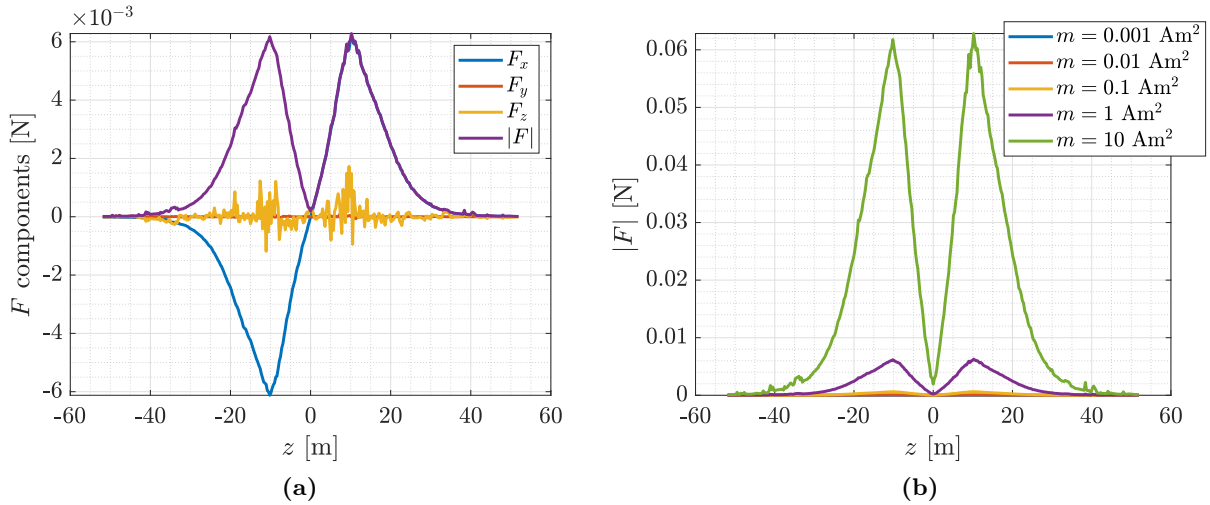

Figure 4.22: Magnetic force vector inside the FCC-hh detector cavern along z with $x = 0$ m and $y = 10$ m with $\theta = \phi = 10$ deg: force components with $m = 1$ Am^2 (a) and magnitude of the magnetic force vector with m varying from 0.001 to 10 Am^2 (b).

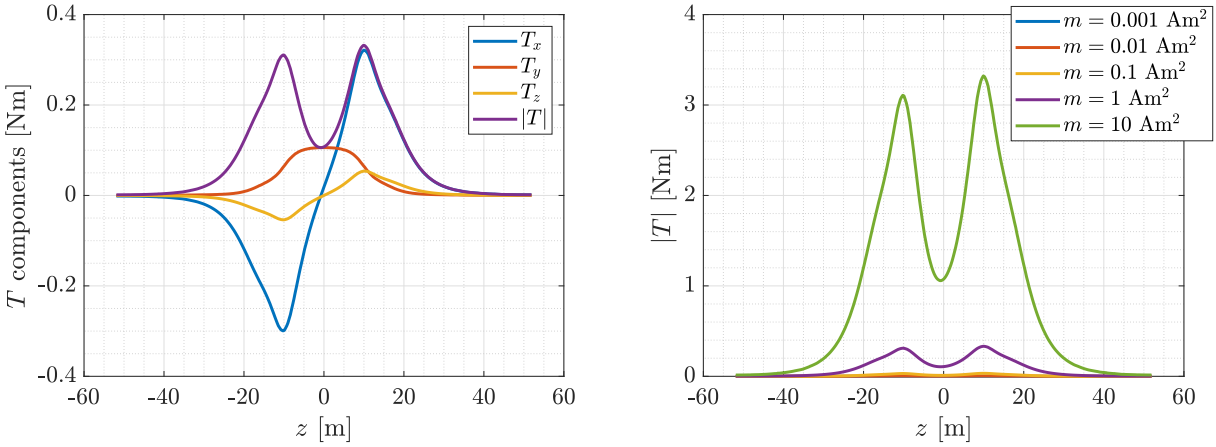

Figure 4.23: Magnetic torque vector inside the FCC-hh detector cavern along z with $x = 0$ m and $y = 10$ m with $\theta = \phi = 10$ deg: torque components with $m = 1$ Am^2 (a) and magnitude of the magnetic torque vector with m varying from 0.001 to 10 Am^2 (b).

Figure 4.20a shows the components of the force vector calculated using equation (4.3) as y varies with x fixed at 0 m and z fixed at -25 m. Recall that this choice is based on the architecture of the cavern and it is dictated by the presence of components and obstacles reported in Figure 4.5. These components depicted in Figure 4.20a have been obtained by imagining that the magnetic moment vector has a magnitude equal to 1 Am^2 and has a generic orientation in space. Its orientation was defined by spherical coordinates with $\theta = \phi = 10$ deg. Analyzing the Figure 4.20a, it is possible to notice that when climbing in altitude, the blimp undergoes a greater force in the negative x direction. The other two components, on the other hand, are nil on average. The order of magnitude of the forces can be obtained from Figure 4.20b where the modulus of $\boldsymbol{F}$ is reported as the magnitude of $\boldsymbol{m}$ varies with fixed orientation. If the magnetic moment has a module of 1 Am^2 then the disturbance is of the order of mN, however, we note that with a module of 10 Am^2 the force increases by an order of magnitude.

For the same scenario of ascent to altitude, the magnetic torques to which the magnetic moment will be subjected were simulated. These are visible in Figure 4.21a where the components of the magnetic torque have been obtained thanks to the equation (4.6). Also in this case the chosen magnetic moment has a magnitude of 1 Am^2 and orientation dictated by θ and ϕ angles in spherical coordinates equal to 10 deg. In Figure 4.21a it is possible to notice that the magnetic moment with the same modulus and orientation will feel more the influence of the torques rather than of the forces as these have an order of magnitude more than the corresponding magnetic forces shown in Figure 4.20a. This reasoning also extends to Figure 4.21b in which the values of the torque modulus are reported as the magnitude of the magnetic moment varies. Once again if we go from 1 to 10 Am^2 the magnetic torques scale by a factor of 10.

In Figure 4.22a the components of the magnetic force with $m = 1$ Am^2 and $\theta = \phi = 10$ deg are reported as z varies for $x = 0$ m and $y = 10$ m. In Figure 4.22b the modulus of the force vector as the modulus of $\boldsymbol{m}$ varies with fixed orientation have been reported for the same scenario. In this case the blimp having reached the altitude of 10 m runs the length of the solenoid overlapping it from above. In Figure 4.22a the main force component is F_x and the order of magnitude is

always mN, if we consider to the parametric graph in m (Figure 4.22b) the force modulus increases considerably by increasing the value m.

Finally, for the same scenario, Figure 4.23 shows the torques felt by the magnetic moment that moves with that orientation along the abscissa z. As was the other case, the components of the torques (Figure 4.23a) of a magnetic moment of module equal to 1 Am^2 are greater than the force components that it receives. In Figure 4.23b, on the other hand, for the same orientation in space, a parametric study is performed as the modulus of $\boldsymbol{m}$ varies.

These graphs do not give us the exact calculation of the magnetic disturbances because there are many other factors to take into account, however they are of extreme importance as regards the familiarization of the orders of magnitude of the magnetic field, of the field gradient and of the relative forces and torques that a generic magnetic moment undergoes being inside the field. In particular, we can see from the graphs of forces and torques that in general the latter are in magnitude greater than their respective forces. This can be explained by examining the formulas (4.3) and (4.6). Indeed the components of the magnetic force depend on the components of the gradient of the field while, on the other hand, the components of the magnetic torque directly depend on the $\boldsymbol{B}$ components. From the comparison of the two it is clear that the torques are greater than the forces as the field of our interest does not vary abruptly and this involves a softer gradient.

4.4 Trajectory generation

In section 4.3 we talked about directions and spaces in which the blimp can move and areas inaccessible to it, this in reference to Figure 4.5 which shows the cross section of the FCC-hh detector with all the fundamental components for its functioning. It is therefore important to define particular trajectories that the blimp can follow with respect to the environment in which it is located. In this section we will explain the method used to generate the reference trajectory that the blimp must perform inside the detector cavern.

By the term *trajectory* we mean a time history of position, velocity, and acceleration for each degree of freedom of the system. To generate a trajectory, we always start from what is the initial and final position that the system must reach and at what instant of time. However, many times assigning the initial and final configuration is not enough, think about the problem of generating a trajectory that must avoid certain obstacles present in the flight environment, which is very probable and crucial in the detector environment. Therefore it is necessary to specify the motion in much more detail for instance giving a sequence of desired *via points*[5]. Thus the blimp, in its motion, going from the initial to final position, must pass through a set of intermediate positions and orientations as described by the via points. In addition, it is also possible to attribute temporal properties such as the travel times between via points. Another important property that we try to obtain in the trajectory generation process is that the motion of the blimp has to be smooth. We define as smooth, a function that is continuous and has a continuous first derivative [26].

In the next paragraphs we will see the problem of moving the blimp from its initial position to a final position by passing through a certain number of via points in a certain amount of time. This requires a function whose value at t_0 is the starting position and the value at t_f is the desired

[5]Intermediate points between the initial and final positions.

position of the blimp with the aim of obtaining a smooth path.

4.4.1 Cubic polynomials for a path with via points

Let us consider a generic variable $\theta(t)$ that describes the time course of a degree of freedom of the system. The first technique to obtain a smooth motion for $\theta(t)$ is to interpolate the via points with cubic polynomials. For doing this, we need at least four constraints for $\theta(t)$. Two constraints on the value of the function come from the selection of the initial and final values and the other two come from the fact that the function must be continuous in velocity.

$$\begin{aligned} \theta(0) &= \theta_0 \\ \theta(t_f) &= \theta_f \end{aligned} \tag{4.8}$$

$$\begin{aligned} \dot{\theta}(0) &= \dot{\theta}_0 \\ \dot{\theta}(t_f) &= \dot{\theta}_f \end{aligned} \tag{4.9}$$

The four constraints given by (4.8) and (4.9) are satisfied by a unique cubic polynomial which has the form

$$\theta(t) = a_0 + a_1 t + a_2 t^2 + a_3 t^3 \tag{4.10}$$

Hence, the blimp velocity and acceleration along this path are:

$$\begin{aligned} \dot{\theta}(t) &= a_1 + 2a_2 t + 3a_3 t^2 \\ \ddot{\theta}(t) &= 2a_2 + 6a_3 t \end{aligned} \tag{4.11}$$

Combining (4.10) and (4.11) with the four desired constraints yields four equations in four unknowns.

$$\begin{aligned} \theta_0 &= a_0 \\ \theta_f &= a_0 + a_1 t_f + a_2 t_f^2 + a_3 t_f^3 \\ \dot{\theta}_0 &= a_1 \\ \dot{\theta}_f &= a_1 + 2a_2 t_f + 3a_3 t_f^2 \end{aligned}$$

Solving these equations for the a_i coefficients, we obtain

$$\begin{aligned} a_0 &= \theta_0 \\ a_1 &= \dot{\theta}_0 \\ a_2 &= \frac{3}{t_f^2}(\theta_f - \theta_0) - \frac{2}{t_f}\dot{\theta}_0 - \frac{1}{t_f}\dot{\theta}_f \\ a_3 &= -\frac{2}{t_f^3}(\theta_f - \theta_0) + \frac{1}{t_f^2}(\dot{\theta}_f + \dot{\theta}_0) \end{aligned} \tag{4.12}$$

Substituting these four coefficients in equation (4.10) we obtain the cubic polynomial that connects any initial and final positions with any initial and final velocities.

4.4.2 Higher-order polynomials

If we want to introduce information on acceleration, we need not four but six constraints for the $\theta(t)$ function so we obtain a quintic polynomial:

$$\theta(t) = a_0 + a_1 t + a_2 t^2 + a_3 t^3 + a_4 t^4 + a_5 t^5 \tag{4.13}$$

where the constraints are given as

$$\begin{aligned}
\theta_0 &= a_0 \\
\theta_f &= a_0 + a_1 t_f + a_2 t_f^2 + a_3 t_f^3 + a_4 t_f^4 + a_5 t_f^5 \\
\dot{\theta}_0 &= a_1 \\
\dot{\theta}_f &= a_1 + 2a_2 t_f + 3a_3 t_f^2 + 4a_4 t_f^3 + 5a_5 t_f^4 \\
\ddot{\theta}_0 &= 2a_2 \\
\ddot{\theta}_f &= 2a_2 + 6a_3 t_f + 12a_4 t_f^2 + 20a_5 t_f^3
\end{aligned}$$

These constraints specify a linear set of six equations with six unknowns, whose solution is

$$\begin{aligned}
a_0 &= \theta_0 \\
a_1 &= \dot{\theta}_0 \\
a_2 &= \frac{\ddot{\theta}_0}{2} \\
a_3 &= \frac{20\theta_f - 20\theta_0 - (8\dot{\theta}_f + 12\dot{\theta}_0)t_f - (3\ddot{\theta}_0 - \ddot{\theta}_f)t_f^2}{2t_f^3} \\
a_4 &= \frac{30\theta_f - 30\theta_f + (14\dot{\theta}_f + 16\dot{\theta}_0)t_f - (3\ddot{\theta}_0 - \ddot{\theta}_f)t_f^2}{2t_f^4} \\
a_5 &= \frac{12\theta_f - 12\theta_0 - (6\dot{\theta}_f + 6\dot{\theta}_0)t_f - (\ddot{\theta}_0 - \ddot{\theta}_f)t_f^2}{2t_f^5}
\end{aligned}$$

Substituting these six coefficients in equation (4.13) we obtain the quintic polynomial that connects any initial and final positions with any initial and final velocities and accelerations.

4.4.3 Linear function with parabolic blends with via points

Another very interesting method to generate a smooth trajectory for the blimp are the linear functions with parabolic blends which will be the method we will use in Chapter 5. The path of the system consists of sections that connect the via points and each section is formed by a linear function and then parabolic blends are added around each via points to create a path which is continuous in position and velocity. Figure 4.24 shows a set of via points for some state variable $\theta(t)$. If we consider three neighbouring path points, which we will call points j, k and l, the duration of the blend region at path point k is t_k, the duration of the linear portion between points j and k is t_{jk}. The overall duration of the segment connecting points j and k is t_{djk}. The velocity during the linear portion is $\dot{\theta}_{jk}$, and the acceleration during the blend at point j is $\ddot{\theta}_j$ [26].

If we assign as known data all the path points θ_k, the desired duration t_{djk} and the blending

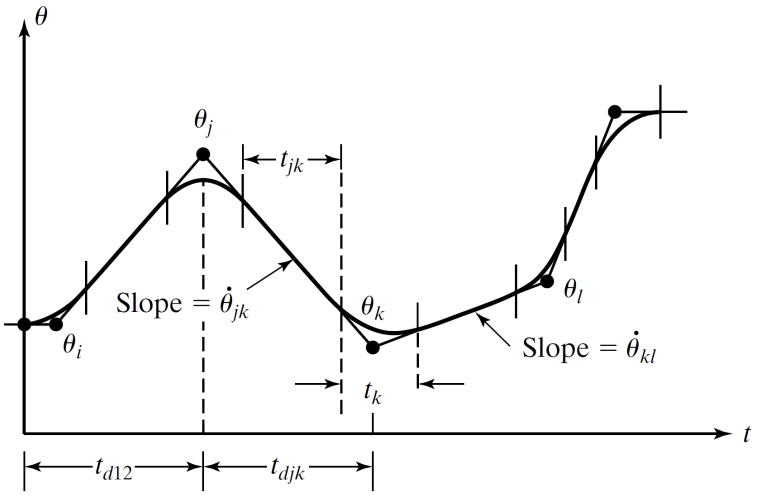

Figure 4.24: Linear functions with parabolic blends definitions. From [26].

times t_k, then we can compute the acceleration to use at each path point. First we analyze the internal points

$$\begin{aligned} t_{jk} &= t_{djk} - \frac{1}{2}t_j - \frac{1}{2}t_k \\ \dot{\theta}_{jk} &= \frac{\theta_k - \theta_j}{t_{djk}} \\ \ddot{\theta}_k &= \frac{\dot{\theta}_{kl} - \dot{\theta}_{jk}}{t_k} \end{aligned} \tag{4.14}$$

and then the other quantities are calculated for the first and last point. For the first segment:

$$\begin{aligned} t_{12} &= t_{d12} - t_1 - \frac{1}{2}t_2 \\ \dot{\theta}_{12} &= \frac{\theta_2 - \theta_1}{t_{d12} - \frac{1}{2}t_1} \\ \ddot{\theta}_1 &= \frac{\dot{\theta}_{12}}{t_1} \end{aligned} \tag{4.15}$$

For the last segment we have:

$$\begin{aligned} t_{(n-1)n} &= t_{d(n-1)n} - t_n - \frac{1}{2}t_{(n-1)} \\ \dot{\theta}_{(n-1)n} &= \frac{\theta_n - \theta_{(n-1)}}{t_{d(n-1)n} - \frac{1}{2}t_n} \\ \ddot{\theta}_n &= \frac{\dot{\theta}_{(n-1)n}}{t_n} \end{aligned} \tag{4.16}$$

4.4.4 Generation of blimp-space path

What we have seen in the (4.14), (4.15) and (4.16) formulas is the procedure for calculating all the parameters of each section of the trajectory for linear functions with parabolic blends method. This data then has to be used by the so-called *path generator* at run time to calculate θ, $\dot{\theta}$, and $\ddot{\theta}$. The calculation of the time t is also maintained to establish whether we are in the linear portion or in

the parabolic portion. If we are in the linear portion, the trajectory for $\theta(t)$ is calculated as

$$\begin{aligned}\theta &= \theta_j + \dot{\theta}_{jk} t \\ \dot{\theta} &= \dot{\theta}_{jk} \\ \ddot{\theta} &= 0\end{aligned}$$

If, on the other hand, we are in the parabolic region, the trajectory is calculated as

$$\begin{aligned}t_{inb} &= t - \left(\frac{1}{2} t_j + t_{jk}\right) \\ \theta &= \theta_j + \dot{\theta}_{jk}(t - t_{inb}) + \frac{1}{2}\ddot{\theta}_k t_{inb}^2 \\ \dot{\theta} &= \dot{\theta}_{jk} + \ddot{\theta}_k t_{inb} \\ \ddot{\theta} &= \ddot{\theta}_k\end{aligned}$$

And this process continues, with t being reset to $\frac{1}{2}t_k$ when a new linear segment is entered, until we get to the last segment.

4.5 Conclusion

In this chapter we have analyzed in detail the flight environment of the blimp. In particular, the main characteristic of the physical environment in which the robotic system will operate is the magnetic field generated by the solenoids system of the FCC-hh detector. This system is made up of three solenoids, one of which is the main solenoid and two are the forward solenoids. The magnetic field generated inside this system is 4 T field. What we were interested in was the characterization of the residual field, i.e., the magnetic field outside this structure which coincides with the blimp's working space. Once the map of the field has been characterized through two different simulations, we have moved on to the characterization of the forces and torques that act on a magnetic dipole which, being inside this space, will feel the presence of the magnetic field generated by the detector. In this case we have imagined a generic magnetic dipole vector with a particular orientation in space and for each position we have determined the value of the force and torque components that act on it, becoming aware of the order of magnitude of the disturbance to which the electric motors will be subject. Finally, to conclude the chapter we have provided the necessary tools for the generation of trajectories through the definition of an initial and final position and of the via points through which we want the blimp to pass, both to observe areas of interest to the inspection and to avoid obstacles present in that area.

Chapter 5

Stability and Control

5.1 Introduction

In Chapter 4 we have shown a method to be able to design a trajectory of desired states that the mini airship must follow. In this chapter we introduce the control system which has the task of ensuring that the blimp performs exactly the desired motion despite the presence of disturbances that tend to make it deviate from the path. If the control system calculates the inputs that the actuators must give in order to follow the trajectory and reject the disturbances, then the system is called an *autopilot*. The autopilot does not replace the human operator, but assists the control phase of the vehicle making it autonomous and no longer requiring the constant manual control done by the human and therefore allows the operator to focus on other aspects.

Before simulating control strategies, in section 5.2 we explain why it is necessary to use a feedback-based closed loop control to ensure that the system follows a desired motion. In section 5.3 we give an overview of the state of the art of blimp control by explaining which are the most commonly used control strategies in modern practice. So once we have chosen the path of linearization of the equations of motion, in section 5.4 we are going to outline the steps that lead us to the linearization of the 6 DOF nonlinear dynamics equation with the creation of two linear and decoupled subsystems that describe the motion of the blimp in two planes: longitudinal and lateral. After having linearized the equations, two different controllers are adopted which are the Proportional Integrative Derivative (PID) and Linear Quadratic Regulator (LQR). Then, it was fundamental to develop a method for estimating the magnetic disturbances that are added to the dynamics equations. Section 5.7 shows the method of estimating magnetic disturbances through the knowledge of the magnetic field in each point where the blimp is located and on the basis of the magnetic moment that represents the particular electric motor of the system. In section 5.8, therefore, two simulations based on PID and LQR controllers applied to the linear equations of the system are carried out and the results of a trajectory tracking control simulation are reported. For the case of the PID controller the magnetic disturbances are added while the simulation based on the LQR controller is performed without magnetic disturbances.

5.2 Feedback and closed loop control

With the design of the trajectory, made in section 4.4, we have the time sequence of the desired state variables and we would like the blimp to follow them. This is a typical control system problem and to achieve this goal we can act on the system only through the use of actuators that are controlled in terms of forces and torques. Therefore the state of the system, i.e. position, velocity and acceleration, can be controlled at will only with the use of specific actuator devices such as electric propeller motors which exert forces and moments on the system, varying its motion and hence its status. In this context, the control system through the dynamics of the blimp calculates the exact commands of the actuators that cause the desired motion to be achieved. Hence through the trajectory generation we give $\boldsymbol{\eta}_d(t)$, $\dot{\boldsymbol{\eta}}_d(t)$ and $\ddot{\boldsymbol{\eta}}_d(t)$, $\boldsymbol{\xi}_d(t)$, $\dot{\boldsymbol{\xi}}_d(t)$ and $\ddot{\boldsymbol{\xi}}_d(t)$ so we could use (2.21) to compute:

$$\boldsymbol{\tau} = \boldsymbol{M}\dot{\boldsymbol{\xi}}_d + \boldsymbol{C}(\boldsymbol{\xi}_d)\boldsymbol{\xi}_d + \boldsymbol{D}(\boldsymbol{\xi}_d)\boldsymbol{\xi}_d + \boldsymbol{g}(\boldsymbol{\eta}_d) \tag{5.1}$$

In this way we calculate the desired forces and torques to make the system follow the desired trajectory. However this would be true if our dynamics fully represent what is happening in reality, but as we have seen in Chapter 2, the dynamics represent an approximation of the behavior of a mini airship. In addition, the inaccuracy of the actuators, the measurement noise of the sensors and most of all disturbances must also be considered. With all these factors, the continued use of (5.1) would not make it execute the desired trajectory. This type of approach is called an *open-loop* scheme, because the control is based only on the values of the desired trajectory $\boldsymbol{\eta}_d$ and its derivatives, and is not a function of the current trajectory that is the actual state of the blimp. To base the control not on the desired state but on the current state, we need to make use of sensors which measure the true position of the system and use this information to calculate the controls. This other technique is called *closed loop* scheme. The way in which sensor measurements are used to calculate the forces and moments that tend to make the blimp follow the trajectory, is called *feedback*. Most control systems make use of closed loop control laws based on sensor feedback [26].

Figure 5.1 shows a very general representation of the control scheme based on feedback. The block called *Trajectory generator* sends to the system the values of the desired state at each instant of time, the block called *Control system* reads both the desired state and the true state sent as feedback from the sensors that measure the vectors of positions and attitude, $\boldsymbol{\eta}$, and linear and angular velocities, $\boldsymbol{\xi}$. The feedback is used to compute any servo error through the difference between the desired and the actual state.

$$\boldsymbol{e}_\eta = \boldsymbol{\eta}_d - \boldsymbol{\eta}$$
$$\dot{\boldsymbol{e}}_\eta = \dot{\boldsymbol{\eta}}_d - \dot{\boldsymbol{\eta}}$$

On the basis of the comparison between the two, the control system decides to send the input value $\boldsymbol{\tau}$ to the actuators such that the difference between the two is zero, i.e. that the current state coincides with the desired one.

Once the closed loop control system has been designed, it typically has to meet certain requirements and performance. The most important requirement is that the system is stable, i.e. when errors remain small during the control procedure even in the presence of disturbances.

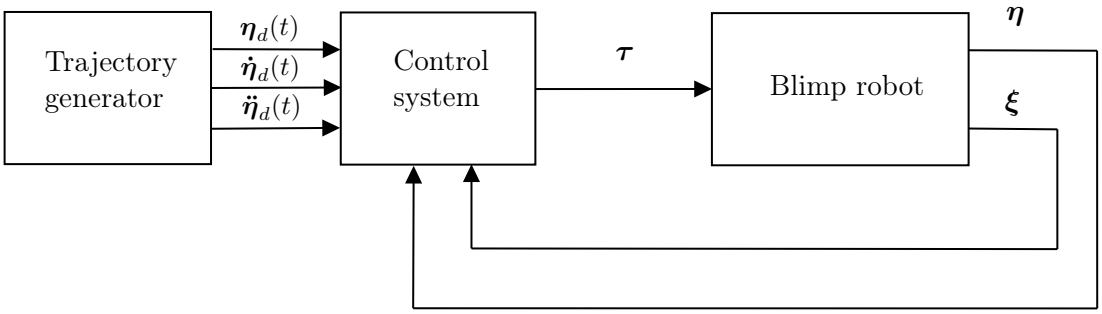

Figure 5.1: High-level block diagram of a robot-control system.

5.3 State of the art on blimp controllers

In the literature there are many works on the control of the motion of blimp. These generally fall into three broad categories: stabilization, trajectory tracking and path tracking. The stabilization problem focuses on stabilizing the blimp in a precise desired position. The trajectory tracking problem is based on the design of a control law that forces the blimp to follow a trajectory that is defined in terms of the temporal sequence of desired positions. The path following problem differs from the previous method since the path to follow is not specified as a temporal law [3]. If one considers that the blimp has low maneuverability, the path following controller would be preferable to the trajectory tracking controller [96].

Having done an in-depth research activity for the problem of motion controllers developed for small indoor blimp, it has been noted that controllers can generally be divided into two broad categories: the first category is more traditional, i.e. it concerns the design of control laws and algorithms based on the dynamic and kinematic model of the blimp. The second category is more modern, the controllers in this category depend less on the blimp model or are even completely free from the knowledge of the dynamic parameters of the system and rely on advanced learning techniques.

Regarding the first category of controllers, a nonlinear control technique often used is feedback linearization (also called dynamic inversion). Since the blimp model is highly nonlinear, feedback control law can be designed in such a way to cancel the nonlinear terms of the blimp system and then to transform the closed loop control system into a linear one. This is why this technique is called feedback linearization [20, 54]. An application of this technique is found in the work of [95] where the authors use feedback linearization in conjunction with a PID controller. Another example can be found in [67] where the dynamic inversion controller is used for the path following technique of the AURORA airship. The disadvantage of using this control technique lies in the fact that in order to be able to implement it and therefore cancel all the non-linearities of the system, it is necessary to know perfectly all the terms that appear in the dynamics, therefore these techniques are typically associated with other control projects complementary to this which make the closed loop system robust to model uncertainties and other disturbances [35]. Since it is a very used control technique, we have reported its development and a simulation example in Appendix C.

Another nonlinear technique often used for controlling the blimp model is the backstepping method. This control algorithm is based on dividing the controller of the complete system into a sequence of control problems for minor subsystems by choosing suitable Lyapunov functions. In general, the backstepping method finds a feedback controller that guarantees the stability of the

nonlinear system and at the same time ensures the robustness to uncertainties [8, 54]. Below are reported some examples of applications of the backstepping technique to the problem of controlling the motion of the blimp. In the work of [39] there is an application of the backstepping technique to design an image-based controller. Another example is in the paper of [45] in which the authors propose a nonlinear control approach designing a backstepping controller for the path-tracking of an autonomous underactuated airship including wind disturbances and considering also actuators saturation. Then we can cite the work of [15] whose authors investigated the problem of designing a tracking feedback control for an underactuated blimp using an integrator backstepping approach and Lyapunov theory for trimmed ascent and descent flight. Many others could be mentioned but the main problem of the backstepping technique lies in the fact that the order of the system increases and the control becomes more complicated to design especially in the choice of Lyapunov functions.

The examples cited above use nonlinear techniques to control the motion of the blimp, however the complexity of the nonlinear 6 DOF equation of motion leads to the choice of linearizing the dynamics of the system. To derive the linear dynamics model for the small indoor blimp, the first step is to define a reference equilibrium state, the second step is therefore to write the equations of motion for small perturbations with respect to the equilibrium state. Linear controllers fit into this context and the most popular linear control techniques for a Multi Input Multi Output (MIMO) system are the Pole Placement (PP) and the Linear Quadratic Regulator (LQR). PP allows to allocate the poles of the MIMO system to desired locations however, this strategy does not confer any stability robustness to the closed loop system. This instead is what we are looking for above all because the model that we want to control is an approximation of the nonlinear model, which in turn is an approximation of reality. Furthermore, the PP does not even take into consideration disturbances that are present in the environment or that come from the measurement noise of the sensors, and here too the robustness to errors in the model parameters and disturbances are a fundamental prerequisite in the choice of our controller. One of the most used controllers that falls into the PP category is the Proportional Integral Derivative (PID) controller. It is the most used as it is very simple to implement and the use of the integral action allows to reach the asymptotic regulation even in the presence of disturbances such as the uncertainty of the parameters [54]. There are many works in the literature that use PID control for indoor blimp. For example, in the work of [93] the design of a LTA autonomous robot was developed that flew once assigned to the robot a sequence of landmarks and trajectories. Instead, the PID controller was used by [87] to carry out station keeping and docking control for a LTA vehicle based on visual input. While [38] uses the PID controller to design an autonomous blimp for a surveillance system. Even if its use is widespread in the literature, the PID controller needs a careful analysis on the choice of the gains that must be manually tuned and this could take a long time.

Alternatively, optimal control methods are more interesting because they allow for better handling of MIMO systems. The Linear Quadratic regulator (LQR) controller is an example of this type of problem, that is a solution of an optimization problem. The LQR controller solves the minimization of a cost function that represents the energy of the states and automatically ensures a stable closed loop system, achieving guaranteed levels of robustness in stability; it is also simple to calculate. The minimization process involves the use of two weight matrices, one for the state and one for control. Varying these matrices, the controller designer can balance the errors of the state and the efforts required from the actuators. Many works can be found in literature in which

the LQR technique is used. For example in the thesis of [6] a LQR control law is used to allow the airship to navigate through several via points under specified wind conditions. In this other work [13], the author considers the LQR control method to control the motion of an indoor blimp by combining the data of the Inertial Mass Unit (IMU) and a camera to estimate its position.

Let's now talk about the second category of controllers, in which the gains do not require a thorough knowledge of the system parameters but are generated by a learning process. An example is the Artificial Neural Network (ANN) that can be trained to obtain the parameters of the dynamics through the state of the system even without knowing the dynamics of this [75]. We can now report some applications of this method on indoor blimps. An example is present in [18] in which the authors present a biologically based controller that provides course stabilization, altitude and drift control, and collision avoidance. Another example is in [97] in which ANN controllers are evolved in simulation to map visual input into motor commands in order to steer the flying robot forward as fast as possible while avoiding collisions. Finally in [76], author proposed to use a yaw controller based on ANN and human operations for a path following mission. Despite the interesting application of this technique, however, it also contains disadvantages. This is a learning technique based on training data from which the dynamics must be reconstructed, therefore it is very sensitive to these training data which may very often not fully cover the reality and this happens when the system is very complex.

A second widely used technique is reinforcement learning. This method is based on the fact that the system moving inside an environment and interacting with it can perform actions that can be positive and negative for it. In technical jargon we often talk about rewards or penalties. The method therefore aims to ensure that the system maximizes the rewards as consequences of its actions [53]. An example on blimps is present in [79] in which is presented an approach that applies the reinforcement learning principle to the problem of learning height control policies for aerial blimps. In [55] authors utilize the reinforcement learning technique for the blimp dynamics identification. This is done by training a Gaussian process on the residual between the nonlinear model and ground truth training data.

The last controllers we can mention as belonging to the second category are fuzzy logic controllers. These are based on a transformation technique from a linguistic control strategy into an automatic control strategy [61]. In [77] the fuzzy controllers are employed and optimized using an improved genetic algorithm for a 3D path tracking problem. While in [4] the architecture of the fuzzy control is introduced for an autonomous embedded blimp system. The main disadvantages in using the fuzzy logic controller is the decision of fuzzy logic rules and fuzzy sets.

5.4 Linear blimp equation of motion

As we have already said, the complexity of the equations of the nonlinear dynamics of the blimp justifies the search for a linear model to represent the motion and consequently to be used to derive a control strategy. To develop a model of linear dynamics we need an equilibrium state in which the derivatives of the state are zero. Once the reference equilibrium state has been determined, the second step is to write the equations for small disturbances around the trimmed equilibrium. With this procedure, it is possible to decouple the motion in a *longitudinal* and *lateral* dynamics which can therefore be analyzed and controlled separately. Once the nonlinear dynamic system has

been divided into two linear and decoupled subsystems, it is possible to deal with these with the typical control tools of linear systems whose characteristics are determined by the state transition matrix and in particular by its eigenvalues and eigenvectors. For instance, if we want a stable robot blimp it is necessary that the real part of the eigenvalues of the state transition matrix must be negative. The eigenvectors, on the other hand, provide information on the magnitude and phase of the response of one state with respect to another [82].

In this section we want to write and derive the linear equation of motion for an indoor blimp starting from the full 6 DOF nonlinear dynamics (2.21) which we can rewrite adding a small perturbation to the reference equilibrium state [87] as

$$\boldsymbol{M}\dot{\boldsymbol{x}}(t) = \boldsymbol{f}(\boldsymbol{x}(t), \boldsymbol{\tau}(t)) \tag{5.2}$$

with

$$\begin{aligned} \boldsymbol{x}(t) &= \boldsymbol{x}_0(t) + \Delta\boldsymbol{x}(t) \\ \boldsymbol{\tau}(t) &= \boldsymbol{\tau}_0(t) + \Delta\boldsymbol{\tau}(t) \end{aligned}$$

where $\Delta\boldsymbol{x}(t)$, $\Delta\boldsymbol{\tau}(t)$ are small perturbations around some equilibrium condition $\boldsymbol{x}_0(t)$, $\boldsymbol{\tau}_0(t)$. The linearized system around the equilibrium condition is given by:

$$\Delta\dot{\boldsymbol{x}}(t) = \boldsymbol{A}\Delta\boldsymbol{x}(t) + \boldsymbol{B}\Delta\boldsymbol{\tau}(t)$$

where

$$\begin{aligned} \boldsymbol{A} &= \frac{\partial \boldsymbol{f}}{\partial \boldsymbol{x}}(\boldsymbol{x}_0(t), \boldsymbol{\tau}_0(t)) \\ \boldsymbol{B} &= \frac{\partial \boldsymbol{f}}{\partial \boldsymbol{\tau}}(\boldsymbol{x}_0(t), \boldsymbol{\tau}_0(t)) \end{aligned}$$

are Jacobian matrices obtained from a first order Taylor expansion of $\boldsymbol{f}(\boldsymbol{x}(t), \boldsymbol{\tau}(t))$ about the equilibrium. As we said previously, once the matrix $\boldsymbol{A}$, which is also called *state transition matrix*, is obtained, the stability of the blimp robot can be analyzed by calculating the eigenvalues and eigenvectors of $\boldsymbol{A}$. Their real part must be negative to guarantee stability and if we are dealing with real and distinct eigenvalues, these represent non-oscillatory modes otherwise, complex and conjugated eigenvalues $\lambda_{1,2} = \sigma \pm j\omega_0$ represent oscillatory modes whose natural frequency and damping ratio can be evaluated by σ and ω_0.

We want to linearize the system in equation (5.2) around $\phi = \theta = 0$ that corresponds to small roll and pitch angles, which is a reasonable condition for blimp operation; in fact the only angle able to vary, during the motion, is the yaw. Furthermore, the products and squares of the perturbation variables become very small and therefore all Coriolis terms and centrifugal terms can be neglected. With these hypotheses we obtain that linearization process leads to the decoupling of the dynamics in the *longitudinal* (xz plane) and *lateral* model (xy plane) that we will analyze in the following sections.

5.4.1 Longitudinal model

The longitudinal model describes the motion of the blimp in the xz plane in the body-fixed reference. The state and input vectors are

$$\Delta \boldsymbol{x} = \begin{bmatrix} \Delta v_x & \Delta v_z & \Delta \omega_y & \Delta \theta \end{bmatrix}^T$$
$$\Delta \boldsymbol{\tau} = \begin{bmatrix} \Delta T_{cmn} & \Delta T_v \end{bmatrix}^T$$

The pitch angle was included in the longitudinal state vector to accommodate the restoring force so as to obtain square matrices. Making the derivatives with respect to the state variables of the equation of motion (2.21), we obtain the following equations of the linearized longitudinal model:

$$\boldsymbol{M}\dot{\boldsymbol{x}} = \boldsymbol{A}\boldsymbol{x} + \boldsymbol{B}\boldsymbol{\tau}$$

where

$$\boldsymbol{M} = \begin{bmatrix} m'_x & 0 & mz_G & 0 \\ 0 & m'_z & 0 & 0 \\ mz_G & 0 & I'_y & 0 \\ 0 & 0 & 0 & 1 \end{bmatrix}$$
$$\boldsymbol{A} = \begin{bmatrix} -D_{v_x} & 0 & 0 & f_B - f_G \\ 0 & -D_{v_z} & 0 & 0 \\ 0 & 0 & -D_{\omega_y} & -z_G f_G \\ 0 & 0 & 1 & 0 \end{bmatrix}$$
$$\boldsymbol{B} = \begin{bmatrix} 1 & 0 \\ 0 & 1 \\ d_z & 0 \\ 0 & 0 \end{bmatrix}$$

Multiplying by the inverse of the mass matrix we can write the linear system in canonical form, where the matrices $\boldsymbol{A}$ and $\boldsymbol{B}$ are redefined. At this point the step preceding the control technique is to evaluate the controllability of the system. In particular, the Kalman condition must be satisfied, that is, if the rank of the controllability matrix is maximum (in our case 4) then the system is controllable.

5.4.2 Lateral model

The lateral dynamics model describes the motion of the blimp in the xy plane of the body-fixed frame. The state and controls variables are the following

$$\Delta \boldsymbol{x} = \begin{bmatrix} \Delta v_y & \Delta \omega_x & \Delta \omega_z & \Delta \phi \end{bmatrix}^T$$
$$\Delta \boldsymbol{\tau} = \Delta T_{diff}$$

Here, too, roll is added as a fourth variable. Executing the necessary derivatives, the linearized model becomes

$$\boldsymbol{M}\dot{\boldsymbol{x}} = \boldsymbol{A}\boldsymbol{x} + \boldsymbol{B}\boldsymbol{\tau}$$

where

$$\boldsymbol{M} = \begin{bmatrix} m'_y & -mz_G & 0 & 0 \\ -mz_G & I'_x & 0 & 0 \\ 0 & 0 & I'_z & 0 \\ 0 & 0 & 0 & 1 \end{bmatrix}$$

$$\boldsymbol{A} = \begin{bmatrix} -D_{v_y} & 0 & 0 & f_G - f_B \\ 0 & -D_{\omega_x} & 0 & -z_G f_G \\ 0 & 0 & -D_{\omega_z} & 0 \\ 0 & 1 & 0 & 0 \end{bmatrix}$$

$$\boldsymbol{B} = \begin{bmatrix} 0 \\ 0 \\ d_y \\ 0 \end{bmatrix}$$

Again multiplying by the inverse of the mass matrix we obtain the standard linear system and we test the controllability and then proceed to the control.

5.5 PID controller

Once we have obtained the longitudinal and lateral linear system we can use a classic control technique that is the PID controller which is the most widely used feedback control law. Consider a linear time invariant system of the type

$$\begin{cases} \dot{x} &= Ax + Bu \\ y &= Cx + Du \end{cases} \tag{5.3}$$

where x is the state variable, y is the output variable and u is the input variable. The mathematical form of the PID control law is the following

$$u(t) = K\left(e(t) + \frac{1}{T_i}\int_0^t e(\tau)d\tau + T_d\frac{de(t)}{dt}\right) \tag{5.4}$$

where $u(t)$ is the control signal and $e(t)$ is the control error which is calculated as $e(t) = y_{des}(t) - y(t)$ where $y(t)$ is the measured process variable and $y_{des}(t)$ is the desired variable. The controller parameters are proportional gain K, integral time T_i, and derivative time T_d. The controller is often presented in the equivalent form

$$u(t) = K_p e(t) + K_i\int_0^t e(\tau)d\tau + K_d\frac{de(t)}{dt}$$

in which the tuning parameters are K_p, K_i and K_d, that are the proportional, integral and derivative gains, respectively, are related to those in (5.4) by

$$\begin{aligned} K_p &= K \\ K_i &= \frac{K}{T_i} \\ K_d &= KT_d \end{aligned}$$

The integral, proportional and derivative part can be interpreted as control actions based on the past, the present and the future.

5.6 LQR controller

The LQR problem is a control technique based on solving an optimization problem. Its goal is to find the closed loop state feedback control law of the type

$$\Delta \boldsymbol{u} = -\boldsymbol{K}\Delta \boldsymbol{x}$$

such that this minimizes a quadratic performance index subject to dynamic constraints [31]. The performance index is a cost function which has this form:

$$J = \int_0^\infty (\Delta \boldsymbol{x}^T \boldsymbol{Q} \Delta \boldsymbol{x} + \Delta \boldsymbol{u}^T \boldsymbol{R} \Delta \boldsymbol{u}) dt \tag{5.5}$$

The two matrices $\boldsymbol{Q}$ and $\boldsymbol{R}$ are called weight matrices. $\boldsymbol{Q}$ is a diagonal $(n \times n)$ matrix typically positive semi-definite, where n is the number of state variables, while $\boldsymbol{R}$ is a positive definite diagonal $(m \times m)$ matrix where m is the number of inputs. The choice of these two matrices influences the performance of the control algorithm and there are various methods in the literature to select the two matrices. In general, the elements of these two matrices are considered as weights that represent how much a state counts on the effort of the control to regulate it [33]. Below are a couple of examples that show methods to derive the two matrices $\boldsymbol{Q}$ and $\boldsymbol{R}$. One method is to calculate $\boldsymbol{Q} = \boldsymbol{C}^T\boldsymbol{C}$ and $\boldsymbol{R} = \boldsymbol{B}\boldsymbol{B}^{\boldsymbol{T}}$ with subsequent tuning practice to obtain the desired performance [36]. A second very effective method for the selection of the matrices $\boldsymbol{Q}$ and $\boldsymbol{R}$ is the one based on Bryson's law. This law chooses the diagonal matrix $\boldsymbol{Q}$ with the elements equal to the inverse of the maximum allowed value for each state, while for the matrix $\boldsymbol{R}$, the choice falls in diagonal matrix with the values equal to the inverse of the maximum allowed value of each input [1].

Therefore, after having correctly selected the weight matrices, the LQR problem is solved in the following way. Consider a linear time invariant system of the type

$$\begin{cases} \dot{\boldsymbol{x}} = \boldsymbol{A}\boldsymbol{x} + \boldsymbol{B}\boldsymbol{u} \\ \boldsymbol{y} = \boldsymbol{C}\boldsymbol{x} + \boldsymbol{D}\boldsymbol{u} \end{cases} \tag{5.6}$$

where $\boldsymbol{y}(t)$ is the output vector. So if all states are measurable then the state feedback law can be used

$$\boldsymbol{u} = -\boldsymbol{K}\boldsymbol{x} \tag{5.7}$$

where $\boldsymbol{K}$ is the gain matrix of the control law which gives the desired properties of the closed loop system. If we substitute equation (5.7) into the linear system (5.6) we obtain

$$\dot{\boldsymbol{x}} = (\boldsymbol{A} - \boldsymbol{B}\boldsymbol{K})\boldsymbol{x} = \boldsymbol{A}_{cl}\boldsymbol{x} \tag{5.8}$$

where $\boldsymbol{A}_{cl}$ is the closed loop matrix. Substituting equation (5.7) in the cost function J defined in (5.5) yields

$$J = \frac{1}{2}\int_0^\infty (\boldsymbol{x}^T(\boldsymbol{Q} + \boldsymbol{K}^T\boldsymbol{R}\boldsymbol{K})\boldsymbol{x})dt \tag{5.9}$$

Denoting by $\boldsymbol{P}$ a constant matrix, the optimal feedback matrix $\boldsymbol{K}$ such that J is minimal satisfies the following

$$\frac{d}{dt}(\boldsymbol{x}^T\boldsymbol{P}\boldsymbol{x}) = -\boldsymbol{x}^T(\boldsymbol{Q} + \boldsymbol{K}^T\boldsymbol{R}\boldsymbol{K})\boldsymbol{x} \tag{5.10}$$

and substituting (5.10) into (5.9) results in

$$J = \frac{1}{2}\int_0^\infty \frac{d}{dt}(\boldsymbol{x}^T\boldsymbol{P}\boldsymbol{x})dt = \frac{1}{2}\boldsymbol{x}^T(0)\boldsymbol{P}\boldsymbol{x}(0)$$

In this way, the cost function J depends only on the matrix $\boldsymbol{P}$ and on the initial conditions. Substituting now equation (5.10) into equation (5.8) yields

$$\boldsymbol{x}^T(\boldsymbol{A}_{cl}^T\boldsymbol{P} + \boldsymbol{P}\boldsymbol{A}_{cl} + \boldsymbol{Q} + \boldsymbol{K}^T\boldsymbol{R}\boldsymbol{K})\boldsymbol{x} = 0$$

thus

$$\boldsymbol{A}_{cl}^T\boldsymbol{P} + \boldsymbol{P}\boldsymbol{A}_{cl} + \boldsymbol{Q} + \boldsymbol{K}^T\boldsymbol{R}\boldsymbol{K} = 0 \tag{5.11}$$

Substituting (5.8) into (5.11) yields:

$$\boldsymbol{A}^T\boldsymbol{P} + \boldsymbol{P}\boldsymbol{A} + \boldsymbol{Q} + \boldsymbol{K}^T\boldsymbol{R}\boldsymbol{K} - \boldsymbol{K}^T\boldsymbol{B}^T\boldsymbol{P} - \boldsymbol{P}\boldsymbol{B}\boldsymbol{K} = 0 \tag{5.12}$$

If we choose $\boldsymbol{K} = \boldsymbol{R}^{-1}\boldsymbol{B}^T\boldsymbol{P}$ inside equation (5.12), we obtain the Algebraic Riccati Equation

$$\boldsymbol{A}^T\boldsymbol{P} + \boldsymbol{P}\boldsymbol{A} + \boldsymbol{Q} - \boldsymbol{P}\boldsymbol{B}\boldsymbol{R}^{-1}\boldsymbol{B}^T\boldsymbol{P} = 0$$

The feedback gain matrix $\boldsymbol{K}$ obtained earlier for the LQR problem, solves the position regulation problem. This problem sets the values of all states of the system to zero. However, at least at the simulation level we are interested in the trajectory tracking problem. The control law that is taken into account is the following

$$\boldsymbol{u} = -\boldsymbol{K}(\boldsymbol{x} - \boldsymbol{x}_{des}) + \boldsymbol{u}_{des}$$

where $\boldsymbol{x}$ is the state vector, $\boldsymbol{x}_{des}$ is the value of the desired state at the current flight time, $\boldsymbol{u}_{des}$ are the trim inputs at the same flight condition and $\boldsymbol{K}$ is the LQR gain matrix. Figure 5.2 shows the control scheme of a trajectory tracking controller.

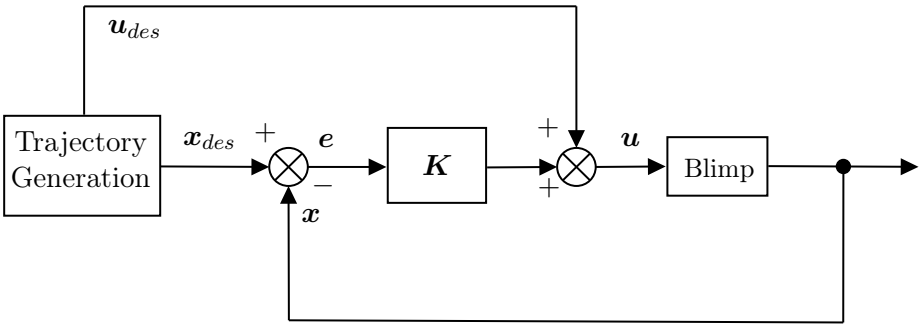

Figure 5.2: Block diagram of a LQR trajectory tracking controller.

5.7 Disturbance Estimation

We have reached the crucial point that represents what the purpose of the thesis is: the control of the blimp in the presence of magnetic disturbances that act on the ferromagnetic parts of the motors and which are due to the presence of the strong magnetic field of the CERN FCC-hh detector, which we have analyzed and discussed in detail in Chapter 4. Before proceeding with the trajectory tracking simulations, it is necessary to add to the control system the disturbance that acts on the blimp in its motion inside the detector cavern. To estimate the magnetic disturbance we need the magnetic dipole moment of the electric motors and the magnetic field inside the detector. As regards the former we have seen in Chapter 3 how to estimate the magnetic moment of a motor immersed in an external magnetic field as a vector sum of the internal dipole moment of the PM rotor and the dipole moment that is generated by the magnetization of the stator. As for the magnetic field, in Chapter 4 we have shown the three-dimensional map of the magnetic field obtained with a CST software simulation that characterizes the physical environment inside and in the proximity of the main solenoid and the forward solenoids of the FCC-hh detector.

Hence we have all the necessary tools to be able to calculate the magnetic disturbance at each time step in terms of forces and torques acting on the blimp in a particular position and orientation $\boldsymbol{\eta}$. It is good to remember that in this simulation we are considering the constant magnetic moment of the motors. In reality, as already mentioned in Chapter 3 magnetic dipole moment of the motors strongly depends on the magnitude of the external field since, depending on its value, the metal cover of the motor assumes a different magnetization. However it has been pointed out that the blimp, moving in the vicinity of the detector will fly in magnetic field areas that have an average modulus of 0.3 T and therefore we can as a first approximation say that the magnetic moment of the blimp motors remains the same as it moves in the space.

Another fundamental aspect to focus on is that linked to the number of magnetic moments that are present on the system, these will be as many as the motors of the blimp. Since we have obtained the equations of motion in the body-fixed reference, we are interested in estimating a magnetic disturbance vector in the same reference frame which can be thought of as the force and torque vector of a single total magnetic moment associated with the body interacting with the field. This total magnetic moment must combine all the magnetic moments that characterize each electric motor (which in turn are the superposition of the rotor and stator dipole moment). The only total magnetic dipole vector associated with the rigid body with which all the sub moments of the motors are taken into account, will generally have components on the three body axes of the

system $\boldsymbol{X}_b$, $\boldsymbol{Y}_b$ and $\boldsymbol{Z}_b$. However, this vector is not a constant vector in modulus and direction, as the individual sub moments from which it is generated are rotating in space due to the rotation of the rotors and are also variable in modulus over time as, moving in areas of magnetic field variable, the magnetization effect of the motor covers is variable, and this has an impact on the individual moments of each motor and therefore on the total moment of the rigid body. For our simulations, let's imagine we have a unique moment with components on the body axes that are constant in magnitude and direction. In particular, we will consider components equal along the $\boldsymbol{X}_b$ and $\boldsymbol{Z}_b$ axis and zero along the $\boldsymbol{Y}_b$ axis.

Therefore, starting from the information of the magnetic moment in the body-fixed reference frame, this is then transformed into the earth-fixed reference frame (which is the NED frame) through the following relationship:

$$\boldsymbol{m}^n = \boldsymbol{R}_n^b(\boldsymbol{\eta}_2^n)\boldsymbol{m}^b$$

where $\boldsymbol{R}_n^b(\boldsymbol{\eta}_2^n)$ is the transformation matrix from the body-fixed reference F_b to the inertial reference F_n defined in (2.5). However, the magnetic field resulting from the CST simulation has been defined in an inertial reference system different from that used for the dynamic model of the blimp (NED), which we called FCC frame. Then a further change of coordinates is made from NED to the FCC reference whose matrix is defined as

$$\boldsymbol{R}_{FCC}^n = \begin{bmatrix} 0 & -1 & 0 \\ 0 & 0 & -1 \\ 1 & 0 & 0 \end{bmatrix}$$

Hence, to obtain the magnetic moment in the FCC frame we apply this transformation

$$\boldsymbol{m}^{FCC} = \boldsymbol{R}_{FCC}^n \boldsymbol{m}^n$$

We now have the magnetic moment in the FCC frame. The external magnetic field is expressed in the same reference frame, therefore we have to transform the position of the blimp from the NED frame to the FCC frame with the $\boldsymbol{R}_{FCC}^n$ matrix. Once we have obtained $\boldsymbol{\eta}_1^{FCC}$ we can proceed to the calculation of magnetic forces and torques.

$$\begin{cases} \boldsymbol{f}_m^{FCC} = \boldsymbol{\nabla}(\boldsymbol{m}^{FCC} \cdot \boldsymbol{B}(\boldsymbol{\eta}_1^{FCC})) \\ \boldsymbol{\tau}_m^{FCC} = \boldsymbol{m}^{FCC} \times \boldsymbol{B}(\boldsymbol{\eta}_1^{FCC}) \end{cases}$$

At this point to generate the $\boldsymbol{\tau}_{dist}$ disturbance vector it is necessary to transform these vectors from the FCC reference frame to the body-fixed reference frame, passing through the NED reference frame. From FCC frame to NED frame we have

$$\begin{bmatrix} \boldsymbol{f}_m^n \\ \boldsymbol{\tau}_m^n \end{bmatrix} = \begin{bmatrix} (\boldsymbol{R}_{FCC}^n)^T & \boldsymbol{0}_{3\times3} \\ \boldsymbol{0}_{3\times3} & (\boldsymbol{R}_{FCC}^n)^T \end{bmatrix} \begin{bmatrix} \boldsymbol{f}_m^{FCC} \\ \boldsymbol{\tau}_m^{FCC} \end{bmatrix}$$

Then from NED frame to body-fixed frame

$$\boldsymbol{\tau}_{dist} = \begin{bmatrix} \boldsymbol{f}_m^b \\ \boldsymbol{\tau}_m^b \end{bmatrix} = \begin{bmatrix} (\boldsymbol{R}_n^b)^T(\boldsymbol{\eta}_2^n) & \boldsymbol{0}_{3\times3} \\ \boldsymbol{0}_{3\times3} & (\boldsymbol{R}_n^b)^T(\boldsymbol{\eta}_2^n) \end{bmatrix} \begin{bmatrix} \boldsymbol{f}_m^n \\ \boldsymbol{\tau}_m^n \end{bmatrix}$$

These steps are best shown in Figure 5.3 in which the flow chart of the magnetic disturbance calculation is present.

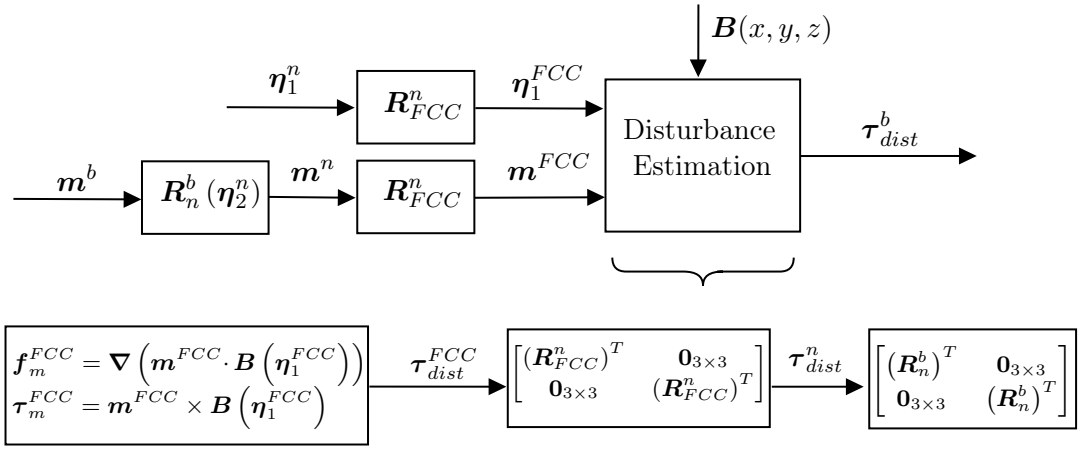

Figure 5.3: Disturbance estimation flow chart.

5.8 Simulations and results

In this section we will carry out simulations based on the trajectory tracking, however passing to the experimental case we will test the platform with position regulation control like the station keeping test. The simulated trajectory was chosen in the longitudinal plane xz and is represented in the FCC reference frame that we have shown in section 4.2. The trajectory is based on a specific scenario that sees the blimp rise from the ground in the detector cavern, arrive at an altitude at which it has exceeded the height of the detector, then travel longitudinally the entire length of the detector and then land on the opposite side. The reference trajectory was constructed with the method of linear functions with parabolic blends as reported in section 4.4. The via points in the FCC frame are given as follow:

$$\boldsymbol{\eta}_{1,1}^{FCC} = \begin{bmatrix} 0 \\ -10 \\ -40 \end{bmatrix} m \quad \boldsymbol{\eta}_{1,2}^{FCC} = \begin{bmatrix} 0 \\ 10 \\ -40 \end{bmatrix} m \quad \boldsymbol{\eta}_{1,3}^{FCC} = \begin{bmatrix} 0 \\ 10 \\ 40 \end{bmatrix} m \quad \boldsymbol{\eta}_{1,4}^{FCC} = \begin{bmatrix} 0 \\ -10 \\ 40 \end{bmatrix} m$$

As for the time frame in which the blimp has to fly, the start and end times are

$$t_0 = 0\ s \qquad t_f = 400\ s$$

and the trajectory update rate has been set at $f = 10$ Hz, i.e. with a time interval of $dt = 0.1$ s. The duration of the distance between path points are

$$t_{d12} = 100\ s \qquad t_{d23} = 200\ s \qquad t_{d34} = 100\ s$$

while the duration of blend regions are

$$t_1 = 5\ s \qquad t_2 = 10\ s \qquad t_3 = 10\ s \qquad t_4 = 5\ s$$

The first step when dealing with control is to check the stability of the open-loop system, therefore without any feedback control. As we have already said to investigate the stability of a linear time invariant system it is possible to calculate the eigenvalues of matrix $\boldsymbol{A}$ and see if these have a negative real part. The values are obtained with the *eig* function of MATLAB which calculates the vector of the eigenvalues of the squared matrix. In particular, the longitudinal model has two real eigenvalues, $\lambda_1 = -0.1718$ and $\lambda_2 = -0.1066$, and one complex conjugate, $\lambda_{3,4} = -0.1081 \pm 0.7201i$; the same for the lateral model which has two real eigenvalues, $\lambda_1 = -0.1067$ and $\lambda_2 = -0.1994$, and one complex conjugate, $\lambda_{3,4} = -0.1043 \pm 0.7162i$.

For the longitudinal model we can give a meaning to the eigenvalues and the corresponding eigenvectors. The first eigenvalue represents the behavior of the velocity v_x along x and is called the *surge mode*, the second eigenvalue indicates the behavior of the vertical velocity v_z along z and is called *heave mode* while the complex eigenvalues which refer to the angular velocity ω_y and the pitch angle θ show a pendulum behavior called *longitudinal pendulum mode*.

Another important feature of the system to be verified is the controllability that can be calculated with the *ctrb* function of MATLAB. Hence, being $\boldsymbol{A}$ the state transition matrix and $\boldsymbol{B}$ the input matrix, controllability is verified if the matrix

$$\boldsymbol{R} = \begin{bmatrix} \boldsymbol{B} & \boldsymbol{AB} & \boldsymbol{A}^2\boldsymbol{B} & \dots & \boldsymbol{A}^{n-1}\boldsymbol{B} \end{bmatrix}$$

has full rank.

We now have all the necessary tools to be able to simulate a control system based on one of the two controllers mentioned above, namely the PID and LQR. Therefore, after obtaining the linearized model, the control system is simulated in MATLAB with the use of the real parameters of the blimp, which will be specified in Chapter 6 (section 6.3). These controllers obtain the input values of the motors that allow the tracking of the trajectory and are based on the linearized model. These values are then inserted into the complete nonlinear dynamics at 6 DOF to simulate what happens in a real situation. The system receives the commands from the on-board system and the actuators execute them. So we have implemented the 6 DOF dynamics plant in MATLAB that receives the control inputs generated with the controllers based on the linearized model and inserts them into the complete dynamics, then an integration is carried out that simulates the movement of the blimp after the application of that particular input.

5.8.1 PID controller simulation with magnetic disturbance

For the PID controller the state equation (5.3) is transformed in Laplace domain

$$s\boldsymbol{x}(s) = \boldsymbol{A}\boldsymbol{x}(s) + \boldsymbol{B}\boldsymbol{u}(s)$$
$$s\boldsymbol{y}(s) = \boldsymbol{C}\boldsymbol{x}(s) + \boldsymbol{D}\boldsymbol{u}(s)$$

With this form is possible to calculate the solution for the state equation

$$\boldsymbol{x}(s) = (s\boldsymbol{I} - \boldsymbol{A})^{-1}\boldsymbol{B}\boldsymbol{u}(s) = \boldsymbol{H}(s)\boldsymbol{u}(s)$$

where $\boldsymbol{I}$ is the identity matrix and $\boldsymbol{H}(s)$ is the Input/Output transfer function. From the longitudinal and lateral models it is possible to calculate three single-input single-output (SISO) transfer

function from the three input of the propellers (T_{cmn}, T_v and T_{diff}) to the output v_x, v_z and ω_z. They are given by:

$$H_1(s) = \frac{v_x}{T_{cmn}} = \frac{17.94s^2 + 3.576s + 9.113}{s^3 + 0.388s^2 + 0.5674s + 0.09113}$$
$$H_2(s) = \frac{v_z}{T_v} = \frac{10.66}{s + 0.1066}$$
$$H_3(s) = \frac{\omega_z}{T_{diff}} = \frac{0.9968}{s + 0.1994}$$

The gains of the control are shown in the Table 5.1. The identification of the gains of the PID controller K_p, K_i and K_d is called tuning. The tuning can be performed manually by changing the value of the gains and testing the corresponding behavior of the system, this manual technique needs a lot of experience, many times it is said to be an art and is also time consuming. In MATLAB/SIMULINK there is a PID tuner in which it is possible to choose the gains based on the response time and robustness.

	PID gains		
	H_1	H_2	H_3
K_p	0.5166	0.8141	2.963
K_i	0.5031	0.727	1.314
K_d	0.004807	0.0085	0.08293

Table 5.1: Controller parameters.

This simulation was also performed with magnetic disturbance on motors to make the trajectory of the blimp inside the detector environment as realistic as possible. Regarding the total magnetic moment in the body-fixed reference frame, this has been defined as follows:

$$\boldsymbol{m}^b = \begin{bmatrix} 1 & 0 & 1 \end{bmatrix}^T \text{Am}^2$$

The results from the PID controller show good agreement with the desired states. In Figures 5.4 and 5.5 we have indicated with the term *real* the variables of the state $\boldsymbol{\eta}$ and $\boldsymbol{\xi}$ which are obtained from the integration of the complete nonlinear 6 DOF equations, while with *lin* we indicate the linearized state variables, that is, obtained from the longitudinal and lateral models. On the other hand Figure 5.6 shows the 3D trajectories in the FCC reference frame. The first is the one obtained by integrating the nonlinear equation of motion with the controls obtained from the PID method, the second is the desired trajectory while the third is the trajectory obtained by integrating the linearized equations of motion.

Figure 5.7 shows the disturbing magnetic forces and torques that act during the real trajectory in the body fixed reference frame of the blimp and have been determined with the method shown in section 5.7. While Figure 5.8 shows the components of the magnetic field along the trajectory in Tesla in the FCC reference system. From these graphs we noticed that the order of magnitude of the forces is 10^{-3} N while for the torques there is a peculiar behavior, namely that the highest value of the torque occurs around the $\boldsymbol{Y}_b$ axis with a peak at 0.84 Nm in correspondence of the half of the path that corresponds to the moment in which the blimp flies over the greater length of

the detector, at that instant the flux lines of the magnetic field are approximately parallel to the direction of motion and the vertical motor for which we have assumed that the moment is aligned with the motor axis and therefore in this case the $\boldsymbol{Z}_b$ axis, provides the greatest torque (in fact the magnetic moment and the magnetic field have an angle of 90 degrees to each other). The maximum value in the middle of the path is confirmed by the fact that at this point, the longitudinal magnetic field value (which for the FCC reference is along Z_{FCC}) has its maximum value in modulus of 0.63 T (see Figure 5.8).

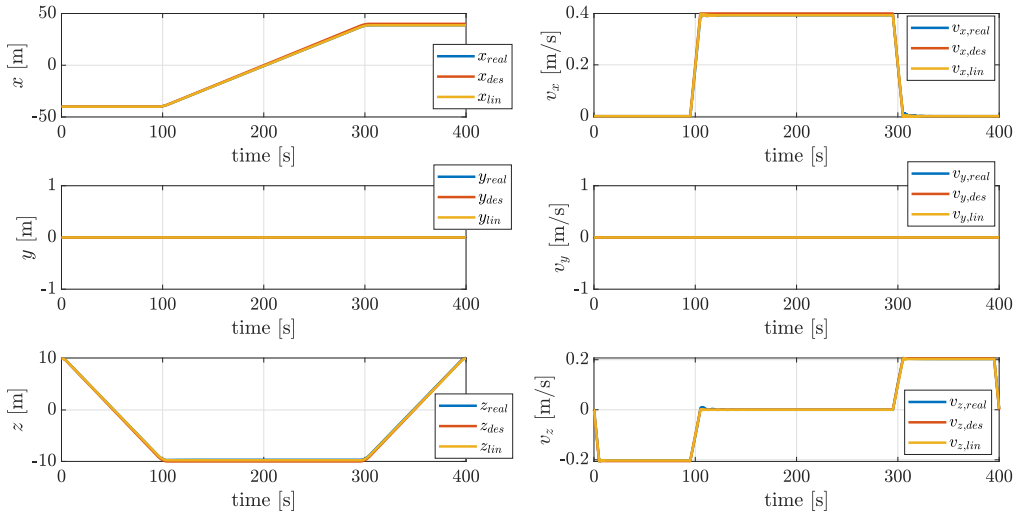

Figure 5.4: Linear positions displacements, x, y, z in the inertial reference frame R_n, and the linear velocities, v_x, v_y and v_z in the body reference frame R_b for the closed loop simulation of the PID controller with magnetic disturbance.

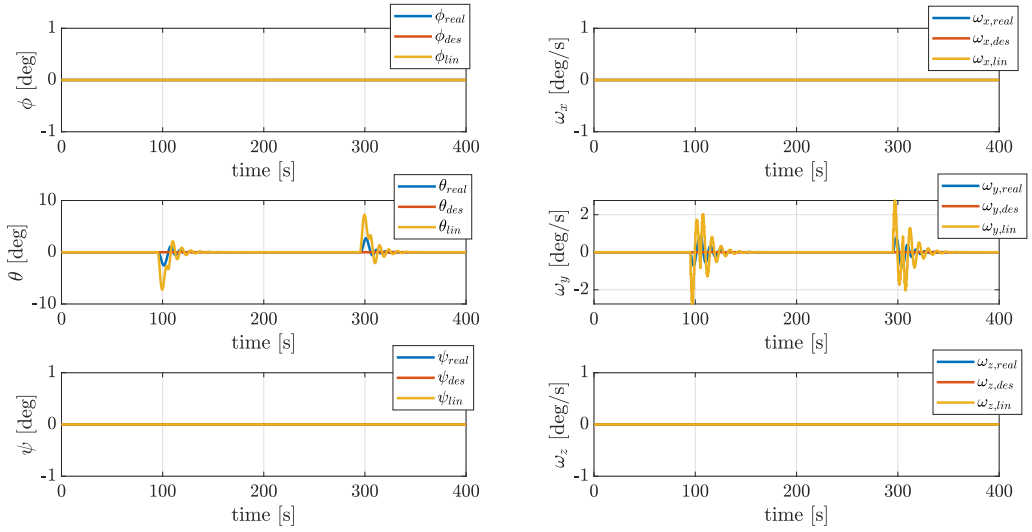

Figure 5.5: Angular displacements ϕ, θ and ψ in the inertial reference frame R_n, and the angular velocities ω_x, ω_y and ω_z in the body reference frame R_b for the closed loop simulation of the PID controller with magnetic disturbance.

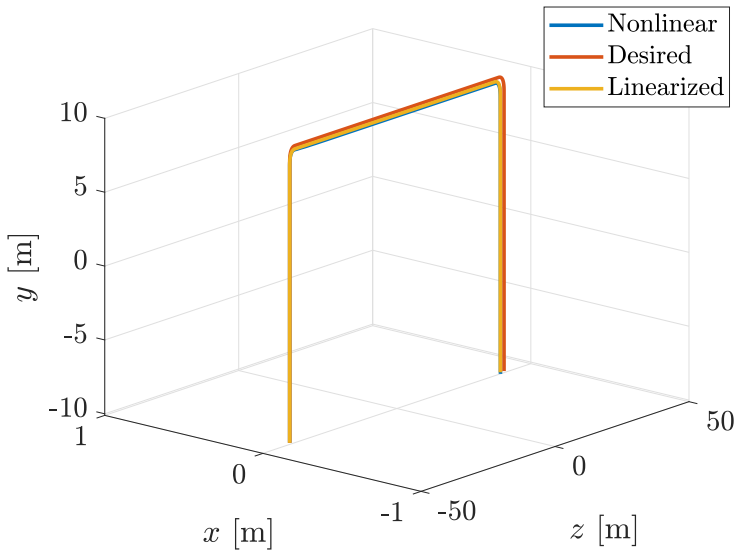

Figure 5.6: Linear and nonlinear controlled versus desired trajectory in the *FCC* reference frame for the closed loop simulation of the PID controller with magnetic disturbance.

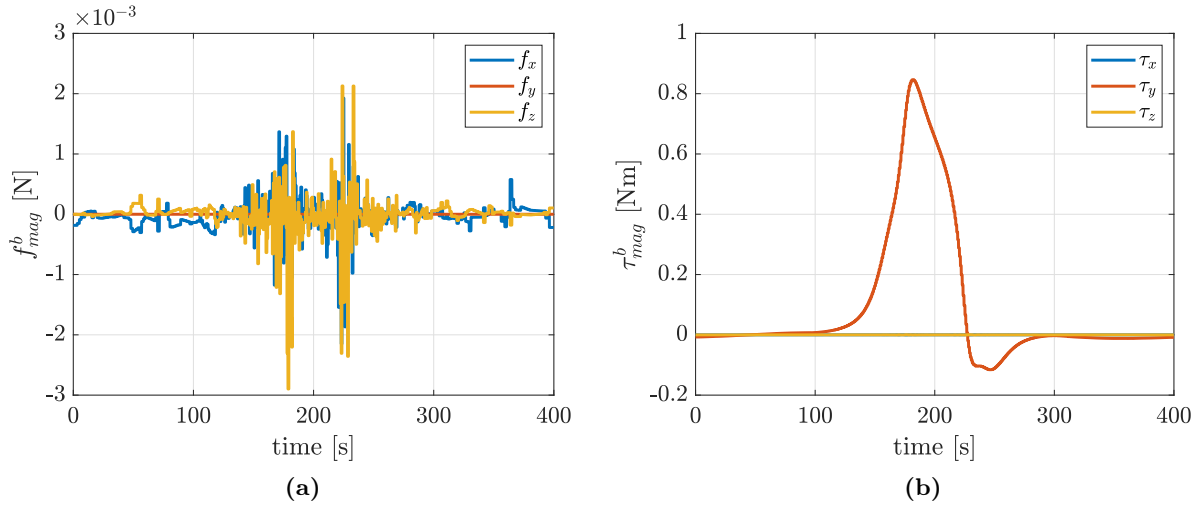

Figure 5.7: Magnetic disturbance force (a) and torque (b) in the body-fixed frame during the real trajectory for the closed loop simulation of the PID controller.

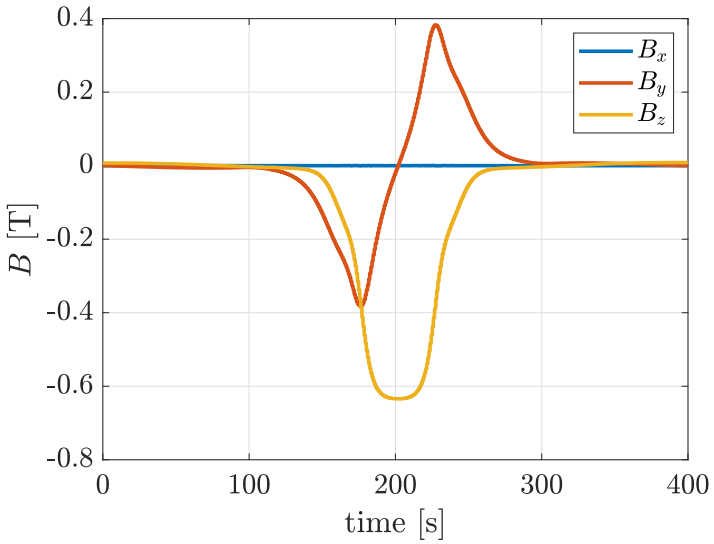

Figure 5.8: Magnetic field componets during the real trajectory in the *FCC* reference frame for the closed loop simulation of the PID controller.

5.8.2 LQR controller simulation without disturbance

A slightly different simulation is performed for the LQR controller. First of all the magnetic disturbance is no longer considered and in addition the controller is only tested for longitudinal dynamics. Also in this case, Figure 5.9 and 5.10 show the state variables $\boldsymbol{\eta}$ and $\boldsymbol{\xi}$ in the inertial and body fixed reference frame respectively. With *real* we mean the state variables obtained by integrating the nonlinear 6 DOF equations of motion with the controls obtained by the LQR method, with *des* instead we indicate the desired state variables, i.e. obtained with the trajectory generation process. Both figures therefore show that the LQR method is effective and allows the blimp to follow the generated trajectory. An important aspect to notice is the behavior of the pitch angle in correspondence with the change of path of the blimp in which it must pass from the vertical path to the horizontal one. In that case, small oscillations are observed which remain around 2 degrees. This was already foreseen by the complex and conjugate eigenvalues which represent the longitudinal pendulum mode. On the other hand, Figure 5.11 shows the thrusts that the longitudinal and vertical motors give to follow the trajectory. It can be noted that in the horizontal section the vertical motor does not provide any contribution even if gravity is present and in this case the simulation has taken into account that the buoyancy force equals the force of gravity, we will see that this it can be a real good assumption when the helium inflating is enough to keep the blimp floating. Finally, Figure 5.12 shows the 3D trajectory by comparing the desired one with the controlled one obtained by inserting the input controls shown in Figure 5.11 inside the complete system of blimp dynamics.

5.9 Conclusion

In this chapter we have analyzed a fundamental part of the thesis work concerning the control of the blimp in the presence of the magnetic disturbance acting on it. To achieve this we made use of two different controllers based on the closed loop feedback control system that work on linear

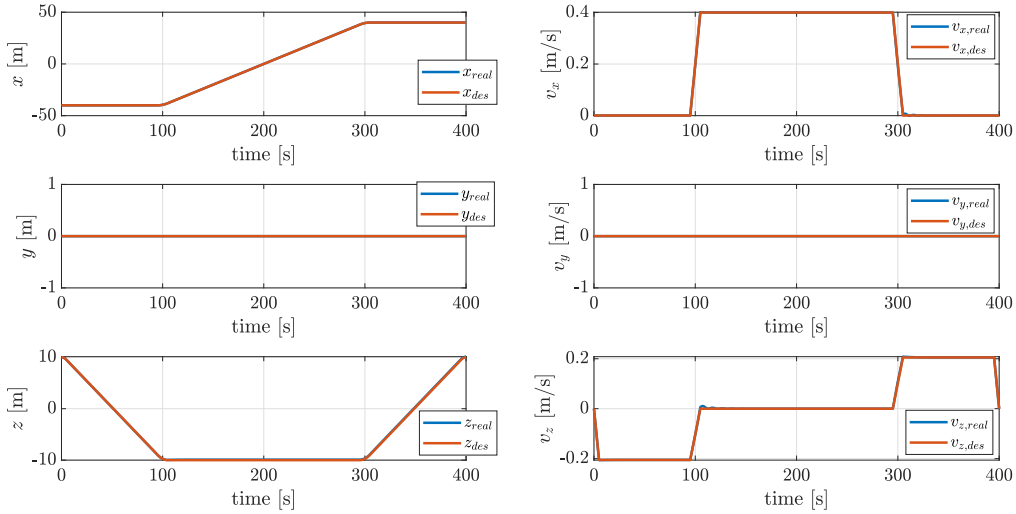

Figure 5.9: Linear positions displacements, x, y, z in the inertial reference frame R_n, and the linear velocities, v_x, v_y and v_z in the body reference frame R_b for the closed loop simulation of the LQR controller without magnetic disturbance.

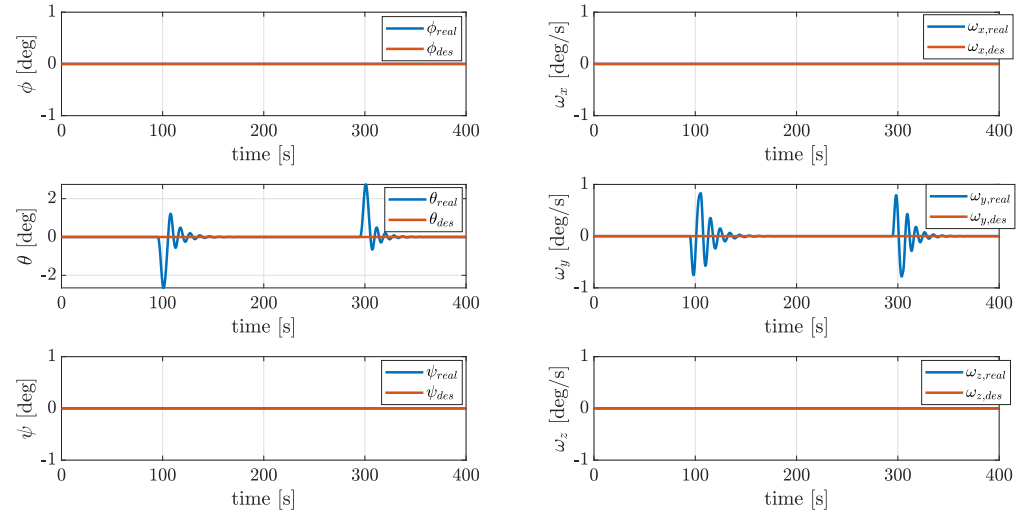

Figure 5.10: Angular displacements ϕ, θ and ψ in the inertial reference frame R_n, and the angular velocities ω_x, ω_y and ω_z in the body reference frame R_b for the closed loop simulation of the LQR controller without magnetic disturbance.

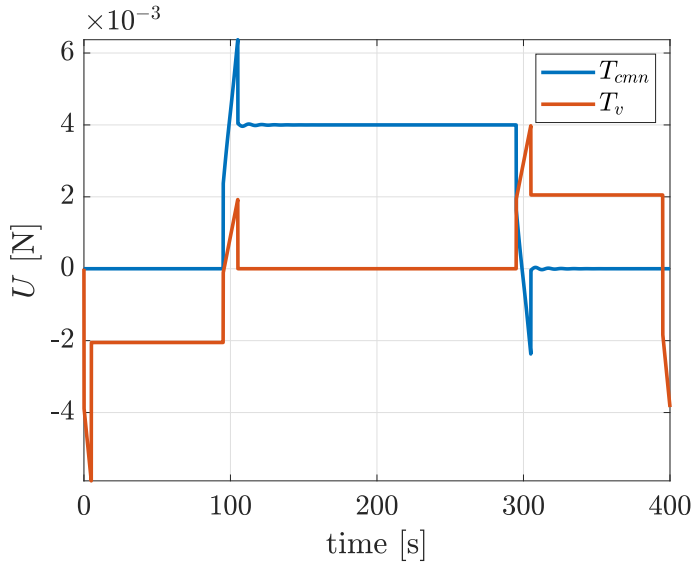

Figure 5.11: Longitudinal input vector in the body reference frame R_b, for the closed loop simulation of the LQR controller without magnetic disturbance.

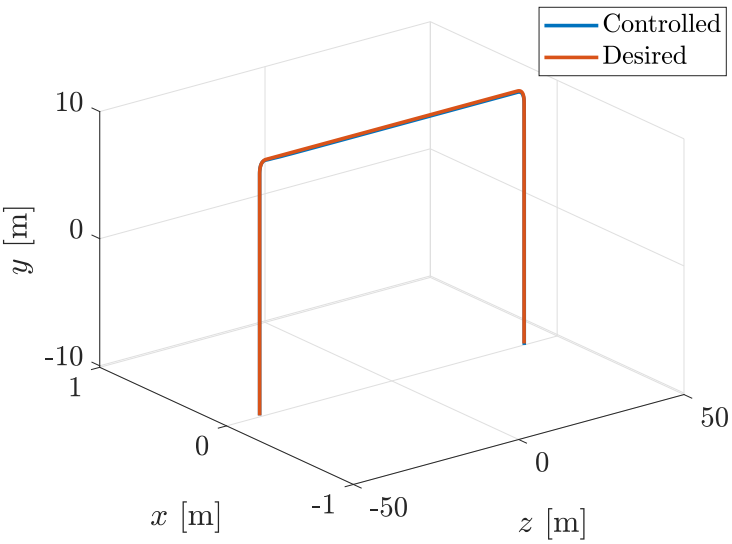

Figure 5.12: Nonlinear controlled versus desired trajectory in the FCC reference frame for the closed loop simulation of the LQR controller without magnetic disturbance.

systems. Indeed, after having recalled all the possibilities of control systems for indoor blimp, we have chosen the world of linear control system with the application of PID and LQR controllers. After explaining their operating principle, we moved on to software simulations with a trajectory tracking scenario. In particular, for the PID controller we have also implemented the estimate of the magnetic disturbance for its rejection. These control simulations are a first approach to the problem as there are still many aspects that remain open. The most critical aspect is the definition of the magnetic disturbance. As we saw in Chapter 4, the disturbance force and moment vector acting on the motors is calculated through the interactions between a magnetic dipole and an external magnetic field. Although with the simulations that we have done to be able to map the field generated by the solenoids, we know the data on the value of the field relatively well, it is the estimate of the magnetic dipole of the motors the concept that still remains at a preliminary stage. The questions that are still open are numerous and concern: the position of the magnetic dipole vector of a motor which, as we have mentioned, could rotate in space following the rotation of the motor rotor, the magnitude of the dipole moment vector could not be constant since it depends from the magnetization of the external cover, and last not least, the way in which the three motors and consequently the three dipoles, with which they can be represented, interact with each other to form what we have called the total magnetic moment defined in the body-fixed reference that is the one we have used to perform the control simulation.

Chapter 6

Experiments And Results

6.1 Introduction

This chapter ends the study of this thesis and adds that experimental and test part that has not been introduced up to now. It was written during my internship period at CERN in which I had the opportunity and the good chance to be able to put into practice what has so far been studied, analyzed and simulated. In my internship at CERN, my work activity has focused on the assembly and control of a real blimp. The blimp robot that was used is the Blimpduino 2 provided by jjrobots [50] which is a system already on the market that we have chosen to test. Then, after we assembled and tested it, we moved on to modifying its features and adapting it to our needs. This chapter is structured as follows.

In section 6.2 an overview of how the system is made up, its assembly method, its software and hardware characteristics is provided. However, our idea was to test this platform by introducing changes to the on board software as regards the control, but in any case this remains a qualitative study of the system as in the future the project involves the design from scratch of the system starting from the knowledge and experience acquired with this preliminary system.

Section 6.3 reports the entire parameter identification procedure that was performed on this particular system and which was then used both for the control simulations reported in Chapter 5 and in the simulations based on the experimental test reported in section 6.5. In this section we have tried to calculate all the parameters that appear in the dynamics of the system based on the real platform that we had available.

In section 6.4 the whole setup procedure of the experiment that was used to monitor the flight status of the blimp is presented. As we will see, the test was performed without disturbances in a cleanroom laboratory and the blimp was monitored both with a motion capturing system (PhaseSpace) installed inside the testing room and with the on board sensors telemetry. Before performing the real test, the motion capturing system needed a calibration and alignment to fix a reference system.

Finally, section 6.5 describes the experiment carried out. The objective was to obtain a station keeping with a fixed altitude and yaw angle value. To do this we have modified the control board of the Blimpduino and set an automatic control with the via points already loaded on board. In this section we have also shown how to post process the PhaseSpace data, which having a high sampling frequency is subject to measurement noise and finally we have shown the comparison between the

test and the simulation results based on the same scenario with the simulated model that is known thanks to the identification of the parameters defined in section 6.3.

6.2 Blimpduino 2 robot system

In this section we are going to describe the characteristics of the robotic system with which we carried out the control test. As a first choice to be able to analyze the problem of autonomous inspection of the detector environment, the EP-DT-EO R&D team at CERN has chosen to test a LTA robotic system such as an indoor blimp. Instead of designing it from scratch, they have chosen to initially test a COTS system. Therefore, in the thesis work, experiments were carried out on this already existing platform but adding small changes to the flight code. The goal of future work, after gaining experience in the operation of blimp control, will be to design a more performing robotic system, robust to magnetic disturbance and optimal for flight inside the detector cavern which represents a harsh environment for the presence of high magnetic fields and radiation.

The blimp chosen for this preliminary phase is the Blimpduino 2 sold by jjrobots [50]. Figure 6.1 shows all the fundamental elements for assembling the system. Blimpduino 2 is a low cost open source autonomous blimp, its name derives from the fact that the blimp mounts an Arduino M0 control board equipped with an ATMEL ARM M0 processor which is shown in Figure 6.2. Another fundamental equipment of Blimpduino 2 is an on board Wi-Fi module (ESP-12F) with which it is possible to control the platform through an app interface available for both Android and iOS system. Furthermore the system mounts a LIDAR sensor and a MPU-9250 Nine-Axis (Gyro + Accelerometer + Compass) MEMS MotionTracking sensor. As actuators it has the possibility to mount up to four motors but it actually use three BLDC motors. This reflects the choice that we used during the course of the thesis, that is two longitudinal motors for the motion along $\boldsymbol{X}_b$ and for the change of heading and a vertical motor to control the altitude along $\boldsymbol{Z}_b$. Finally it is powered by a 3.7 V LIPO cell battery.

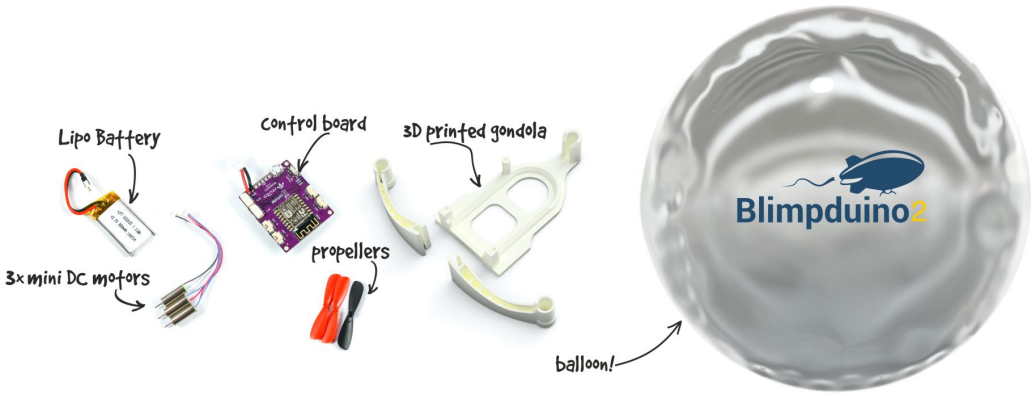

Figure 6.1: The elements needed to create the Blimpduino: a small LIPO battery, 3 brushless motors, propellers, the control board, the gondola and a balloon. From [50].

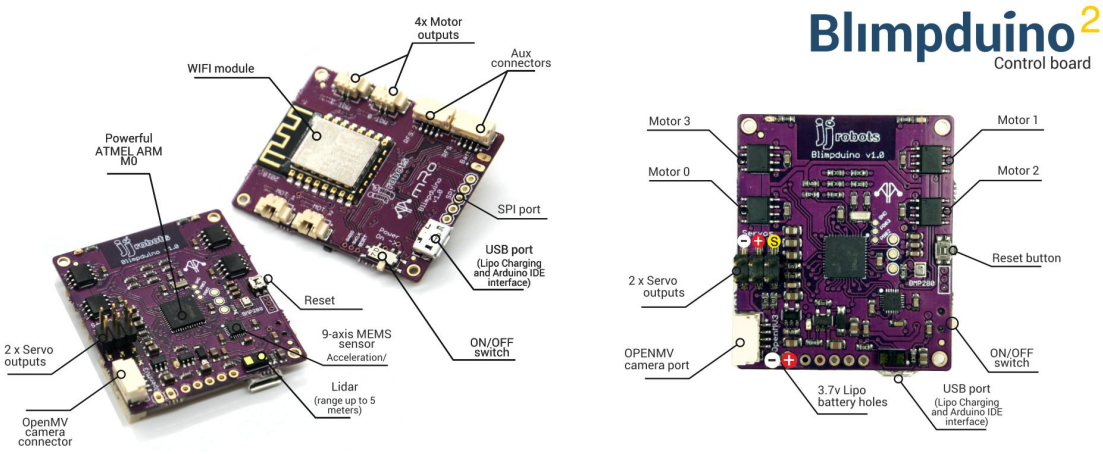

Figure 6.2: The Blimpduino 2 control board details. It mounts an ARM M0 processor, it has a powerful MPU-9250 Nine-Axis MotionTracking sensor, LIDAR sensor, OpenMV camera connector, 2 servo outputs, LIPO charging module (via USB). From [50].

6.2.1 Blimpduino 2 assembly

The fundamental component of Blimpduino that allows to keep the control board, the motors and the battery together is the supporting structure. The system we purchased did not come with the gondola so we proceeded to 3D print it. Figure 6.3 shows the gondola STL file obtained with CAD software used for 3D printing. This structure has been designed to be strong and light at the same time, this is fundamental to prevent the gondola from vibrating when the motors are delivering maximum torque. The 3D printing was carried out with a Formlabs 3D printer present in the CERN laboratories. Figure 6.4 shows the print bed of Formlabs 3D printer with two just printed gondolas on it.

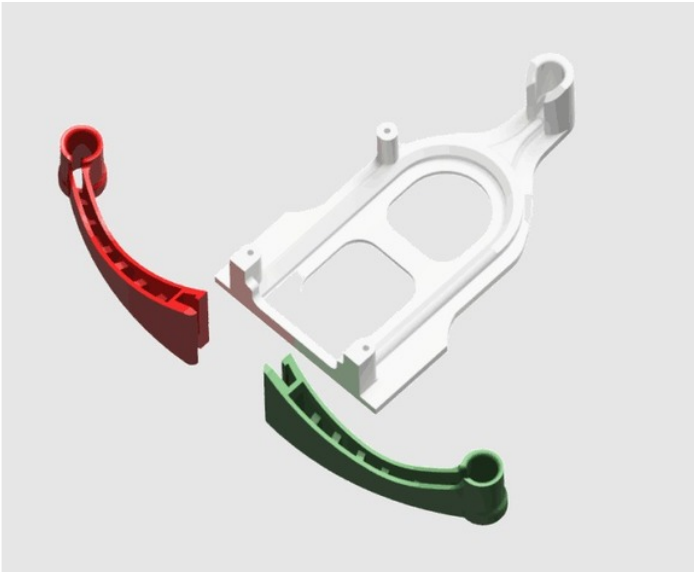

Figure 6.3: STL file of the Blimpduino 2 gondola (frame + wings) used for 3D print. From [50].

Once the gondola was printed we had all the necessary tools to assemble the system. The gondola is formed by a central body where the vertical motor, the battery and the control board are allocated, and by two wings structures that fit into the side channels of the main frame and at

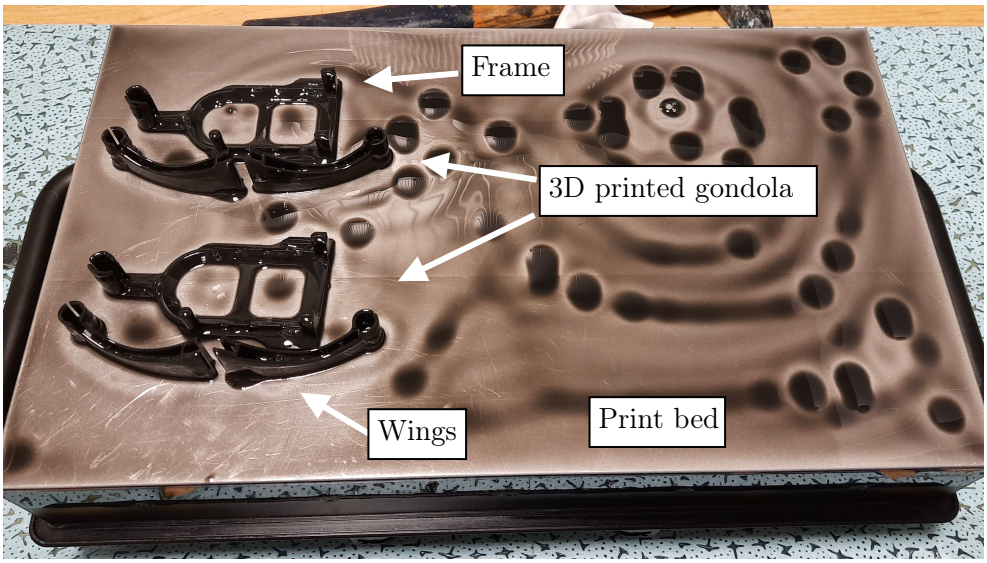

Figure 6.4: Photo of the Formlabs print bed with two Blimpduino gondolas printed on it.

their ends are equipped with supports for the longitudinal motors as it is shown in Figures 6.5 and 6.6. The DC motors of the wings rotate in opposite directions to compensate for the torque. After inserting the motors in the appropriate holes, the propellers are mounted on each of them. The Blimpduino 2 uses two counterclockwise and one clockwise propellers which are mounted as shown in Figure 6.7. Figure 6.8 shows the photo of the Blimpduino 2 gondola and motors assembly.

Figure 6.5: Fitting wings motors and frame of the Blimpduino 2. From [50].

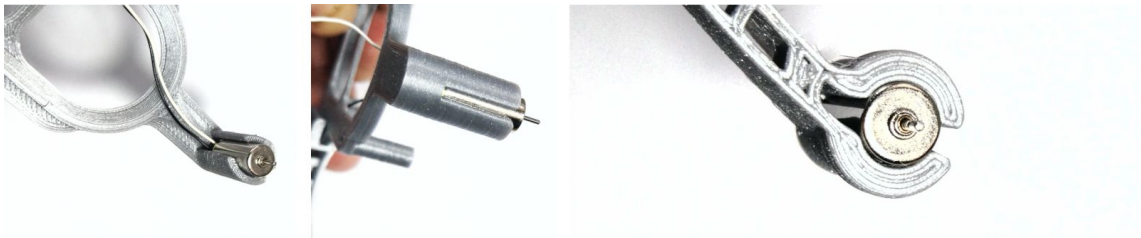

Figure 6.6: Fitting motors inside wings of the Blimpduino 2. From [50].

At this point the battery is attached and the control board are fixed to the gondola with screws as shown in Figure 6.9. The Blimpduino board has a USB LIPO charger module and is equipped with a LIDAR sensor to accurately measure the distance to an object. Another very important sensor that allows navigation and control is the MPU-9250 Nine-Axis MotionTracking device sensor

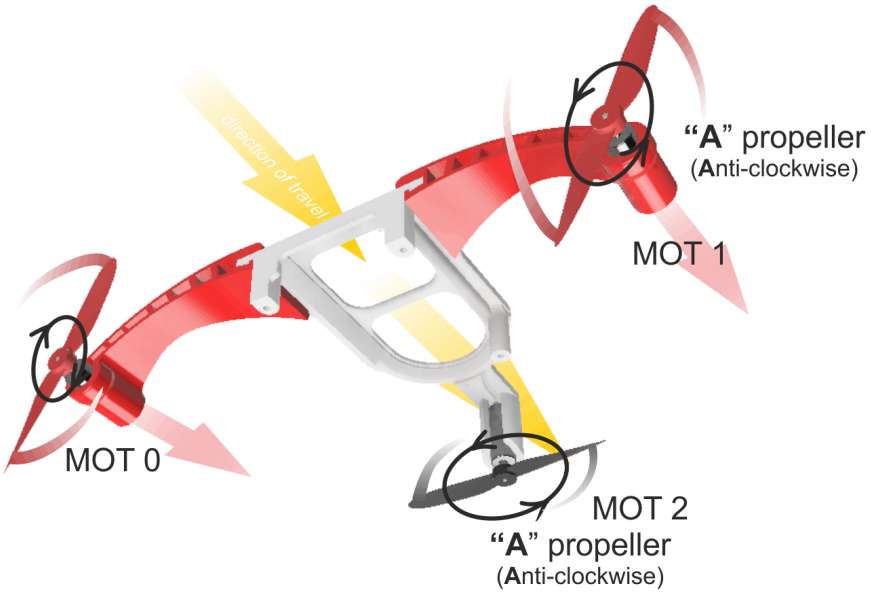

Figure 6.7: Propellers configuration of the Blimpduino 2. From [50].

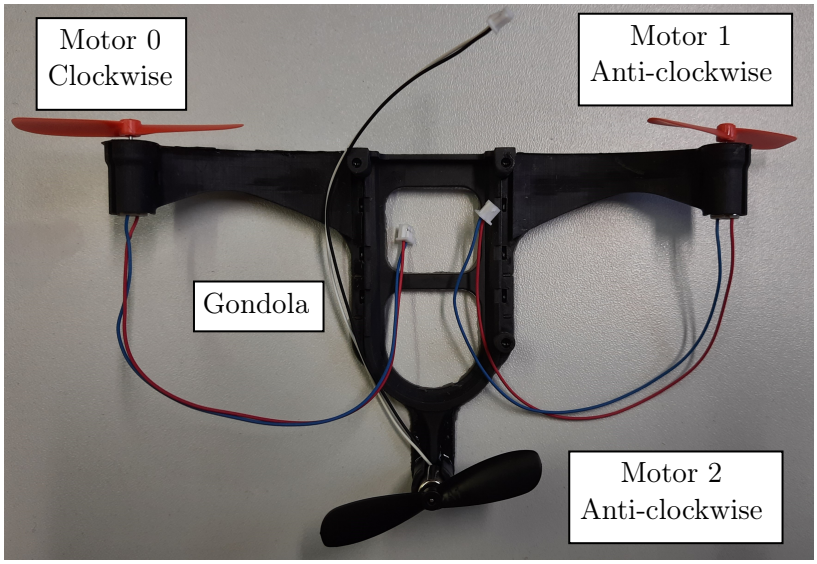

Figure 6.8: Photo of the gondola and motors assembly fase of Blimpduino 2.

that measures and reports body accelerations and angular rates. In Figure 6.10 we show a photo of the assembly of the board and battery to the gondola.

The last step of assembling the Blimpduino 2 is to attach the gondola to the balloon which has been inflated with Helium (Figure 6.11). The balloon shape can work as an *aerodynamic rudder*, making sudden turns more difficult and facilitating smooth sailing. In this phase it is necessary to check that the propellers of the lateral motors do not interfere in their movement with the surface of the balloon.

The buoyancy of the blimp is a crucial factor: too much buoyancy will push the system upwards and therefore will force the vertical motor to deliver more power to keep the blimp close to the floor. In this case, once the battery is discharged, the LTA robot will begin to rise and could be lost. On the other hand, a much greater weight force than the buoyancy force will require more power from the vertical motor to make the blimp stay up and therefore this will have more impact on the battery. In this case, once the battery is finished, the blimp will drop too abruptly downwards, colliding with the ground in case no one goes to retrieve it first. We remind that the choice of the mini airship for the robotic surveillance and measurement application inside the detector cavern was moved above all for the safety reason so that in the event of failure, the system does not fall violently on the accelerator equipment. This can cause significant structural and economic damage with immediate consequences on the progress of the mission. There is an exact point to choose where the buoyancy is slightly negative, this ensures that the system, left free to fly without input from the motors, will float in the air and slowly fall downwards (as if it were a leaf falling from a tree).

After having completely assembled the system with the attachment of the balloon to the gondola, we tested the blimp in the laboratory to check its buoyancy. Figure 6.12 shows a photo of the blimp in an instant of flight inside the laboratory where a scale model of detector can be seen in the background.

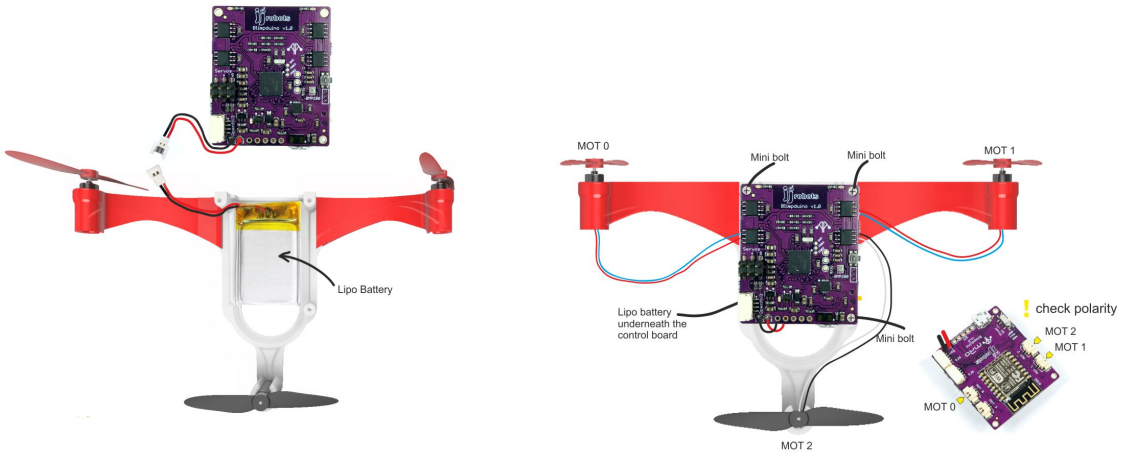

Figure 6.9: Connections of the LIPO battery to the control board of the Blimpduino 2. From [50].

6.2.2 Blimpduino 2 control board

Blimpduino 2 can be controlled through a smartphone connected to the Wi-Fi network of the on board system. Figure 6.13 shows the graphic interface of the Blimpuino control app. This is very

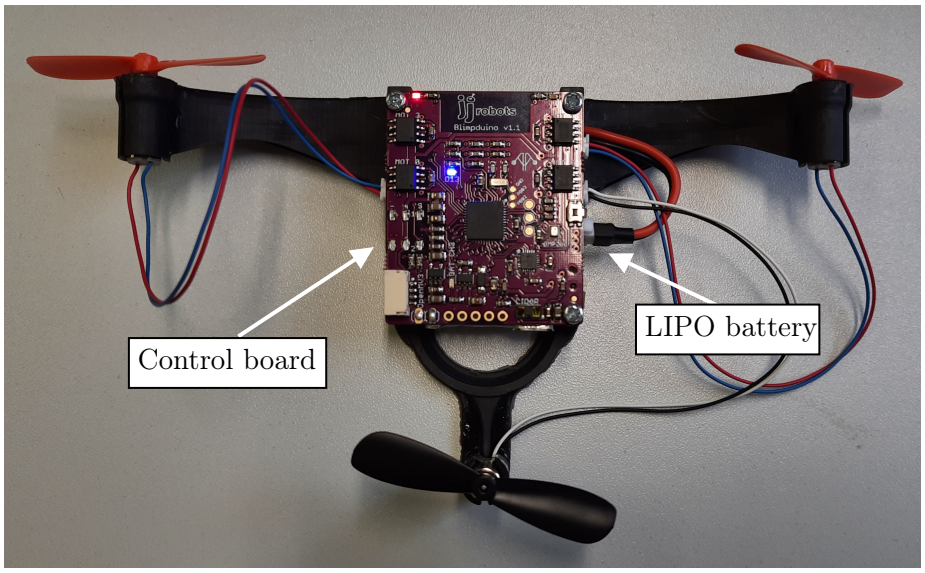

Figure 6.10: Photo of the LIPO battery and the control board of the Blimpduino 2.

Figure 6.11: Attack of the balloon to Blimpduino's gondola. From [50].

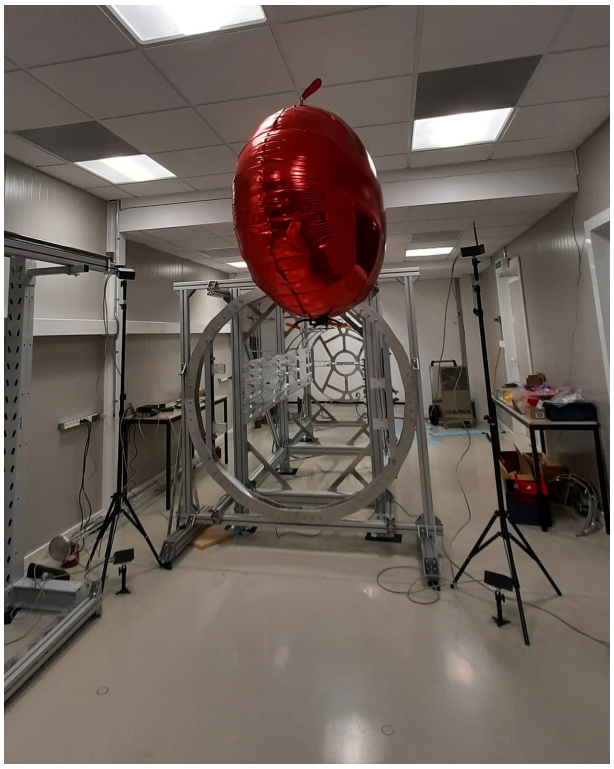

Figure 6.12: Photo of Blimpduino 2 completely assembled and portrayed in a moment of flight inside the laboratory.

simple but effective: there are two main cursors, the heading and the forward/backwards controls. Altitude, on the other hand, is controlled by two buttons, up and down. If they are kept pushed, the airship will start to go up or down depending on the command.

A positive note of the system is the possibility of assisted navigation. In fact, the blimp has two elements that allow to control the system in a semi-autonomous way, this happens thanks to the joint action of the MPU and the LIDAR sensor. In particular, the MPU calculates in real time the orientation and direction of the airship and the accelerations undergone during maneuvers and tries to level them with filters. The MPU is used to measure the angle of yaw and a PID controller is implemented within the code that tries to keep this direction fixed by the user if he presses the YAW OFF option. The LIDAR, on the other hand, measures the distances from the bottom of the board to the ground or any object that enters its visibility. Therefore this sensor is used for altitude control. The user who guides the blimp at a certain altitude can select the ALT OFF button to decide to keep the altitude recorded in that instant of time. In this case the system with a PD controller will try to reset the error between the altitude measured by the sensor and that saved by the user. It is also possible to activate both at the same time.

However, what is the aim of this experimental part of the thesis is not only to test the Blimpduino platform with its controls already implemented on board but once tested as it is, the idea is to modify the control for our purposes. Starting with the ALT OFF and YAW OFF functions, we would like to modify these by setting a preset value already uploaded on board. So we are going to modify the Blimpduino control board, i.e. the Arduino M0, making the control more automatic and less user-dependent. Therefore, we would like the blimp to perform *station keeping* test maintaining a certain altitude and yaw angle. We achieve this starting from the PID controllers already present

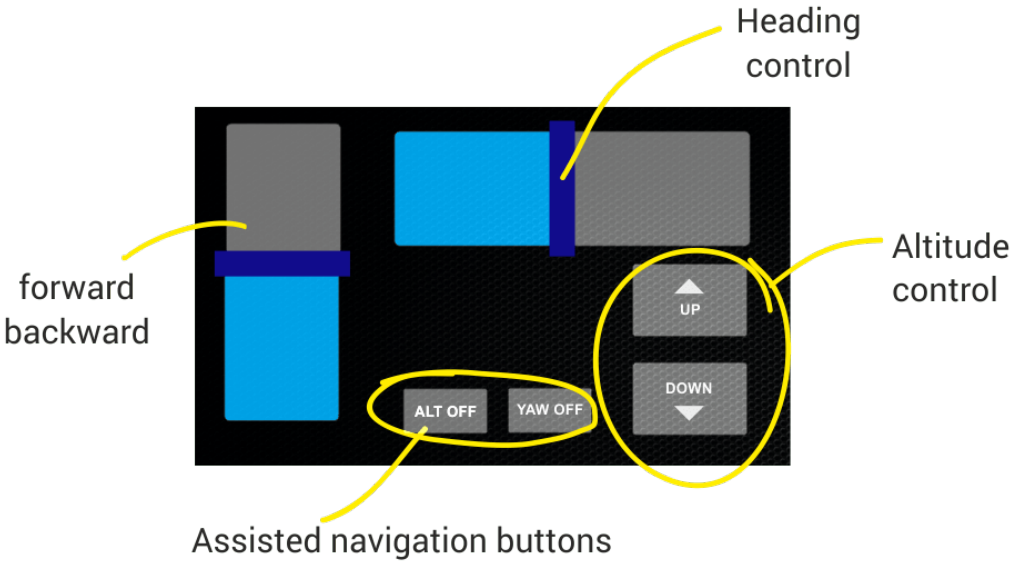

Figure 6.13: Blimpduino control APP graphic interface. From [50].

but modifying the interface with the user, currently when the user presses the control button on the app interface, at that point the sensors (LIDAR and MPU) fix the height measurement value and yaw at that instant of time and activate the PID control technique. What we would like to do is that once the automatic control mode has been activated, the blimp already knows what state it must reach which does not necessarily have to be the one measured at that moment. For example, the blimp must reach a certain altitude and orientation starting from the ground.

Furthermore, it was found that the on board LIDAR measurement was not very accurate and had an important noise that caused the altitude measurement to fluctuate. To improve this aspect, we have implemented a filter within the Arduino code to smooth the noise of the LIDAR measurements. The technique used is called *exponential smoothing*, it is an empirical technique that allows us to smooth out noisy data from time series using the exponential window function, this function assign exponentially decreasing weights over time to the various measures. Exponential smoothing acts as a low-pass filter to remove high-frequency noise from noisy signals presented as a time series of measurements. Let's imagine that the sequence of measurements starts at the instant $t = 0$. At the generic instant of time $t-1$ the sensor supplies a measurement equal to x_{t-1}. The exponential smoothing algorithm aims to provide a better estimate of the value of x at the next instant t, i.e. the best estimate of x_t, by joining the measure at the previous step $t-1$ plus the current measure at step t applying a weight to the two. We call s_t the best estimate of the measure at time t provided by the exponential smoothing algorithm, this is given by:

$$\begin{cases} s_0 = x_0, & t = 0 \\ s_t = \alpha x_t + (1-\alpha) s_{t-1}, & t > 0 \end{cases}$$

where α is the *smoothing factor* with $0 < \alpha < 1$. Hence the variable s_t is a simple weighted average of the current observation x_t and of the previous smoothed estimate s_{t-1}. In the extreme case in which α is 0 the smoothing is maximum and there is no sensitivity to the change of the measure given by the new observation x_t, in the other opposite case when α is 1 the output of the algorithm is simply the current measure and we loses the smoothing effect and gives more weight to changes

in measurements. For the choice of α there is no rule that imposes a value, its value can be varied by performing a sort of tuning until it converges to the best solution.

To carry out these changes on the control of the blimp and on the filtering of sensor data, obviously we acted at the programming level in the Arduino Integrated Development Environment (IDE) which consists of a cross-platform application in Java [47].

6.2.3 Blimpduino communication system

Blimpduino is able to communicate by establishing a Wi-Fi connection thanks to the ESP-12F module which is integrated in its on board card. Our goal for data processing with MATLAB was to track in real time the motion of the blimp during the experiment. We managed to do this through two methods: the first is the sensors telemetry stream that we channeled into a wireless communication to a computer and then the external data provided by a motion tracking system that we will discuss in section 6.4.

As for the on board sensors telemetry, the Blimpduino system was only able to send telemetry in real time through the smartphone interface and not allowing to save data. Therefore we established a connection via computer to the Blimpduino Wi-Fi network and set a communication channel for the transmission of telemetry data in order to be able to save and process them later. To do this, it was necessary to use a network protocol[1], in particular the Internet Protocol (IP) and the User Data Protocol (UDP). The Blimpduino IP address has two ports on which messages are transmitted through UDP packets. In one of the two ports the messages relating to the control of the blimp travel and they consist of a 4 bytes header and 16 bytes payload (8 channels of int16 values with sign). Of the 8 channels only 4 are used in which the following values are sent:

1. Throttle
2. Steering (yaw)
3. Height control
4. Mode

The Mode channel can assume different voices which are: *manual*, *manual control with altitude hold*, *yaw stabilization*, *yaw stabilization with altitude hold*, *stop motors*.

To set the sensors telemetry communication we used the other port conveying the messages not on the Android graphic interface but on a second device which is the computer. The telemetry packets, in the form of a text string, have been modified according to the original ones and it has been chosen to send the battery value, the yaw angle, the laser height and the value of the inputs to the three motors. After working at a code level in the Arduino IDE platform for the choice of the type of data to be sent to the user, a software (Wireshark [90]) was used on the computer for protocol analysis (packet sniffer). This allowed us to observe all the traffic present on the network and to analyze the acquired data in real time by filtering the information relating only to the UDP protocol which was the one used for the transmission of telemetry. Finally, we could control the blimp via app and at the same time have its real time telemetry on the computer.

[1]It is a set of rules specified by means of protocols that define the communication modalities between two or more entities.

6.3 Parameter identification

Once the Blimpduino was purchased, the process of identifying the parameters that appear in the dynamics and that we had estimated up to this point was fundamental in the assembly phase. Some parameters were directly measured with the physical components, others were simulated once the exact dimensions and properties of the system were obtained. To be more precise, the dynamic parameters to be estimated for the simulations were the following:

- a: semi-major axis [m];
- b: semi-minor axis [m];
- m: total mass [kg];
- I_{RB}: rigid body inertia matrix [kg·m^2];
- $\boldsymbol{r}_G$: CG vector with respect to CV [m];
- V: ellipsoid volume [m^3];
- D: damping matrix [kg/s];
- d_y: half distance between the longitudinal motors [m];
- d_z: distance of the vertical motor with respect to CV [m];
- f_B: buoyancy force [N];
- T_{max}: maximum motor thrust [N].

The geometric parameters of the ellipsoid were measured once the balloon was obtained. In particular, for the test, as we will see later, two different balloons sizes were used. This choice was dictated by the presence of the additional mass. Indeed, the Blimpduino system is able with the supplied balloon to fly without further mass additions. Instead in our case, in order to use the PhaseSpace motion capture system, we needed to add a mass to the system relating to the presence of the LED markers and the microdriver that powers them. Furthermore, for a real estimate of the buoyancy force, a test was carried out in which the balloon in question inflated with Helium was placed on a scale linked to a standard weight of 100 g and the weight reduction was measured starting from 100 g. This empirical buoyancy determination is shown in Figure 6.14. Table 6.1 shows the measured data for the characteristics of the balloon.

a	0.4064 m
b	0.1500 m
V	0.0294 m^3
m_{hull}	0.0260 kg
f_B	0.3532 N

Table 6.1: Blimpduino balloon characteristics.

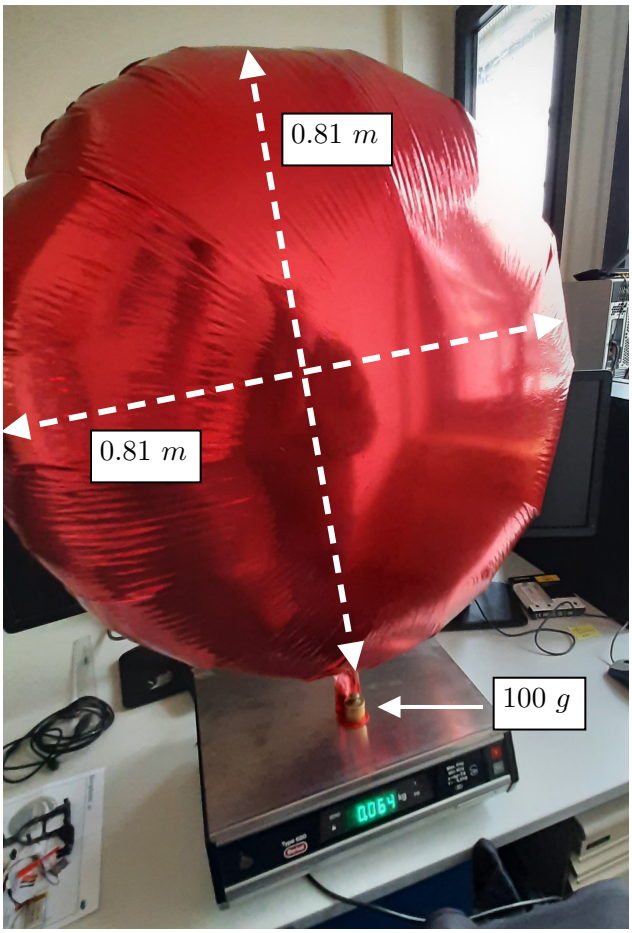

Figure 6.14: Photo of the empirical determination test for the Blimpduino buoyancy force by connecting the balloon to a standard weight of 100 g.

Having all the components of the system, we weighed them with a precision balance, all the weights components are reported in Table 6.2. Finally adding all the masses we obtain the total mass of the rigid body. However, this calculation does not take into account the mass of the Helium that is inside the balloon in a given thermodynamic state. Knowing the volume, pressure and temperature of the gas it is possible to determine the mass by calculating the number of moles with the use of the ideal gas law.

$$pV = nRT$$

where p is the pressure to which the gas is subject, V is the occupied volume which is the volume of the balloon, n is the amount of substance, R is the universal gas constant which is equal to 8.314 $J{\cdot}K^{-1}{\cdot}mol^{-1}$ and T is the temperature of the gas. Calculating from this law the number of moles of Helium, it is possible through the knowledge of the molar mass to obtain the mass through the following relationship:

$$m = M_{He}n$$

where M_{He} is the molar mass of the Helium which is equal to 4 $g{\cdot}mol^{-1}$.

To determine the inertia matrix and the position of the center of gravity with respect to the center of volume as well as other geometric quantities such as the distances d_y and d_z, it was necessary to reproduce the Computer Aided Design (CAD) model of the system. CAD modeling aims to

Brushless motors (3)	0.4064 kg
Hull	0.026 kg
Gondola	0.008 kg
Control board	0.008 kg
Battery	0.010 kg
Propellers	≈ 0.000 kg
Total mass	0.058 kg

Table 6.2: Blimpduino components masses

Figure 6.15: Photo of the weight determination of the gondola through a scale.

create models of a mechanical system and the software used is CATIA, a commercial platform of the European company Dassault Systèmes. To obtain the CAD sketch, the original dimensions and the masses placed in Tables 6.1 and 6.2 were respected. This CAD modeling represents a simplified version of the Blimpduino as it is possible to notice from Figures 6.16, 6.17 and 6.18 that the propellers of the brushless motors have not been reproduced since their weight is approximate to zero, hence they do not contribute to the computation of the inertia matrix of the body. Figures 6.17 and 6.18 show four views of the rendering of the CAD model obtained with CATIA.

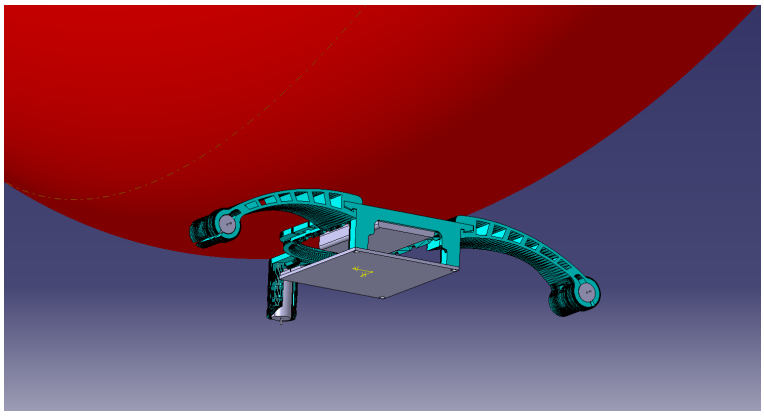

Figure 6.16: CAD model in CATIA of the Blimpduino system.

Once the CAD modeling of the system was finished, we moved on to measuring the inertia and the CG. The inertia matrix in the body-fixed reference frame (located at the CV of the balloon) is

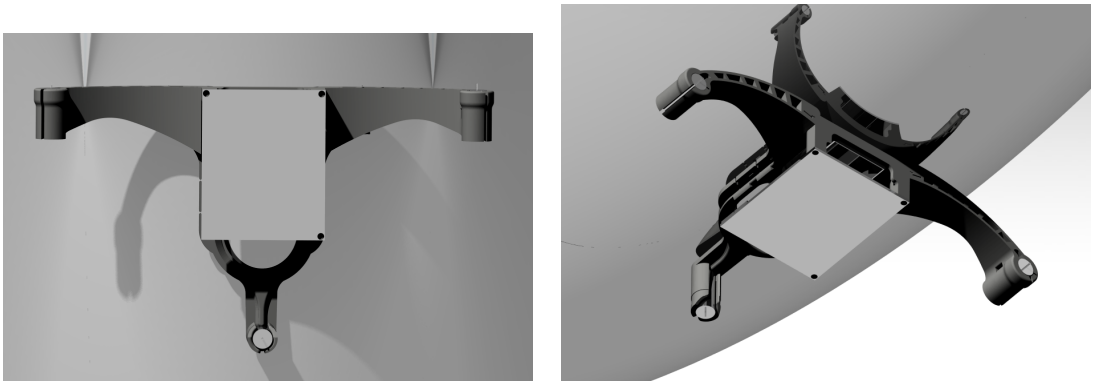

(a) **(b)**

Figure 6.17: 3D rendering CAD model in CATIA of the Blimpduino system seen from the bottom with the control board (a) and from the front (b).

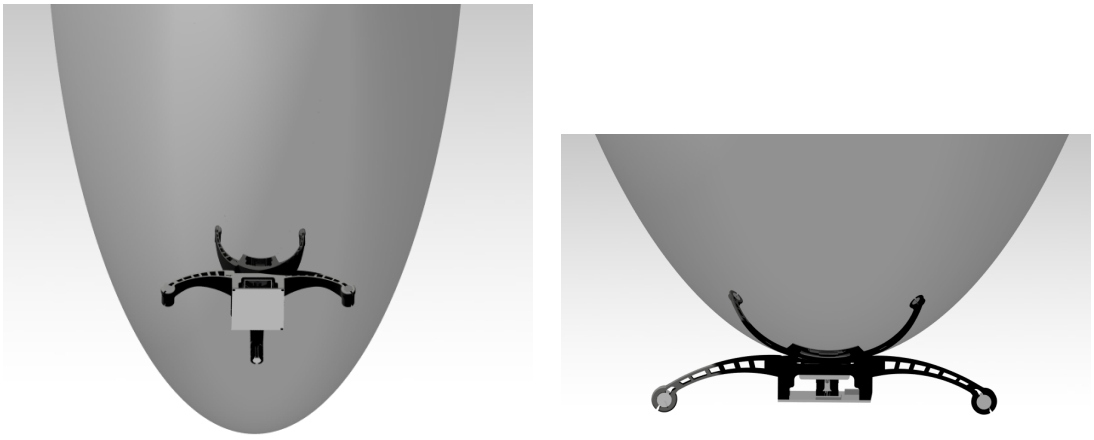

(a) **(b)**

Figure 6.18: 3D rendering CAD model in CATIA of the Blimpduino system seen from the bottom with the balloon (a) and from the front (b).

given by the following expression.

$$I_{RB} = \begin{bmatrix} 0.006 & -2.83 \cdot 10^{-7} & 5.205 \cdot 10^{-5} \\ \cdot & 0.007 & 1.69 \cdot 10^{-5} \\ \cdot & \cdot & 0.002 \end{bmatrix} kg \cdot m^2$$

Finally the vector $\boldsymbol{r}_G$ indicating the CG has been calculated as

$$\boldsymbol{r}_G = \begin{bmatrix} -2.833 \\ -0.92 \\ 185.755 \end{bmatrix} mm$$

From these data it is possible to note that the simplified assumptions made in section 2.2 are in agreement with what is the actual real model of the indoor blimp. In particular, it can be assumed that the inertia matrix is very close to being diagonal since the off-diagonal elements are at least two orders of magnitude lower than those on the main diagonal. Furthermore, from the vector $\boldsymbol{r}_G$ it is possible to note that the preponderant component is the one along z so this confirms that the CG is aligned to the z-axis of the body-fixed reference system and lower due to the presence of the gondola.

The last parameter identification process was to characterize the maximum thrust of the Blimpduino motors. To do this, some low-cost tests were carried out, giving maximum torque to the motor which was fixed to a support of a certain weight placed on a scale. The weight reduction, similar to the buoyancy test, gives us the grams of force that the motor is able to lift.

6.4 Testing environment setup

In this section we analyze the setup of the environment in which the blimp control experiments were carried out. As a first approach to the problem, it was decided to test the blimp in an environment without disturbances, neither magnetic nor of any other type, such as the presence of wind or the change in environmental conditions in terms of temperature and pressure. In particular, the latter greatly affect the thermodynamic conditions of the Helium present in the balloon, which in turn affects the buoyancy force which therefore has an effect on the entire dynamics of the system. The cleanroom of the CERN laboratory where the tests were carried out is shown in Figure 6.20.

Within this work environment, a motion capture system was implemented in the room to track the movement of the robot, obtaining its position and orientation in space. This is the *PhaseSpace Impulse X2E* which is the fastest real time motion capture system on the market. Four main steps are required for the PhaseSpace system setup process:

1. Initial setup of the cameras;
2. Registering the LED devices;
3. Calibration of the system;
4. Alignment of the system.

The Figure 6.19 shows the useful components that are needed to operate the PhaseSpace motion capture system. The basic requirements are cameras that have a 60° field of vision and a RF camera which is required for the system to operate. Then another important requirement is a calibration object (called Calibration Wand) which is a LED device used for calibration and alignment. We also needed a server containing the hub for the cameras, microdrivers that powers LED devices and drives their LED markers. Finally we needed a computer to access the PhaseSpace Master Client application, as well as a web browser to access the Configuration Manager. The PhaseSpace Master Client is a calibration and motion capture data recording program. It allows users to stream and record motion capture data and to conduct system calibration and alignment entirely within one application. Data from Master Client can be saved as 3D point data to be used in other software. The Configuration Manager is the main interface for configuring and monitoring PhaseSpace systems which enables remote configuration of the motion capture system. Before being able to use it for tracking the blimp it was necessary to go through the system setup procedures which are described in the following paragraphs.

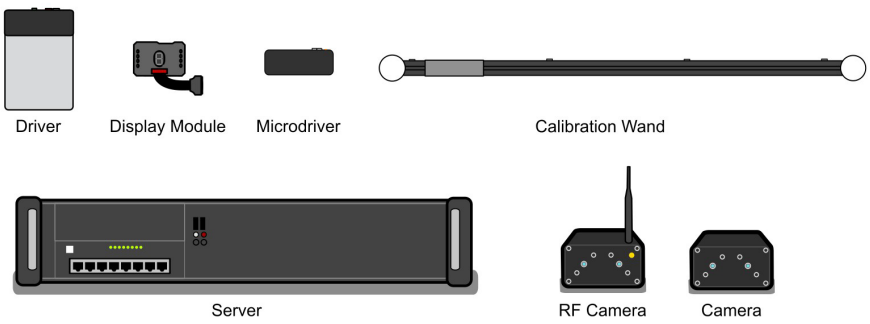

Figure 6.19: List of devices essential to the operation of the PhaseSpace motion capture system. From [73]

6.4.1 Initial setup

For the initial setup of the PhaseSpace system we first placed the cameras around the space we want to capture which in our case was the cleanroom CERN laboratory where we tested the blimp. Once we have positioned the cameras correctly we connected them in a chain through Ethernet cables from the server hub. Then we connected the computer to the same server and access the Configuration Manager to check the list of cameras. Figure 6.20 shows the actual eight cameras configuration we have made. The setting is structured in the positioning of cameras in four corners by putting two on each side, one above and one below. In this way we have guaranteed a complete coverage of the capture area. Figure 6.21 shows a screen of the PhaseSpace Master Client application where it is possible to check the position in space and the fields of view of the cameras. In order to accurately capture the space, cameras will need to be positioned so that they have some overlap as shown in Figure 6.22.

6.4.2 Registering devices

The following step of the general setup is the LED devices registration. LED devices are used to convey motion data to the PhaseSpace system. In order for devices to be tracked by the system,

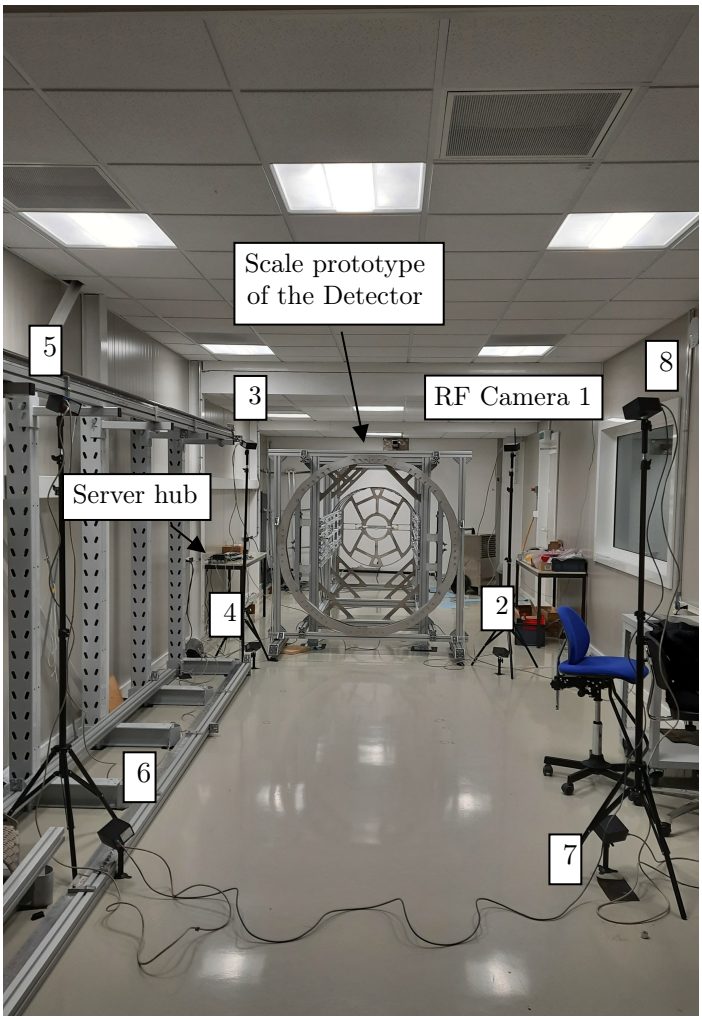

Figure 6.20: Photo of the cleanroom inside the CERN laboratory where the control tests of Blimpduino took place.

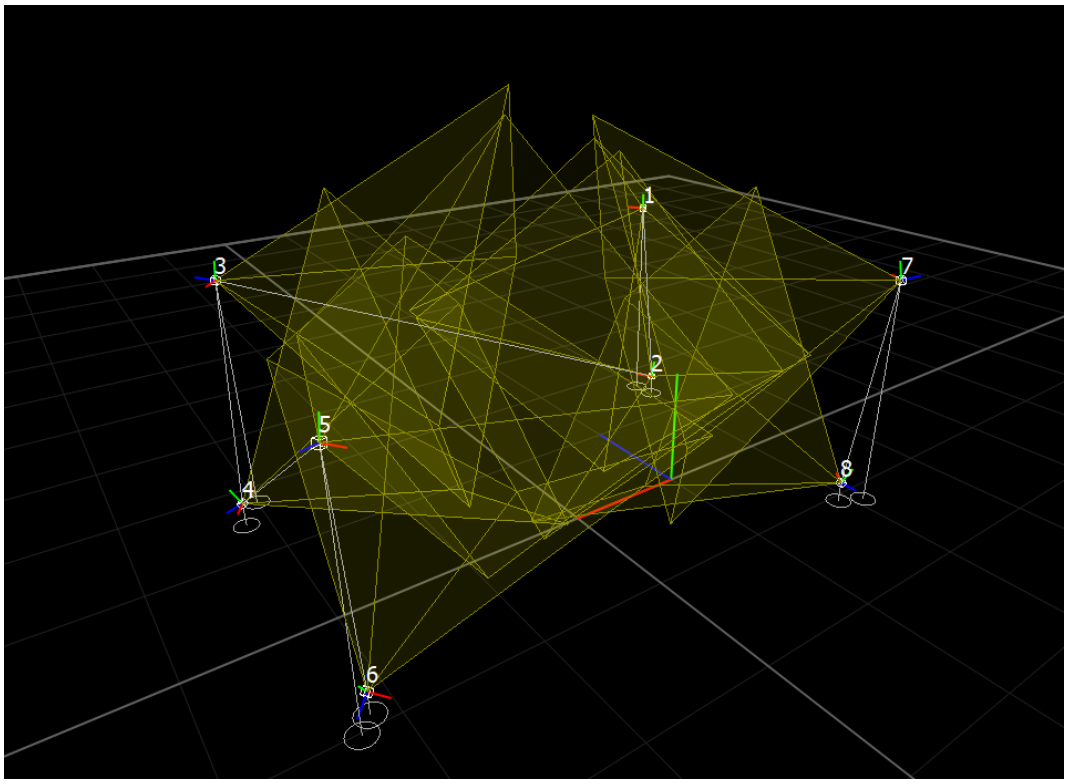

Figure 6.21: Cameras configuration and reference frame position of the PhaseSpace system.

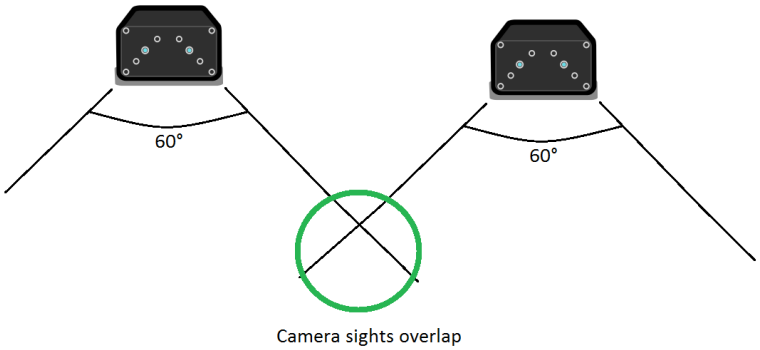

Figure 6.22: Overlapping of the PhaseSpace system cameras to ensure correct coverage. From [73].

they first need to be registered. This is a simple process, where we scanned for new devices in the Configuration Manager, and then pair the device's drivers to the server. A driver is what powers the LED devices and once drivers are successfully paired, they will be tracked in the space while connected to their LED devices.

6.4.3 Calibration

To calibrate the system we needed a paired driver and a calibration object, in this case we have used a Calibration Wand composed by four LED. Once the server is selected in the OWL Configuration panel of the PhaseSpace Master Client we opened Tools menu and select Calibration to enter calibration mode as shown in Figure 6.23. This will open the Calibration dialog box and automatically connect to the server. If the calibration wand is successfully activated, in the capture space, white points corresponding to the wand's markers should appear in the camera views in the Master Client 2D panel. There are also colored lines going through the white points which represent the light levels the cameras are detecting from the LEDs on the wand and to each color corresponds a detection which may be too weak or too strong. The goal of calibration is to collect calibration data by moving the object, that must be visible as much as possible by all cameras, in the capture space.

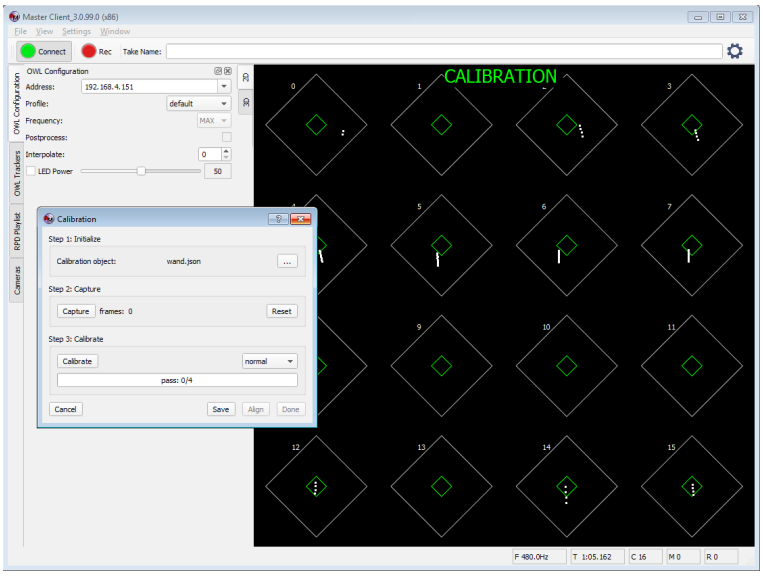

Figure 6.23: Calibration dialog box in the PhaseSpace Master Client application. From [73].

6.4.4 Alignment

The final step in setting up the system is the alignment process. This will orient the system, creating (x, y, z) coordinates to give points in the space context. Three points are needed for alignment: the origin and points to determine the x and z axes. We standed in the center of the capture space and face the direction that will be determined as *forward*. We set the origin of the capture space by placing the wand on the ground upright and still as shown in Figure 6.25. Then by moving the micro wand forward and to the right, the two perpendicular axes x and z appear defined as illustrated in Figure 6.26. Our alignment of the system with the consequent position of the reference frame is shown in Figure 6.21.

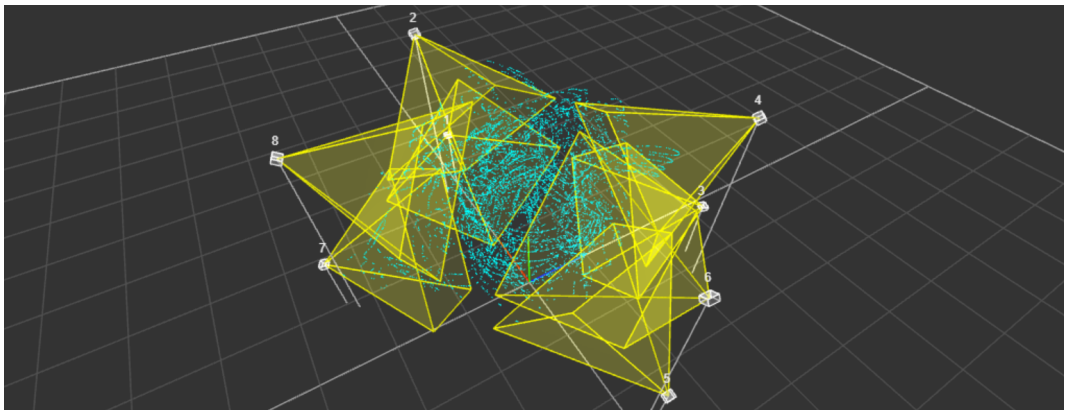

Figure 6.24: 3D calibration view in the Configuration Manager.

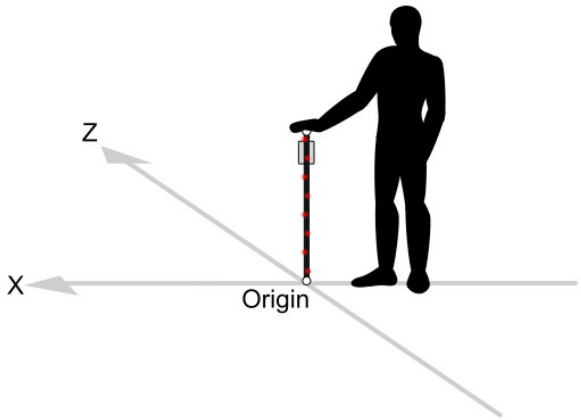

Figure 6.25: Position of the micro wand for setting the origin of coordinate of PhaseSpace system. From [73].

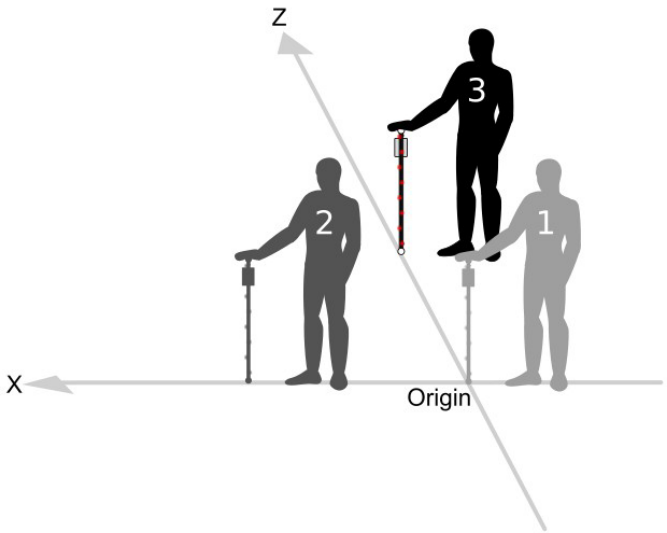

Figure 6.26: Defining of the x and z axes moving the PhaseSpace micro wand. From [73].

6.4.5 Streaming motion capture data

Once we have prepared the motion capture system with calibration and alignment, the system is ready for the acquisition phase of the tracking data. In particular, with the use of the reference LEDs it is possible to choose the object to monitor. Our choice fell on the tracking of the rigid body. To create a rigid body from markers in the live stream, we need to select a group of at least three markers in the 3D view and add a rigid body tracker on the system. The assembly phase of the LED tracking system on the blimp was very delicate because the three minimum LEDs, necessary for the creation of the body reference system, weighed down the system itself due to the presence of the microdriver that powers the LEDs. At this stage we have opted for the choice of a larger balloon than the current one, i.e. 36 inches instead of 32 inches of diameter. The greater buoyancy (which increases with the volume of the hull) compensates for the increase in weight due to the addition of the tracking system equipment. Once a tracking triad was created, it was modified thanks to the Rigid Body Editor inside the PhaseSpace Master Client application (see Figure 6.27) in such a way that the reference frame that the motion capture system tracked was exactly the body-fixed reference frame F_b defined in section 2.3 which has its center in the CV of the balloon.

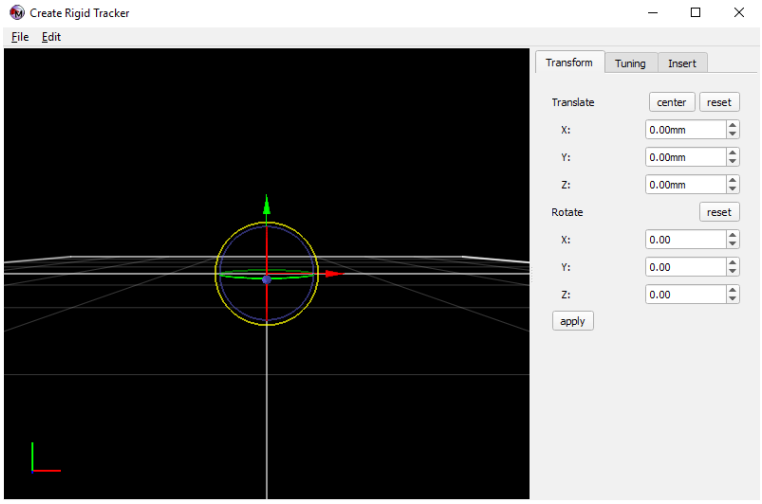

Figure 6.27: Rigid Body editor defining rigid body reference frame to be captured in the PhaseSpace system. From [73].

6.5 Station keeping test

In the previous sections we discussed the architecture of the chosen platform and the setup of the laboratory where the tests were performed. In this section we show the results of the tests carried out on Blimpduino. The control strategy chosen is that of a *station keeping* test in which we wanted the blimp to maintain a certain fixed altitude and yaw angle. As we have seen, these controls were already implemented within the flight code of the Arduino board. However, it was necessary to make these controls independent of the user. In particular, when they were activated by the user, the platform recorded the current value of the state and activated the control to keep these values through a PID controller based on the measurement of the LIDAR and the IMU. What we decided to change was the height and yaw angle that the blimp had to keep. We wanted that starting from any position it could reach and keep the preset values fixed over time independently. The app

interface was kept active only to turn on or off the platform control which independently controlled its motion in order to carry out the station keeping strategy.

The control, as we have already said, is achieved with a PID controller which, through the measurement of the on board sensors, is able to calculate the error between the desired variable and the measured one. On the basis of this error, through the use of gains, it generates a control law that modulates the thrust of the motors so that errors tend to zero (see Figure 6.28). A PID law was used to control the yaw, while a PD strategy was used to control the altitude. The tests were also carried out with the choice of different gains by performing a sort of manual tuning of the gains to establish which combination gave the most satisfactory results in terms of response performance.

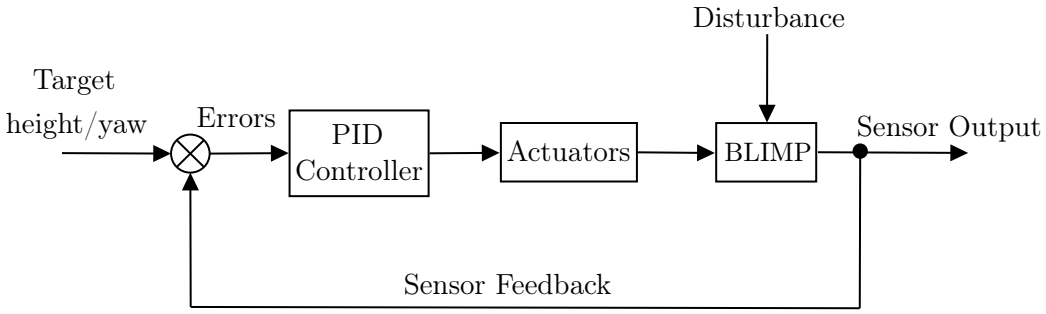

Figure 6.28: Blimpduino control system scheme based on a PID controller.

6.5.1 Mathematical altitude-yaw model

In this paragraph we will make assumptions that will lead us to build the mathematical model useful to reproduce and simulate the real control test in order to compare the two results and check that the process of identifying the parameters and the development of the equations of motion of the blimp are correct. In accordance with the hypotheses made in Chapter 5, the blimp moves at a low speed therefore we can assume that:

Assumption 6.1. *Since the blimp is slow moving then roll ϕ and pitch θ angles are zero.*

The Assumption 6.1 has the consequence that $\phi = \dot{\phi} = \theta = \dot{\theta} = 0$. Taking up the equation of the kinematics that links the angular velocities to the derivatives of the Euler angles (2.8) and substituting at ϕ and θ the null value we obtain

$$\begin{bmatrix} \omega_x^b \\ \omega_y^b \\ \omega_z^b \end{bmatrix} = \begin{bmatrix} 1 & 0 & 0 \\ 0 & 1 & 0 \\ 0 & 0 & 1 \end{bmatrix} \begin{bmatrix} \dot{\phi} \\ \dot{\theta} \\ \dot{\psi} \end{bmatrix} \tag{6.1}$$

from which it is clear that the angular velocities $\omega_x^b = \omega_y^b = 0$. Therefore with Assumption 6.1 we basically eliminated 2 degrees of freedom from the system.

The other assumption concerns the forces and moments of the propulsive system. As we have seen in section 6.2, the actuators of the Blimpduino system are three brushless motors mounted on the gondola as shown in the Figure 6.7. The following assumption applies to actuators:

Assumption 6.2. *The vertical motor affects only in the direction of the $\boldsymbol{Z}_n$-axis and the other two motors act only in the horizontal plane parallel to $\boldsymbol{O}_n\boldsymbol{X}_n\boldsymbol{Y}_n$.*

The third assumption, on the other hand, concerns the damping term and it is always linked to the slow motion of the blimp.

Assumption 6.3. *Given the slow motion of the blimp, the damping matrix (A.49) contains only linear terms, i.e.*

$$\boldsymbol{D}(\boldsymbol{\xi}^b) = -diag\begin{bmatrix} D_{v_x} & D_{v_y} & D_{v_z} & D_{\omega_x} & D_{\omega_y} & D_{\omega_z} \end{bmatrix}^T$$

From the 6 DOF dynamic model (2.22), with Assumptions 6.1, 6.2 and 6.3 the model is simplified to

$$\begin{cases} m'_x \dot{v}^b_x - m'_y \omega^b_z v^b_y - D_{v_x} v^b_x = f_{px} \\ m'_y \dot{v}^b_y + m'_x \omega^b_z v^b_x - D_{v_y} v^b_y = f_{py} \\ m'_z \dot{v}^b_z - D_{v_z} v^b_z + (f_B - f_G) = f_{pz} \\ I'_z \dot{\omega}^b_z + (m'_y - m'_x) v^b_x v^b_y - D_{\omega_z} \omega^b_z = \tau_{pz} \end{cases} \tag{6.2}$$

From the simplified model (6.2) we can deduce the following remark

Remark 6.1. *The altitude motion and the planar motion are independent and decoupled, so the control problem can be analyzed separately.*

In our case we consider separately the altitude dynamics and the yaw dynamics which, as we will see with another assumption, will be decoupled from the motion along $\boldsymbol{X}_b$ and $\boldsymbol{Y}_b$.

6.5.2 Simplified altitude movement model

From Remark 6.1, we have said that the altitude motion along $\boldsymbol{Z_n}$ is considered separate and independent from the plane motion, therefore considering the equation (6.2) and extrapolating the altitude dynamics we have

$$m'_z \dot{v}^b_z - D_{v_z} v^b_z + (f_B - f_G) = f_{pz} \tag{6.3}$$

In addition, recalling the kinematic model (2.10) and applying the Assumption 6.1, the new kinematic model is obtained as follows

$$\dot{\boldsymbol{\eta}}^n_1 = \begin{bmatrix} \dot{x}^n \\ \dot{y}^n \\ \dot{z}^n \end{bmatrix} = \begin{bmatrix} \cos\psi & -\sin\psi & 0 \\ \sin\psi & \cos\psi & 0 \\ 0 & 0 & 1 \end{bmatrix} \begin{bmatrix} v^b_x \\ v^b_y \\ v^b_z \end{bmatrix} \tag{6.4}$$

from which we can deduce that $\dot{z}^n = v^b_z$ and $\ddot{z}^n = \dot{v}^b_z$ and then rewriting the equation (6.3) we obtain

$$m'_z \ddot{z} - D_{v_z} \dot{z} + (f_B - f_G) = f_{pz} \tag{6.5}$$

As we reported in Chapter 2 $f_{pz} = T_v$. In this case superscript $(\cdot)^n$ for the altitude z is omitted for simplicity of notation. Hence the equation (6.5) represents the nominal model for the altitude motion of the blimp that we will use for the control part.

6.5.3 Simplified yaw model

The planar motion of the blimp is derived from the remaining part of (6.2):

$$\begin{cases} m'_x \dot{v}_x^b - m'_y \omega_z^b v_y^b - D_{v_x} v_x^b = f_{px} \\ m'_y \dot{v}_y^b + m'_x \omega_z^b v_x^b - D_{v_y} v_y^b = f_{py} \\ I'_z \dot{\omega}_z^b + (m'_y - m'_x) v_x^b v_y^b - D_{\omega_z} \omega_z^b = \tau_{pz} \end{cases} \tag{6.6}$$

For the horizontal plane, we can define a horizontal configuration vector

$$\boldsymbol{\eta}_{Horiz}^n = \begin{bmatrix} x^n & y^n & \psi \end{bmatrix}^T$$

and an instantaneous horizontal velocity vector

$$\boldsymbol{\xi}_{Horiz}^b = \begin{bmatrix} v_x^b & v_y^b & \omega_z^b \end{bmatrix}^T$$

Always taking up the kinematics equation (2.10) and applying the Assumption 6.1, we can notice that the derivative in time of the yaw angle is equivalent to the angular velocity ω_z^b, i.e. $\omega_z^b = \dot{\psi}$. We can rewrite the blimp kinematics equation for horizontal motion as follows

$$\begin{bmatrix} x^n \\ y^n \\ \psi \end{bmatrix} \begin{bmatrix} \cos\psi & -\sin\psi & 0 \\ \sin\psi & \cos\psi & 0 \\ 0 & 0 & 1 \end{bmatrix} \begin{bmatrix} v_x^b \\ v_y^b \\ \omega_z^b \end{bmatrix} \tag{6.7}$$

Then we recall how the propulsive forces were defined in Chapter 2.

$$\begin{cases} f_{px} = T_{cmn} \\ f_{py} = 0 \\ \tau_{pz} = T_{diff} d_y \end{cases} \tag{6.8}$$

where d_y is the half distance between the two motors. Now looking at the third equation of (6.6) we can do the following remark:

Remark 6.2. *The difference that appears between the masses m'_y and m'_x causes instability in yaw motion. To avoid and simplify this problem we assume that the longitudinal and lateral apparent mass are equal i.e. $m'_x \approx m'_y = m_{Horiz}$, and therefore the instability of the yaw no longer appears.*

In this case, with Remark 6.2, the equation of yaw is decoupled from the equations that describe the longitudinal and lateral motion and therefore we can consider it alone. Taking the third equation of (6.6), applying Remark 6.2 and replacing $\omega_z^b = \dot{\psi}$, $\dot{\omega}_z^b = \ddot{\psi}$ we obtain

$$I'_z \ddot{\psi} - D_{\omega_z} \dot{\psi} = \tau_{pz} \tag{6.9}$$

which we will use for applying the control.

6.5.4 Tests and results

In this paragraph we will show the tests that were carried out with the two balloons. We remind that the choice of the two balloons was dictated by the fact that the additional mass of the motion capturing system due to the LED markers and the microdriver, did not make the Blimpduino motors able to take off the system, with the use of the original balloon. The weight of the gondola plus the tracking system is 75 g, while to evaluate the buoyancy force a test was carried out in which both balloons were connected to a known standard weight and after the balloon was applied, the decrease in the weight of the object was measured. The result is that the original balloon has a buoyancy force of 36 g while the bigger one has a force of 141 g. The smaller original balloon was not able to keep the blimp in level flight and the difference was such that not even the motors were able to lift the mass difference (about 40 grams). This resulted in two types of tests, one with only the on board telemetry data supplied with the Blimpduino sensors and a test with both active tracking systems (telemetry and motion capturing) with the largest balloon.

- **Balloon 1 (telemetry)**

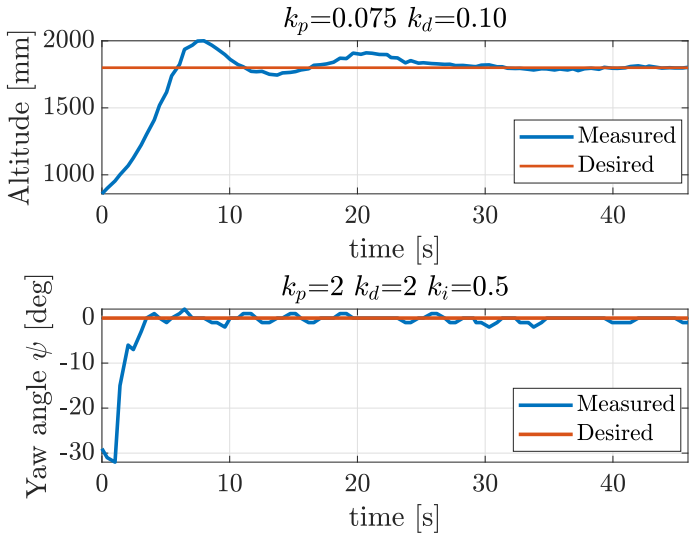

Figure 6.29: Station keeping test 1 results for the balloon 1.

In Figures 6.29, 6.30 and 6.31 the results of station keeping are shown, i.e. the maintenance of the altitude and of the yaw angle for the smallest balloon where the measured value reported is the one received by the telemetry on board by sending packets via UDP data. The desired value is 1800 mm for the altitude and 0 degrees for the yaw angle. From Figure 6.29 we can see that the rise time of the altitude value is around 5 seconds, i.e., in about 5 seconds the blimp goes from 10% to 90% of the steady state value (1800 mm) without making oscillations. As for the yaw angle, the rise time is shorter, i.e. the system responds faster in the orientation control; the rise time for the yaw angle is around 3 seconds. These results hold true also for Figure 6.30. For Figure 6.31 we must emphasize that the control was started a few seconds after the capture of the telemetry, indeed it can be clearly seen that the altitude of the blimp initially drops[2] and then begins to rise with the

[2]This is because in the absence of control the gravitational force is slightly greater than the buoyancy force.

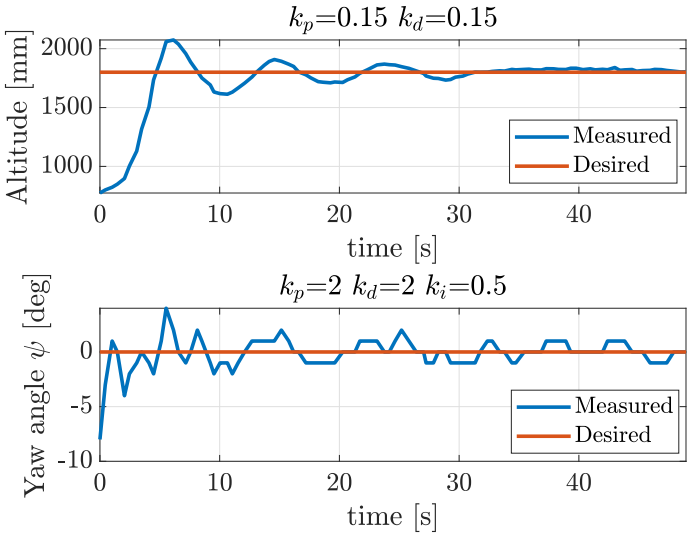

Figure 6.30: Station keeping test 2 results for the balloon 1.

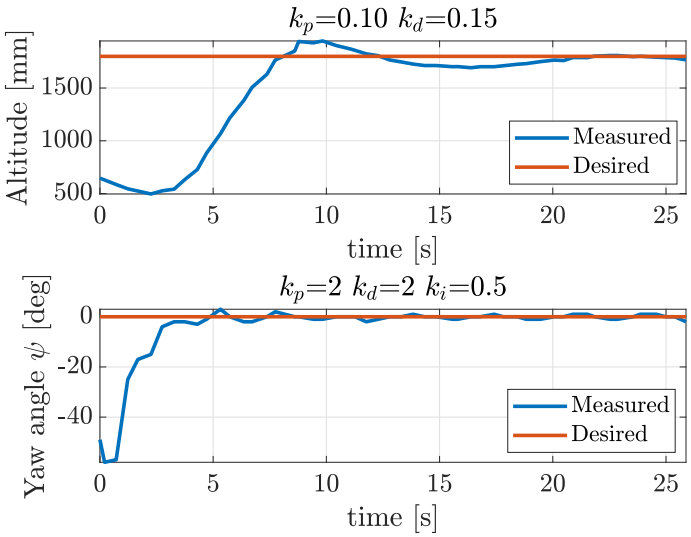

Figure 6.31: Station keeping test 3 results for the balloon 1.

same trend as the previous figures. For the tests shown in the previous figures, the settling time[3] is around 30 seconds for altitude and 10 seconds for orientation. Ultimately as reported at the top of each figure there are the gains of the PD control law of the altitude controller and of the PID law for the yaw angle through which the various responses of the blimp were tested to find the optimal responses.

- **Balloon 2 (telemetry)**

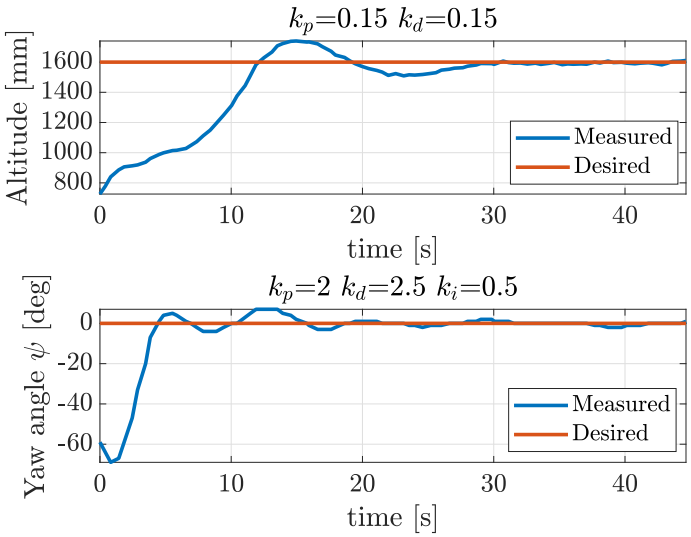

Figure 6.32: Station keeping test 1 results for the balloon 2.

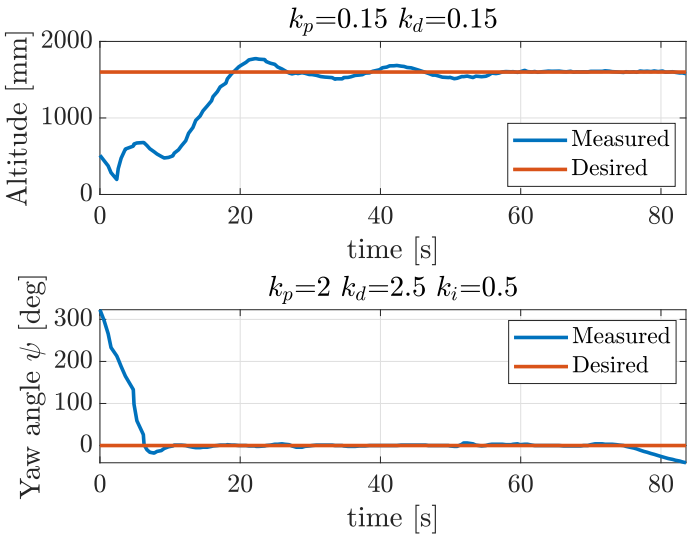

Figure 6.33: Station keeping test 2 results for the balloon 2.

Figures 6.32, 6.33 and 6.34 show the results of three station keeping tests carried out with the largest balloon by comparing the on board telemetry measured by the sensors and the desired

[3]It is the time required for the response to enter a certain band close to the steady state value (generally referring to deviations of 2 or 5%) without leaving it.

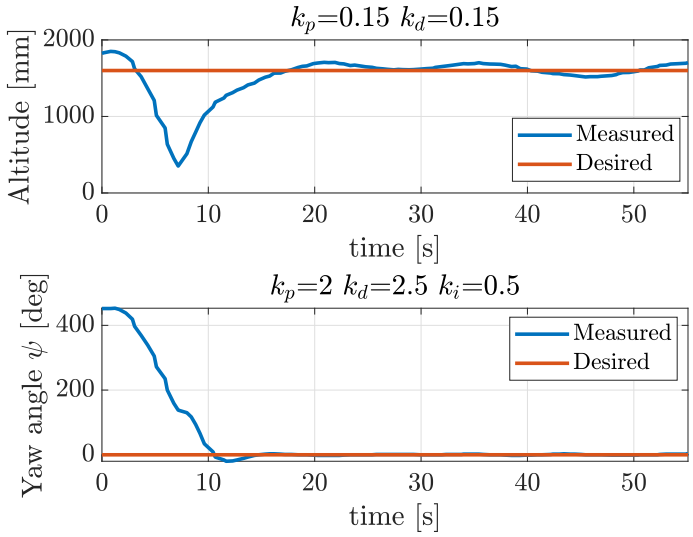

Figure 6.34: Station keeping test 3 results for the balloon 2.

stationary value. This time the desired value for the altitude has been set at 1600 mm while for the yaw angle always 0 degrees. Since the balloon 2 is more voluminous, this necessarily has a greater inertia and in fact we have noticed a greater slowness in the movements compared to the smaller balloon which, in the same test, proved to be more agile. This therefore translates into a slower response time. Hence, it is possible to notice from the three figures above that the rise time for the altitude passes from 5 seconds for balloon 1 to more than 10 seconds for balloon 2, while the yaw angle remains more reactive than the altitude with a rise time of about 5 seconds. Also in this case it can be seen from Figures 6.33 and 6.34 that in the initial instants of the control the balloon does not rise immediately, this is because we first established the telemetry contact and then we started the control through the app interface. As regards the settling time, also in this case we can see a time equal to about 30 seconds for the altitude because the response is around the steady state value, for the orientation after 20 seconds the yaw remains around the value 0 degrees not moving away with errors greater than 5%.

- **Balloon 2 (telemetry + motion capture)**

We will now also add the PhaseSpace motion capture system data. Only balloon 2 with a greater volume is able to raise the total mass of the system which is increased by the presence of the LED markers and the microdriver. The PhaseSpace system is a very advanced motion capture system with which it is possible to track a moving body with a frequency of 960 Hz. What we noticed from the experiments was that such a high frequency associated with not perfect calibration of the cameras can generate noise problems on the recorded signal. Therefore, in the data comparison between PhaseSpace tracking and telemetry, there are quite large localized discrepancies. The errors we are talking about cannot be associated with additive white Gaussian noise but there were two specific behaviors we experienced: *jumps* and *jitters*.

Jumps are relatively large discontinuities in the movement of a marker that can vary within a range of 1 cm to 10 cm. These jumps are caused by slight calibration errors that generate areas of the plotted space where tracking is incorrect. In particular, the jump can happen when the

marker passes from one area of visibility to another, therefore where the passage from the cone of one camera to another takes place. This causes the marker to pass short periods of time in both locations. In general, there is no unique method to remove the presence of jumps, however, definitely re-calibration can reduce the amount of jumps.

The jitter is another typical problem of position registration of the markers; it is always present in the measure with respect to the jumps that instead, take place in precise points of the space. The jitter problem is related to the behavior of cameras which are good detectors depending on how far away the marker is. The sub-pixel position noise of each detector produces this random jitter whose magnitude may also be due to some background interference affecting the detector's display of the marker or that the marker is viewed from a grazing angle. This type of errors can be solved instead of acting on the re-calibration of the cameras, rather in the post-processing phase of the data through the use of a low pass filter.

In Figure 6.35, before showing the result of the control for the balloon 2, we want to report the raw data of PhaseSpace underlining the presence of jumps and jitters in the measurement of the position of the LED markers. The same figure shows the smoothed data after applying a filter. The filter we used to smooth the data and remove noise is the 1D *median filter*. The median filter is a robust non-linear filter used for image and signal processing and its major advantage over linear filters is that the median filter can eliminate the effect of input noise. When using the median filter, it is necessary to specify an order which is a positive integer scalar. When n is odd $y(k)$ is the median of

$$x\left(k - \frac{n-1}{2} : k + \frac{n-1}{2}\right)$$

when n is even, $y(k)$ is the median of

$$x\left(k - \frac{n}{2} : k + \frac{n}{2}\right)$$

From now on we will therefore show the control results coming from PhaseSpace after applying the filtering explained above. For the same test that we have shown in Figure 6.35 we want to compare the results with the data coming from the on board telemetry for a scenario in which balloon 2 must maintain the altitude of 1600 mm. From Figure 6.36 it is possible to see that the two data are perfectly in agreement with each other, this shows us that the two data communication systems are well functioning and therefore we have the double check that the platform has performed that movement that has been seen in real time.

- **Motor input tests**

In the following tests reported in Figures 6.37, 6.38 and 6.39, we will show the station keeping experiment performed on the two balloons with the information of the input data of the motors exerting forces and torques in order to reach the desired position. The input data are dimensionless quantities ranging from -500 to 500 and represent the signal the controller sends to the Blimpduino actuators.

From figures 6.37, 6.38 and 6.39 it is possible to notice that the inputs that the on board controller calculates with the PD and PID control laws are continuous in time and tend to zero when the steady state is reached. The inputs of the motors are calculated by the on board controller in such a way that the errors tend to zero.

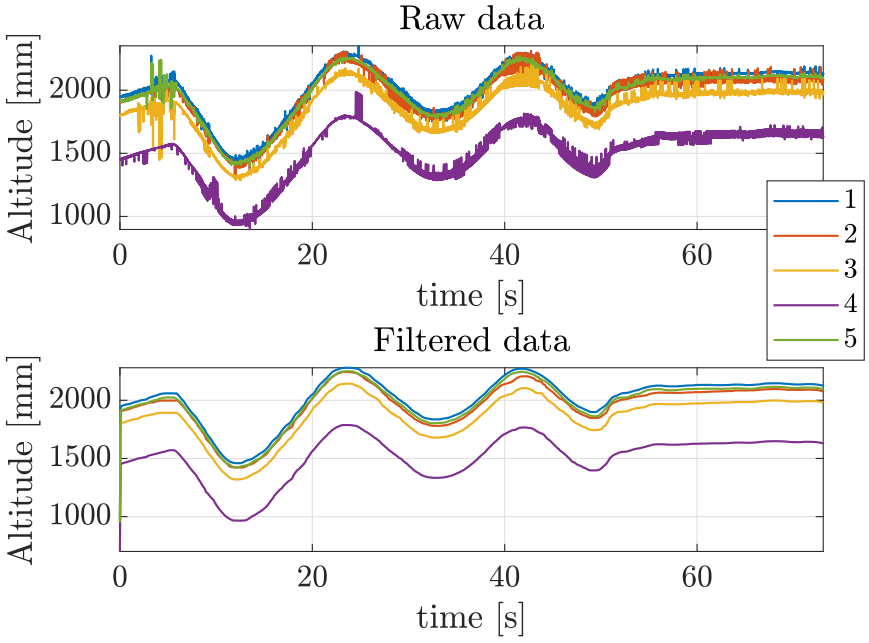

Figure 6.35: Comparison of raw data from PhaseSpace's tracking system and filtered data for the movement of 5 LED markers placed on the surface of the blimp balloon 2.

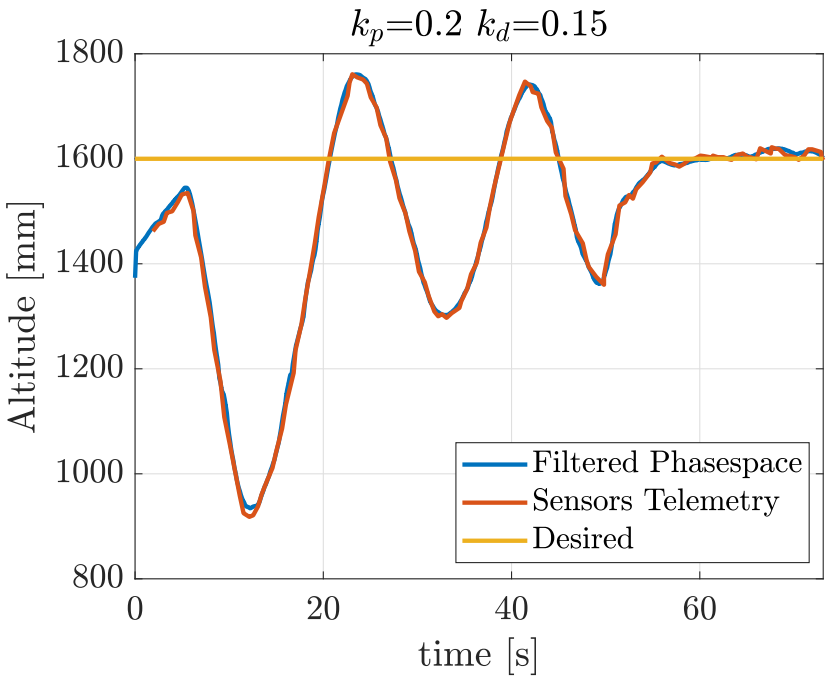

Figure 6.36: Comparison of on board telemetry data and PhaseSpace tracking data filtered with altitude control for balloon 2.

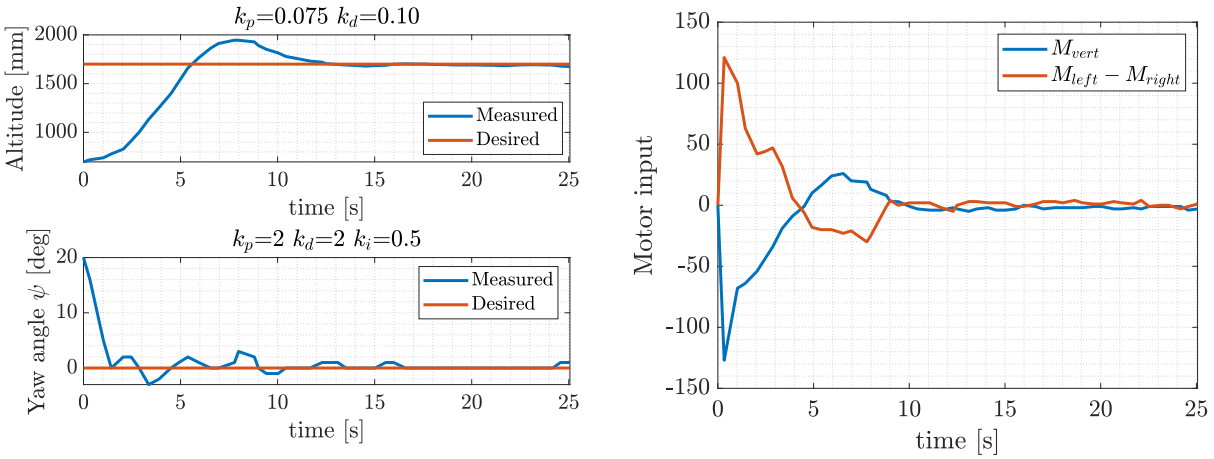

(a) **(b)**

Figure 6.37: Results of the station keeping test 1 for balloon 1, with the control of the altitude and the yaw angle as a function of the time in which the value measured by the on board telemetry is compared with the desired steady state (a). Input of the motors as the time varies for the station keeping test in which the trend of the vertical motor thrust and the torque around the yaw motion are compared (b).

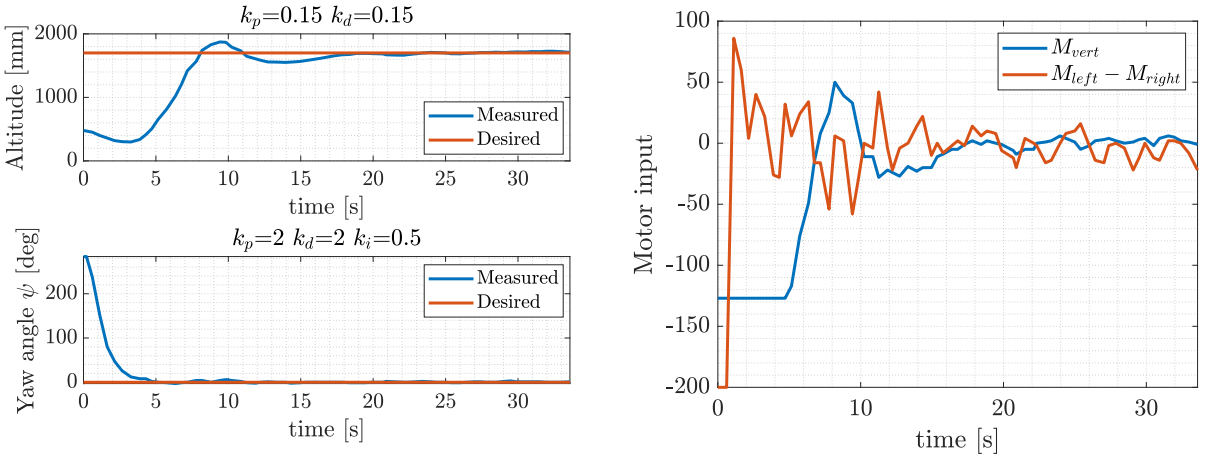

(a) **(b)**

Figure 6.38: Results of the station keeping test 2 for balloon 1, with the control of the altitude and the yaw angle as a function of the time in which the value measured by the on board telemetry is compared with the desired steady state (a). Input of the motors as the time varies for the station keeping test in which the trend of the vertical motor thrust and the torque around the yaw motion are compared (b).

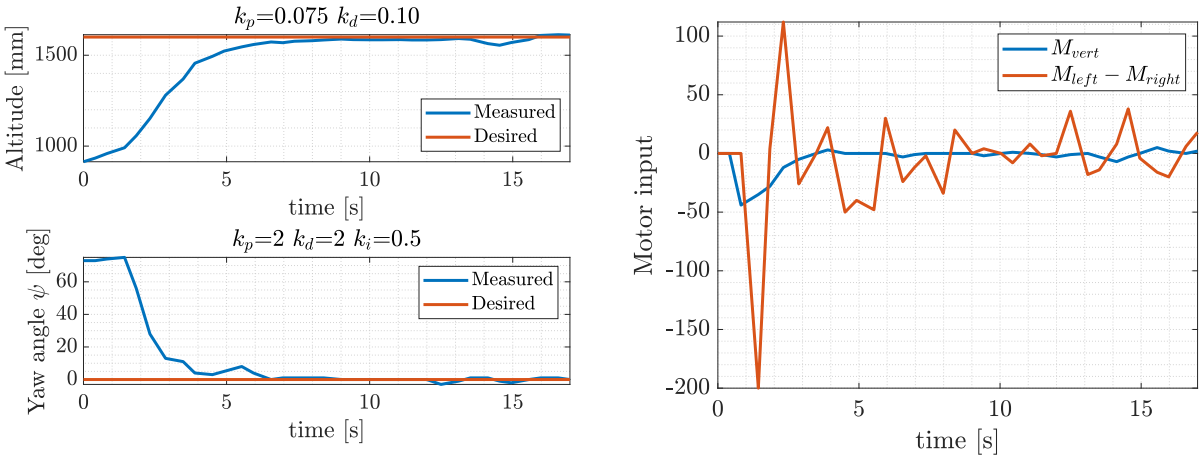

Figure 6.39: Results of the station keeping test for balloon 2, with the control of the altitude and the yaw angle as a function of the time in which the value measured by the on board telemetry is compared with the desired steady state (a). Input of the motors as the time varies for the station keeping test in which the trend of the vertical motor thrust and the torque around the yaw motion are compared (b).

- **Simulation and test comparison**

The last result we want to show concerns the comparison between the station keeping test carried out and the simulation of the same scenario based on the numerical integration of the equations of motion that we have reported in the section 6.5. In the simulation we will reproduce the same test and compare the trends of the altitude and the yaw angle over time. We discovered that the two trends are in agreement with each other. This shows us that the parameters used in the dynamics that have been determined downstream of the identification of the parameters (section 6.3) are exact and the equations of motion of the dynamics model reproduce exactly what also happens in reality. The accuracy of the dynamic model guarantees us to be able to predict and simulate motion scenarios of the blimp.

In Figure 6.40 we can see that the MATLAB software that numerically integrates the equations of motion with the use of the parameters of the Blimpduino that we have estimated, faithfully reproduces the trend of the altitude and of the yaw angle over time after the application of the PD control law for altitude and PID for yaw angle. The gains were obviously kept identical between the simulation and the on board controller installed in the Arduino. This result shows us that the analytical model of the equations of motion, built on the basis of our indoor blimp, correctly represents the dynamics of the system and allows us to predict the motion following the application of a certain force and moment.

6.6 Conclusion

In this final chapter we have reported all the activities and results that was carried out during the internship period at CERN. In this great opportunity that I had, it was possible for me to build, assemble and test a real blimp.

The first activities carried out were to assemble the blimp and 3D print the missing components such as the gondola. Furthermore, the functioning of Blimpduino was analyzed in detail and small

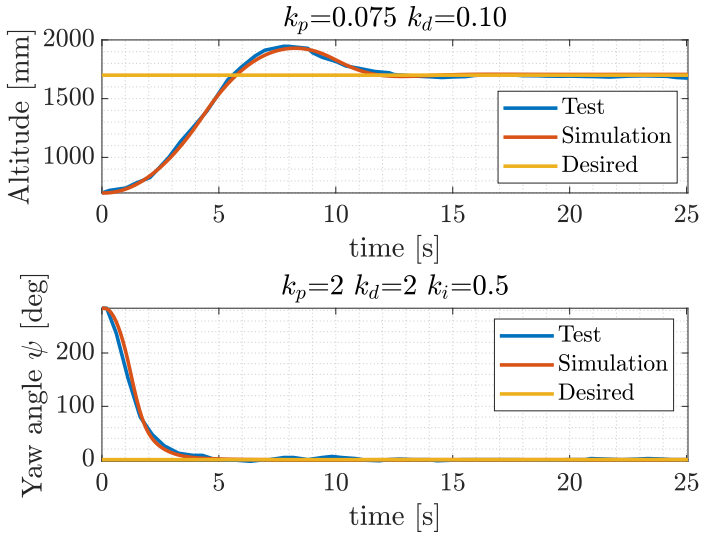

Figure 6.40: Comparison between the station keeping test and the MATLAB numerical simulation for balloon 1.

changes were applied to its flight software implemented in the Arduino board. These changes involved the application of a filter to the LIDAR measurements, the modification of the altitude and yaw angle controller by inserting preset steady state values and changing the gains of the controllers, finally the creation of a wireless communication channel for sending the telemetry of the on board sensors to a computer for post-processing of the data.

Before testing the platform for the first time, the parameter identification process was carried out with which all the parameters that appear in the dynamics equations of the system are determined. To do this, in addition to the measurement and weight of the physical components, a Blimpduino CAD model in CATIA has also been created through which it was possible to determine the inertia and the CG.

The other fundamental activity carried out was that of setting the environment in which to perform the test. This was done in a CERN laboratory that houses a cleanroom with constant environmental conditions where there is no presence of magnetic field or other disturbances. This choice is indeed based on a preliminary study of the problem since as we know the final purpose of the mission will be to fly the blimp inside a harsh environment such as that characterized by a high magnetic field. However, even before testing the disturbance that will act on the blimp, it was necessary to become familiar with the operation of the platform without the presence of disturbances. Once we have become experts on the control and dynamics of the system then we will face the test of the platform in another scenario. A motion tracking system was implanted inside the laboratory. To put it into operation the PhaseSpace system was necessary to go through several steps such as calibration, alignment and the creation of a triad body to be tracked. In the setting phase we also realized that the original Blimpduino balloon was not able to lift the total weight including the additional mass due to the motion tracking system. This led us to the adoption of a new balloon that had a greater volume and therefore a greater buoyancy force.

With all the complete settings and with the assembled system, we carried out the control tests based on the station keeping strategy which ensures that the system maintains a fixed altitude and orientation. The test results were satisfactory for both balloons and several tests were done as the

controllers' gains varied. It was also necessary to carry out a post-processing on the data of the motion capture system due to the presence of jumps and jitters on the temporal sequences of the motion.

The last activity carried out was to compare the results of one of the real tests with the analogous test simulated through the numerical integration of the dynamics with the use of the real parameters of Blimpduino previously obtained. The results of this comparison are very satisfying and show us that the flight code implemented on MATLAB allows us to correctly predict the real behavior of the blimp.

What has been done so far in the context of the blimp robotic system has been something preliminary which, however, has allowed us to learn many things about the operation and control of this kind of platform. Future implementations will surely lead us to the design of a new system, more performing and robust to the type of disturbance to which it is subject. Furthermore, an improvement that can be achieved is to communicate with the tracking system in real time through the use of its API which, through a Python code, can provide in real time on a computer the position of the blimp in space. Another important future development will be to move the control to a ground computer that can send the control law on board in real time based on the positions provided by the motion capture system.

Chapter 7

Conclusion and Future Works

In this thesis we have studied the problem of the dynamic interaction of an indoor blimp inside the magnetic environment of the FCC-hh detector cavern at CERN. Furthermore, we have developed and built a real blimp with which we have performed some control tests in an environment free from magnetic disturbances. The thesis work is divided into a first theoretical part where all the tools necessary for the study of the problem are provided and all the simulations that have been carried out are shown. Finally the practical part of the thesis is reported, this is related to my internship period at CERN in Engineering Office (EO) section of the Detector Technologies (DT) group in the Experimental Physics (EP) department. This part shows all the activities we have done and the test results. Let's now retrace the contents present in the various chapters and appendices, outlining the results and possible future developments.

Chapter 1 introduces the definition of the problem to which the thesis work is addressed and the motivation for studying robotics in a harsh environment is explained in the context of the EP R&D. In this case it is also explained why the choice of the blimp as the optimal solution to the problem.

Chapter 2 presents the development of the mathematical model of an indoor blimp through which it is possible to describe the motion with the equations of kinematics and dynamics. In order to be able to write the complex system of equations of motion, general simplifying hypotheses are assigned that allow modeling the behavior of a mini airship. In the development of the dynamic model we have only reported the fundamental terms of the equations without deriving them. This work is postponed in Appendix A where the demonstration and the steps necessary to arrive at the complete dynamic model are reported.

Chapter 3 introduces the problem of magnetic disturbance acting on the indoor blimp inside the detector cavern. In particular, we focused on the study of brushless electric motors as an element of interaction between blimp and physical environment. To understand what kind of interaction these motors can have when immersed in an external field, it was necessary to understand their operating principle. Once this was understood, the first activity carried out was that of characterizing the motor from a magnetic point of view by calculating the external residual magnetic field; this was done with static electromagnetic simulation software which is FEMM. By calculating the residual external magnetic field we compared this with that generated by a magnetic dipole and from the comparison between the two, we came to the conclusion that it is possible to represent and characterize a motor, seen from the outside, as a magnetized object that has a global magnetic moment

which depends on its internal components. To better understand the behavior of a motor and its interaction with an external field we have refined our simulation using the CST software, imagining a scenario in which the motor is rotated within a uniform magnetic field. From the calculation of the torques acting on its internal components it was deduced that the magnetic moment is determined by two contributions (permanent magnet of the inner rotor and external stator ferromagnetic cover). Furthermore, by carrying out the same simulation as the motor parameters vary, we have seen how the torque acting on the components varies with the dimension of the internal magnet and the value of the external field. This simulation was designed to be reproduced in a real test in which an electric motor is placed on a rotating plate immersed in the uniform magnetic field of a magnet and the torque value was recorded for each angle of rotation with a specific instrument. This is certainly a future development of this thesis which needs to further investigate the problem of the magnetic interaction of motors within a high non uniform magnetic field.

The next future steps will concern the refinement of the simulations with more details in the modeling of the motors and the carrying out of tests with real BLDC motors in order to confirm what the simulations will show. In particular, what is not taken into account in the modeling is the rotation of the rotor during the functioning of the motors itself. This rotation, which is the basis of the operation of an electric motor, involves a consequent rotation of the magnetic moment of the rotor, which in turn will rotate the global moment of the motor. If the moment of the external cover is fixed in direction then, the final result could be that of a preceding motion of the total moment around the axis of the motor. Even these assumptions should be verified with suitable experimental tests.

One possible solution to the problem of the interaction between electric motor and external magnetic field would be that of the so-called *magnetic shield*. Magnetic shielding involves the use of shields made of materials with high magnetic permeability. The materials used can be metal alloys such as permalloy and mumetal sheets or nanocrystalline grain structures such as ferromagnetic metal coatings. However, these materials do not block the magnetic field, but rather draw it into themselves, creating preferential paths for the magnetic field lines which then bypass the shielded volume and thicken in the shield layer. For this reason, the problem of blimp demagnetization is something difficult to obtain because in this case we will always have the presence of a highly permeable material which will therefore be characterized by its own magnetic moment that interacts with the external field. Furthermore, the effectiveness of the shielding should be studied, this depends on the permeability of the material used, which decreases both for very low and very high fields where saturation is reached, in this last case, the solution concerns the use of shields made by several layers, one on top of the other, which gradually reduce the field for the next underlying layer. Another method of passive magnetic shielding could be that which exploits the Meissner effect through the use of superconducting materials. The Meissner effect concerns the ejection of a magnetic field from a superconductor when it is below the critical temperature. Passive shielding, however, could have negative consequences linked to the weighting of the motors and therefore of the whole system. These techniques could actually shield only the motors but they themselves would be highly magnetic volumes that would raise the question of magnetizing the blimp again. Due to the aforementioned limitations of passive shielding, an alternative could be that of active shielding. This technique is often used with static or low-frequency fields and involves the use of elements that generate electromagnetic fields that can cancel the locally present field. An example

could be solenoids or Helmholtz coils. From this we understand that the study of electric motors in magnetic fields is a still open topic that had not been addressed until now and whose future developments are numerous.

Chapter 4 analyzes and studies the physical environment in which the blimp will fly, which is the future detector cavern of FCC-hh. After having framed the project of the future particle accelerator within the CERN programs, we moved on to describe the structure of the detector and in particular its magnetic field source which consists in a system of three solenoids that generates a field of intensity of 4 T. This was crucial in order to be able to virtually map the magnetic field throughout the space. This data is fundamental to then estimate the magnetic disturbance of the blimp in that environment. With the use of software simulations (FEMM and CST) it was possible to model the solenoid system in order to generate the magnetic field that will be present in that area, both inside and outside the detector system. We were able also to report the value of the magnetic field in particular cutting planes and in particular directions. With these results, we have become familiar with what will be the orders of magnitude of the field that will have to be mapped by the blimp and which in turn will disturb it with the action of forces and torques on the electric motors. We also reported the value of the field gradient and the value of magnetic forces and torques resulting from the interaction of a magnetic dipole with a non-uniform field. Finally we discussed and developed a method for the generation of a trajectory given the initial and final points of the motion with the information of particular via points that the blimp will have to cross.

Regarding the future developments of this topic, although the estimate of the field is not exact given that it comes from the simulation and modeling of the detector on a software, the element of greatest weakness in the accuracy of the estimation of magnetic interactions comes from the knowledge of the magnetic moment of the motor. The limitation of our study was to have imagined that the entire robotic system had a magnetic moment vector with particular components on the body axes of the blimp. With these components, the force and torque resulting from the dynamic interaction with the field was calculated. However, a preliminary estimate still remains, since in fact the disturbance should be considered individually on the total number of electric motors, and based on their position these provide a particular disturbance calculated with respect to the body-fixed frame. Therefore, the topic of greatest interest remains that of being able to magnetically and dynamically model an electric motor in order to consequently know what interactions with the outside world are and in particular those of the magnetic type. Another strong hypothesis we made during the development of these analyzes was to consider that the magnetic moment of the motors was constant over time, this is not completely true as the blimp that moves in space encounters variable values of magnetic field both in module and in direction. However the hypothesis that the moment remains constant can be accepted by the fact that the motion of the blimp is very slow with respect to the spatial variation velocity of the field that is its spatial gradient. The behavior of the magnetization of the cover when the external field varies has been shown in the Chapter 3 but future developments may concern the modeling of this phenomenon.

Chapter 5 analyzes the problem of stability and control of indoor blimps. After having reported the state of the art of the control of mini airships with the control techniques that have been used in other projects, it was decided to linearize the equations of motion with the construction of two linear and decoupled models that describe the longitudinal and lateral motion. Therefore, on the basis of the linear models, two typical controllers were chosen which are the PID and LQR through which a

control MATLAB simulation was carried out in the case of trajectory tracking for a simple scenario in which the blimp rises vertically up to a certain altitude and then runs the length of the detector and then descends to the ground. In this case, the magnetic disturbance acting on the blimp at every point of the current trajectory was also taken into account. Also in this case we considered a magnetic dipole moment constant over time and fixed with respect to the body reference. This control study is a preliminary simulation of what true blimp control will be. Therefore, the purpose of the mission will be rather to move in space and by keeping a particular point fixed, perform the magnetic field measurement.

Chapter 6 describes all the activities and results obtained during the internship period at CERN. First of all it presents the real blimp that has been chosen to test, which is the Blimpduino 2 from jjrobots. In particular, it has been shown all the steps that led to the assembly of the entire system such as the 3D printing of the gondola, the assembly of the motors, the battery and the on-board card. In addition, the way in which the blimp is controlled is also specified, which is via an app interface that communicates wireless with an WiFi module installed in an Arduino board. The control used for this platform was the PID type with the use of the measurements of two sensors for the altitude and for the yaw angle. Then there were activities to establish a communication system through which it was possible to follow the motion of the blimp. This happened with the sending of on board telemetry and the real time streaming of the blimp positions through a motion capture system. Before testing the blimp, a careful analysis of the identification of the parameters was carried out in order to build a software that could simulate the true motion of the system through the use of the equations of motion obtained from the dynamics. The identification of the parameters involved both the physical dimensions of the system and the CAD modeling for the estimation of some fundamental parameters such as inertia. Finally, all the setup activity of the experiment was shown in which the fundamental part was to put the PhaseSpace motion capture system into operation, which involved the setting of the cameras, the creation of a communication server, the calibration and alignment of the system and finally the setting of the tracking data stream. The test was carried out in a cleanroom laboratory at CERN without the presence of magnetic disturbances and involved a station keeping experiment in which the blimp had to keep a certain altitude and a certain yaw angle fixed over time. This experiment was also simulated analytically in which the simplified mathematical model with which the motion of the system was reproduced is reported. The test was performed with two balloons of different sizes as the presence of additional masses linked to the motion capture system did not allow the original balloon (32 inches) to be able to lift the mass despite the maximum thrust of the motors. The test results were satisfactory and also in relation to the comparison between the two tracking methods whose measurements are in agreement. Regarding the motion capture system, it is also explained that there was the need to clean up the PhaseSpace signal from noise and errors related to the calibration of the cameras. Finally, the same test was simulated numerically with the use of the dynamics equations and the parameters of the true blimp, the results compared are in perfect agreement. This shows that the mathematical model used represents very well what happens in reality.

On this last very interesting practical part there are numerous future developments that will have to be addressed within the WP4 of the EP-DT-EO R&D group. What we analyzed in this chapter was the problem of controlling a blimp without the presence of disturbances. The choice to buy a COTS platform and test its operation by inserting small changes to the flight software was

dictated by the fact that having no experience in the field of LTA robots, the CERN robotics team preferred to use a system already present on the market and functioning to become familiar with its operation and perform tests to understand if it was actually the optimal choice for the type of mission required. Obviously in a future development of the robotics project this type of system will be designed from scratch, modified to fulfill the mission requirements. A first change to be made will be on the Blimpduino motors, which currently can exert a very low maximum thrust and this was noticed when with the addition of the tracking system mass, the blimp was unable to lift its own weight even with the presence of buoyancy force.

Furthermore, the design of the gondola will certainly be changed to make it even lighter and at the same time resistant. The modification on the gondola may be dictated by the choice of a possible additional motor (four instead of three). This possibility could allow us to have an actuation on the lateral degree of freedom as for now with the three motors configuration the system is said to be under-actuated. The architecture could also have five motors as suggested in [94] with the presence of two vertically mounted motors used to change the altitude, two horizontal motors which enable the blimp to fly horizontally and change the heading angle, finally one side-way motion motor used to move laterally. Another hypothesis for the choice of the actuation system could be that suggested by [98] in which, with a combination of propeller motors positioned on the balloon, forces and moments are generated which guarantee an action on all six degrees of freedom. This goal is achieved with the use of eight motors.

The use of the Arduino board is instead an optimal choice because it is easy to implement and modify. The future intent regarding the development of the flight software, however, will be to move the brain that calculates the control not on board but on the ground with the use of a computer that would make the computing power significantly greater than that of the Arduino board, which would be limited only to read the force and moment value received in real time by the controller present in the computer and to send it to the actuators. Furthermore, the controller implemented in the ground computer could base the calculation of the control law not on the basis of the measurements of the on-board sensors sent by the telemetry but on the value of the positions and orientations measured by the motion capture system which have a much higher sampling frequency and better accuracy as long as the system is clearly visible and the cameras are well calibrated.

In this context, therefore, it is necessary to use the PhaseSpace system API in which with a Python code it is possible to obtain in real time the status of the system that can be used both to calculate the controls to be sent on board, and to generate graphs in real time of the position of the blimp in space. This activity was started in my internship period in which we were able to make the PhaseSpace system communicate in real time with Python by generating graphs of the respective positions of the LED markers as a function of time. This code will have to be improved in order to also generate the control forces and torques based on the same PhaseSpace positions to be sent on board with an Arduino WiFi connection.

Another question still open is precisely on the system of communication and tracking. With the experiments we have shown that the motion capture system works correctly and it is possible to track the position of the blimp that moves in space when in visibility of the cameras. However, this last point is crucial in future developments and in particular in the application of the blimp control inside the detector cavern. In that case, since the environment is very large and full of obstacles, it will be necessary to imagine how it could be possible to extend and implant the motion capture

system inside the cavern, also in relation to the fact that many more cameras could be needed compared to the eight we have used, and the positioning of the same will have to be studied in detail.

Alternatively, one could think of a different localization system from the one used up to now. In fact, it could be possible to make use of IPS which consists of a network of devices used to locate objects or people in places where it is not possible to use GPS satellite technology, that is, in closed and shielded places such as the detector cavern. There are many indoor positioning techniques that make use of smartphones, WiFi antennas, Bluetooth, digital cameras and clocks.

Another development belonging to the study of the control of the blimp within the high magnetic field environment would be to use a control system in addition to that of the propeller motors, that is, a system of very large coils that mounted around the balloon can interact with the magnetic field through their dipole moment thus providing the forces and torques on the system necessary for movement and attitude control. This is also a possible future development that we can think of analyzing to exploit the presence of the field and make it a useful source for controlling the platform. The coils can be powered by currents which generate dipole moments suitable for keeping the blimp in a determined position.

Ultimately, the final scenario to be achieved for this mission would be to have a swarm of blimps flying together inspecting space, taking measurements and communicating with each other. In this case a wireless network should be installed between all UAV's and with a ground station that collects downlink data and sends uplink data. In doing this, it may be necessary to develop optimization algorithms for the UAV's trajectories and for power transmission as suggested by [29].

Bibliography

[1] J. A. E. Bryson and Y.-C. Ho. *Applied Optimal Control*. Hemisphere Publishing Corporation, 1975.

[2] A. S. Abada A., Abbrescia M. and others. Fcc-hh: The hadron collider. *The European Physical Journal Special Topics*, 228(4):755–1107, Jul 2019.

[3] A. P. Aguiar and J. P. Hespanha. Trajectory-tracking and path-following of underactuated autonomous vehicles with parametric modeling uncertainty. *IEEE Transactions on Automatic Control*, 52(8):1362–1379, 2007.

[4] R. Al-Jarrah and H. Roth. Design blimp robot based on embedded system and software architecture with high level communication and fuzzy logic. In *2013 9th International Symposium on Mechatronics and its Applications (ISMA)*, pages 1–6, 2013.

[5] M. Z. Ashraf and M. A. Choudhry. Dynamic modeling of the airship with matlab using geometrical aerodynamic parameters. *Aerospace Science and Technology*, 25:56–64, 2013.

[6] G. M. Atmeh. *Guidance And Control Of Unmanned Airships For Waypoint Navigation In The Presence Of Wind*. PhD thesis, Aerospace Engineering, 2012.

[7] F. N. S. Authority. *French Nuclear Regulation*. Autorité de sûreté nucléaire, 2012.

[8] J. R. Azinheira, A. Moutinho, and E. C. de Paiva. A backstepping controller for path-tracking of an underactuated autonomous airship. *International Journal of Robust and Nonlinear Control*, 19:418–441, 2009.

[9] K. Baltzis. The femm package: A simple, fast, and accurate open source electromagnetic tool in science and engineering. *Journal of Engineering Science and Technology Review*, 1, 06 2008.

[10] K. Baltzis. The finite element method magnetics (femm) freeware package: May it serve as an educational tool in teaching electromagnetics? *Education and Information Technologies*, 15:19–36, 03 2010.

[11] I. Barbalat. Systems d'equations differentielles d'oscillations nonlinéaires. *Revue Roumaine de Mathématique Pures et Appliquées*, 4(2):267–270, 1959.

[12] G. Battistoni and others. Overview of the FLUKA code. *Annals Nucl. Energy*, 82:10–18, 2015.

[13] E. Bayraktar. *Design And Control Of An Autonomous Blimp*. PhD thesis, Department of Mechatronics Engineering, 2013.

[14] A. K. Bejczy. *Robot arm dynamics and control.* Jet Propulsion Laboratory Technical Memo 33–669, 1974.

[15] L. Beji and A. Abichou. Tracking control of trim trajectories of a blimp for ascent and descent flight manoeuvres. *International Journal of Control*, 78(10):706–719, 2005.

[16] M. Benedikt, A. Blondel, O. Brunner, M. Capeans Garrido, F. Cerutti, J. Gutleber, P. Janot, J. M. Jimenez, V. Mertens, A. Milanese, K. Oide, J. A. Osborne, T. Otto, Y. Papaphilippou, J. Poole, L. J. Tavian, and F. Zimmermann. Future Circular Collider - European Strategy Update Documents. Technical report, CERN, Geneva, Jan 2019.

[17] M. Benedikt, M. Capeans Garrido, F. Cerutti, B. Goddard, J. Gutleber, J. M. Jimenez, M. Mangano, V. Mertens, J. A. Osborne, T. Otto, J. Poole, W. Riegler, D. Schulte, L. J. Tavian, D. Tommasini, and F. Zimmermann. Future Circular Collider - European Strategy Update Documents. Technical report, CERN, Geneva, Jan 2019.

[18] S. Bermudez i Badia, P. Pyk, and P. Verschure. A biologically based flight control system for a blimp-based uav. In *Proceedings of the 2005 IEEE International Conference on Robotics and Automation*, pages 3053–3059, 2005.

[19] N. Bessert and O. Frederich. Nonlinear airship aeroelasticity. *Journal of Fluids and Structures*, 21:731–742, 12 2005.

[20] E. N. J. Brian L. Stevens, Frank L. Lewis. *Aircraft Control and Simulation: Dynamics, Controls Design, and Autonomous Systems.* John Wiley & Sons, 3 edition, 2015.

[21] CERN. `https://ep-dep-dt.web.cern.ch/`.

[22] CERN Experimental Physics Department. *Strategic R&D Programme on Technologies for Future Experiments*, 2021.

[23] C. G. A. Chae H. An and J. Hollerbach. *Model-Based Control of a Robot Manipulator.* The MIT Press, 1988.

[24] M. Chari and S. Salon. *Numerical Methods in Electromagnetism.* Academic Press, 2000.

[25] I. C. Cheeseman. Fluid-dynamic drag: Practical information on aerodynamic drag and hydrodynamic resistance. hoerner fluid dynamics. *The Aeronautical Journal*, 80(788), 1976.

[26] J. J. Craig. *Introduction to Robotics: Mechanics and Control, Ed.3.* Pearson, 2005.

[27] T. D. Crouch. *Lighter Than Air: An Illustrated History of Balloons and Airships.* Johns Hopkins University Press, 2009.

[28] H. Curtiss, D. Hazen, and W. Putman. Lta aerodynamic data revisited. *Journal of Aircraft*, 13:835–844, 1976.

[29] L. De Simone, Y. Zhu, W. Xia, T. Dagiuklas, and K. K. Wong. Multi-agent learning approach for uavs enabled wireless networks. In *2021 13th International Conference on Wireless Communications and Signal Processing (WCSP)*, pages 1–6, 2021.

[30] K. U. Devi and M. Y. Sanavullah. Performance analysis of exterior(outer) rotor permanent magnet brushless dc (erpmbldc) motor by finite element method. *2011 3rd International Conference on Electronics Computer Technology*, 3:426–430, 2011.

[31] P. Dorato, V. Cerone, and C. Abdallah. *Linear-Quadratic Control: An Introduction*. Simon & Schuster, Inc., 1994.

[32] A. H. B. Drury. *Electric Motors and Drives. Fundamentals, Types and Applications*. Newnes, 2013.

[33] O. I. Elgerd. *Control Systems Theory*. McGraw-Hill, 1967.

[34] A. Ferrari, P. R. Sala, A. Fasso, and J. Ranft. FLUKA: A multi-particle transport code (Program version 2005). Technical report, INFN, 2005.

[35] T. I. Fossen. *Guidance and Control of Ocean Vehicles*. Wiley, 1994.

[36] G. F. Franklin, D. J. Powell, and A. Emami-Naeini. *Feedback Control of Dynamic Systems*. Prentice Hall PTR, 4th edition, 2001.

[37] M. T. Frye, S. M. Gammon, and C. Qian. The 6-dof dynamic model and simulation of the tri-turbofan remote-controlled airship. In *2007 American Control Conference*, pages 816–821, 2007.

[38] T. Fukao, K. Fujitani, and T. Kanade. An autonomous blimp for a surveillance system. In *Proceedings 2003 IEEE/RSJ International Conference on Intelligent Robots and Systems (IROS 2003) (Cat. No.03CH37453)*, volume 2, pages 1820–1825 vol.2, 2003.

[39] T. Fukao, K. Fujitani, and T. Kanade. Image-based tracking control of a blimp. In *42nd IEEE International Conference on Decision and Control (IEEE Cat. No.03CH37475)*, volume 5, pages 5414–5419 Vol.5, 2003.

[40] E. Furlani. *Permanent Magnet and Electromechanical Devices, Materials, Analysis, and Applications*. Academic Press, 2001.

[41] S. Gomes. *An investigation into the flight dynamics of airships with application to the YEZ-2A*. PhD thesis, Cranfield Institute of Technology, 1990.

[42] W. Gracey. The additional-mass effect of plates as determined by experiments. Technical report, University of North Texas Libraries, UNT Digital Library, 1941.

[43] D. J. Griffiths. *Introduction to Electrodynamics*. Cambridge University Press, 4 edition, 2017.

[44] D. C. Hanselman. *Brushless Permanent Magnet Motor Design*. Magna Physics Pub, 2006.

[45] E. Hygounenc, I.-K. Jung, P. Souères, and S. Lacroix. The autonomous blimp project of laas-cnrs: Achievements in flight control and terrain mapping. *I. J. Robotic Res.*, 23:473–511, 04 2004.

[46] ICRP. The 2007 Recommendations of the International Commission on Radiological Protection. *ICRP Publication*, 103(37), 2007.

[47] A. IDE. `https://www.arduino.cc/`.

[48] F. H. Imlay. The complete expressions for added mass of a rigid body moving in an ideal fluid. In *Tecnical Report David Taylor Model Basin Washington DC*, 1961.

[49] J. D. Jackson. *Classical Electrodynamics*. Wiley, 2 edition, 1975.

[50] jjrobots. `https://www.jjrobots.com/blimpduino-2/`.

[51] jjrobots. `https://www.jjrobots.com/blimpduino-assembly-guide/`.

[52] H. C. S. Joachim Stöhr. *Magnetism*. Springer, 2006.

[53] L. P. Kaelbling, M. L. Littman, and A. W. Moore. Reinforcement learning: A survey. *Journal of Artificial Intelligence Research*, 4:237–285, 1996.

[54] H. K. Khalil. *Nonlinear systems; 3rd ed.* Prentice-Hall, Upper Saddle River, NJ, 2002.

[55] J. Ko, D. J. Klein, D. Fox, and D. Haehnel. Gaussian processes and reinforcement learning for identification and control of an autonomous blimp. In *Proceedings 2007 IEEE International Conference on Robotics and Automation*, pages 742–747, 2007.

[56] R. Krishnan. *Permanent Magnet Synchronous and Brushless DC Motor Drives*. CRC Press, 2010.

[57] U. Kumaravelu and S. Yakub. Simulation of outer rotor permanent magnet brushless dc motor using finite element method for torque improvement. *Modelling and Simulation in Engineering*, 2012, 08 2012.

[58] H. Lamb. Hydrodynamics. *Cambridge University Press, London*, 1932.

[59] M. G. Lara. Sensorless brushless dc motors. development and comparison of different fault tolerant control algorithms. Master's thesis, Corso di Laurea in Ingegneria Aerospaziale, Politecnico di Torino, 2018.

[60] J. LaSalle and S. Lefschetz. *Stability by Liapunov's Direct Method with Applications*. Academic Press, New York, 1961.

[61] C. Lee. Fuzzy logic in control systems: fuzzy logic controller. i. *IEEE Transactions on Systems, Man, and Cybernetics*, 20(2):404–418, 1990.

[62] A. Liapounoff. Problème général de la stabilité du mouvement. *Annales de la Faculté des sciences de Toulouse : Mathématiques*, 2e série, 9:203–474, 1907.

[63] E. Magnetics. `https://www.eclipsemagnetics.com/`.

[64] B. Markiewicz. *Analysis of the computed torque drive method and comparison with conventional position servo for a computer-controlled manipulator*. Jet Propulsion Laboratory Technical Memo 33–601, 1973.

[65] Maxon. Maxon brushless dc motors. `https://www.maxongroup.co.uk/maxon/view/content/Overview-brushless-DC-motors`.

[66] D. Meeker. *Finite Element Method Magnetics*, version 4.2 edition, 5 2020.

[67] A. Moutinho and J. Azinheira. Stability and robustness analysis of the aurora airship control system using dynamic inversion. In *Proceedings of the 2005 IEEE International Conference on Robotics and Automation*, pages 2265–2270, 2005.

[68] M. M. Munk. *Aerodynamics of Airships*, pages 32–48. Springer Berlin Heidelberg, 1936.

[69] E. Okafor, P. Okon, and C. C. Okoro. Magnetic field mapping of a direct current electrical machine using finite element method. *Journal of Applied Sciences Research*, 5(11):1889–1898, 2009.

[70] R. Parker. *Advances in Permanent Magnetism*. John Wiley and Sons, 2 edition, 1990.

[71] R. P. Paul. *Modelling, trajectory calculation and servoing of a computer controlled arm*. Stanford University Artificial Intelligence Laboratory, 1972.

[72] D. E. Perrault, N. Bose, S. D. O'Young, and C. D. Williams. Sensitivity of auv added mass coefficients to variations in hull and control plane geometry. *Ocean Engineering*, 30:645–671, 2003.

[73] PhaseSpace. `https://www.phasespace.com/`.

[74] V. M. Popov. *Hyperstability of Control Systems*. Springer-Verlag Berlin Heidelberg, 1973.

[75] D. Psaltis, A. Sideris, and A. Yamamura. A multilayered neural network controller. *IEEE Control Systems Magazine*, 8(2):17–21, 1988.

[76] J. Rao, Z. Gong, J. Luo, Z. Jiang, S. Xie, and W. fa Liu. Robotic airship mission path-following control based on ann and human operator's skill. *Transactions of the Institute of Measurement & Control*, 29:15 – 5, 2007.

[77] J. Rao, Z. Gong, J. Luo, and S. Xie. A flight control and navigation system of a small size unmanned airship. In *IEEE International Conference Mechatronics and Automation, 2005*, volume 3, pages 1491–1496 Vol. 3, 2005.

[78] W. Riegler. Fcc-hh detector, fcc cdr summary report, status of detailed reportr. `https://indico.cern.ch/event/727555/contributions/3461232/attachments/1869213/3075082/fcc_hh_detector_brussels_june_2019_riegler.pdf/`.

[79] A. Rottmann, C. Plagemann, P. Hilgers, and W. Burgard. Autonomous blimp control using model-free reinforcement learning in a continuous state and action space. In *2007 IEEE/RSJ International Conference on Intelligent Robots and Systems*, pages 1895–1900, 2007.

[80] S. Sagatun and T. Fossen. Lagrangian formulation of underwater vehicles' dynamics. *Conference Proceedings 1991 IEEE International Conference on Systems, Man, and Cybernetics*, pages 1029–1034 vol.2, 1991.

[81] J. Sankaran. *Real-time computed torque control of flexible-joint robots*. PhD thesis, Department of Mechanical and Industrial Engineering, University of Toronto, 1997.

[82] Y. B. Sebbane. *Lighter than Air Robots*. Springer Netherlands, 2012.

[83] J. Severholt. *Generic 6-DOF Added Mass Formulation for Arbitrary Underwater Vehicles based on Existing Semi-Empirical Methods*. PhD thesis, Aeronautical and Vehicle Engineering, Naval Systems., 2017.

[84] J. E. Slotine and W. Li. *Applied Nonlinear Control*. Prentice-Hall, Englewood Cliffs, NJ, 1991.

[85] J.-J. Slotine and L. Weiping. Adaptive manipulator control: A case study. *IEEE Transactions on Automatic Control*, 33(11):995–1003, 1988.

[86] The CLIC Collaboration. Clic Conceptual Design Report. Technical Report February, CERN, 2012.

[87] S. van der Zwaan, A. Bernardino, and J. Santos-Victor. Vision based station keeping and docking for an aerial blimp. In *Proceedings. 2000 IEEE/RSJ International Conference on Intelligent Robots and Systems (IROS 2000) (Cat. No.00CH37113)*, volume 1, 2000.

[88] vex. `https://motors.vex.com/brushed-brushless?q=&locale.name=English`.

[89] Y. Wang. *Development of a blimp robot for indoor operation*. PhD thesis, Ecole centrale de Lille, 2019.

[90] Wireshark. `https://www.wireshark.org/`.

[91] C. Wong, E. Yang, X.-T. Yan, and D. Gu. Autonomous robots for harsh environments: A holistic overview of current solutions and ongoing challenges. *Systems Science & Control Engineering*, 6:213–219, 01 2018.

[92] P. World. Europe unveils successor to the large hadron collider. `https://physicsworld.com/a/europe-unveils-successor-to-the-large-hadron-collider/`.

[93] B. I. Wyeth G. An autonomous blimp. *Field and Service Robotics, Springer*, pages 464–470, 1998.

[94] N. Yao, Q. Tao, W. yu Liu, Z. Liu, Y. Tian, P. Wang, T. Li, and F. Zhang. Autonomous flying blimp interaction with human in an indoor space. *Frontiers of Information Technology & Electronic Engineering*, 20:45–59, 2019.

[95] H. Zhang and J. Ostrowski. Visual servoing with dynamics: control of an unmanned blimp. In *Proceedings 1999 IEEE International Conference on Robotics and Automation (Cat. No.99CH36288C)*, volume 1, pages 618–623 vol.1, 1999.

[96] Z. Zheng, W. Huo, and Z. Wu. Autonomous airship path following control: Theory and experiments. *Control Engineering Practice*, 21:769–788, 2013.

[97] J.-C. Zufferey, A. Guanella, A. Beyeler, and D. Floreano. Flying over the reality gap: From simulated to real indoor airships. *Autonomous Robots*, 21, 11 2006.

[98] G. Åman. *Indoor Blimp Control*. PhD thesis, Department of Automatic Control, 2021.

Appendix A

Blimp Dynamic Model

A.1 Introduction

In this appendix we will show the complete method for deriving the equations of motion that were written in Chapter 2. To do this, we will follow one of the two possible approaches for the derivation of rigid body dynamics which are the *Newton-Euler* method and the *Lagrangian* method; we will follow the former. We will also see that other terms will have to be added to the classic rigid body model to fully describe the motion of a blimp which are the aerodynamic forces and moments and additional masses. This will be justified by the great analogy that is made between airships and underwater vehicles. In this appendix we will follow the approach of [35] to deriving the 6 DOF motion model for the blimp.

A.1.1 Newton-Euler formulation

To derive the equation of motion through the Newton-Euler formulation we must go back to the principles of dynamics which are the physical laws that describe the relationships between the motion of a body and the entities that modify it. They are also called Newton's principles because they were enunciated as axioms by Isaac Newton (1743-1727) in his treatise *Philosophiae Naturalis Principia Mathematica* in 1687. The *Newton's Second Law* states that

$$m\dot{\boldsymbol{v}}_c = \boldsymbol{f}_c$$

where m is the mass, $\dot{\boldsymbol{v}}_c$ is the acceleration and $\boldsymbol{f}_c$ is the force with respect to the center of gravity of a rigid body.

The contribution of Leonard Euler (1707-1783) in the description of the motion of a rigid body in Newtonian mechanics is the expression of *Newton's Second Law* in terms of conservation of both linear and angular momentum (*Novi Commentarii Academiae Scientiarium Imperialis Petropolitane*). The linear momentum with respect to the CG of the rigid body is defined as

$$\boldsymbol{p}_c = m\boldsymbol{v}_c$$

and the angular momentum is defined as

$$\boldsymbol{h}_c = \boldsymbol{I}_c\boldsymbol{\omega}$$

where $\boldsymbol{\omega}$ is the angular velocity vector and $\boldsymbol{I}_c$ is the inertia tensor about the CG of the rigid body. These results are known as *Euler's First and Second Axioms*, respectively, which translate into the first and second cardinal equations.

$$\begin{cases} \dot{\boldsymbol{p}}_c = \boldsymbol{f}_c \\ \dot{\boldsymbol{h}}_c = \boldsymbol{m}_c; \end{cases} \tag{A.1}$$

where $\boldsymbol{f}_c$ and $\boldsymbol{m}_c$ are the forces and moments with respect to the rigid body CG.

A.1.2 Lagrangian formulation

Lagrangian mechanics is a formulation of mechanics introduced in the 18th century by Joseph-Louis Lagrange (1736-1813) as a reformulation of Newtonian mechanics in terms of energy. For the Lagrangian formulation we must first obtain the expressions of the kinetic T and potential energy V of the body and then calculate the Lagrangian L according to

$$L = T - V$$

Finally, we apply the *Lagrange equation*:

$$\frac{d}{dt}\left(\frac{\partial L}{\partial \dot{\boldsymbol{\eta}}}\right) - \frac{\partial L}{\partial \boldsymbol{\eta}} = \boldsymbol{J}^{-T}(\boldsymbol{\eta})\boldsymbol{\tau} \tag{A.2}$$

that written in components corresponds to the six differential equations of the second order that are obtained identical with the Newton-Euler method. If we write the equation (A.2) in terms of generalized coordinates then this is valid in any coordinate system. In our case, given that the system is not subject to any constraint for motion, then the number of independent and generalized coordinates is equal to the number of degrees of freedom (DOF). To describe the motion of the blimp we have chosen the following generalized coordinates

$$\boldsymbol{\eta} = \begin{bmatrix} x & y & z & \phi & \theta & \psi \end{bmatrix}^T$$

As we will see later it will be convenient to derive the equations of motion in the coordinates defined in the body-fixed reference frame which are

$$\boldsymbol{\xi} = \begin{bmatrix} v_x & v_y & v_z & \omega_x & \omega_y & \omega_z \end{bmatrix}^T$$

The problem that appears here, however, is that by integrating these we do not obtain a generalized coordinate system in terms of positions and orientations and since $\int_0^t \boldsymbol{\xi} d\tau$ has not immediate physical interpretation, we cannot use the Lagrangian approach to formulate the dynamics of a blimp in a body-fixed reference system. However, the *Quasi-Lagrangian* approach can be used to overcome this problem applying *Kirchhoff's equations* of motion.

To derive *Kirchhoff's equations* of motion, the force $\boldsymbol{\tau}_1$ and torque $\boldsymbol{\tau}_2$ are written in terms of kinetic energy by showing the body-fixed linear velocity vector $\boldsymbol{v} = [v_x, v_y, v_z]^T$ and the body-fixed angular velocity vector $\boldsymbol{\omega} = [\omega_x, \omega_y, \omega_z]^T$.

$$T = \frac{1}{2}\boldsymbol{\xi}^T \boldsymbol{M} \boldsymbol{\xi}$$

and written in vector terms

$$\frac{d}{dt}\left(\frac{\partial T}{\partial \boldsymbol{v}}\right) + \boldsymbol{\omega} \times \frac{\partial T}{\partial \boldsymbol{v}} = \boldsymbol{\tau}_1 \tag{A.3}$$

$$\frac{d}{dt}\left(\frac{\partial T}{\partial \boldsymbol{\omega}}\right) + \boldsymbol{\omega} \times \frac{\partial T}{\partial \boldsymbol{\omega}} + \boldsymbol{v} \times \frac{\partial T}{\partial \boldsymbol{v}} = \boldsymbol{\tau}_2 \tag{A.4}$$

We have reported the *Kirchhoff's equations* (A.3) and (A.4), as we will see later they will be fundamental for the derivation of the Coriolis and centripetal matrix in section A.2.3. They do not include the gravitational forces.

A.2 Rigid body dynamics

Euler's first and second axioms allow to derive the rigid body equation of motion and from now on we will use this approach for the rest of the appendix. Consider the rigid body in Figure A.1, two reference frames are defined: F_b is the body-fixed frame whose origin is $\boldsymbol{O}$, F_i is the inertial frame which locates its origin in a generic point of space. We note that the body-fixed reference has been placed at a point that is not the CG but is a generic point $\boldsymbol{O}$ belonging to the body. In deriving the equations of motion we will make the following assumptions:

1. The blimp is a rigid body;
2. The earth-fixed reference frame is inertial.

The first assumption allows us to follow Newton Euler's approach for rigid body dynamics, for our application we are therefore forced to affirm that the Helium balloon is also considered a rigid body. Moreover, it allows to cancel the effect of forces between the same elements of the body by considering it precisely as rigid.

The second assumption eliminates the forces due to the fact that a reference system fixed to the Earth is not inertial due to the motion of the Earth itself with respect to the inertial star-fixed reference frame. Typically for space guidance and control applications a star-fixed reference frame or a earth-fixed rotating reference frame are used, but for our application of flight within the atmosphere and near the surface the assumption made has reason to exist.

In the procedure of writing the rigid body dynamics we will express the blimp equations in the body-fixed frame F_b because as we will see later it will be more convenient. The first quantity that we obtain for the rigid body represented in Figure A.1 is the inertia tensor $\boldsymbol{I}_0$ with respect to the center of the F_b reference frame:

$$\boldsymbol{I}_0 = \begin{bmatrix} I_x & -I_{xy} & -I_{xz} \\ -I_{yx} & I_y & -I_{yz} \\ -I_{zx} & -I_{zy} & I_z \end{bmatrix}; \qquad \boldsymbol{I}_0 = \boldsymbol{I}_0^T > 0 \tag{A.5}$$

The inertia tensor is a symmetric matrix and the components on the main diagonal I_x, I_y and I_z are called *moments of inertia* about the $\boldsymbol{X}_b$, $\boldsymbol{Y}_b$ and $\boldsymbol{Z}_b$-axes while the off diagonal terms $I_{xy} = I_{yx}$, $I_{xz} = I_{zx}$ and $I_{yz} = I_{zy}$ are called *products of inertia* and they are defined as:

$$I_x = \int_V (y^2 + z^2)\rho dV \qquad I_{xy} = I_{yx} = \int_V xy\rho dV$$
$$I_y = \int_V (x^2 + z^2)\rho dV \qquad I_{xz} = I_{zx} = \int_V xz\rho dV$$
$$I_z = \int_V (x^2 + y^2)\rho dV \qquad I_{yz} = I_{zy} = \int_V yz\rho dV$$

The ρdV quantity is the infinitesimal mass calculated as the product between the density of the rigid body ρ and the infinitesimal element of volume dV as shown in Figure A.1. The inertia tensor can also be obtained through the skew-symmetric matrix as follows

$$\boldsymbol{I}_0 = -\int_V \boldsymbol{S}(\boldsymbol{r})\boldsymbol{S}(\boldsymbol{r})\rho dV = \int_V (\boldsymbol{r}^T\boldsymbol{r}\boldsymbol{I} - \boldsymbol{r}\boldsymbol{r}^T)\rho dV$$

where $\boldsymbol{S}(\cdot)$ is the skew-symmetric matrix operator defined as

$$\boldsymbol{S}(\boldsymbol{a}) := \begin{bmatrix} 0 & -a_3 & a_2 \\ a_3 & 0 & -a_1 \\ -a_2 & a_1 & 0 \end{bmatrix} \tag{A.6}$$

A useful expression that we will need later is the product of the inertia matrix and the angular velocity which can be written as

$$\boldsymbol{I}_0\boldsymbol{\omega} = \int_V \boldsymbol{r} \times (\boldsymbol{\omega} \times \boldsymbol{r})\rho dV \tag{A.7}$$

The entire mass of the rigid body can be obtained by integrating the ρdV product over the entire volume V

$$m = \int_V \rho dV$$

Then, assuming that the mass is time-invariant[1], i.e. $\dot{m} = 0$, we can derive the $\boldsymbol{r}_G$ which is the vector from the origin of F_b to the rigid body CG:

$$\boldsymbol{r}_G = \frac{1}{m}\int_V \boldsymbol{r}\rho dV \tag{A.8}$$

The body-fixed reference frame, which is the reference with respect to which we want to derive the equations of motion, is not localized in the CG of the rigid body. If we know a vector $\boldsymbol{u}$ in the body-fixed frame, to calculate it in the inertial frame then we have to apply the change of basis equation

$$\boldsymbol{u}^i = \boldsymbol{R}_i^b\boldsymbol{u}^b$$

where $\boldsymbol{R}_i^b$ is the rotation matrix from F_i to F_b. If we take the time derivatives on both sides

$$\frac{d}{dt}\boldsymbol{u}^i = \boldsymbol{R}_i^b\left(\frac{d}{dt}\boldsymbol{u}^b\right) + \dot{\boldsymbol{R}}_i^b\boldsymbol{u}^b$$

[1]This is a correct assumption given the absence of mass losses during the flight of the blimp because propulsion is through electric motors.

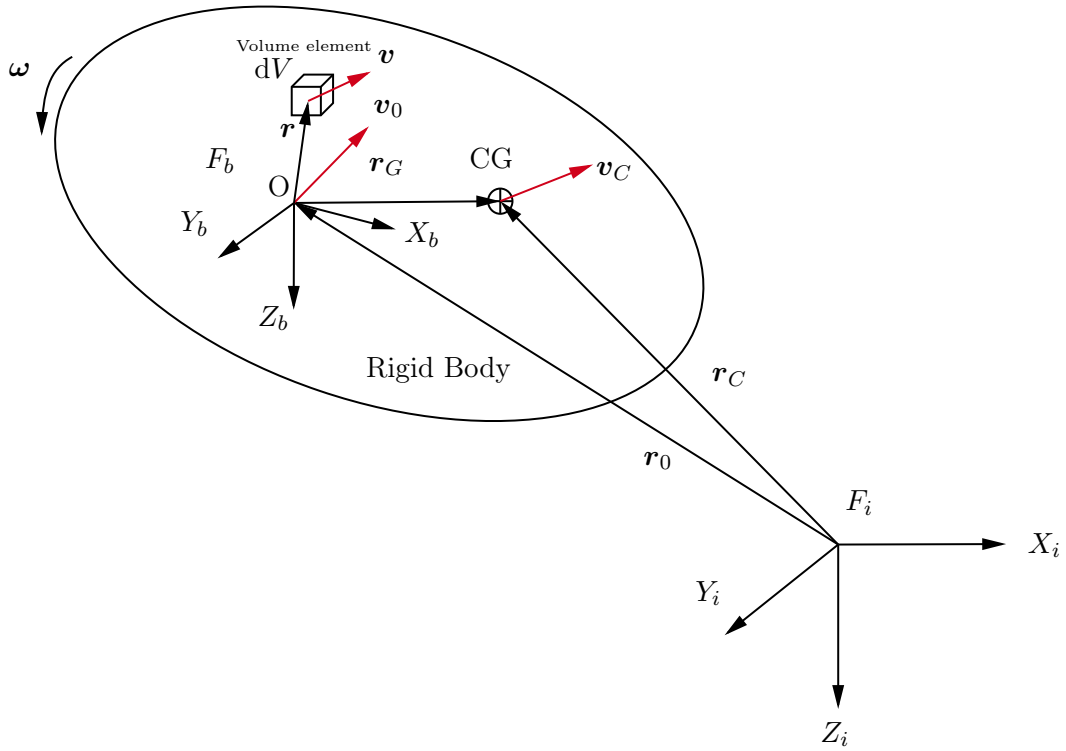

Figure A.1: Inertial frame $\boldsymbol{X_i Y_i Z_i}$ and body-fixed frame $\boldsymbol{X_b Y_b Z_b}$ for the rigid body.

.

and we multiply both sides with $(\boldsymbol{R}_i^b)^T$

$$(\boldsymbol{R}_i^b)^T \frac{d}{dt}\boldsymbol{u}^i = \frac{d}{dt}\boldsymbol{u}^b + \boldsymbol{S}(\boldsymbol{\omega}^b)\boldsymbol{u}^b \tag{A.9}$$

Here we have applied the relation $(\boldsymbol{R}_i^b)^T \boldsymbol{R}_i^b = I_{3\times 3}$ and $(\boldsymbol{R}_i^b)^T \dot{\boldsymbol{R}}_i^b = S(\boldsymbol{\omega}^b)$. Equation (A.9) represents the relation between the time derivative of $\boldsymbol{u}$ as seen in the inertial frame F_i but expressed in body-fixed frame F_b (left-hand side term) and the time derivative of the same vector $\boldsymbol{u}$ with respect to moving body-fixed frame F_b expressed again in F_b (first right-hand side term), $\boldsymbol{\omega}^b$ is the angular velocity of F_b with respect to F_i, expressed in F_b. We can rewrite (A.9) as

$$(\dot{\boldsymbol{u}})^i = (\dot{\boldsymbol{u}})^b + \boldsymbol{\omega}^b \times \boldsymbol{u}^b \tag{A.10}$$

Therefore, the brackets show the reference with respect to which the derivation is being made. In the following sections we will omit the superscripts for simplicity, leaving only those relating to the brackets that indicate the references for the derivations.

A.2.1 Translational motion

We want to derive the three equations of motion for translational dynamics. From Figure A.1, the $\boldsymbol{r}_C$ vector is given by

$$\boldsymbol{r}_C = \boldsymbol{r}_0 + \boldsymbol{r}_G \tag{A.11}$$

If we want to calculate the velocity of the CG we take the time derivatives of the members in equation (A.11) obtaining

$$(\dot{\boldsymbol{r}}_C)^i = (\dot{\boldsymbol{r}}_0)^i + (\dot{\boldsymbol{r}}_G)^i \tag{A.12}$$

We can write the left-hand side term of (A.12) as $\boldsymbol{v}_C$. Now let's focus on the first term of right-hand side of equation (A.12), it is the velocity of the origin $\boldsymbol{O}$ seen in inertial frame F_i and expressed in F_b, we can call it $\boldsymbol{v}_0$ while for the second term of right-hand side, we can apply equation (A.10) for rewriting it

$$(\dot{\boldsymbol{r}}_G)^i = (\dot{\boldsymbol{r}}_G)^b + \boldsymbol{\omega} \times \boldsymbol{r}_G = \boldsymbol{\omega} \times \boldsymbol{r}_G \tag{A.13}$$

where $(\dot{\boldsymbol{r}}_G)^b = 0$ for rigid body. Hence, we can write the velocity of the CG as

$$\boldsymbol{v}_C = \boldsymbol{v}_0 + \boldsymbol{\omega} \times \boldsymbol{r}_G \tag{A.14}$$

Now we want to obtain the acceleration of the CG, taking time derivative on both sides, we obtain

$$(\dot{\boldsymbol{v}}_C)^i = (\dot{\boldsymbol{v}}_0)^i + (\dot{\boldsymbol{\omega}})^i \times \boldsymbol{r}_G + \boldsymbol{\omega} \times (\dot{\boldsymbol{r}}_G)^i$$

Let's express all the terms in the body-fixed frame, for $(\dot{\boldsymbol{v}}_0)^i$ we use equation (A.10), $(\dot{\boldsymbol{\omega}})^i = (\dot{\boldsymbol{\omega}})^b$ because the angular acceleration in the inertial frame is equal in the body-fixed frame and for $(\dot{\boldsymbol{r}}_G)^i$ we use (A.13):

$$(\dot{\boldsymbol{v}}_C)^i = (\dot{\boldsymbol{v}}_0)^b + \boldsymbol{\omega} \times \boldsymbol{v}_0 + (\dot{\boldsymbol{\omega}})^b \times \boldsymbol{r}_G + \boldsymbol{\omega} \times (\boldsymbol{\omega} \times \boldsymbol{r}_G)$$

We got the expression of the acceleration of the CG that we can replace in the Euler's First Axiom (A.1)

$$m\left((\dot{\boldsymbol{v}}_0)^b + \boldsymbol{\omega} \times \boldsymbol{v}_0 + (\dot{\boldsymbol{\omega}})^b \times \boldsymbol{r}_G + \boldsymbol{\omega} \times (\boldsymbol{\omega} \times \boldsymbol{r}_G)\right) = \boldsymbol{f}_0 \tag{A.15}$$

In this expression all the vectors are expressed in the body-fixed frame F_b. In the case in which the origin $\boldsymbol{O}$ coincides with the CG, we have $\boldsymbol{r}_G = [0, 0, 0]^T$. Therefore equation (A.15) with $\boldsymbol{f}_0 = \boldsymbol{f}_C$ and $\boldsymbol{v}_0 = \boldsymbol{v}_C$, yields:

$$m\left((\dot{\boldsymbol{v}}_C)^b + \boldsymbol{\omega} \times \boldsymbol{v}_C\right) = \boldsymbol{f}_C$$

A.2.2 Rotational motion

Now we want to obtain the equations of the rotational dynamics for the other three DOF of the system using Euler's Second Axiom (A.1). Also in this case the equations will be obtained with respect to the origin $\boldsymbol{O}$ in Figure A.1. We start with the calculation of the absolute angular momentum about $\boldsymbol{O}$

$$\boldsymbol{h}_0 = \int_V \boldsymbol{r} \times \boldsymbol{v} \rho dV \tag{A.16}$$

We take the time derivative of the members of equation: (A.16)

$$(\dot{\boldsymbol{h}}_0)^i = \int_V \boldsymbol{r} \times (\dot{\boldsymbol{v}})^i \rho dV + \int_V (\dot{\boldsymbol{r}})^i \times \boldsymbol{v} \rho dV \tag{A.17}$$

The first term on right-hand side is called moment vector and it is defined as

$$\boldsymbol{m}_0 = \int_V \boldsymbol{r} \times (\dot{\boldsymbol{v}})^i \rho dV \tag{A.18}$$

For the second term on the right-hand side of (A.17) we want to obtain an expression for $(\dot{\boldsymbol{r}})^i$. From Figure A.1, it can be seen that

$$\boldsymbol{v} = (\dot{\boldsymbol{r}}_0)^i + (\dot{\boldsymbol{r}})^i \Longrightarrow \dot{\boldsymbol{r}} = \boldsymbol{v} - \boldsymbol{v}_0 \tag{A.19}$$

Now we substitute (A.18) and (A.19) into (A.17), using the fact that $\boldsymbol{v} \times \boldsymbol{v} = 0$ we obtain

$$(\dot{\boldsymbol{h}}_0)^i = \boldsymbol{m}_0 - \boldsymbol{v}_0 \times \int_V (\dot{\boldsymbol{r}})^i \rho dV \tag{A.20}$$

which can be also written as

$$(\dot{\boldsymbol{h}}_0)^i = \boldsymbol{m}_0 - \boldsymbol{v}_0 \times \int_V (\boldsymbol{v}_0 + (\dot{\boldsymbol{r}})^i) \rho dV = \boldsymbol{m}_0 - \boldsymbol{v}_0 \times \int_V (\dot{\boldsymbol{r}})^i \rho dV \tag{A.21}$$

The second term on the right-hand side of the equation (A.20) can be written in an alternative way. Considering the time derivative of equation (A.8) we get

$$m(\dot{\boldsymbol{r}}_G)^i = \int_V (\dot{\boldsymbol{r}})^i \rho dV \tag{A.22}$$

From equation (A.13) we know that $(\dot{\boldsymbol{r}}_G)^i = \boldsymbol{\omega} \times \boldsymbol{r}_G$, substituting (A.13) in (A.22) we obtain

$$\int_V (\dot{\boldsymbol{r}})^i \rho dV = m(\boldsymbol{\omega} \times \boldsymbol{r}_G) \tag{A.23}$$

If we replace equation (A.23) into (A.20) there is

$$(\dot{\boldsymbol{h}}_0)^i = \boldsymbol{m}_0 - m\boldsymbol{v}_0 \times (\boldsymbol{\omega} \times \boldsymbol{r}_G) \tag{A.24}$$

Now we want to express the angular momentum (A.16) in another way. In the expression (A.16) we substitute $\boldsymbol{v} = \boldsymbol{v}_0 + \boldsymbol{\omega} \times \boldsymbol{r}$ obtaining

$$\boldsymbol{h}_0 = \int_V \boldsymbol{r} \times \boldsymbol{v}_0 \rho dV + \int_V \boldsymbol{r} \times (\boldsymbol{\omega} \times \boldsymbol{r}) \rho dV \tag{A.25}$$

In the first term on the right-hand side we can use the definition (A.8):

$$\int_V \boldsymbol{r} \times \boldsymbol{v}_0 \rho dV = \left(\int_V \boldsymbol{r} \rho dV \right) \times \boldsymbol{v}_0 = m\boldsymbol{r}_G \times \boldsymbol{v}_0 \tag{A.26}$$

For the second term on the right-hand side of equation (A.25) we recognise the definition of the inertia tensor (A.7). Substituting (A.26) and (A.7) into (A.25) we have

$$\boldsymbol{h}_0 = \boldsymbol{I}_0 \boldsymbol{\omega} + m\boldsymbol{r}_G \times \boldsymbol{v}_0$$

Now we take the derivative on both sides of this equation

$$(\dot{\boldsymbol{h}}_0)^i = \boldsymbol{I}_0 (\dot{\boldsymbol{\omega}})^b + \boldsymbol{\omega} \times (\boldsymbol{I}_0 \boldsymbol{\omega}) + m(\dot{\boldsymbol{r}}_G)^i \times \boldsymbol{v}_0 + m\boldsymbol{r}_G \times (\dot{\boldsymbol{v}}_0)^i$$

Expressing $(\dot{\boldsymbol{r}}_G)^i$ in the body-fixed frame using (A.13) and the same for $(\dot{\boldsymbol{v}}_0)^i$ we get

$$(\dot{\boldsymbol{h}}_0)^i = \boldsymbol{I}_0(\dot{\boldsymbol{\omega}})^b + \boldsymbol{\omega} \times (\boldsymbol{I}_0\boldsymbol{\omega}) + m(\boldsymbol{\omega} \times \boldsymbol{r}_G) \times \boldsymbol{v}_0 + m\boldsymbol{r}_G \times \Big((\dot{\boldsymbol{v}}_0)^b + \boldsymbol{\omega} \times \boldsymbol{v}_0\Big) \tag{A.27}$$

Rearranging this expression we obtain

$$\boldsymbol{I}_0(\dot{\boldsymbol{\omega}})^b + \boldsymbol{\omega} \times (\boldsymbol{I}_0\boldsymbol{\omega}) + m\boldsymbol{r}_G \times \Big((\dot{\boldsymbol{v}}_0)^b + \boldsymbol{\omega} \times \boldsymbol{v}_0\Big) = (\dot{\boldsymbol{h}}_0)^i + m\boldsymbol{v}_0 \times (\boldsymbol{\omega} \times \boldsymbol{r}_G) \tag{A.28}$$

where we recognise that the right-hand side is equal to $\boldsymbol{m}_0$ from (A.24). Notice that we have used the following property

$$(\boldsymbol{\omega} \times \boldsymbol{r}_G) \times \boldsymbol{v}_0 = -\boldsymbol{v}_0 \times (\boldsymbol{\omega} \times \boldsymbol{r}_G)$$

Finally equation (A.28) becomes

$$\boldsymbol{I}_0(\dot{\boldsymbol{\omega}})^b + \boldsymbol{\omega} \times (\boldsymbol{I}_0\boldsymbol{\omega}) + m\boldsymbol{r}_G \times \Big((\dot{\boldsymbol{v}}_0)^b + \boldsymbol{\omega} \times \boldsymbol{v}_0\Big) = \boldsymbol{m}_0 \tag{A.29}$$

If we write in components these expressions we obtain the rotational equations of motion which are often referred to as the Euler equations. Also here, as for equation (A.15), all the vectors are expressed in the body-fixed frame F_b. We want to remind that they are written in the case in which origin $\boldsymbol{O}$ of F_b is different from CG, if the two coincide, equation (A.29) simplifies to

$$\boldsymbol{I}_0(\dot{\boldsymbol{\omega}})^b + \boldsymbol{\omega} \times (\boldsymbol{I}_0\boldsymbol{\omega}) = \boldsymbol{m}_C$$

A.2.3 6 DOF rigid body dynamic model

After having obtained the rigid body dynamics following the *Newtonian* and *Eulerian* formulation, we want to write by components the six nonlinear equations that represent the 6 DOF rigid body dynamics. We also look for a more compact form like the matrix one and specify the properties of each matrix. To write the equations of motion into components we use the following notation

$$\begin{aligned}
\boldsymbol{f}_0 = \boldsymbol{\tau}_1 &= \begin{bmatrix} f_x & f_y & f_z \end{bmatrix}^T && \text{external forces} \\
\boldsymbol{m}_0 = \boldsymbol{\tau}_2 &= \begin{bmatrix} \tau_x & \tau_y & \tau_z \end{bmatrix}^T && \text{moment of external forces about } \boldsymbol{O} \\
\boldsymbol{v}_0 = \boldsymbol{v} &= \begin{bmatrix} v_x & v_y & v_z \end{bmatrix}^T && \text{linear velocity of rigid body expressed in } F_b \\
\boldsymbol{\omega} &= \begin{bmatrix} \omega_x & \omega_y & \omega_z \end{bmatrix}^T && \text{angular velocity of rigid body expressed in } F_b \\
\boldsymbol{r}_G &= \begin{bmatrix} x_G & y_G & z_G \end{bmatrix}^T && \text{coordinate of CG in } F_b
\end{aligned}$$

and $\boldsymbol{I}_0$ is defined by (A.5). Then, applying this notation we can decompose the equations (A.15) and (A.29) which represent the equations of transnational and rotational dynamics respectively

$$\begin{aligned}
m[\dot{v}_x - v_y\omega_z + v_z\omega_y - x_G(\omega_y^2+\omega_z^2) + y_G(\omega_x\omega_y - \dot{\omega}_z) + z_G(\omega_x\omega_z + \dot{\omega}_y)] &= f_x \\
m[\dot{v}_y - v_z\omega_x + v_x\omega_z - y_G(\omega_z^2+\omega_x^2) + z_G(\omega_y\omega_z - \dot{\omega}_x) + x_G(\omega_y\omega_x + \dot{\omega}_z)] &= f_y \\
m[\dot{v}_z - v_x\omega_y + v_y\omega_x - z_G(\omega_x^2+\omega_y^2) + x_G(\omega_z\omega_x - \dot{\omega}_y) + y_G(\omega_z\omega_y + \dot{\omega}_x)] &= f_z \\
I_x\dot{\omega}_x + (I_z - I_y)\omega_y\omega_z - (\dot{\omega}_z + \omega_x\omega_y)I_{xz} + (\omega_z^2 - \omega_y^2)I_{yz} + (\omega_x\omega_z - \dot{\omega}_y)I_{xy} & \\
+m[y_G(\dot{v}_z - v_x\omega_y + v_y\omega_x) - z_G(\dot{v}_y - v_z\omega_x + v_x\omega_z)] &= \tau_x \\
I_y\dot{\omega}_y + (I_x - I_z)\omega_z\omega_x - (\dot{\omega}_x + \omega_y\omega_z)I_{xy} + (\omega_x^2 - \omega_z^2)I_{zx} + (\omega_y\omega_x - \dot{\omega}_z)I_{yz} & \\
+m[z_G(\dot{v}_x - v_y\omega_z + v_z\omega_y) - x_G(\dot{v}_z - v_x\omega_y + v_y\omega_x)] &= \tau_y \\
I_z\dot{\omega}_z + (I_y - I_x)\omega_x\omega_y - (\dot{\omega}_y + \omega_z\omega_x)I_{yz} + (\omega_y^2 - \omega_x^2)I_{xy} + (\omega_z\omega_y - \dot{\omega}_x)I_{zx} & \\
+m[x_G(\dot{v}_y - v_z\omega_x + v_x\omega_z) - y_G(\dot{v}_x - v_y\omega_z + v_z\omega_y)] &= \tau_z
\end{aligned} \tag{A.30}$$

If we want to better understand the meaning of these equations it is now convenient to adopt a matrix form. The six equations in (A.30) can then be rewritten as follows

$$\boldsymbol{M}_{RB}\dot{\boldsymbol{\xi}} + \boldsymbol{C}_{RB}(\boldsymbol{\xi})\boldsymbol{\xi} = \boldsymbol{\tau}_{RB} \tag{A.31}$$

where

$$\begin{aligned}
\boldsymbol{\xi} &= \begin{bmatrix}(\boldsymbol{v})^T & (\boldsymbol{\omega})^T\end{bmatrix}^T = \begin{bmatrix}v_x & v_y & v_z & \omega_x & \omega_y & \omega_z\end{bmatrix}^T \\
\boldsymbol{\tau}_{RB} &= \begin{bmatrix}(\boldsymbol{\tau}_1)^T & (\boldsymbol{\tau}_2)^T\end{bmatrix}^T = \begin{bmatrix}f_x & f_y & f_z & \tau_x & \tau_y & \tau_z\end{bmatrix}^T
\end{aligned}$$

are the linear and angular velocity vector and the vector of external forces and moments respectively. All of these vectors are expressed in the body-fixed frame. $\boldsymbol{M}_{RB}$ is called the rigid body inertia matrix and $\boldsymbol{C}_{RB}$ is the rigid body Coriolis and centripetal matrix. Now we want to describe the matrices that appear in equation (A.31) giving their properties.

Property A.1. *The parametrization of $\boldsymbol{M}_{RB}$ satisfies the following properties:*

$$\boldsymbol{M}_{RB} = \boldsymbol{M}_{RB}^T > 0; \qquad \dot{\boldsymbol{M}}_{RB} = 0$$

where

$$\boldsymbol{M}_{RB} = \begin{bmatrix} mI_{3\times3} & -m\boldsymbol{S}(\boldsymbol{r}_G) \\ m\boldsymbol{S}(\boldsymbol{r}_G) & \boldsymbol{I}_0 \end{bmatrix} = \begin{bmatrix} m & 0 & 0 & 0 & mz_G & -my_G \\ 0 & m & 0 & -mz_G & 0 & mx_G \\ 0 & 0 & m & my_G & -mx_G & 0 \\ 0 & -mz_G & my_G & I_x & -I_{xy} & -I_{xz} \\ mz_G & 0 & -mx_G & -I_{yx} & I_y & -I_{yz} \\ -my_G & mx_G & 0 & -I_{zx} & -I_{zy} & I_z \end{bmatrix} \tag{A.32}$$

with $I_{3\times3}$ the 3×3 identity matrix, $\boldsymbol{I}_0 = \boldsymbol{I}_0^T > 0$ the inertia tensor with respect to $\boldsymbol{O}$ and $\boldsymbol{S}(\boldsymbol{r}_G)$ the skew-symmetric matrix of $\boldsymbol{r}_G$ as defined in (A.6).

The matrix $\boldsymbol{C}_{RB}$ is the parameterization of the Coriolis terms $\boldsymbol{\omega}\times\boldsymbol{v}$ and the centripetal terms

$\boldsymbol{\omega} \times (\boldsymbol{\omega} \times \boldsymbol{r}_G)$. These terms are present because we are representing the equations of motion in a non-inertial reference such as F_b. To derive the skew-symmetric representation of $\boldsymbol{C}_{RB}$ we will make use of Kirchoff's equation.

Theorem A.1. *The Coriolis and centripetal matrix can be parametrized such that*

$$\boldsymbol{C}(\boldsymbol{\xi}) = -\boldsymbol{C}^T(\boldsymbol{\xi})$$

by defining:

$$\boldsymbol{C}(\boldsymbol{\xi}) = \begin{bmatrix} \boldsymbol{0}_{3\times 3} & -\boldsymbol{S}(\boldsymbol{M}_{11}\boldsymbol{v} + \boldsymbol{M}_{12}\boldsymbol{\omega}) \\ -\boldsymbol{S}(\boldsymbol{M}_{11}\boldsymbol{v} + \boldsymbol{M}_{12}\boldsymbol{\omega}) & -\boldsymbol{S}(\boldsymbol{M}_{21}\boldsymbol{v} + \boldsymbol{M}_{22}\boldsymbol{\omega}) \end{bmatrix} \tag{A.33}$$

where $\boldsymbol{M}_{ij}\,(i,j=1,2)$ *are the four* 3×3 *sub-matrices of the* 6×6 *inertia matrix* $\boldsymbol{M} > 0$ *defined as:*

$$\boldsymbol{M} = \begin{bmatrix} \boldsymbol{M}_{11} & \boldsymbol{M}_{12} \\ \boldsymbol{M}_{21} & \boldsymbol{M}_{22} \end{bmatrix} \tag{A.34}$$

Proof. We write the kinetic energy T as a quadratic form:

$$T = \frac{1}{2}\boldsymbol{\xi}^T\boldsymbol{M}\boldsymbol{\xi} \tag{A.35}$$

we expand the quadratic form by substituting (A.34) in (A.35)

$$T = \frac{1}{2}(\boldsymbol{v}^T\boldsymbol{M}_{11}\boldsymbol{v} + \boldsymbol{v}^T\boldsymbol{M}_{12}\boldsymbol{\omega} + \boldsymbol{\omega}^T\boldsymbol{M}_{21}\boldsymbol{v} + \boldsymbol{\omega}^T\boldsymbol{M}_{22}\boldsymbol{\omega})$$

Differentiating with respect to $\boldsymbol{v}$ and $\boldsymbol{\omega}$ we obtain

$$\frac{\partial T}{\partial \boldsymbol{v}} = \boldsymbol{M}_{11}\boldsymbol{v} + \boldsymbol{M}_{12}\boldsymbol{\omega} \tag{A.36}$$

$$\frac{\partial T}{\partial \boldsymbol{\omega}} = \boldsymbol{M}_{21}\boldsymbol{v} + \boldsymbol{M}_{22}\boldsymbol{\omega} \tag{A.37}$$

From Kirchhoff's equations (A.3) and (A.4) we recognize that:

$$\boldsymbol{C}(\boldsymbol{\xi})\boldsymbol{\xi} = \begin{bmatrix} \boldsymbol{\omega} \times \dfrac{\partial T}{\partial \boldsymbol{v}} \\ \boldsymbol{\omega} \times \dfrac{\partial T}{\partial \boldsymbol{\omega}} + \boldsymbol{v} \times \dfrac{\partial T}{\partial \boldsymbol{v}} \end{bmatrix} = \begin{bmatrix} \boldsymbol{0}_{3\times 3} & -\boldsymbol{S}\left(\dfrac{\partial T}{\partial \boldsymbol{v}}\right) \\ -\boldsymbol{S}\left(\dfrac{\partial T}{\partial \boldsymbol{v}}\right) & -\boldsymbol{S}\left(\dfrac{\partial T}{\partial \boldsymbol{\omega}}\right) \end{bmatrix} \begin{bmatrix} \boldsymbol{v} \\ \boldsymbol{\omega} \end{bmatrix} \tag{A.38}$$

Therefore, if we replace (A.36) and (A.37) in (A.38) proves (A.33). This result was first proven by Sagatun and Fossen [80] □

Property A.2. *From Theorem A.1 the parametrization of* $\boldsymbol{C}_{RB}(\boldsymbol{\xi})$ *guarantees that the rigid body Coriolis and centripetal matrix is skew-symmetrical:*

$$\boldsymbol{C}_{RB}(\boldsymbol{\xi}) = -\boldsymbol{C}_{RB}^T(\boldsymbol{\xi}) \quad \forall \boldsymbol{\xi} \in \mathbb{R}^6$$

The equation (A.31) represents the 6 DOF nonlinear dynamics of a rigid body written in matrix terms. However, this equation alone is not sufficient to mathematically model the motion of an LTA vehicle such as a blimp. To those terms we must therefore add the aerodynamic contribution that

plays an important role in modeling the dynamics of an airship. In particular, the blimp having an Helium inflated balloon shows a density similar to that of the ambient air and this generates aerodynamic effects in terms of forces and moments. This phenomenon is also found in underwater vehicles and therefore can be studied in the same way [35]. The exact derivation of the aerodynamic forces and moments are beyond the scope of this thesis, [35] contains more details. We will limit the derivation of dynamic model providing conclusions regarding this topic. The overall aerodynamic forces and moments $\boldsymbol{\tau}_H$ can be written as

$$\boldsymbol{\tau}_H = -\boldsymbol{M}_{Added}\dot{\boldsymbol{\xi}} - \boldsymbol{C}_{Added}(\boldsymbol{\xi})\boldsymbol{\xi} - \boldsymbol{D}(\boldsymbol{\xi})\boldsymbol{\xi} - \boldsymbol{g}(\boldsymbol{\eta}) \tag{A.39}$$

The first two terms on the right-hand side $-\boldsymbol{M}_{Added}\dot{\boldsymbol{\xi}} - \boldsymbol{C}_{Added}(\boldsymbol{\xi})\boldsymbol{\xi}$ represent the contribution of the inertia of the fluid surrounding the body which acts both on the inertia matrix and on the Coriolis and centripetal matrix. The third term on the right-hand side $-\boldsymbol{D}(\boldsymbol{\xi})$ is the total hydrodynamic damping matrix, which is a sum of various components such as radiation induced potential damping effects due to forced body oscillations, linear and quadratic skin friction due to laminar and turbulent boundary layers, wave drift damping and damping due to vortex shedding [35]. The fourth term on the right-hand side $\boldsymbol{g}(\boldsymbol{\eta})$ is the restoring forces vector due to the gravitational and buoyant forces. The left-hand side term of the equation (A.39) which are the hydrodynamic forces and moment $\boldsymbol{\tau}_H$ it must therefore be integrated into the $\boldsymbol{\tau}_{RB}$ vector of rigid body forces and moments which is reported in the right-hand side term of equations (A.30) and (A.31). However, it is not the only contribution that must be made in order to enrich the model, another fundamental one is that of environmental forces and moments $\boldsymbol{\tau}_E$ that are considered as disturbances which act on the dynamics of the rigid body. Finally we have to consider the propulsion forces vector $\boldsymbol{\tau}$ generated by actuators which in our case represents the vector of the forces and moments of the electric motors with the propellers. Therefore we can make the $\boldsymbol{\tau}_{RB}$ term explicit by adding the three terms specified above:

$$\boldsymbol{\tau}_{RB} = \boldsymbol{\tau}_H + \boldsymbol{\tau}_E + \boldsymbol{\tau} \tag{A.40}$$

Now we can put things together by combining the equation (A.31) with (A.40). Hence the 6 DOF dynamic model of the blimp robot is given by

$$\boldsymbol{M}\dot{\boldsymbol{\xi}} + \boldsymbol{C}(\boldsymbol{\xi})\boldsymbol{\xi} + \boldsymbol{D}(\boldsymbol{\xi})\boldsymbol{\xi} + \boldsymbol{g}(\boldsymbol{\eta}) = \boldsymbol{\tau}_E + \boldsymbol{\tau}$$

where

$$\boldsymbol{M} = \boldsymbol{M}_{RB} + \boldsymbol{M}_{Added}$$
$$\boldsymbol{C}(\boldsymbol{\xi}) = \boldsymbol{C}_{RB}(\boldsymbol{\xi}) + \boldsymbol{C}_{Added}(\boldsymbol{\xi})$$

As regards environmental disturbances, these are evaluated in Chapter 4 as a consequence of the interaction of the blimp with the external magnetic field present inside the FCC-hh detector; in particular disturbing magnetic forces and torques that act on electric motors. By ignoring the environmental disturbances $\boldsymbol{\tau}_E$ acting on the blimp, the dynamic model is obtained as

$$\boldsymbol{M}\dot{\boldsymbol{\xi}} + \boldsymbol{C}(\boldsymbol{\xi})\boldsymbol{\xi} + \boldsymbol{D}(\boldsymbol{\xi})\boldsymbol{\xi} + \boldsymbol{g}(\boldsymbol{\eta}) = \boldsymbol{\tau} \tag{A.41}$$

and if we remember that the 6 DOF dynamic model it was written with respect to the body-fixed frame F_b we can add the superscripts for the vectors and it becomes

$$\boldsymbol{M}\dot{\boldsymbol{\xi}}^b + \boldsymbol{C}(\boldsymbol{\xi}^b)\boldsymbol{\xi}^b + \boldsymbol{D}(\boldsymbol{\xi}^b)\boldsymbol{\xi}^b + \boldsymbol{g}(\boldsymbol{\eta}^n) = \boldsymbol{\tau}^b \tag{A.42}$$

We will discuss the terms in (A.42) in more detail in the following sections.

A.3 Added mass inertia matrix

Let us now analyze the term of added mass inertia matrix $\boldsymbol{M}_{Added}$ of the blimp. We can first of all give a physical interpretation to this term. The additional mass also called virtual mass is one of the fundamental aspects in fluid mechanics and in particular in the dynamic modeling of a system that moves in a fluid like an underwater vehicle or an airship vehicle. The problem arises when a body accelerates or decelerates in a fluid that surrounds it, which in our case is the air. The fluid is therefore disturbed and accelerated accordingly. If the vehicle moved in a vacuum this phenomenon would not exist because there would be no fluid particles to move but if the vehicle is immersed in a fluid, the force necessary to accelerate must be greater. The added mass depends on the density of the fluid in which the body is moving. This effect is often neglected for bodies that have a higher density than the fluid (as in the case of aircraft). For situations where the fluid density is comparable to or greater than the density of the body (such as in the case of airships or submarines) the added mass can often be greater than the body mass and neglecting it can introduce significant errors. Thinking in terms of energy, the increase in inertia can be interpreted as the contribution of the energy needed to create a flow of fluid that allows the body to pass through it. To quantify this phenomenon, not only the density of the surrounding fluid is important but also the geometry of the body as energy acts as a normal pressure on the surface and therefore in this case the geometry of the body plays an important role [72, 83].

The additional mass is an effect linked to the forces and moments induced by the pressure that the fluid exerts on the balloon and that is pushed to accelerate with the vehicle itself. Consequently the forces and moments necessary for the movement will be greater than those in the case in which the vehicle moves in a vacuum because it is also necessary to accelerate the surrounding fluid. Ideally the additional mass then translates into a volume of fluid that surrounds the body and accelerates with it. This is a simplifying hypothesis as the fluid particles surrounding the body will have different accelerations between them but to facilitate the calculation we consider a finite volume of fluid that has the same acceleration as the body, this generates an inertia added to the rigid body. This phenomenon has been studied for a long time and it was Friedrich Bessel (1784-1846) who first proposed the concept of added masses in 1828 [42] and much research has been done since then to model these effects. Indeed, there are many methods that have been developed to analyze the problem and most are semi-empirical methods. To quantify the terms of added masses we first represent the blimp as a spheroid and at this point we can apply the semi-empirical method developed by Horace Lamb (1849-1934) [58]. This method is widely used in the literature for dynamic modeling of blimp [5, 37, 97].

We assume that the indoor blimp robot is characterized by a slow motion and it has an ellipsoid

shape with three planes of symmetry. The added-inertia can be expressed as [35]

$$\boldsymbol{M}_{Added} = diag\begin{bmatrix} m_{A_x} & m_{A_y} & m_{A_z} & I_{A_x} & I_{A_y} & I_{A_z} \end{bmatrix}^T \tag{A.43}$$

The added mass factors present in (A.43) are estimated through the semi-empirical method that uses the geometry of the body and the kinetic energy of an ideal fluid volume around the moving ellipsoid. The added or virtual mass is equal to the density of the surrounding fluid multiplied by a volume that depends only on the geometric shape of the body and results in a fraction of the volume of the ellipsoid [68]. The method developed by Lamb results in the definition of factors called precisely Lamb's k-factors [58], which are then multiplied by the terms of the inertia matrix of the rigid body and added to $\boldsymbol{M}_{RB}$. The equation of the standard ellipsoid in a Cartesian coordinate system is

$$\frac{x^2}{a^2} + \frac{y^2}{b^2} + \frac{z^2}{c^2} = 1$$

where a, b and c are the semi-axes reported in Figure A.2. A prolate spheroid is an ellipsoid of revolution obtained by letting $b = c$ and $a > b$.

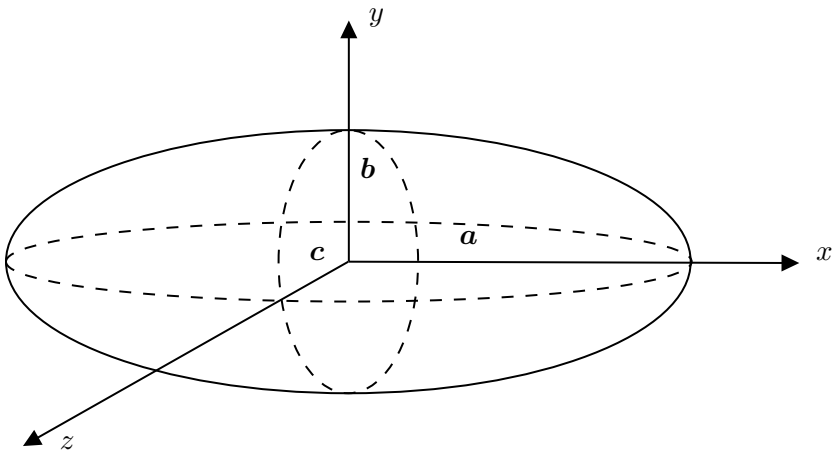

Figure A.2: Ellipsoid with semi-axes a, b and c.

In the case of an ellipsoid of revolution with semi-axes a and b (with $a \geq b$), i.e., a prolate ellipsoid, the moment of inertia is

$$I_{yh} = I_{zh} = \frac{4}{5}\pi\rho a b^2(a^2 + b^2) \tag{A.44}$$

Now we apply the Lamb's k-factors to calculate the added-mass terms

$$\begin{cases} m_{A_x} = k_1 m \\ m_{A_y} = m_{A_z} = k_2 m \\ I_{A_x} = 0 \\ I_{A_y} = I_{A_z} = k' I_{zh} \end{cases} \tag{A.45}$$

where the Lamb's k-factors are defined by

$$\begin{cases} k_1 = \dfrac{\alpha_0}{2-\alpha_0} \\ k_2 = \dfrac{\beta_0}{2-\beta_0} \\ k' = \dfrac{e^4(\beta_0-\alpha_0)}{(2-e^2)[2e^2-(2-e^2)(\beta_0-\alpha_0)]} \\ \alpha_0 = \dfrac{2(1-e^2)}{e^3}\left(\dfrac{1}{2}\ln\dfrac{1+e}{1-e}-e\right) \\ \beta_0 = \dfrac{1}{e^2}-\dfrac{1-e^2}{2e^3}\ln\dfrac{1+e}{1-e} \end{cases} \tag{A.46}$$

where e is the eccentricity of the ellipsoid:

$$e = \sqrt{1-\left(\frac{b}{a}\right)^2} \tag{A.47}$$

More details about the derivatives of added mass for other body symmetries can be found in [48]. In Figure A.3 we have reported the k-factors as a function of the ellipsoid aspect ratio. From the graph we can notice that when we consider a balloon with $a/b = 1$ which is a spherical balloon, $k_1 = k_2 = 0.5$ and $k' = 0$, this means that the balloon has an added mass equal to the 50% of the rigid body mass while the inertia does not change. If we start to elongate the shape transforming the spherical balloon in an ellipsoid one we have an increase in the added moment of inertia k' and in the lateral added mass k_2. The longitudinal added mass k_1 instead decreases.

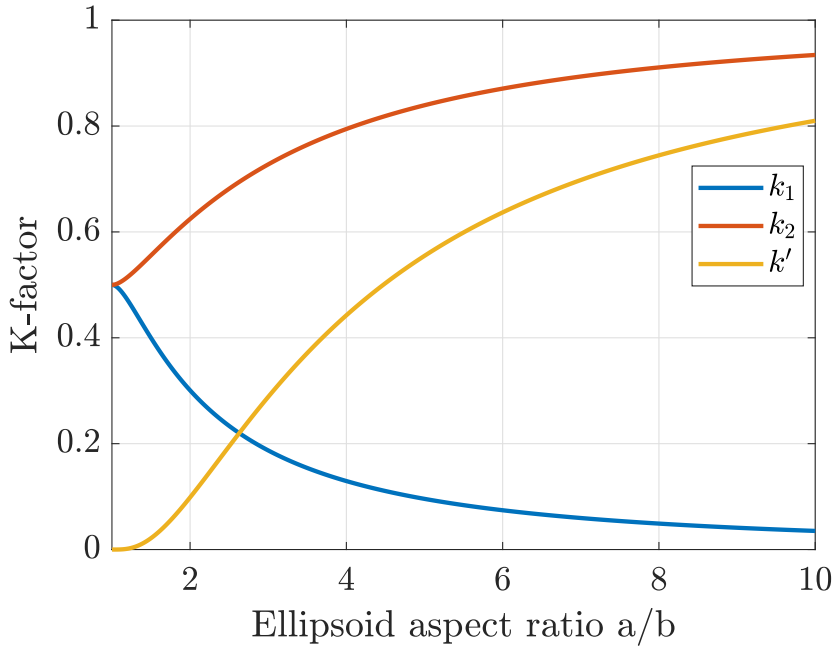

Figure A.3: Lamb's k-factors as a function of the ellipsoid hull aspect ratio.

A.4 Added mass forces and moments

In this section we want to derive the forces and moments of the added masses and we use the same approach of the rigid body Coriolis and centripetal matrix derivation (section A.2.3). Again, Kirchhoff's equations are used for the calculation of the kinetic energy of the fluid to derive the forces and moments acting on the blimp [35]. If we consider a rigid body moving in an ideal fluid, the added Coriolis and centripetal matrix satisfies the following property.

Property A.3. *The parametrization of* $\boldsymbol{C}_{Added}(\boldsymbol{\xi})$ *guaranties that the added Coriolis and centripetal matrix is skew-symmetrical:*

$$\boldsymbol{C}_{Added}(\boldsymbol{\xi}) = -\boldsymbol{C}_{Added}^{T}(\boldsymbol{\xi}) \quad \forall \boldsymbol{\xi} \in \mathbb{R}^6$$

by defining:

$$\boldsymbol{C}_{Added}(\boldsymbol{\xi}) = \begin{bmatrix} \boldsymbol{0}_{3\times 3} & -S(\boldsymbol{A}_{11}\boldsymbol{v} + \boldsymbol{A}_{12}\boldsymbol{\omega}) \\ -S(\boldsymbol{A}_{11}\boldsymbol{v} + \boldsymbol{A}_{12}\boldsymbol{\omega}) & -S(\boldsymbol{A}_{21}\boldsymbol{v} + \boldsymbol{A}_{22}\boldsymbol{\omega}) \end{bmatrix} \tag{A.48}$$

where $\boldsymbol{A}_{ij}$ $(i, j = 1, 2)$ *are the four* 3×3 *sub-matrices of the added inertia matrix* $\boldsymbol{M}_{Added}$.

Proof. If we substitute

$$\boldsymbol{M} = \boldsymbol{M}_{Added} = \begin{bmatrix} \boldsymbol{A}_{11} & \boldsymbol{A}_{12} \\ \boldsymbol{A}_{21} & \boldsymbol{A}_{22} \end{bmatrix}$$

into (A.33) in Theorem A.1 we can prove (A.48). □

Substituting (A.43) using the diagonal form into (A.48), we can express the added mass Coriolis and centripetal matrix in component:

$$\boldsymbol{C}_{Added}(\boldsymbol{\xi}) = \begin{bmatrix} 0 & 0 & 0 & 0 & -m'_z v_z & m'_y v_y \\ 0 & 0 & 0 & m'_z v_z & 0 & -m'_x v_x \\ 0 & 0 & 0 & -m'_y v_y & m'_x v_x & 0 \\ 0 & -m'_z v_z & m'_y v_y & 0 & -I'_z \omega_z & I'_y \omega_y \\ m'_z v_z & 0 & -m'_x v_x & I'_z \omega_z & 0 & -I'_x \omega_x \\ -m'_y v_y & m'_x v_x & 0 & -I'_y \omega_y & I'_x \omega_x & 0 \end{bmatrix}$$

A.5 Damping forces and moments

In this section we analyze the term $\boldsymbol{D}(\boldsymbol{\xi})$ that is the 6×6 aerodynamic dumping matrix due to air friction which is a function of the velocity of the body. Regarding the theory of friction we will not go into detail, what we say is that in general we can distinguish two fundamental regions for friction: linear friction due to laminar boundary layers and quadratic friction due to turbulent boundary layers [25, 28]. Matrix $\boldsymbol{D}(\boldsymbol{\xi})$ also contains the effects of vortex shedding along the flow line of the airship's hull [87]. For a rigid-body moving through an ideal fluid, the total hydrodynamic damping matrix which incorporates all these aerodynamic effects satisfies the following property.

Property A.4. *The hydrodynamic damping matrix* $\boldsymbol{D}(\boldsymbol{\xi})$ *is a real, non-symmetrical and strictly positive matrix which means that*

$$\boldsymbol{D}(\boldsymbol{\xi}) > 0 \quad \forall \boldsymbol{\xi} \in \mathbb{R}^6$$

Proof. The property (A.4) is demonstrated by the dissipative nature of the damping forces. Ideed, writing the quadratic form we obtain

$$\boldsymbol{\xi}^T \boldsymbol{D}(\boldsymbol{\xi})\boldsymbol{\xi} > 0 \quad \forall \boldsymbol{\xi} \neq 0$$

□

However, for the practical determination of the damping matrix it is very difficult to quantify all the terms of $\boldsymbol{D}(\boldsymbol{\xi})$. As proposed by [35], for underwater vehicles moving at low velocity, terms above the second order can be ignored and a diagonal structure is proposed with only the contribution of linear and quadratic terms

$$\boldsymbol{D}(\boldsymbol{\xi}^b) = -diag \begin{bmatrix} D_{v_x} + D_{v_x^2}|v_x^b| \\ D_{v_y} + D_{v_y^2}|v_y^b| \\ D_{v_z} + D_{v_z^2}|v_z^b| \\ D_{\omega_x} + D_{\omega_x^2}|\omega_x^b| \\ D_{\omega_y} + D_{\omega_y^2}|\omega_y^b| \\ D_{\omega_z} + D_{\omega_z^2}|\omega_z^b| \end{bmatrix} \tag{A.49}$$

where D_{v_x}, D_{v_y}, D_{v_z}, D_{ω_x}, D_{ω_y}, D_{ω_z} are the linear damping coefficients, and $D_{v_x^2}$, $D_{v_y^2}$, $D_{v_z^2}$, $D_{\omega_x^2}$, $D_{\omega_y^2}$, $D_{\omega_z^2}$ are the quadratic damping coefficients. This structure in equation (A.49) is therefore a valid approximation for low-speed vehicles with a symmetrical ellipsoid shape. Another author [97], sharing this model, proposed an experimental method to be able to identify the twelve damping coefficients. The test is based on providing a known thrust to the system and by measuring the linear and angular velocity it is possible to determine the coefficients by fitting the results of the model with that of the tests.

A.6 Restoring forces and moments

In this section we analyze the term $\boldsymbol{g}(\boldsymbol{\eta}^n)$ which is the combination of gravity and buoyancy forces and moments; in the hydrodynamic terminology they are called restoring forces. The buoyancy is an aerostatic lift force acting on an airship which is independent of flight speed. The buoyancy force is explained by the famous Archimedes principle, it is equivalent to the weight of the displaced fluid that is occupied by the volume of the blimp. The combination of gravity and buoyancy is called restoring force because the union of the two allows the airship to stay up in the air without feeling the gravitational effect, having an upward restore that counteracts the downward force. The magnitude of gravitational and buoyancy forces are expressed by

$$\begin{cases} f_G = mg \\ f_B = \rho_{air} V g \end{cases} \tag{A.50}$$

where $V = \frac{4}{3}\pi ab^2$ is the volume of the ellipsoidal balloon with semi-axes a and b, m is the mass of the blimp, g is the Earth gravitational acceleration and ρ_{air} is the air density. Now we want to express the gravity and buoyant force in the body-fixed frame applying the change of basis equation

(2.5):

$$\boldsymbol{f}_G^b = \boldsymbol{R}_b^n \boldsymbol{f}_G^n = (\boldsymbol{R}_n^b)^T \boldsymbol{f}_G^n = (\boldsymbol{R}_n^b)^T \begin{bmatrix} 0 \\ 0 \\ f_G \end{bmatrix}$$

$$\boldsymbol{f}_B^b = \boldsymbol{R}_b^n \boldsymbol{f}_B^n = (\boldsymbol{R}_n^b)^T \boldsymbol{f}_B^n = (\boldsymbol{R}_n^b)^T \begin{bmatrix} 0 \\ 0 \\ f_B \end{bmatrix}$$

Hence, we can write the restoring vector expressing the forces and moments in the F_b reference frame.

$$\boldsymbol{g}(\boldsymbol{\eta}^n) = - \begin{bmatrix} \boldsymbol{f}_G^b + \boldsymbol{f}_B^b \\ \boldsymbol{r}_G^b \times \boldsymbol{f}_G^b + \boldsymbol{r}_B^b \times \boldsymbol{f}_B^b \end{bmatrix} \tag{A.51}$$

Making it explicit we have

$$\boldsymbol{g}(\boldsymbol{\eta}^n) = - \begin{bmatrix} -(f_G - f_B)\sin\theta \\ (f_G - f_B)\cos\theta\sin\phi \\ (f_G - f_B)\cos\theta\cos\phi \\ (y_G f_G - y_B f_B)\cos\theta\cos\phi - (z_G f_G - z_B f_B)\cos\theta\sin\phi \\ (z_G f_G - z_B f_B)\sin\theta - (x_G f_G - x_B f_B)\cos\theta\cos\phi \\ (x_G f_G - x_B f_B)\cos\theta\sin\phi + (y_G f_G - y_B f_B)\sin\theta \end{bmatrix} \tag{A.52}$$

A.7 Vector representations of equation of motion

Up to now we have represent the equations of motion expressed in the body-fixed reference frame. However it is possible to write the dynamics in the earth-fixed reference frame which can be obtained from the body-fixed with the use of the kinematics equation.

- **Body-fixed vector representation**

In equation (A.41) we have already shown the nonlinear equation of motion in the body-fixed which we report here

$$\boldsymbol{M}\dot{\boldsymbol{\xi}} + \boldsymbol{C}(\boldsymbol{\xi})\boldsymbol{\xi} + \boldsymbol{D}(\boldsymbol{\xi})\boldsymbol{\xi} + \boldsymbol{g}(\boldsymbol{\eta}) = \boldsymbol{\tau} \tag{A.53}$$

and we recall from (2.11) the kinematics equation

$$\dot{\boldsymbol{\eta}} = \boldsymbol{J}(\boldsymbol{\eta})\boldsymbol{\xi} \tag{A.54}$$

In both (A.53) and (A.54) we have omitted the superscript ^{b} and ^{n} because we know in which reference frame $\boldsymbol{\xi}$ and $\boldsymbol{\eta}$ are defined.

- **Earth-fixed vector representation**

To obtain the equations of motion in the earth-fixed reference frame, $\dot{\boldsymbol{\eta}}$ and $\ddot{\boldsymbol{\eta}}$ must appear in place of $\boldsymbol{\xi}$ and $\dot{\boldsymbol{\xi}}$ inside equation (A.53). To find the relationship between $\boldsymbol{\eta}$ and $\boldsymbol{\xi}$ we make use of the equation of kinematics (A.54) and write the following relationships (assuming that $\boldsymbol{J}(\boldsymbol{\eta})$ is not

singular):

$$\dot{\boldsymbol{\eta}} = \boldsymbol{J}(\boldsymbol{\eta})\boldsymbol{\xi} \Longleftrightarrow \boldsymbol{\xi} = \boldsymbol{J}^{-1}(\boldsymbol{\eta})\dot{\boldsymbol{\eta}}$$
$$\ddot{\boldsymbol{\eta}} = \boldsymbol{J}(\boldsymbol{\eta})\dot{\boldsymbol{\xi}} + \dot{\boldsymbol{J}}(\boldsymbol{\eta})\boldsymbol{\xi} \Longleftrightarrow \dot{\boldsymbol{\xi}} = \boldsymbol{J}^{-1}(\boldsymbol{\eta})\big[\ddot{\boldsymbol{\eta}} - \dot{\boldsymbol{J}}(\boldsymbol{\eta})\boldsymbol{J}^{-1}(\boldsymbol{\eta})\dot{\boldsymbol{\eta}}\big]$$

With these transformation equations we can therefore redefine the matrices that appear in (A.53) in this way:

$$\begin{aligned}
\boldsymbol{M}_{\boldsymbol{\eta}}(\boldsymbol{\eta}) &= \boldsymbol{J}^{-T}(\boldsymbol{\eta})\boldsymbol{M}\boldsymbol{J}^{-1}(\boldsymbol{\eta}) \\
\boldsymbol{C}_{\boldsymbol{\eta}}(\boldsymbol{\xi},\boldsymbol{\eta}) &= \boldsymbol{J}^{-T}(\boldsymbol{\eta})\big[\boldsymbol{C}(\boldsymbol{\xi}) - \boldsymbol{M}\boldsymbol{J}^{-1}(\boldsymbol{\eta})\dot{\boldsymbol{J}}(\boldsymbol{\eta})\big]\boldsymbol{J}^{-1}(\boldsymbol{\eta}) \\
\boldsymbol{D}_{\boldsymbol{\eta}}(\boldsymbol{\xi},\boldsymbol{\eta}) &= \boldsymbol{J}^{-T}(\boldsymbol{\eta})\boldsymbol{D}(\boldsymbol{\xi})\boldsymbol{J}^{-1}(\boldsymbol{\eta}) \\
\boldsymbol{g}_{\boldsymbol{\eta}}(\boldsymbol{\eta}) &= \boldsymbol{J}^{-T}(\boldsymbol{\eta})\boldsymbol{g}(\boldsymbol{\eta}) \\
\boldsymbol{\tau}_{\boldsymbol{\eta}}(\boldsymbol{\eta}) &= \boldsymbol{J}^{-T}(\boldsymbol{\eta})\boldsymbol{\tau}
\end{aligned} \tag{A.55}$$

Using this nomenclature we then write the dynamics equation in the earth-fixed vector representation

$$\boldsymbol{M}_{\boldsymbol{\eta}}(\boldsymbol{\eta})\ddot{\boldsymbol{\eta}} + \boldsymbol{C}_{\boldsymbol{\eta}}(\boldsymbol{\xi},\boldsymbol{\eta})\dot{\boldsymbol{\eta}} + \boldsymbol{D}_{\boldsymbol{\eta}}(\boldsymbol{\xi},\boldsymbol{\eta})\dot{\boldsymbol{\eta}} + \boldsymbol{g}_{\boldsymbol{\eta}}(\boldsymbol{\eta}) = \boldsymbol{\tau}_{\boldsymbol{\eta}} \tag{A.56}$$

A.7.1 Properties of the body-fixed vector representation

We have seen separately the properties of the matrices related to the equation of rigid body dynamics (A.31), now we give the properties of the total matrices also with the contribution of the added terms. For the inertia matrix $\boldsymbol{M}$ of a rigid body holds the following property.

Property A.5. *$\boldsymbol{M}$ is strictly positive if and only if $\boldsymbol{M}_{Added} > 0$, that is:*

$$\boldsymbol{M} = \boldsymbol{M}_{RB} + \boldsymbol{M}_{Added} > 0$$

If we assume that the body moves at a low speed then the inertia matrix is symmetrical and therefore being strictly positive it is also positive definite.

$$\boldsymbol{M} = \boldsymbol{M}^T > 0$$

Proof. If we want that $\boldsymbol{M} = \boldsymbol{M}_{RB} + \boldsymbol{M}_{Added}$ is positive definite then the two matrices $\boldsymbol{M}_{RB}$ and $\boldsymbol{M}_{Added}$ must necessarily be positive definite too. □

As for the Coriolis and centripetal matrix of a rigid body which moves in an ideal fluid, the following property holds.

Property A.6. *$\boldsymbol{C}(\boldsymbol{\xi})$ is skew-symmetrical, i.e.:*

$$\boldsymbol{C}(\boldsymbol{\xi}) = -\boldsymbol{C}^T(\boldsymbol{\xi}) \quad \forall \boldsymbol{\xi} \in \mathbb{R}^6$$

Proof. If we want that $\boldsymbol{C}(\boldsymbol{\xi})$ is skew-symmetrical then the two matrices $\boldsymbol{C}_{RB}(\boldsymbol{\xi})$ and $\boldsymbol{C}_{Added}(\boldsymbol{\xi})$ must be skew-symmetrical too. □

A.7.2 Properties of the earth-fixed vector representation

For the matrices that appear in the dynamic model written in the earth-fixed frame (A.56), the following properties are valid.

(1) $\boldsymbol{M}_{\boldsymbol{\eta}}(\boldsymbol{\eta}) = \boldsymbol{M}_{\boldsymbol{\eta}}{}^{T}(\boldsymbol{\eta}) > 0 \quad \forall \boldsymbol{\eta} \in \mathbb{R}^6$

(2) $\boldsymbol{s}^T[\dot{\boldsymbol{M}}_{\boldsymbol{\eta}}(\boldsymbol{\eta}) - 2\boldsymbol{C}_{\boldsymbol{\eta}}(\boldsymbol{\xi}, \boldsymbol{\eta})]\boldsymbol{s} = 0 \quad \forall \boldsymbol{s} \in \mathbb{R}^6,\ \boldsymbol{\xi} \in \mathbb{R}^6,\ \boldsymbol{\eta} \in \mathbb{R}^6$

(3) $\boldsymbol{D}_{\boldsymbol{\eta}}(\boldsymbol{\xi}, \boldsymbol{\eta}) > 0 \quad \forall \boldsymbol{\xi} \in \mathbb{R}^6,\ \boldsymbol{\eta} \in \mathbb{R}^6$

if $\boldsymbol{M} = \boldsymbol{M}^T > 0$ and $\dot{\boldsymbol{M}} = 0$. It should be notated that $\boldsymbol{C}_{\boldsymbol{\eta}}(\boldsymbol{\xi}, \boldsymbol{\eta})$ will not be skew-symmetrical although $\boldsymbol{C}(\boldsymbol{\xi})$ is skew-symmetrical.

Appendix B

Electromagnetic Field Theory

B.1 Introduction to magnetostatics

In this appendix we want to provide the basic notions of magnetostatics which are fundamental to understand the developments in the study of electric motors and magnetic disturbances. Magnetostatics is the branch of electromagnetism that studies static magnetic fields, that is, invariant over time. In electrostatics it is stationary electric charges that generate electrostatic fields, while in magnetostatics it is electric currents that generate static magnetic fields. This recall of the theory of magnetism is inspired by [40, 43, 49].

B.1.1 The magnetic field of a steady current

As we have already said, static currents generate magnetic fields that are constant over time, i.e., static and this gives rise to magnetostatics study. Let's start by defining the magnetic field generated by an infinitesimal element of steady current, the formula that defines this field is called Biot-Savart's law

$$\boldsymbol{B}(\boldsymbol{r}) = \frac{\mu_0}{4\pi} \int \frac{I d\boldsymbol{l}' \times (\boldsymbol{r} - \boldsymbol{r}')}{|\boldsymbol{r} - \boldsymbol{r}'|^3} = \frac{\mu_0 I}{4\pi} \int \frac{d\boldsymbol{l}' \times (\boldsymbol{r} - \boldsymbol{r}')}{|\boldsymbol{r} - \boldsymbol{r}'|^3} \tag{B.1}$$

where $d\boldsymbol{l}'$ is an element of length of wire in which current flows, $(\boldsymbol{r} - \boldsymbol{r}')$ is the vector that indicates the point in which the field is to be determined and originates in the source of the field and it is represented in Figure B.1. The integration of Biot Savart's law (B.1) is carried out along the path and in the direction of the current. The constant μ_0 is the magnetic permeability of free space and it is defined as

$$\mu_0 = 4\pi \times 10^{-7} \text{ N/A}^2$$

The units of $\boldsymbol{B}$ are N/(Am) or Tesla (T).

The Biot-Savart law can also be extended to current distributions on surfaces and on volumes, in this case we have

$$\boldsymbol{B}(\boldsymbol{r}) = \frac{\mu_0}{4\pi} \int \frac{\boldsymbol{K}(\boldsymbol{r}') \times (\boldsymbol{r} - \boldsymbol{r}')}{|\boldsymbol{r} - \boldsymbol{r}'|^3} ds'$$

$$\boldsymbol{B}(\boldsymbol{r}) = \frac{\mu_0}{4\pi} \int \frac{\boldsymbol{J}(\boldsymbol{r}') \times (\boldsymbol{r} - \boldsymbol{r}')}{|\boldsymbol{r} - \boldsymbol{r}'|^3} dv'$$

respectively.

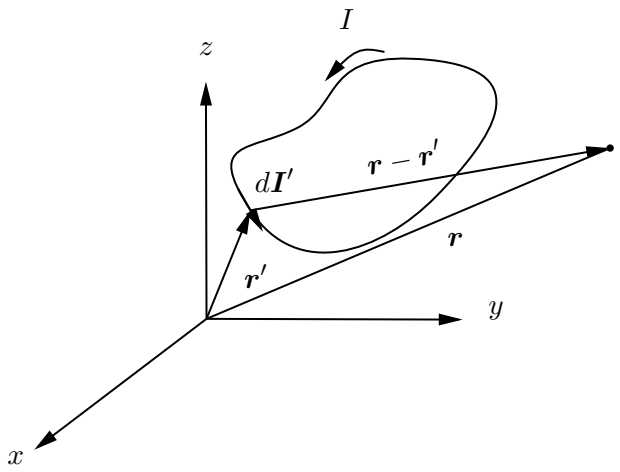

Figure B.1: Point $\boldsymbol{r}$ at which the magnetic field of a steady line current is calculated.

B.1.2 The divergence and curl of B

Now we want to obtain two important quantities that are typically calculated in electromagnetism, i.e. the divergence and the rotor of $\boldsymbol{B}$ which lead to the definition of what are called the basic equations that describe magnetism, i.e. the Maxwell equations. We rewrite here the Biot-Savart law for the case in which we have a volume current

$$\boldsymbol{B}(\boldsymbol{r}) = \frac{\mu_0}{4\pi}\int \frac{\boldsymbol{J}(\boldsymbol{r}')\times(\boldsymbol{r}-\boldsymbol{r}')}{|\boldsymbol{r}-\boldsymbol{r}'|^3}dv' \tag{B.2}$$

We can interpret this formula looking at Figure B.2 where we have the point at which we want to calculate the magnetic field that is defined by the vector $\boldsymbol{r} = (x, y, z)$. The field is calculated as an integral over the current distribution $\boldsymbol{J}(x', y', z')$ over the primed coordinates but the field $\boldsymbol{B}$ then is a function of not primed variables (x, y, z). The quantity at the denominator is defined as follow

$$(\boldsymbol{r}-\boldsymbol{r}') = (x-x')\hat{\boldsymbol{x}} + (y-y')\hat{\boldsymbol{y}} + (z-z')\hat{\boldsymbol{z}}$$

and the integration element of volume is

$$dv' = dx'dy'dz'$$

Now we want to determine the divergence of the magnetic field and we can use equation (B.2) applying the operator at both sides, obtaining

$$\boldsymbol{\nabla}\cdot\boldsymbol{B}(\boldsymbol{r}) = \frac{\mu_0}{4\pi}\int_V \boldsymbol{\nabla}\cdot\left(\boldsymbol{J}(\boldsymbol{r}')\times\frac{(\boldsymbol{r}-\boldsymbol{r}')}{|\boldsymbol{r}-\boldsymbol{r}'|^3}\right)dv' \tag{B.3}$$

In the right-hand side we can apply the following product role

$$\boldsymbol{\nabla}\cdot(\boldsymbol{A}\times\boldsymbol{B}) = \boldsymbol{B}\cdot(\boldsymbol{\nabla}\times\boldsymbol{A}) - \boldsymbol{A}\cdot(\boldsymbol{\nabla}\times\boldsymbol{B})$$

and this leads to

$$\boldsymbol{\nabla}\cdot\left(\boldsymbol{J}(\boldsymbol{r}')\times\frac{(\boldsymbol{r}-\boldsymbol{r}')}{|\boldsymbol{r}-\boldsymbol{r}'|^3}\right) = \frac{(\boldsymbol{r}-\boldsymbol{r}')}{|\boldsymbol{r}-\boldsymbol{r}'|^3}\cdot(\boldsymbol{\nabla}\times\boldsymbol{J}(\boldsymbol{r}')) - \boldsymbol{J}(\boldsymbol{r}')\cdot\left(\boldsymbol{\nabla}\times\frac{(\boldsymbol{r}-\boldsymbol{r}')}{|\boldsymbol{r}-\boldsymbol{r}'|^3}\right) \tag{B.4}$$

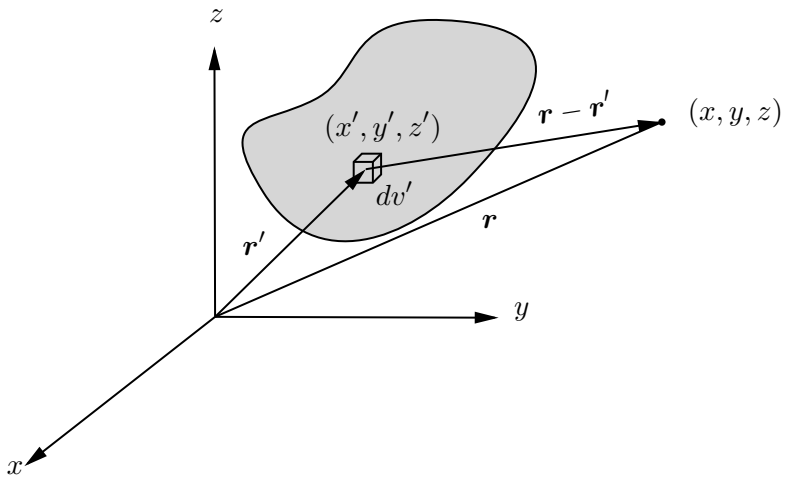

Figure B.2: Point $\boldsymbol{r}$ at which the magnetic field of a volume current is calculated.

The first term on the right-hand side is zero, $\boldsymbol{\nabla} \times \boldsymbol{J}(\boldsymbol{r}') = 0$, because the divergence is calculated with respect to the primed variables while $\boldsymbol{J}(\boldsymbol{r}')$ doesn't depend on the unprimed variables. The second term on the right-hand side

$$\boldsymbol{\nabla} \times \frac{(\boldsymbol{r} - \boldsymbol{r}')}{|\boldsymbol{r} - \boldsymbol{r}'|^3} = 0$$

So, we have proved that the entire right-hand side of (B.4) is zero and therefore substituting this result inside equation (B.3) we obtain that the divergence of the magnetic field is zero.

$$\boldsymbol{\nabla} \cdot \boldsymbol{B}(\boldsymbol{r}) = 0$$

Now we want to calculate the curl to equation (B.2).

$$\boldsymbol{\nabla} \times \boldsymbol{B}(\boldsymbol{r}) = \frac{\mu_0}{4\pi} \int_V \boldsymbol{\nabla} \times \left(\boldsymbol{J} \times \frac{(\boldsymbol{r} - \boldsymbol{r}')}{|\boldsymbol{r} - \boldsymbol{r}'|^3} \right) dv' \tag{B.5}$$

In this case we use another product rule for the double cross product which is

$$\boldsymbol{\nabla} \times (\boldsymbol{A} \times \boldsymbol{B}) = (\boldsymbol{B} \cdot \boldsymbol{\nabla})\boldsymbol{A} - (\boldsymbol{A} \cdot \boldsymbol{\nabla})\boldsymbol{B} + \boldsymbol{A}(\boldsymbol{\nabla} \cdot \boldsymbol{B}) - \boldsymbol{B}(\boldsymbol{\nabla} \cdot \boldsymbol{A}) \tag{B.6}$$

Using this for the integrand function of (B.5) yields

$$\boldsymbol{\nabla} \times \left(\boldsymbol{J}(\boldsymbol{r}') \times \frac{(\boldsymbol{r} - \boldsymbol{r}')}{|\boldsymbol{r} - \boldsymbol{r}'|^3} \right) = \boldsymbol{J}(\boldsymbol{r}') \left(\boldsymbol{\nabla} \cdot \frac{(\boldsymbol{r} - \boldsymbol{r}')}{|\boldsymbol{r} - \boldsymbol{r}'|^3} \right) - (\boldsymbol{J}(\boldsymbol{r}') \cdot \boldsymbol{\nabla}) \frac{(\boldsymbol{r} - \boldsymbol{r}')}{|\boldsymbol{r} - \boldsymbol{r}'|^3} \tag{B.7}$$

Let's analyze the first term on the right-hand side

$$\boldsymbol{\nabla} \cdot \left(\frac{(\boldsymbol{r} - \boldsymbol{r}')}{|\boldsymbol{r} - \boldsymbol{r}'|^3} \right) = 4\pi \delta^3(\boldsymbol{r} - \boldsymbol{r}') \tag{B.8}$$

where $\delta^3(\boldsymbol{r})$ is three dimensional delta function defined as

$$\delta^3(\boldsymbol{r}) = \delta(x)\delta(y)\delta(z)$$

with δ the one-dimensional Dirac delta function defined as

$$\delta(x) = \begin{cases} 0, & \text{if } x \neq 0 \\ \infty, & \text{if } x = 0 \end{cases}$$

and

$$\int_{-\infty}^{\infty} \delta(x)dx = 1$$

We will now demonstrate that the second term on the right-hand side integrates to zero. Since the derivatives inside $\boldsymbol{\nabla}$ act on the ratio $(\boldsymbol{r} - \boldsymbol{r}')/|\boldsymbol{r} - \boldsymbol{r}'|^3$, we can change $\boldsymbol{\nabla}$ with $\boldsymbol{\nabla}'$ with the appearance of a minus sign.

$$-(\boldsymbol{J}(\boldsymbol{r}') \cdot \boldsymbol{\nabla}) \frac{(\boldsymbol{r} - \boldsymbol{r}')}{|\boldsymbol{r} - \boldsymbol{r}'|^3} = (\boldsymbol{J}(\boldsymbol{r}') \cdot \boldsymbol{\nabla}') \frac{(\boldsymbol{r} - \boldsymbol{r}')}{|\boldsymbol{r} - \boldsymbol{r}'|^3} \tag{B.9}$$

We use now another product role for the right-hand side, which is

$$\boldsymbol{\nabla} \cdot (f\boldsymbol{A}) = f(\boldsymbol{\nabla} \cdot \boldsymbol{A}) + \boldsymbol{A} \cdot (\boldsymbol{\nabla} f)$$

and if we focus on one component of (B.9), for instance the x component, we obtain

$$(\boldsymbol{J}(\boldsymbol{r}') \cdot \boldsymbol{\nabla}') \left(\frac{x - x'}{|\boldsymbol{r} - \boldsymbol{r}'|^3} \right) = \boldsymbol{\nabla}' \cdot \left[\frac{(x - x')}{|\boldsymbol{r} - \boldsymbol{r}'|^3} \boldsymbol{J}(\boldsymbol{r}') \right] - \left(\frac{x - x'}{|\boldsymbol{r} - \boldsymbol{r}'|^3} \right) (\boldsymbol{\nabla}' \cdot \boldsymbol{J}(\boldsymbol{r}')) \tag{B.10}$$

The second term in the right-hand side is the divergence of $\boldsymbol{J}(\boldsymbol{r}')$ which for steady currents is zero. Therefore equating the remaining term (the first in the right-hand side of (B.10) with the left-hand side of (B.9)), we obtain

$$\left[-(\boldsymbol{J}(\boldsymbol{r}') \cdot \boldsymbol{\nabla}') \frac{x - x'}{|\boldsymbol{r} - \boldsymbol{r}'|^3} \right]_x = \boldsymbol{\nabla}' \cdot \left[\frac{(x - x')}{|\boldsymbol{r} - \boldsymbol{r}'|^3} \boldsymbol{J}(\boldsymbol{r}') \right]$$

This is how we have transformed the second term of the right-hand side of equation (B.7) that now must to be integrated

$$\int_V \boldsymbol{\nabla}' \cdot \left[\frac{(x - x')}{|\boldsymbol{r} - \boldsymbol{r}'|^3} \boldsymbol{J}(\boldsymbol{r}') \right] dv' = \oint_S \frac{(x - x')}{|\boldsymbol{r} - \boldsymbol{r}'|^3} \boldsymbol{J}(\boldsymbol{r}') \cdot d\boldsymbol{s}' \tag{B.11}$$

Here we have used, the divergence theorem, also known Ostrogradsky's theorem (or Gauss's theorem) which relates flux through the surface (i.e. the surface integral over a closed surface) to the volume integral of the divergence over the region inside the surface. To prove that this integral is zero we consider a large enough volume such that to include all the current inside, in this way on the external surface the current is zero and hence the integral (B.11) is zero.

In conclusion, by using this result and the expression (B.8) inside the curl (B.5) we obtain

$$\boldsymbol{\nabla} \times \boldsymbol{B}(\boldsymbol{r}) = \frac{\mu_0}{4\pi} \int_V \boldsymbol{J}(\boldsymbol{r}') 4\pi \delta^3(\boldsymbol{r} - \boldsymbol{r}') dv' = \mu_0 \boldsymbol{J}(\boldsymbol{r})$$

The equation for the curl of $\boldsymbol{B}$,

$$\boldsymbol{\nabla} \times \boldsymbol{B} = \mu_0 \boldsymbol{J}$$

in differential form is also called Ampère's law.

B.1.3 Magnetic vector potential

In the previous section we have found the two basic differential laws of magnetostatics, also called Maxwell equations which are the divergence and the curl of the magnetic field.

$$\begin{cases} \boldsymbol{\nabla} \cdot \boldsymbol{B} = 0, & \text{(No name)} \\ \boldsymbol{\nabla} \times \boldsymbol{B} = \mu_0 \boldsymbol{J}, & \text{(Ampère's law)} \end{cases} \tag{B.12}$$

Now we are interested in finding a way to solve them. Let us first analyze a simple case in which there are no distributions of currents $\boldsymbol{J}$. In this case, therefore, the curl of $\boldsymbol{B}$ is zero.

$$\boldsymbol{\nabla} \times \boldsymbol{B} = 0$$

This means that there exists a magnetic scalar potential Φ_M for which $\boldsymbol{B}$ can be written as minus the gradient of the magnetic scalar potential.

$$\boldsymbol{B} = -\boldsymbol{\nabla} \Phi_M$$

In this particular case equations (B.12) can be transformed into the Laplace equation for Φ_M [49].

If in the general case the distribution of currents $\boldsymbol{J}$ is non-zero, then in order to solve the Maxwell equations in the differential form (B.12), it is possible to make use of the divergence of $\boldsymbol{B}$. Indeed, since it is valid that $\boldsymbol{\nabla} \cdot \boldsymbol{B} = 0$ in all space then the magnetic field $\boldsymbol{B}$ is the rotor of a vector field $\boldsymbol{A}(\boldsymbol{r})$ called vector potential.

$$\boldsymbol{B} = \boldsymbol{\nabla} \times \boldsymbol{A} \tag{B.13}$$

If we substitute (B.13) into the second equation in (B.12), we find

$$\boldsymbol{\nabla} \times (\boldsymbol{\nabla} \times \boldsymbol{A}) = \mu_0 \boldsymbol{J}$$

Applying the product role of double cross product (B.6), we obtain

$$\boldsymbol{\nabla}(\boldsymbol{\nabla} \cdot \boldsymbol{A}) - \nabla^2 \boldsymbol{A} = \mu_0 \boldsymbol{J} \tag{B.14}$$

The potential $\boldsymbol{A}$ satisfies the Coulomb gauge condition, that is

$$\boldsymbol{\nabla} \cdot \boldsymbol{A} = 0 \tag{B.15}$$

Therefore, we can substitute this property (B.15) of the vector potential $\boldsymbol{A}$ into equation (B.14) obtaining

$$\nabla^2 \boldsymbol{A} = -\mu_0 \boldsymbol{J} \tag{B.16}$$

Now we can find a solution to equation (B.16). We express this solution in the integral form using the free space Green's function for ∇^2 [40] which is defined as

$$G(\boldsymbol{r}, \boldsymbol{r}') = -\frac{1}{4\pi} \frac{1}{|\boldsymbol{r} - \boldsymbol{r}'|}$$

Hence the vector potential $\boldsymbol{A}$ becomes

$$\boldsymbol{A}(\boldsymbol{r}) = \frac{\mu_0}{4\pi}\int_V \frac{\boldsymbol{J}(\boldsymbol{r'})}{|\boldsymbol{r}-\boldsymbol{r'}|}dv' \tag{B.17}$$

Once we know the vector potential $\boldsymbol{A}$, we can compute the $\boldsymbol{B}$-field from equation (B.13) which gives

$$\boldsymbol{B}(\boldsymbol{r}) = \boldsymbol{\nabla}\times\boldsymbol{A}(\boldsymbol{r}) = \frac{\mu_0}{4\pi}\int_V \boldsymbol{\nabla}\times\frac{\boldsymbol{J}(\boldsymbol{r'})}{|\boldsymbol{r}-\boldsymbol{r'}|}dv' = \frac{\mu_0}{4\pi}\int_V \frac{\boldsymbol{J}(\boldsymbol{r'})\times(\boldsymbol{r}-\boldsymbol{r'})}{|\boldsymbol{r}-\boldsymbol{r'}|^3}dv'$$

And of course we find the Biot-Savart law that we defined in (B.2).

B.1.4 Multipole expansion of the vector potential

We have seen from equation (B.17) that to calculate the vector potential it is necessary to know the distribution of currents in space. An alternative approach could be that of using an approximate formula that allows to know the value of $\boldsymbol{A}$ at a point distant from the source. To do this, we will use the multipole expansion which is a widely used concept in the study of electromagnetic and gravitational fields, where the fields in distant points are given in terms of sources in a small region. With the multipole expansion we write the magnetic potential with a power series of the type $1/r$ with r the distance of the point in question from the source. This situation is shown in Figure B.3. In the series development, the distance at which we set the point to calculate the potential is fundamental, if this is sufficiently large then the dominant terms in the power series will be those of lower order while the higher order terms will tend to vanish more. The multipolar expansion is expressed as the sum of terms called moments. The first (zero-order) term is called the monopolar moment, the second (first-order) term is called the dipolar moment, the third (second-order) term is called quadrupole moment, the fourth (third-order) term is called the octuple moment, and etc. A multipole expansion can provide an exact description of the potential i.e., it can converge. However, this typically occurs under two conditions: the first is if the sources are close to the origin and the point where the potential is to be observed is far from the origin; the second condition is the opposite of the first that is, if the sources are far from the origin and the potential is observed close to the origin. In the first case the coefficients of the series expansion are called external multipolar moments while in the second case they are called internal multipolar moments. To obtain the multipole expansion let's consider the triangle in Figure B.3 and let's apply the law of cosines to it.

$$|\boldsymbol{r}-\boldsymbol{r'}| = r^2 + (r')^2 - 2rr'\cos\alpha = r^2\left[1+\left(\frac{r'}{r}\right)^2 - 2\left(\frac{r'}{r}\right)\cos\alpha\right] \tag{B.18}$$

where we can see from Figure B.3 that α is the angle between $\boldsymbol{r}$ and $\boldsymbol{r'}$. Now if we define the quantity ϵ as

$$\epsilon = \left(\frac{r'}{r}\right)\left(\frac{r'}{r} - 2\cos\alpha\right) \tag{B.19}$$

we can rewrite equation (B.18) substituting (B.19) inside.

$$|\boldsymbol{r}-\boldsymbol{r'}| = r\sqrt{1+\epsilon} \tag{B.20}$$

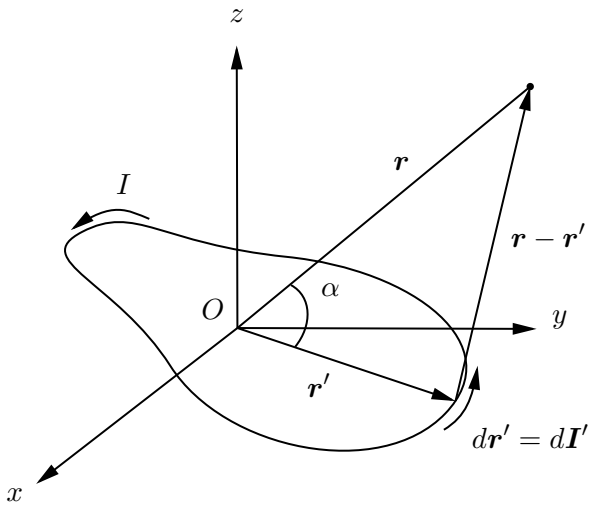

Figure B.3: Vector definition for multipole expansion of vector potential.

The quantity we are interested in is the inverse of (B.20), which is

$$\frac{1}{|\boldsymbol{r}-\boldsymbol{r}'|} = \frac{1}{r}(1+\epsilon)^{-1/2} \tag{B.21}$$

If we assume that we want to observe the potential at a great distance from the current source, i.e. $r'/r \ll 1$, then the quantity ϵ is much less than 1. Therefore we apply a binomial expansion to equation (B.21).

$$\frac{1}{|\boldsymbol{r}-\boldsymbol{r}'|} = \frac{1}{r}(1+\epsilon)^{-1/2} = \frac{1}{r}\left(1 - \frac{1}{2}\epsilon + \frac{3}{8}\epsilon^2 - \frac{5}{16}\epsilon^3 + \cdots\right)$$

If we make explicit ϵ in terms of r, r', and α, we obtain

$$\frac{1}{|\boldsymbol{r}-\boldsymbol{r}'|} = \frac{1}{r}\left[1 - \frac{1}{2}\left(\frac{r'}{r}\right)\left(\frac{r'}{r} - 2\cos\alpha\right) + \frac{3}{8}\left(\frac{r'}{r}\right)^2\left(\frac{r'}{r} - 2\cos\alpha\right)^2 - \frac{5}{16}\left(\frac{r'}{r}\right)^3\left(\frac{r'}{r} - 2\cos\alpha\right)^3 + \cdots\right]$$

$$= \frac{1}{r}\left[1 + \left(\frac{r'}{r}\right)(\cos\alpha) + \left(\frac{r'}{r}\right)^2\left(\frac{3\cos^2\alpha - 1}{2}\right) + \left(\frac{r'}{r}\right)^3\left(\frac{5\cos^3\alpha - 3\cos\alpha}{2}\right) + \cdots\right]$$

In this last step we can recognize that the coefficients that multiply the powers terms of (r'/r) are the Legendre polynomials which can be written as $P_n(\cos\alpha)$. The final result for the expansion of $|\boldsymbol{r}-\boldsymbol{r}'|$ is the following

$$\frac{1}{|\boldsymbol{r}-\boldsymbol{r}'|} = \frac{1}{r}\sum_{n=0}^{\infty}\left(\frac{r'}{r}\right)^n P_n(\cos\alpha) \tag{B.22}$$

Now we want to determine the vector potential $\boldsymbol{A}(\boldsymbol{r})$ using this result in equation (B.22) and calculating it for a current loop. Taking equation (B.17) we obtain

$$\boldsymbol{A}(\boldsymbol{r}) = \frac{\mu_0 I}{4\pi}\oint\frac{d\boldsymbol{l}'}{|\boldsymbol{r}-\boldsymbol{r}'|} = \frac{\mu_0 I}{4\pi}\sum_{n=0}^{\infty}\frac{1}{r^{n+1}}\oint(r')^n P_n(\cos\alpha)d\boldsymbol{l}'$$

or, explaining the Legendre polynomials:

$$\boldsymbol{A}(\boldsymbol{r}) = \frac{\mu_0 I}{4\pi}\left[\frac{1}{r}\oint d\boldsymbol{l}' + \frac{1}{r^2}\oint r'\cos\alpha d\boldsymbol{l}' + \frac{1}{r^3}\oint (r')^2\left(\frac{3}{2}\cos^2\alpha - \frac{1}{2}\right)d\boldsymbol{l}' + ...\right] \tag{B.23}$$

Equation (B.23) is the multipole expansion of the vector potential for a current loop truncated at the third term. Now we want to analyze the three moments that appear in this expression. The first term goes like $1/r$ and it represents the monopole moment term, the second goes like $1/r^2$ and it is the dipole moment, the third goes like $1/r^3$ and it is called quadrupole moment, and so on. Let's focus on the magnetic monopole term, we can see that

$$\oint d\boldsymbol{l}' = 0$$

because is the integral of the total vector displacement around a closed loop. This result has a very important significance because it reflects the fact that magnetic monopoles does not exist. Hence, if we observe the potential at a great distance from the source we can also say that the quadrupole term is negligible compared to that of dipole, therefore the dominant term in the series development of the vector potential is given by the magnetic dipole moment. In this case the vector potential becomes:

$$\boldsymbol{A}_{dip}(\boldsymbol{r}) = \frac{\mu_0 I}{4\pi r^2}\oint r'\cos\alpha d\boldsymbol{l}' = \frac{\mu_0 I}{4\pi r^2}\oint (\hat{\boldsymbol{r}}\cdot\boldsymbol{r}')d\boldsymbol{l}' \tag{B.24}$$

Now we can rewrite the integral in a different way

$$\oint (\hat{\boldsymbol{r}}\cdot\boldsymbol{r}')d\boldsymbol{l}' = -\hat{\boldsymbol{r}}\times\int_S d\boldsymbol{s}'$$

then substituting this transformation into equation (B.24) we find

$$\boldsymbol{A}_{dip}(\boldsymbol{r}) = \frac{\mu_0}{4\pi}\frac{\boldsymbol{m}\times\boldsymbol{r}}{r^3} = \frac{\mu_0}{4\pi}\frac{\boldsymbol{m}\times\hat{\boldsymbol{r}}}{r^2} \tag{B.25}$$

where $\boldsymbol{m}$ is the magnetic dipole moment defined as

$$\boldsymbol{m} = I\int_S d\boldsymbol{s} = I\boldsymbol{s} \tag{B.26}$$

where $\boldsymbol{s}$ is the *vector area* of the loop; in the case in which we have a coil (the loop is flat), then $\boldsymbol{s}$ is the area enclosed by the coil with the direction assigned by the right-hand rule. If we have a volume current $\boldsymbol{J}$ instead of a line current, we can write the dipole moment as

$$\boldsymbol{m} = \frac{1}{2}\int_V (\boldsymbol{r}\times\boldsymbol{J})dv$$

in which we have used this relation

$$\boldsymbol{s} = \int_S d\boldsymbol{s} = \frac{1}{2}\oint \boldsymbol{r}\times d\boldsymbol{l}$$

If we analyze equation (B.26) we can see that the magnetic dipole moment does not depend on the choice of origin and this is true because the magnetic monopole moment is always zero. With

the expression of the vector potential $\boldsymbol{A}_{dip}(\boldsymbol{r})$ in (B.25) we can now calculate the magnetic field $\boldsymbol{B}_{dip}$ of a dipole as the rotor of the vector potential using equation (B.13) which gives

$$\boldsymbol{B}_{dip}(\boldsymbol{r}) = \frac{\mu_0}{4\pi}\frac{1}{r^3}[3(\boldsymbol{m}\cdot\hat{\boldsymbol{r}})\hat{\boldsymbol{r}} - \boldsymbol{m}]$$

For simplicity we can put $\boldsymbol{m}$ at the origin and let it point in the z-direction as shown in Figure B.4. With this choice we can represent the point at which we want to calculate the $\boldsymbol{B}$-field in its spherical coordinate (r,θ,ϕ) instead of its Cartesian coordinates (x,y,z), where r is the distance from the origin (the magnitude of the position vector $\boldsymbol{r}$), θ (down from the z-axis) is the polar angle, and ϕ (from the x-axis) is the azimuthal angle. The relationship between the Cartesian and the spherical coordinates are the following

$$\begin{cases} x = r\sin\theta\cos\phi \\ y = r\sin\theta\sin\phi \\ z = r\cos\theta \end{cases}$$

According to this relations we write the vector potential $\boldsymbol{A}_{dip}(\boldsymbol{r})$ in equation (B.25) at point (r,θ,ϕ):

$$\boldsymbol{A}_{dip}(\boldsymbol{r}) = \frac{\mu_0}{4\pi}\frac{m\sin\theta}{r^2}\hat{\boldsymbol{\phi}}$$

and consequently the magnetic field becomes

$$\boldsymbol{B}_{dip}(\boldsymbol{r}) = \boldsymbol{\nabla}\times\boldsymbol{A} = \frac{\mu_0 m}{4\pi r^3}(2\cos\theta\hat{\boldsymbol{r}} + \sin\theta\hat{\boldsymbol{\theta}}) \tag{B.27}$$

This expression is important and is indeed used to compare the results of the magnetic field emitted to the outside by an electric motor with the expression of the magnetic field generated by a magnetic dipole. The results are reported in Chapter 3.

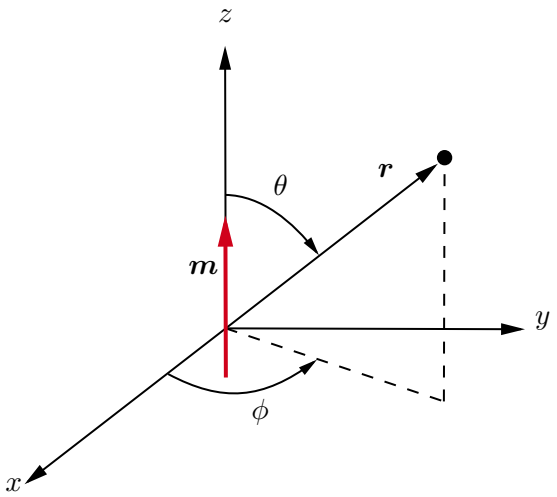

Figure B.4: Spherical reference frame for calculating the magnetic field of a (perfect) dipole.

B.2 Magnetic fields in matter

In the previous section we have provided the equations that are the basis of the study of magnetostatics, that is the Maxwell equations and we have also reported a way to solve them through the multipole expansion of the magnetic vector potential. Now we want to continue the study of magnetic fields by adding a fundamental aspect which is magnetism in matter. So far we have implied that the magnetic field was calculated in vacuum but since we use the theory of magnetism to study electric motors, it is necessary to provide in this section the basic notions of how magnetic fields behave in the presence of matter, but more importantly how the bodies are capable of producing a magnetic field.

To understand this last thing we must go back to the concept of magnetism, which includes all those magnetic phenomena that are responsible for the generation of magnetic fields. All these phenomena are generated by electric charges in motion, such as electrons that orbit around their nuclei spinning about their axes. From a macroscopic point of view these orbits can be considered as tiny loops of currents whose magnetic field, as we have seen in the previous section, at a great distance can be represented as that of a magnetic dipole. Typically, given the random distribution of atoms in matter, these dipoles tend to cancel one with each other thus generating a globally zero magnetic effect for the body. However, when we act to align all the magnetic dipoles they can generate a global effect. The external factor that is able to change the distribution of the magnetic moments inside a body is just a magnetic field that generates a net alignment of the dipoles making the body magnetically polarized or simply magnetized. Depending on the type of alignment obtained, we can classify the materials into different categories: diamagnetic, paramagnetic, ferromagnetic, antiferromagnetic and ferrimagnetic which are shown in the Figure B.5.

Diamagnetic materials are those materials that do not have a net magnetic moment at the atomic level and when they are subject to an externally applied magnetic field the currents generated give rise to a bulk magnetization that opposes the external field. An example of a diamagnetic material is Bismuth (Bi).

Paramagnetic materials such as diamagnetic ones do not have a net magnetic moment at the atomic or molecular level because the coupling with the nearby moments is weak but when we apply an external field these moments tend to align with it. However, the degree of alignment is very unstable as if the temperature increases, the degree of alignment can decrease due to the random effect of thermal agitation.

Ferromagnetic materials show a net alignment of the magnetic moments at atomic levels and unlike the paramagnetic materials they have a strong coupling between the neighboring moments. This spontaneous coupling of the magnetic moments at the atomic level gives rise to regions where the moments align together which are called domains. When the material is subject to an external magnetic field the domains undergo further alignment. The peculiar characteristic of ferromagnetic materials is that they maintain their macroscopic alignment, i.e. the magnetization even after the applied field has been removed. Therefore their magnetization depends substantially on their magnetic history and is not only determined by the applied magnetic field.

Finally, antiferromagnetic and ferrimagnetic materials have an alignment between the magnetic moments at the atomic level but this alignment is such that the neighboring moments are antiparallel to each other. For antiferromagnetic materials the near moments are equal and therefore there is

no net magnetic moment, while for ferrimagnetic materials the near moments are different and therefore this gives rise to a resulting net magnetic moment

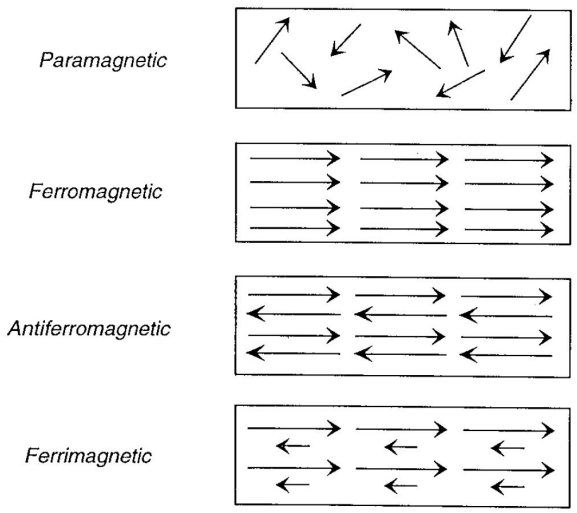

Figure B.5: Classifications of magnetic materials. From [70].

B.2.1 Magnetization

We are interested in studying the phenomenon of magnetization in detail. In particular we have understood that in the presence of an external magnetic field the matter becomes magnetized but depending on the material considered this can generate different magnetic effects at a macroscopic level. The magnetization at the macroscopic level therefore means that the object shows a magnetic field while at the microscopic level we have seen that the numerous tiny magnetic dipoles, that is the tiny loops and currents given by the spin motion of the electrons around its nucleus, give an effect of net alignment in a certain direction. We have said that for diamagnetic materials the moments align in a direction opposite to the applied field while for paramagnetic and ferromagnetic materials the dipoles undergo a couple that makes them align parallel to the applied field. The state of magnetic polarization, also called magnetization, is described by a vector quantity which is a magnetic moment per unit of volume, i.e. the *magnetization vector* $\boldsymbol{M}$.

B.2.2 The field of a magnetized object

In section B.1.4 we have determined the magnetic field starting from the vector potential through the multipole series expansion, now we want to do the same but for the magnetic field of a magnetized object, a body that has a magnetic moment per unit of volume, i.e. a magnetization vector $\boldsymbol{M}$. We recall that the vector potential of a single dipole $\boldsymbol{m}$ is given by equation (B.25) which is

$$\boldsymbol{A}_{dip}(\boldsymbol{r}) = \frac{\mu_0}{4\pi} \frac{\boldsymbol{m}(\boldsymbol{r}') \times (\boldsymbol{r} - \boldsymbol{r}')}{|\boldsymbol{r} - \boldsymbol{r}'|^3}$$

If we take into account a magnetized object as shown in Figure B.6 we have to consider that the body is made of volume elements dv' and each of them carries a dipole moment $\boldsymbol{M}dv'$, thus the

total vector potential is

$$\boldsymbol{A}(\boldsymbol{r}) = \frac{\mu_0}{4\pi}\int \frac{\boldsymbol{M}(\boldsymbol{r}')\times(\boldsymbol{r}-\boldsymbol{r}')}{|\boldsymbol{r}-\boldsymbol{r}'|^3}dv' \tag{B.28}$$

now we can rewrite the integral in another way using the following identity

$$\boldsymbol{\nabla}'\frac{1}{|\boldsymbol{r}-\boldsymbol{r}'|} = \frac{(\boldsymbol{r}-\boldsymbol{r}')}{|\boldsymbol{r}-\boldsymbol{r}'|^3}$$

and substituting inside (B.28) we obtain

$$\boldsymbol{A}(\boldsymbol{r}) = \frac{\mu_0}{4\pi}\int \left[\boldsymbol{M}(\boldsymbol{r}')\times\left(\boldsymbol{\nabla}'\frac{1}{|\boldsymbol{r}-\boldsymbol{r}'|}\right)\right]dv'$$

We use for the integrand the following product rule

$$\boldsymbol{\nabla}\times(f\boldsymbol{A}) = f(\boldsymbol{\nabla}\times\boldsymbol{A}) - \boldsymbol{A}\times(\boldsymbol{\nabla}f)$$

and integrating by parts we obtain

$$\boldsymbol{A}(\boldsymbol{r}) = \frac{\mu_0}{4\pi}\left\{\int \frac{1}{|\boldsymbol{r}-\boldsymbol{r}'|}[\boldsymbol{\nabla}'\times\boldsymbol{M}(\boldsymbol{r}')]d\tau' - \int \boldsymbol{\nabla}'\times\left[\frac{\boldsymbol{M}(\boldsymbol{r}')}{|\boldsymbol{r}-\boldsymbol{r}'|}\right]dv'\right\} \tag{B.29}$$

Now we can use a corollary of divergence theorem to transform the latter as a surface integral, the corollary is the following

$$\int_V(\boldsymbol{\nabla}\times\boldsymbol{v})dv = -\oint_S \boldsymbol{v}\times d\boldsymbol{a}$$

using this result inside (B.29) we obtain

$$\boldsymbol{A}(\boldsymbol{r}) = \frac{\mu_0}{4\pi}\int \frac{1}{|\boldsymbol{r}-\boldsymbol{r}'|}[\boldsymbol{\nabla}'\times\boldsymbol{M}(\boldsymbol{r}')]d\tau' + \frac{\mu_0}{4\pi}\oint \frac{1}{|\boldsymbol{r}-\boldsymbol{r}'|}[\boldsymbol{M}(\boldsymbol{r}')\times d\boldsymbol{a}'] \tag{B.30}$$

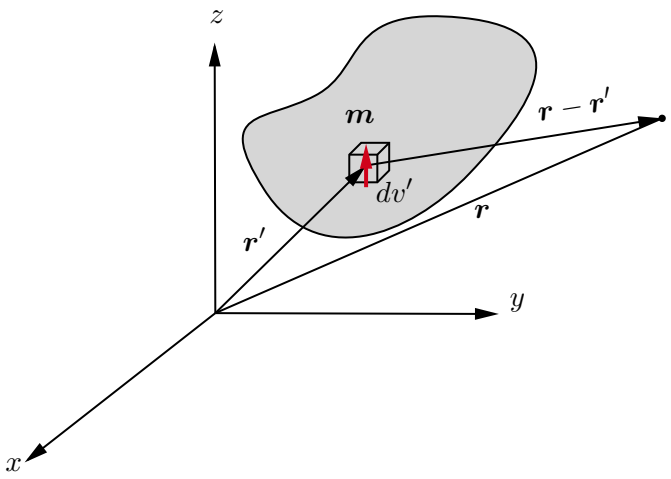

Figure B.6: Dipole moment element of a magnetized object.

If we consider the first term on the right-hand side of equation (B.30) as the potential of a volume current

$$\boldsymbol{J}_b = \boldsymbol{\nabla}\times\boldsymbol{M} \tag{B.31}$$

and the second term on the right-hand side of (B.30) as the potential of a surface current

$$\boldsymbol{K}_b = \boldsymbol{M} \times \hat{\boldsymbol{n}} \tag{B.32}$$

with $\hat{\boldsymbol{n}}$ the normal unit vector, therefore we can rewrite equation (B.30) with these two definitions and obtain

$$\boldsymbol{A}(\boldsymbol{r}) = \frac{\mu_0}{4\pi}\int_V \frac{\boldsymbol{J}_b(\boldsymbol{r}')}{|\boldsymbol{r}-\boldsymbol{r}'|}dv' + \frac{\mu_0}{4\pi}\oint_S \frac{\boldsymbol{K}_b(\boldsymbol{r}')}{|\boldsymbol{r}-\boldsymbol{r}'|}da' \tag{B.33}$$

This result in equation (B.33) is of fundamental importance because it gives us the vector magnetic potential of a magnetized body which can be seen as the combination of two contributions: the vector potential of a volume current $\boldsymbol{J}_b = \boldsymbol{\nabla} \times \boldsymbol{M}$ throughout the material, and the vector potential of a surface current $\boldsymbol{K}_b = \boldsymbol{M} \times \hat{\boldsymbol{n}}$, on the boundary. This development therefore allows not to use the formula (B.28) for the calculation of the vector potential which would force to integrate all the contributes of the infinitesimal dipoles of the object. With this more intuitive method, we see the vector potential as the combination of the fields generated separately by the volume and surface currents of the body.

At this point, we can proceed to the calculus of the magnetic field through the curl of the vector potential using as always equation (B.13) and we obtain

$$\boldsymbol{B}(\boldsymbol{r}) = \frac{\mu_0}{4\pi}\int_V \boldsymbol{J}_b(\boldsymbol{r}') \times \frac{(\boldsymbol{r}-\boldsymbol{r}')}{|\boldsymbol{r}-\boldsymbol{r}'|^3}dv' + \frac{\mu_0}{4\pi}\oint_S \boldsymbol{K}_b(\boldsymbol{r}') \times \frac{(\boldsymbol{r}-\boldsymbol{r}')}{|\boldsymbol{r}-\boldsymbol{r}'|^3}da' \tag{B.34}$$

In this equation we have used the following relationships

$$\begin{aligned}
\boldsymbol{\nabla} \times \frac{\boldsymbol{J}_b(\boldsymbol{r}')}{|\boldsymbol{r}-\boldsymbol{r}'|} &= -\boldsymbol{J}_b(\boldsymbol{r}') \times \boldsymbol{\nabla}\frac{1}{|\boldsymbol{r}-\boldsymbol{r}'|} \\
\boldsymbol{\nabla} \times \frac{\boldsymbol{J}_b(\boldsymbol{r}')}{|\boldsymbol{r}-\boldsymbol{r}'|} &= -\boldsymbol{K}_b(\boldsymbol{r}') \times \boldsymbol{\nabla}\frac{1}{|\boldsymbol{r}-\boldsymbol{r}'|}
\end{aligned}$$

and

$$\boldsymbol{\nabla}\frac{1}{|\boldsymbol{r}-\boldsymbol{r}'|} = -\frac{(\boldsymbol{r}-\boldsymbol{r}')}{|\boldsymbol{r}-\boldsymbol{r}'|^3}$$

B.2.3 The force on a magnetized object

The previous procedure that led us to calculate the magnetic field of a magnetized object (also known as current method) reported in equation (B.34) reduce a magnet to a distribution of equivalent volume and surface current densities $\boldsymbol{J}_b$ and $\boldsymbol{K}_b$ as specified in equations (B.31) and (B.32). In this section we want to determine the magnetic force that acts on a magnetized object when placed in an external magnetic field. In Chapter 4 we have determined the forces acting on an isolated dipole moment and not considering matter. Here we want to determine the force on a magnetized object in an external magnetic field using the following equation

$$\begin{aligned}
\boldsymbol{F} &= \int_V \boldsymbol{J}_b \times \boldsymbol{B}_{ext}\, dv + \oint_S \boldsymbol{K}_b \times \boldsymbol{B}_{ext}\, ds \\
&= \int_V (\boldsymbol{\nabla} \times \boldsymbol{M}) \times \boldsymbol{B}_{ext}\, dv + \oint_S (\boldsymbol{M} \times \hat{\boldsymbol{n}}) \times \boldsymbol{B}_{ext}\, ds
\end{aligned} \tag{B.35}$$

The integration is over the volume V and the surface S of the magnet. We recognise inside the integrals a double cross product for which we can apply the following product rule:

$$\begin{aligned}&\int_V (\boldsymbol{\nabla} \times \boldsymbol{U}) \times \boldsymbol{V} dv - \oint_S (\hat{\boldsymbol{n}} \times \boldsymbol{U}) \times \boldsymbol{V} ds \\ &= \int_V [\boldsymbol{U} \times (\boldsymbol{\nabla} \times \boldsymbol{V}) - \boldsymbol{U}(\boldsymbol{\nabla} \cdot \boldsymbol{V})] dv + \int_V (\boldsymbol{U} \cdot \boldsymbol{\nabla}) \boldsymbol{V} dv\end{aligned}$$

with case $\boldsymbol{U} = \boldsymbol{M}$ and $\boldsymbol{V} = \boldsymbol{B}_{ext}$. Using this relation for equation (B.35) we get

$$\boldsymbol{F} = \int_V (\boldsymbol{M} \cdot \boldsymbol{\nabla}) \boldsymbol{B}_{ext} \, dv \tag{B.36}$$

and we notice that to obtain this equation we have used the property that the divergence of $\boldsymbol{B}_{ext}$ is zero ($\boldsymbol{\nabla} \cdot \boldsymbol{B}_{ext} = 0$), which is always true for the magnetostatics Maxwell equations, and the fact that also the curl of $\boldsymbol{B}_{ext}$ is zero ($\boldsymbol{\nabla} \times \boldsymbol{B}_{ext} = 0$). This is justified because the source of the external magnetic field is far from the integration region of the body being analyzed. Expanding the integrand we obtain

$$\begin{aligned}(\boldsymbol{M} \cdot \boldsymbol{\nabla}) \boldsymbol{B}_{ext} = &\left(M_x \frac{\partial}{\partial x} + M_y \frac{\partial}{\partial y} + M_z \frac{\partial}{\partial z} \right) B_{ext_x} \hat{\boldsymbol{x}} \\ &+ \left(M_x \frac{\partial}{\partial x} + M_y \frac{\partial}{\partial y} + M_z \frac{\partial}{\partial z} \right) B_{ext_y} \hat{\boldsymbol{y}} \\ &+ \left(M_x \frac{\partial}{\partial x} + M_y \frac{\partial}{\partial y} + M_z \frac{\partial}{\partial z} \right) B_{ext_z} \hat{\boldsymbol{z}}\end{aligned}$$

If we analyze the force density from equation (B.36) we find that

$$f = (\boldsymbol{M} \cdot \boldsymbol{\nabla}) \boldsymbol{B}_{ext} \tag{B.37}$$

we can apply another product rule to equation (B.36) which is the following

$$\int_V (\boldsymbol{U} \cdot \boldsymbol{\nabla}) \boldsymbol{V} dv = - \int_V (\boldsymbol{\nabla} \cdot \boldsymbol{U}) \boldsymbol{V} dv + \oint_S (\hat{\boldsymbol{n}} \cdot \boldsymbol{U}) \boldsymbol{V} ds$$

with $\boldsymbol{U} = \boldsymbol{M}$ and $\boldsymbol{V} = \boldsymbol{B}_{ext}$ which gives

$$\boldsymbol{F} = - \int_V (\boldsymbol{\nabla} \cdot \boldsymbol{M}) \boldsymbol{B}_{ext} \, dv + \oint_S (\boldsymbol{M} \cdot \hat{\boldsymbol{n}}) \boldsymbol{B}_{ext} \, ds \tag{B.38}$$

B.2.4 The torque on a magnetized object

In analogy with what we have done for the forces, we want to use the current model to determine the torques acting on a magnetized body in the presence of an external magnetic field. Also in this case these developments provide a more in-depth treatment with respect to what we have done for the estimation of magnetic interactions with electric motors in which the motor is seen not as an extended body but as an object characterized by a dipole moment. Let's consider a magnetized

object and calculate the torque acting on it in presence of an external magnetic field.

$$\begin{aligned}\boldsymbol{T} &= \int_V \boldsymbol{r} \times (\boldsymbol{J}_b \times \boldsymbol{B}_{ext}) dv + \oint_S \boldsymbol{r} \times (\boldsymbol{K}_b \times \boldsymbol{B}_{ext}) ds \\ &= \int_V \boldsymbol{r} \times [(\boldsymbol{\nabla} \times \boldsymbol{M}) \times \boldsymbol{B}_{ext}] dv + \oint_S \boldsymbol{r} \times [(\boldsymbol{M} \times \hat{\boldsymbol{n}}) \times \boldsymbol{B}_{ext}] ds\end{aligned} \tag{B.39}$$

For the calculation of the torque we need the level arm and so $\boldsymbol{r}$ is the vector that indicates the point where we want to calculate the torque and originates from the point with respect to which the torque is calculated. As in the case of the force we use a product rule which is the following

$$\begin{aligned}&\int_V \boldsymbol{r} \times [(\boldsymbol{\nabla} \times \boldsymbol{U}) \times \boldsymbol{V}] dv - \oint_S \boldsymbol{r} \times [(\hat{\boldsymbol{n}} \times \boldsymbol{U}) \times \boldsymbol{V}] ds \\ &= \int_V \boldsymbol{r} \times [\boldsymbol{U} \cdot \boldsymbol{\nabla} \boldsymbol{V} + \boldsymbol{U} \times (\boldsymbol{\nabla} \times \boldsymbol{V}) - \boldsymbol{U}(\boldsymbol{\nabla} \cdot \boldsymbol{V})] dv + \int_V \boldsymbol{U} \times \boldsymbol{V} dv\end{aligned}$$

with $\boldsymbol{U} = \boldsymbol{M}$ and $\boldsymbol{V} = \boldsymbol{B}_{ext}$. Using this expression into (B.39) gives

$$\boldsymbol{T} = \int_V \boldsymbol{r} \times (\boldsymbol{M} \cdot \boldsymbol{\nabla} \boldsymbol{B}_{ext}) dv + \int_V \boldsymbol{M} \times \boldsymbol{B}_{ext}\, dv \tag{B.40}$$

We notice that we have used the fact that the divergence of $\boldsymbol{B}_{ext}$ is zero ($\boldsymbol{\nabla} \cdot \boldsymbol{B}_{ext} = 0$) because of Maxwell equation also the curl of $\boldsymbol{B}_{ext}$ is zero ($\boldsymbol{\nabla} \times \boldsymbol{B}_{ext} = 0$) for the same reason we have already mentioned that is the position of the external magnetic field source which is far from the integration volume of the body. From equation (B.40) we can also notice that if $\boldsymbol{B}_{ext}$ is uniform ($\boldsymbol{\nabla} \boldsymbol{B}_{ext} = 0$), then the torque reduces to a couple.

$$\boldsymbol{T} = \int_V \boldsymbol{M} \times \boldsymbol{B}_{ext}\, dv$$

We can now apply another product rule to equation (B.40) which is the following

$$\boldsymbol{T} = \int_V \boldsymbol{r} \times (\boldsymbol{U} \cdot \boldsymbol{\nabla} \boldsymbol{V}) dv + \int_V \boldsymbol{U} \times \boldsymbol{V} dv = -\int_V (\boldsymbol{\nabla} \cdot \boldsymbol{U})(\boldsymbol{r} \times \boldsymbol{V}) dv + \oint (\hat{\boldsymbol{n}} \cdot \boldsymbol{U})(\boldsymbol{r} \times \boldsymbol{V}) ds$$

with $\boldsymbol{U} = \boldsymbol{M}$ and $\boldsymbol{V} = \boldsymbol{B}_{ext}$. Using this expression for equation (B.40) this gives

$$\boldsymbol{T} = \int_V (-\boldsymbol{\nabla} \cdot \boldsymbol{M})(\boldsymbol{r} \times \boldsymbol{B}_{ext}) dv + \oint (\hat{\boldsymbol{n}} \cdot \boldsymbol{M})(\boldsymbol{r} \times \boldsymbol{B}_{ext}) ds$$

B.2.5 The auxiliary field H

In this section we want to broaden the discussion on magnetism in matter by introducing the concept of auxiliary $\boldsymbol{H}$ field. In the previous sections we have explained in detail how the magnetization mechanism works, its objective is to establish currents in a body, and these currents are of two types: there are currents within the material $\boldsymbol{J}_b = \boldsymbol{\nabla} \times \boldsymbol{M}$ and currents on the surface $\boldsymbol{K}_b = \boldsymbol{M} \times \hat{\boldsymbol{n}}$. In general we call *bound currents* those generated by a magnetization process that can be of volume or surface. The magnetic field due to the magnetization of the medium is that produced only by these bound currents. But as we have seen in section B.1.1, a magnetic field can also be generated by currents that are not those internal to a magnetized material, i.e. bound currents, but can be of another type and we can call them *free currents*. These free currents can flow through wires

of conductive material or even through a magnetized material itself if this is also a conductor. In general, it is good to distinguish the two currents and therefore we can express the total current as the sum of the two.

$$\boldsymbol{J} = \boldsymbol{J}_b + \boldsymbol{J}_f$$

The distinction between the two currents in this case is necessary and dictated by the fact that the sources that generate them are different. Free currents exist as there is a flow of electric charges through a wire while bound currents exist as in a magnetized body where there is the presence of atomic dipole moments that are aligned with each other. We can now write with this distinction made, Ampère's law:

$$\frac{1}{\mu_0}(\boldsymbol{\nabla} \times \boldsymbol{B}) = \boldsymbol{J} = \boldsymbol{J}_b + \boldsymbol{J}_f = \boldsymbol{J}_f + (\boldsymbol{\nabla} \times \boldsymbol{M})$$

If we collect together the two curls, we obtain

$$\boldsymbol{\nabla} \times \left(\frac{1}{\mu_0} \boldsymbol{B} - \boldsymbol{M} \right) = \boldsymbol{J}_f$$

The term in brackets is a candidate to be a magnetic field called auxiliary and named with the letter $\boldsymbol{H}$.

$$\boldsymbol{H} = \frac{1}{\mu_0} \boldsymbol{B} - \boldsymbol{M} \tag{B.41}$$

Hence, we can rewrite the Ampère's law in terms of $\boldsymbol{H}$:

$$\boldsymbol{\nabla} \times \boldsymbol{H} = \boldsymbol{J}_f$$

The introduction of the $\boldsymbol{H}$ field also contains the contribute of the magnetic field of a magnetized object and expresses Ampère's law in terms of the free current only, this is fundamental as the free current is something over which we have a control, we can turn it on or turn it off or make it vary, on the contrary for bound currents we have no control, they depend on the magnetization of the material and its magnetic history.

B.2.6 Linear and nonlinear media

Let us now see in detail the relationship between the three quantities $\boldsymbol{H}$, $\boldsymbol{B}$ and $\boldsymbol{M}$. In the classification of magnetic materials we have seen that for diamagnetic and paramagnetic materials their magnetization depends on the field and is supported by it in the sense that once the $\boldsymbol{B}$ field is removed the magnetization vector $\boldsymbol{M}$ vanishes, i.e. the atomic magnetic dipoles return to their initial random condition. Therefore, we can state that the magnetization for many materials is proportional to the applied magnetic field. The proportionality for linear, homogeneous and isotropic media is expressed by

$$\boldsymbol{M} = \chi_m \boldsymbol{H} \tag{B.42}$$

where the dimensionless constant of proportionality χ_m is called *magnetic susceptibility*. It is positive for paramagnets and negative for diamagnets and is different for each material. Typical values are around 10^{-5}. We can rewrite equation (B.41) for linear, homogeneous and isotropic media as

$$\boldsymbol{B} = \mu_0(\boldsymbol{H} + \boldsymbol{M}) = \mu_0(1 + \chi_m)\boldsymbol{H}$$

From this formula we can notice that also $\boldsymbol{B}$ is proportional to $\boldsymbol{H}$

$$\boldsymbol{B} = \mu \boldsymbol{H}$$

where we have defined

$$\mu = \mu_0(1 + \chi_m)$$

which is called the permeability of the material. If we take the ratio between the permeability and the permeability of free space we have the relative permeability which is defined as

$$\mu_r = \frac{\mu}{\mu_0} = 1 + \chi_m \tag{B.43}$$

If we are in the vacuum in which there is no matter to magnetize the susceptibility χ_m is zero, and the permeability μ is equal to the permeability of free space μ_0, which means $\mu_r = 1$. Formulas for $\boldsymbol{H}$ in terms of $\boldsymbol{B}$ are called constitutive relations.

B.2.7 Ferromagnetism

We saw that for linear materials the magnetization, i.e. the alignment of the atomic dipoles is maintained as long as the external magnetic field exists and this happens in diamagnetic and paramagnetic materials. Ferromagnetic materials that are generally nonlinear behave differently, they do not need an external magnetic field to align the atomic dipoles. The alignment and therefore the magnetization is already included within them and this is due to the nature of the atomic dipoles associated with the spin of the unpaired electrons, which naturally tend to point in the same direction as those close to them. The reason for this interaction behavior is due to quantum mechanics. As we have already mentioned, these alignments take place in particular areas of the material called domains. These domains can be observed under the microscope using etching techniques and can be seen to contain billions of aligned dipoles. At a larger level, however, the domains are randomly oriented but they can in turn be aligned under the effect of an external magnetic field. The dipoles will feel in this case a magnetic torque $\boldsymbol{N} = \boldsymbol{m} \times \boldsymbol{B}$ that will tend to align them parallel with the local magnetic field. This effect generates a movement of the boundaries of the domains and if the field turns out to be too strong, a domain can take over, arriving at a situation of saturation for the material.

Let us now consider a ferromagnetic material with a coil wrapped around it, we want to vary the current I flowing in the coil in order to vary the magnetic field that this generates and see the effect it has on the material to be magnetized. We know in this case that if we increase the current, the filed generated by the coil increases too and the effect that we observe on the material at the microscopic level is that its domain boundaries start to move. By varying the size of the domains, the magnetization of the material also increases accordingly. If we continue to increase the magnetic field, by increasing the current of the coil, we will reach a saturation point for the material where all the dipoles are aligned and a further increase in the magnetic field on the object has no effect on the magnetization vector $\boldsymbol{M}$. We have reached point b in the Figure B.7. At this point we realize that if we want to go back we have to decrease the current then decrease the applied magnetic field but we discover that the material under examination will not decrease its magnetization moment by retracing the curve in reverse until $\boldsymbol{M} = 0$ but there will be a partial return to the initial

random distribution of domains. If we decrease the current to the null value we will not obtain a correspondingly null value of $\boldsymbol{M}$ but we will reach zero of the current with a residual magnetization moment. This means that the material has kept a certain memory of its magnetization and therefore even in the absence of external sources it is now characterized by a residual magnetic moment that makes it a permanent magnet. We have reached the point c in Figure B.7. If we want to eliminate its residual magnetization $\boldsymbol{M}$ then we can continue to decrease the current going towards negative values of I that is by making a current flow in the opposite direction to the previous one, this will generate a magnetic field in the opposite direction. In this case the magnetization moment starts to decrease until to reach the null value (point d in Figure B.7). If we continue to decrease the current then the magnetization moment of the material assumes negative values, i.e. it increases in the opposite direction and also in this case there will be a value of $\boldsymbol{B}$ for which the saturation will be reached (point e in Figure B.7). At this point we can again increase the current, that is to bring it to zero and again the magnetic moment will not go to zero retracing the curve in the opposite direction but will return and go back while maintaining a certain amount of accumulated moment up to the point f of permanent magnetization. We could continue the loop by turning on the current and bringing it to positive values until the magnetization is canceled again by reaching point g, by increasing the current further, the saturation point b is reached again. The complete loop described so far is called the hysteresis loop. This cycle, which can also be described with $\boldsymbol{B}$ against $\boldsymbol{H}$, demonstrates that the magnetization of a ferromagnetic material does not depend only on the applied field but above all on its magnetic history.

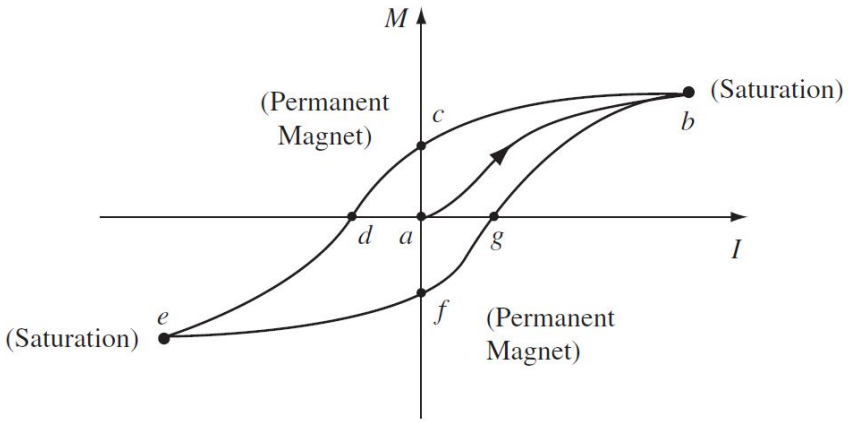

Figure B.7: Hysteresis loop. From [43].

A final important comment to make on the magnetization of ferromagnetic materials is that the alignment of the dipoles of the domains parallel to each other can be ruined by the effect of the temperature which, if very high, can act by destroying the alignment and therefore canceling the magnetization of the material. This temperature is specific for each material and is called the Curie temperature. For example for iron this effect occurs at $770°C$. This temperature is an abrupt change of behaviour and is considered a transition phase in statistical mechanics between ferromagnetic and paramagnetic behavior. If iron is brought to a temperature higher than that of the Curie point, it is no longer ferromagnetic but paramagnetic.

Appendix C

Nonlinear Stability and Control

C.1 Introduction

In this appendix chapter we will analyze in detail the problem of stability and control of the blimp. Dealing with a control system, the first thing to do is investigate the stability of the system. We will introduce one method of stability analysis of nonlinear systems, known as Lyapunov's method [60] and we will apply this for both the open-loop and the closed-loop system.

As for the control methods, we will outline the state feedback linearization control strategy, it is apparently first proposed in [71] in the field of robot manipulator and named the *Computed Torque Control* method (CTC) in [14, 64]. With this method we will apply the nonlinear control strategy to the blimp both in the body-fixed and in the earth-fixed reference frame. However, as we will see, this technique precludes the system from being fully actuated, i.e. it can provide a force or moment for all DOF of the system. This is not the case of the Blimpduino which has three motors and consists of an under actuated system.

C.2 Stability of blimp vehicles

We now introduce the concept of stability for a vehicle such as the blimp. For our purposes we can define stability as the ability of the system to remain in a state of equilibrium or to return to it even after the application of an external disturbance that tends to make the system move from its equilibrium situation and this without corrective action such as that of motors or control surfaces. Another important concept to discuss is that of maneuverability which is defined as the ability to perform certain maneuvers. The concepts of stability and maneuverability are connected to each other and a compromise must be found between the two: if the first is too large than the second this implies that to move the vehicle it takes a greater effort on the part of the control, on the contrary greater maneuverability compared to stability involves an easier control of the platform.

At this point it is therefore important to distinguish between two types of stability which are:

- Control-fixed stability
- Control-free stability

The *control-fixed stability* studies the stability in the case in which the control surfaces are fixed and the thrust of the motors is constant, while *control-free stability* considers the stability study in

the event that both the control surfaces and the thrust of the motors can vary, therefore the control dynamics are included in the stability analysis.

C.3 Nonlinear Lyapunov stability theory

The study of the nonlinear stability of airships is not a simple problem to analyze given the complex structure of the vehicle's equations of motion. According to Lyapunov (1857-1918), a solution is stable if taking an initial condition in the vicinity of the solution, trajectories are generated that remain close to that solution for subsequent times. Instead, we speak of asymptotic stability if, as time increases, the trajectories converge to the solution considered. This analysis is faced with Lyapunov's theory for autonomous and non-autonomous systems and can be applied to both control-fixed and control-free stability analysis. Let's start by defining an autonomous and non-autonomous system. An *autonomous* system is a nonlinear system whose state equation can be written as

$$\boldsymbol{x} = \boldsymbol{f}(\boldsymbol{x})$$

where $\boldsymbol{f}$ is a nonlinear vector function that depends only on the state vector $\boldsymbol{x}$ of the system and not on time t. A *non-autonomous* system, on the other hand, is characterized by a vector of nonlinear functions $\boldsymbol{f}$ that depend both on the state vector and on time, that is:

$$\dot{\boldsymbol{x}} = \boldsymbol{f}(\boldsymbol{x}, t)$$

The Lyapunov stability criterion states that the system will remain arbitrarily close to the equilibrium solution starting from a position sufficiently close to it. This however guarantees that the system will remain in that position, if in addition disturbances act, the so-called *asymptotic stability* is required, i.e. that the system returns to its original position after the application of a disturbance.

C.3.1 Lyapunov stability for autonomous systems

In this section the Lyapunov's direct method is presented. It can be applied only for autonomous systems [62] and it is aimed at finding a scalar function V that represents the mechanical energy of the system through which it can be demonstrated the stability of the system. Lyapunov's direct method for autonomous systems is the following:

Theorem C.1 (Lyapunov's direct method for autonomous systems)**.** *Let us assume that we propose an energy function of the state $V(\boldsymbol{x})$ with continuous first derivatives and which satisfies the following properties:*

(1) $V(\boldsymbol{x}) > 0$ *(positive definite)*

(2) $\dot{V}(\boldsymbol{x}) < 0$ *(negative definite)*

(3) $V(\boldsymbol{x}) \to \infty$ *as* $\|\boldsymbol{x}\| \to \infty$ *(radially unbounded)*

therefore the equilibrium point $\boldsymbol{x}^*$ satisfying $\boldsymbol{f}(\boldsymbol{x}^*) = 0$ is globally asymptotically stable.

If we are looking for the system to be *asymptotically stable* then only conditions (1) and (2) are needed. If, on the other hand, the condition (3) is also satisfied then the system will be *globally*

asymptotically stable. If we only seek that the system is *stable* then condition (2) can be relaxed to $\dot{V}(\boldsymbol{x}) \leq 0$.

C.3.2 Lyapunov stability for non-autonomous system

The stability analysis for non-autonomous systems can be applied in two cases: for systems that are non-autonomous in nature or for systems that, although originally autonomous, are analyzed to study the *stability of motion*, i.e. the stability of a system which must track a reference trajectory (as it is the case of a moving vehicle). Motion stability can be transformed into an equivalent stability problem around an equilibrium point if we consider the error dynamics rather than state dynamics of the system. Therefore in control problems in which we want to track a reference trajectory, the dynamics of the problem is not autonomous even if the original system is intrinsically autonomous. Considering a non-autonomous system, the following Lyapunov theorem holds:

Theorem C.2 (Lyapunov theorem for non-autonomous system)**.** *Let us assume that we propose an energy function of the state and time $V(\boldsymbol{x}, t)$ with continuous first derivatives and which satisfies the following properties:*

(1) $V(\boldsymbol{x}, t) > 0$ *(positive definite)*

(2) $\dot{V}(\boldsymbol{x}, t) < 0$ *(negative definite)*

(3) $V(\boldsymbol{x}, t) \leq V_0(\boldsymbol{x}) \quad \forall t \geq 0$ *where* $V_0(\boldsymbol{x}) > 0$ *(decrescent)*

(4) $V(\boldsymbol{x}, t) \to \infty$ *as* $\|\boldsymbol{x}\| \to \infty$ *(radially unbounded)*

therefore the equilibrium point $\boldsymbol{x}^*$ satisfying $\boldsymbol{f}(\boldsymbol{x}^*, t) = 0$ is globally asymptotically stable.

The Lyapunov stability criterion for non-autonomous systems compared to that of autonomous systems sees the addition of a property for the energy function, which is condition (3), i.e. the condition that the function $V(\boldsymbol{x}, t)$ must be decrescent and this because the energy function explicitly depends on time. Also in this case for the system to be *asymptotically stable* it is sufficient to satisfy conditions (1), (2) and (3). If we require also the *globally asymptotically stable*, we have to add that $V(\boldsymbol{x}, t)$ is radially unbounded (condition (4)).

C.3.3 Lyapunov-like theory

In practical applications conditions (1) to (4) of the Theorem C.2 are difficult to satisfy. A possible solution to this problem is to use the Barbălat's lemma [11] which is a Lyapunov-like lemma [74] based on the results of Barbălat, a Rumanian mathematician. However the lemma does not guarantee stability but the *convergence* of the trajectories of the system at the origin. This does not imply stability as it is possible that, before converging in the equilibrium point, the trajectories may move away from the same point. Hence the origin is unstable from the point of view of Lyapunov's theory. Despite this, the lemma is used from an engineering point of view to demonstrate the convergence of the state in the origin. Barbălat's lemma is defined as follows:

Lemma C.1 (Barbălat's lemma)**.** *If the function $g(t)$ has a finite limit as $t \to \infty$, is differentiable and $\dot{g}(t)$ is uniformly continuous, then $\dot{g}(t) \to 0$ as $t \to \infty$.*

Barbălat's lemma can be revised in a Lyapunov-like version which can be found in [84]. This version is defined as follow:

Lemma C.2 (Lyapunov-like lemma for convergence)**.** *Assume that there exists a scalar function* $V(\boldsymbol{x}, t)$ *satisfying:*

(1) $V(\boldsymbol{x}, t)$ *is lower bounded*

(2) $\dot{V}(\boldsymbol{x}, t)$ *is negative semi-definite*

(3) $\dot{V}(\boldsymbol{x}, t)$ *is uniformly continuous in time*

then $\dot{V}(\boldsymbol{x}, t) \to 0$ *as* $t \to \infty$*.*

To satisfy the first and last conditions, the following sufficient conditions must apply:

Remark C.1 (Lower boundness)**.** *A sufficient condition for the scalar function* $V(\boldsymbol{x}, t)$ *to be lower bounded is that* $V(\boldsymbol{x}, t)$ *is positive semi-definite i.e.*

$$V(\boldsymbol{x}, t) \geq 0 \quad \forall t \geq t_0$$

Remark C.2 (Uniform continuity)**.** *A sufficient condition for a differentiable function* $\dot{V}(\boldsymbol{x}, t)$ *to be uniformly continuous is that its derivative* $\ddot{V}(\boldsymbol{x}, t)$ *is bounded* $\forall t \geq t_0$

C.3.4 Open-loop stability

In this section we will analyze the study of control-fixed stability which we can also call open-loop stability. In this case we do not consider the control inputs so we consider the dynamic system of the type:

$$\boldsymbol{M_\eta}(\boldsymbol{\eta})\ddot{\boldsymbol{\eta}} + \boldsymbol{C_\eta}(\boldsymbol{\xi}, \boldsymbol{\eta})\dot{\boldsymbol{\eta}} + \boldsymbol{D_\eta}(\boldsymbol{\xi}, \boldsymbol{\eta})\dot{\boldsymbol{\eta}} + \boldsymbol{g_\eta}(\boldsymbol{\eta}) = 0 \tag{C.1}$$

This analyses uses hydrodynamic derivatives to find a static stability of the vehicle. If the dynamics of the blimp were linear, studying stability is very simple with the well-known techniques of Routh and Hurwitz. As we have seen in Appendix A the model that describes the dynamics of the blimp is highly nonlinear and therefore to study the stability we will adopt the Lyapunov's direct method. Let us consider the following Lyapunov candidate function V which represents the total mechanical energy of the system, i.e. the sum of the kinetic and potential energy of the blimp. Being an energy, the null value corresponds to the equilibrium point $\boldsymbol{\eta}$ and $\dot{\boldsymbol{\eta}}$

$$V(\boldsymbol{\eta}, \dot{\boldsymbol{\eta}}) = \frac{1}{2}\dot{\boldsymbol{\eta}}^T \boldsymbol{M}_\eta(\boldsymbol{\eta})\dot{\boldsymbol{\eta}} + \int_{\mathbf{0}}^{\boldsymbol{\eta}} \boldsymbol{g}_\eta^T(z)dz \tag{C.2}$$

where $\boldsymbol{M_\eta}$ and $\boldsymbol{g_\eta}$ are the dynamical parameters expressed in the earth-fixed reference frame and reported in (A.55) defined in Section A.7. If the mechanical energy V tends to zero this implies asymptotic stability while if the mechanical energy increases this translates into instability. Let us now differentiate the expression of energy (C.2) with respect to time

$$\dot{V} = \dot{\boldsymbol{\eta}}^T[\boldsymbol{M}_\eta(\boldsymbol{\eta})\ddot{\boldsymbol{\eta}} + \boldsymbol{g_\eta}(\boldsymbol{\eta})]\frac{1}{2}\dot{\boldsymbol{\eta}}^T\dot{\boldsymbol{M}}_{\boldsymbol{\eta}}\dot{\boldsymbol{\eta}} \tag{C.3}$$

In doing this we have assumed that the mass matrix $\boldsymbol{M_\eta}$ satisfies the property of being positive definite, i.e., $\boldsymbol{M_\eta} = \boldsymbol{M_\eta}^T > 0$. By making the Coriolis and centripetal term appear, the equation (C.3) becomes

$$\dot{V} = \dot{\boldsymbol{\eta}}^T[\boldsymbol{M_\eta}(\boldsymbol{\eta})\ddot{\boldsymbol{\eta}} + \boldsymbol{C_\eta}(\boldsymbol{\xi},\boldsymbol{\eta})\dot{\boldsymbol{\eta}} + \boldsymbol{g_\eta}(\boldsymbol{\eta})] + \frac{1}{2}\dot{\boldsymbol{\eta}}^T[\dot{\boldsymbol{M}}_{\boldsymbol{\eta}} - 2\boldsymbol{C_\eta}(\boldsymbol{\xi},\boldsymbol{\eta})]\dot{\boldsymbol{\eta}} \tag{C.4}$$

Applying the skew-symmetric property (2) in section A.7.2

$$\dot{\boldsymbol{\eta}}^T[\dot{\boldsymbol{M}}_{\boldsymbol{\eta}} - 2\boldsymbol{C_\eta}]\dot{\boldsymbol{\eta}} = 0 \quad \forall\dot{\boldsymbol{\eta}}$$

to equation (C.4) we get

$$\dot{V} = \dot{\boldsymbol{\eta}}^T[\boldsymbol{M_\eta}(\boldsymbol{\eta})\ddot{\boldsymbol{\eta}} + \boldsymbol{C_\eta}(\boldsymbol{\xi},\boldsymbol{\eta})\dot{\boldsymbol{\eta}} + \boldsymbol{g_\eta}(\boldsymbol{\eta})]$$

Substituting the dynamical equation for the control-fixed stability (C.1) to the expression $\dot{V}$ this yields

$$\dot{V} = -\dot{\boldsymbol{\eta}}^T\boldsymbol{D_\eta}\dot{\boldsymbol{\eta}} = -\boldsymbol{\xi}^T\boldsymbol{D}\boldsymbol{\xi}$$

At this point, having defined Lyapunov's candidate function V, it is necessary to verify that Lyapunov's theorem is satisfied. Equation (C.1) is that of an *autonomous* system because it does not explicitly depend on time t. Hence, we can apply *Lyapunov's direct method* to prove stability. We can therefore define the following theorem

Theorem C.3. *Sufficient conditions for open-loop stability deriving from Lyapunov's theory are:*

(i) $V = 0$ *for all* $\dot{\boldsymbol{\eta}}, \boldsymbol{\eta} \in \mathbb{R}^n$ *whereas* $\dot{\boldsymbol{\eta}} \neq 0$ *and* $\boldsymbol{\eta} \neq 0$. *Hence*

$$\dot{\boldsymbol{\eta}}^T\boldsymbol{M_\eta}(\boldsymbol{\eta})\dot{\boldsymbol{\eta}} = \boldsymbol{\xi}^T\boldsymbol{M}\boldsymbol{\xi} > 0 \quad \boldsymbol{\xi} \neq 0$$

if and only if the inertia matrix:

$$\boldsymbol{M} > 0$$

Notice that $\boldsymbol{J}^{-1}(\boldsymbol{\eta})$ *is defined for all* $\boldsymbol{\eta} \in \mathbb{R}^n$ *while* $\boldsymbol{J}(\boldsymbol{\eta})$ *is undefined for* $\theta = \pm 90°$.

(ii) $\dot{V} < 0$ *for all* $\boldsymbol{\xi} \in \mathbb{R}^n$ *if and only if the damping matrix:*

$$\boldsymbol{D}(\boldsymbol{\xi}) > 0 \quad \forall\boldsymbol{\xi} \in \mathbb{R}^n$$

(iii) $V \to \infty$ *as* $\|\boldsymbol{\eta}\| \to \infty$ *and* $\|\dot{\boldsymbol{\eta}}\| \to \infty$. *This is satisfied for (C.2).*

Let us now analyze the conditions of the Theorem C.3. The first condition implies that the inertia matrix must be strictly positive. Recall that the global inertia matrix includes both the rigid body inertia and added mass inertia matrix. For blimps vehicle we can assume constant added mass which implies that $\dot{\boldsymbol{M}} = 0$ and $\boldsymbol{M} = \boldsymbol{M}^T > 0$. The second condition concerns the damping matrix which must be strictly positive. This implies that the system must be dissipative which is also true for uncontrolled vehicles.

C.3.5 Closed-loop tracking control

In this section we will analyze the stability and control problem for a non-autonomous system, as we said, even if the system is intrinsically autonomous, analyzing the trajectory tracking problem implies that the system becomes a non-autonomous type. In this case we will see how the *Barbalăt's lemma* can be used to derive a non-autonomous tracking control law. The problem to be analyzed therefore concerns the motion stability which can be transformed into stability around an equilibrium point if we write the system in its error dynamics. To define errors we use as state variables the vehicle's linear and angular velocities. Let the error dynamics be denoted by $\boldsymbol{e}_\xi(t) = \boldsymbol{\xi}_d(t) - \boldsymbol{\xi}(t)$ where $\boldsymbol{\xi}_d(t)$ is the desired state vector. Let us now analyze the stability of the system according to the Lyapunov method. For a mechanical system and in particular a blimp vehicle we define a Lyapunov function candidate as follows:

$$V(\boldsymbol{e}_\xi, t) = \frac{1}{2}\boldsymbol{e}_\xi^T \boldsymbol{M} \boldsymbol{e}_\xi$$

This energy function can be interpreted as a kind of *pseudo-kinetic* energy of the vehicle. Following Lyapunov's criterion we now differentiate with respect to time the energy function $V(\boldsymbol{e}_\xi, t)$ assuming always that the inertia matrix is positive definite, i.e. $\boldsymbol{M} = \boldsymbol{M}^T$ and $\dot{\boldsymbol{M}} = 0$.

$$\dot{V} = \boldsymbol{e}_\xi^T \boldsymbol{M} \dot{\boldsymbol{e}}_\xi \tag{C.5}$$

Substituting the body-fixed equation of motion defined in (A.53) into the expression (C.5) yields:

$$\dot{V} = \boldsymbol{e}_\xi^T [\boldsymbol{\tau} - \boldsymbol{M}\dot{\boldsymbol{\xi}}_d - \boldsymbol{C}(\boldsymbol{\xi})\boldsymbol{\xi}_d - \boldsymbol{D}(\boldsymbol{\xi})\boldsymbol{\xi}_d - \boldsymbol{g}(\boldsymbol{\eta})] - \boldsymbol{e}_\xi^T \boldsymbol{D}(\boldsymbol{\xi}) \boldsymbol{e}_\xi \tag{C.6}$$

In which we have used the skew-symmetric property for the Coriolis and centripetal matrix:

$$\boldsymbol{e}_\xi^T \boldsymbol{C}(\boldsymbol{\xi}) \boldsymbol{e}_\xi = 0 \quad \forall \boldsymbol{e}_\xi \in \mathbb{R}^n$$

To obtain a negative derivative of the energy function we can propose the following control law.

$$\boldsymbol{\tau} = \boldsymbol{M}\dot{\boldsymbol{\xi}}_d + \boldsymbol{C}(\boldsymbol{\xi})\boldsymbol{\xi}_d + \boldsymbol{D}(\boldsymbol{\xi})\boldsymbol{\xi}_d + \boldsymbol{g}(\boldsymbol{\eta}) - \boldsymbol{K}_d \boldsymbol{e}_\xi \tag{C.7}$$

This kind of control law is referred to as the Slotine and Li algorithm in robotics [85] where $\boldsymbol{K}_d$ is a positive regulator gain matrix. Substituting the control action (C.7) into equation (C.6) we obtain:

$$\dot{V} = -\boldsymbol{e}_\xi^T [\boldsymbol{D}(\boldsymbol{\xi}) + \boldsymbol{K}_d] \boldsymbol{e}_\xi \leq 0$$

In particular the relation $V \leq 0$ implies that $V(t) \leq V(0) \quad \forall t \geq 0$, and therefore that $\boldsymbol{e}_\xi$ is bounded. This in turn implies that $\ddot{V}$ is bounded. Hence, $\dot{V}$ must be uniformly continuous. Finally, application of Barbălat's lemma C.2 shows that $\dot{V} \to 0$, which implies that $\boldsymbol{e}_\xi \to 0$ as $t \to \infty$.

C.4 State feedback linearization (Computed torque control)

The nonlinear control technique called state feedback linearization is a control system method which is aimed at transforming a nonlinear system into a linear one which is then controlled with

a classic closed-loop feedback control scheme. This control technique is widely used in robotics and is commonly referred as *Computed Torque Control* (CTC). CTC method is a model-based control technique which makes use of the system dynamics parameters to calculate the control inputs, i.e. the forces and torques that make the state variables follow the desired variables. State feedback linearization is considered a form of *non-linearity cancellation technique* [23] as in the feedback loop the dynamics parameters are used for canceling the same terms in the equations of motion to transform the system into a linear one, effectively deleting its nonlinearities. If the knowledge of the parameters of the dynamics of the system is exact then the linearization process would be perfect and consequently the control technique leads to exact results. Figure C.2 illustrates a generalized CTC system applied to a robot.

Before showing the application of the CTC method for the blimp vehicle, let us consider a slightly different controller based on the simpler mechanical system which is the *damper spring mass* shown in Figure C.1.

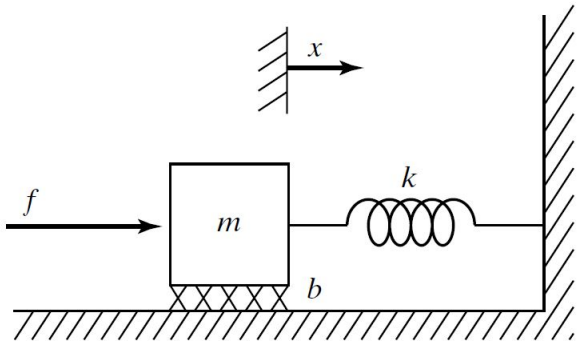

Figure C.1: Dumper spring mass system [26].

We write the simple equation of motion of the system which can be obtained with the free-body diagram of the forces acting on the block in Figure C.1.

$$m\ddot{x} + b\dot{x} + kx = f \tag{C.8}$$

The controller must give the expression of f which brings the system into the desired condition. According to the CTC method, the controller will be characterized by two portions: the *model-based portion* and the *servo portion*. The goal is that the system parameters appear in the model-based portion (i.e., m, b, and k in this case) in such a way that the resulting system is that of a unit mass system. The servo portion will be independent of the system parameters and will have the task of establishing the gains to control a system that appears as one composed of a single unit mass. The model-based portion for equation (C.8) can be defined as follows:

$$f = \alpha f' + \beta \tag{C.9}$$

where α and β are functions or constants which are chosen precisely to transform the system into one with unit mass which has the function f' as a new input. Combining this control law (C.9) with the equation of motion of the dumper spring mass system (C.8) we obtain

$$m\ddot{x} + b\dot{x} + kx = \alpha f' + \beta \tag{C.10}$$

In this case if we want the closed-loop system to appear as a unit mass system with f' as the new input then we have to choose α and β as follows:

$$\begin{cases} \alpha & = m \\ \beta & = b\dot{x} + kx \end{cases}$$

Substituting these parameters inside equation (C.10) we have

$$\dot{x} = f' \tag{C.11}$$

Which is the equation of a unitary mass system. We then proceed as if equation (C.11) were the open-loop system to be controlled. If in particular we want the system to follow a desired trajectory we can define the servo errors as the difference between the desired and actual trajectory $e = x_d - x$. In this case we assume that the trajectory generator provides a time series of desired states for all times t: $x_d(t)$, $\dot{x}_d(t)$, and $\ddot{x}_d(t)$ which constitute a smooth trajectory in space, i.e. that the first and second derivatives are well defined. At this point we need to define the control law that constitutes the servo portion that will make the system follow the trajectory which is the following

$$f' = \ddot{x}_d + k_v\dot{e} + k_p e \tag{C.12}$$

If we substitute the control law (C.12) inside the unit mass equation of motion (C.11) we obtain the error space equation of motion that describe the evolution of state variables errors.

$$\ddot{x} = \ddot{x}_d + k_d\dot{e} + k_p e$$

which leads to

$$\ddot{e} + +k_v\dot{e} + k_p e = 0$$

This second-order differential equation therefore represents the evolution of errors over time and its behavior depends on the parameters that appear which are called position gains k_p and velocity gains k_v, whose combinations of values make the system assume different response trends over time, once it is ensured that the system is stable. Figure C.2 shows a block diagram of our trajectory following controller.

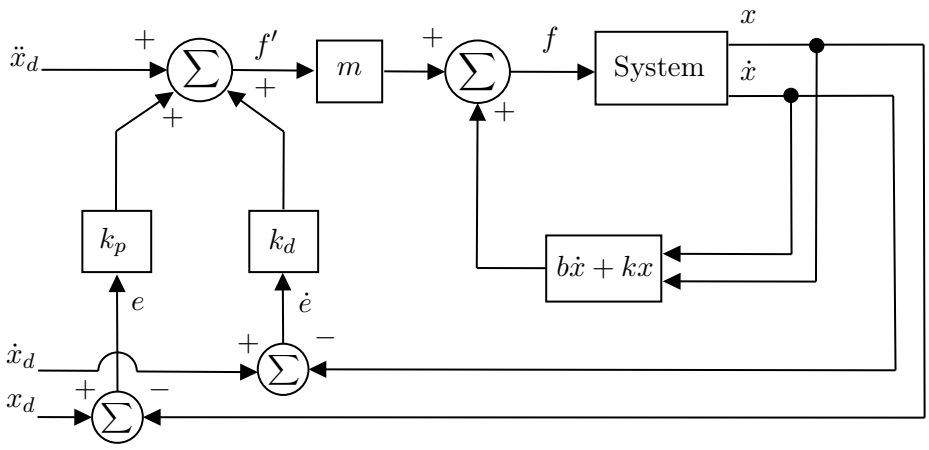

Figure C.2: A trajectory following controller for the dumper spring mass system.

The example we just discussed on the damper spring mass system is a classic example of a single-input single-output (SISO) system. However, the problem of controlling the blimp is different as the blimp vehicle is a multi-input multi-output (MIMO) system. So we have a vector of desired positions, velocities and accelerations, and the quantities we just calculated turn into vectors and matrices. The methodology of partitioning the control law into a model-based and a servo-based portion is preserved. Then the model-based portion reproduces the nonlinearities of the system and reports the dynamics parameters. The control law becomes:

$$\boldsymbol{f} = \boldsymbol{\alpha}\boldsymbol{f}' + \boldsymbol{\beta}$$

If we are dealing with a n DOF system, $\boldsymbol{f}$, $\boldsymbol{f}'$, and $\boldsymbol{\beta}$ are $(n \times 1)$ vectors and $\boldsymbol{\alpha}$ is an $(n \times n)$ matrix. The matrix $\boldsymbol{\alpha}$ can be of any type (diagonal or not) as long as it decouples the n equations of motion. Therefore, with the correct choice of $\boldsymbol{\alpha}$ and $\boldsymbol{\beta}$ the system appears as formed by n unitary and independent masses that have the components of $\boldsymbol{f}'$ as input. This is why in the case of MIMO system the model-based portion of the controller is said a *linearizing* and *decoupling* control law. If again we want the system to perform trajectory tracking, then the servo law for the MIMO system can be chosen as follows

$$\boldsymbol{f}' = \ddot{\boldsymbol{x}}_d + \boldsymbol{K}_d\dot{\boldsymbol{e}} + \boldsymbol{K}_p\boldsymbol{e}$$

where $\boldsymbol{e}$ and $\dot{\boldsymbol{e}}$ are the position and velocity error vectors respectively of size $(n \times 1)$ while $\boldsymbol{K}_d$ and $\boldsymbol{K}_p$ are the gains matrices which in general have constant gains on the diagonal and are of size $(n \times n)$ [26]. To summarize, the CTC method is based on the following steps:

1. Find a model-based control law that exactly reproduces nonlinearities and cancels them so that the system is reduced to a decoupled linear one consisting of n independent masses.

2. Find a servo control law and independently control the n independent unit masses.

However, we must underline that the model-based control law must know perfectly the parameters of the nonlinear dynamics of the system and obviously this is a problem in real applications where there is a need to model the behavior of a system from which all the parameters are not exactly known.

In conclusion the CTC method is a control technique that consists of two portions based on feedback and feedforward parts. The feedforward part is the model-based portion which calculates a part of the control input that implements the inverse dynamics in order to linearize the system; in our case for the blimp application, it contains all the nonlinearities required to compensate for gravitational and bouyancy forces, Coriolis and centripetal forces and dumping forces. The calculation is done on the basis of the current trajectory therefore the definition of the model-based control law implemented in the feedforward branch must work in real time. The feedback control component is the servo-based portion which acts on the linearized system and implements a PD (Proportional Derivative) control law which is meant to calculate a quantity called *corrected acceleration* [23]. The corrected acceleration is what the system should have in order to reach the desired position and velocity in the desired time. It is calculated on the basis of the current and desired trajectory and this too must be generated every sampling period [81]. In the next section we will apply the state feedback linearization control method to the blimp vehicle both in the body-fixed and earth-fixed reference frame.

C.4.1 CTC in the body-fixed reference frame (velocity control)

As we have already shown in the previous section, the objective of the CTC method is to obtain a closed-loop system that is linear, decoupled and made up of n independent masses so that it can be controlled by n PD control laws. In this section we will apply the CTC method to the nonlinear blimp dynamic system expressed in the body-fixed frame to control the linear and angular velocities. The dynamics can be compactly written as:

$$\boldsymbol{M}\dot{\boldsymbol{\xi}} + \boldsymbol{n}(\boldsymbol{\xi}, \boldsymbol{\eta}) = \boldsymbol{\tau} \tag{C.13}$$

where $\boldsymbol{\eta}$ and $\boldsymbol{\xi}$ are assumed to be measured by some sensor and $\boldsymbol{n}(\boldsymbol{\xi}, \boldsymbol{\eta})$ is the nonlinear vector defined as:

$$\boldsymbol{n}(\boldsymbol{\xi}, \boldsymbol{\eta}) = \boldsymbol{C}(\boldsymbol{\xi})\boldsymbol{\xi} + \boldsymbol{D}(\boldsymbol{\xi})\boldsymbol{\xi} + \boldsymbol{g}(\boldsymbol{\eta})$$

After the application of the control law $\boldsymbol{\tau}$ the system to be obtained will be of this type:

$$\dot{\boldsymbol{\xi}} = \boldsymbol{a}_{\xi} \tag{C.14}$$

where $\boldsymbol{a}_{\xi}$ is the corrected acceleration vector (our f' input). The controller that transforms the system into this structure will consist of a model-based portion and a servo portion. The system's nonlinear parameters $\boldsymbol{n}(\boldsymbol{\xi}, \boldsymbol{\eta})$ will appear in the model-based portion while the servo portion will drive the linear system towards the desired state. The control law can be chosen in this way:

$$\boldsymbol{\tau} = \boldsymbol{M}\boldsymbol{a}_{\xi} + \boldsymbol{n}(\boldsymbol{\xi}, \boldsymbol{\eta}) \tag{C.15}$$

The control scheme developed in body-fixed reference frame is shown in Figure C.3. To obtain the closed-loop system we can substitute the control law equation (C.15) into the nonlinear dynamics equations (C.13), obtaining

$$\boldsymbol{M}\dot{\boldsymbol{\xi}} = \boldsymbol{M}\boldsymbol{a}_{\xi}$$

Simplifying the inertia matrix we obtain equation (C.14) which is the dynamic equation of six independent unit masses. Now we proceed by designing the servo control law which is meant to calculate $\boldsymbol{a}_{\xi}$ that will cause trajectory following.

$$\boldsymbol{a}_{\xi} = \dot{\boldsymbol{\xi}}_d + \lambda \boldsymbol{e}_{\xi} \tag{C.16}$$

where $\boldsymbol{e} = \boldsymbol{\xi}_d - \boldsymbol{\xi}$ is the velocity tracking error defined as the difference between the desired and actual linear and angular velocities, λ is the control bandwidth. If we substitute (C.16) inside the equation of motion (C.14) we obtain:

$$\dot{\boldsymbol{\xi}} = \dot{\boldsymbol{\xi}}_d + \lambda \boldsymbol{e}_{\xi}$$

or

$$\dot{\boldsymbol{e}}_{\xi} + \lambda \boldsymbol{e}_{\xi} = 0 \tag{C.17}$$

That is the *error space* equation of motion which describes the evolution of dynamic errors. Recall that if the knowledge of our model was perfect, which imply that $\boldsymbol{n}(\boldsymbol{\xi}, \boldsymbol{\eta})$ exactly reproduced the real model and if there were no noise and no disturbances then the system will follow the desired

trajectory. If we start from an initial error this will tend to zero according to (C.17).

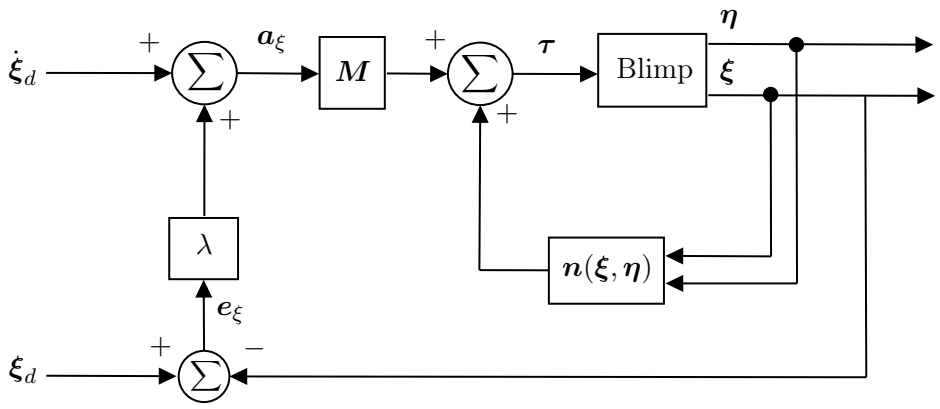

Figure C.3: Nonlinear trajectory-following controller for velocity of the blimp system.

C.4.2 CTC in the earth-fixed reference frame (position and attitude control)

In the previous blimp control scheme we assumed that the desired trajectory was available in terms of velocity and acceleration time sequence of the blimp in the body-fixed reference frame ($\boldsymbol{\xi}_d$ and $\dot{\boldsymbol{\xi}}_d$) therefore we calculated the trajectory errors through the difference between desired and actual values of the quantities expressed in the body-fixed reference frame. It is actually much more intuitive to program a trajectory in the earth-fixed reference frame[1].

Although the trajectory is usually defined in the earth-reference, we have seen that it is easier to write and control nonlinear dynamics in the body-fixed reference frame. Therefore, starting from the information of the temporal sequence of positions, velocities and accelerations of the blimp in the earth-fixed reference frame, these must be somehow converted in order to calculate the vector of forces and torques $\boldsymbol{\tau}$ in the body-fixed reference frame that acts as input to our dynamic system. After the integration of the differential equations of the blimp body-fixed dynamics, the knowledge of the state variables must then be converted into earth-fixed state variables in order to be compared with the desired inertial position, to find errors in inertial space. The control scheme developed in inertial space is shown in Figure C.4.

Let's recall the body-fixed blimps dynamics and kinematics equation:

$$\boldsymbol{M}\dot{\boldsymbol{\xi}} + \boldsymbol{n}(\boldsymbol{\xi},\boldsymbol{\eta}) = \boldsymbol{\tau} \tag{C.18}$$

$$\dot{\boldsymbol{\eta}} = \boldsymbol{J}(\boldsymbol{\eta})\boldsymbol{\xi} \tag{C.19}$$

where we assume that both $\boldsymbol{\eta}$ and $\boldsymbol{\xi}$ are measured by sensors. Also in this case the control law aims to make the system linear and decoupled into n independent masses, that is

$$\ddot{\boldsymbol{\eta}} = \boldsymbol{a}_\eta \tag{C.20}$$

where $\boldsymbol{a}_\eta$ is the earth-fixed commanded acceleration. In order to connect the two representations in the two reference frames, we calculate the derivative with respect to time of the equation of the

[1] Very often we want the blimp to follow a certain trajectory in the space described in the inertial reference.

kinematics (C.19):

$$\ddot{\boldsymbol{\eta}} = \boldsymbol{J}(\boldsymbol{\eta})\dot{\boldsymbol{\xi}} + \dot{\boldsymbol{J}}(\boldsymbol{\eta})\boldsymbol{\xi}$$

Let's make explicit the term $\dot{\boldsymbol{\xi}}$

$$\dot{\boldsymbol{\xi}} = \boldsymbol{J}^{-1}(\boldsymbol{\eta})\big[\ddot{\boldsymbol{\eta}} - \dot{\boldsymbol{J}}(\boldsymbol{\eta})\boldsymbol{\xi}\big] \tag{C.21}$$

Again, we have a vector of desired blimp positions, velocities, and accelerations, and the nonlinear control law must compute a vector of blimp-actuator signals. Our basic scheme, partitioning the control law into a model-based portion and a servo portion, is still applicable. The nonlinear control law takes the same form as before:

$$\boldsymbol{\tau} = \boldsymbol{M}\boldsymbol{a}_{\xi} + \boldsymbol{n}(\boldsymbol{\xi}, \boldsymbol{\eta}) \tag{C.22}$$

Now we apply this control law to the blimps equation of motion (C.18) in which we perform the change of coordinates (C.21), yields:

$$\boldsymbol{M}\big\{\boldsymbol{J}^{-1}(\boldsymbol{\eta})\big[\ddot{\boldsymbol{\eta}} - \dot{\boldsymbol{J}}(\boldsymbol{\eta})\boldsymbol{\xi}\big]\big\} = \boldsymbol{M}\boldsymbol{a}_{\xi}$$

rearranging:

$$\boldsymbol{M}\boldsymbol{J}^{-1}(\boldsymbol{\eta})\big[\ddot{\boldsymbol{\eta}} - \dot{\boldsymbol{J}}(\boldsymbol{\eta})\boldsymbol{\xi} - \boldsymbol{J}(\boldsymbol{\eta})\boldsymbol{a}_{\xi}\big] = 0$$

Defining

$$\boldsymbol{M}_{\eta} = \boldsymbol{J}^{-T}(\boldsymbol{\eta})\boldsymbol{M}\boldsymbol{J}^{-1}(\boldsymbol{\eta})$$

and

$$\boldsymbol{a}_{\eta} = \dot{\boldsymbol{J}}(\boldsymbol{\eta})\boldsymbol{\xi} + \boldsymbol{J}(\boldsymbol{\eta})\boldsymbol{a}_{\xi} \tag{C.23}$$

we obtain the linear decoupled system (C.20):

$$\boldsymbol{M}_{\eta}(\ddot{\boldsymbol{\eta}} - \boldsymbol{a}_{\eta}) = 0 \Longrightarrow \ddot{\boldsymbol{\eta}} = \boldsymbol{a}_{\eta}$$

As for the servo-based control portion that establishes the commanded acceleration $\boldsymbol{a}_{\eta}$, if we want a trajectory tracking motion then this can be chosen as:

$$\boldsymbol{a}_{\eta} = \ddot{\boldsymbol{\eta}}_d + \boldsymbol{K}_d\dot{\boldsymbol{e}}_{\eta} + \boldsymbol{K}_p\boldsymbol{e}_{\eta}$$

where $\dot{\boldsymbol{e}}_{\eta} = \dot{\boldsymbol{\eta}}_d - \dot{\boldsymbol{\eta}}$ and $\boldsymbol{e}_{\eta} = \boldsymbol{\eta}_d - \boldsymbol{\eta}$ are the errors calculated as the difference between the desired and actual values. $\boldsymbol{K}_d$ and $\boldsymbol{K}_p$ are two positive definite matrices, generally with constant gains on the diagonal. The error dynamics becomes:

$$\ddot{\boldsymbol{e}}_{\eta} + \boldsymbol{K}_d\dot{\boldsymbol{e}}_{\eta} + \boldsymbol{K}_p\boldsymbol{e}_{\eta} = 0$$

In the control law (C.22) the commanded acceleration $\boldsymbol{a}_{\xi}$ in the body-fixed reference frame is calculated from (C.23) in the following way:

$$\boldsymbol{a}_{\xi} = \boldsymbol{J}^{-1}(\boldsymbol{\eta})\big[\boldsymbol{a}_{\eta} - \dot{\boldsymbol{J}}(\boldsymbol{\eta})\boldsymbol{\xi}\big]$$

This is shown in Figure C.4 in which the vector of disturbances is also present.

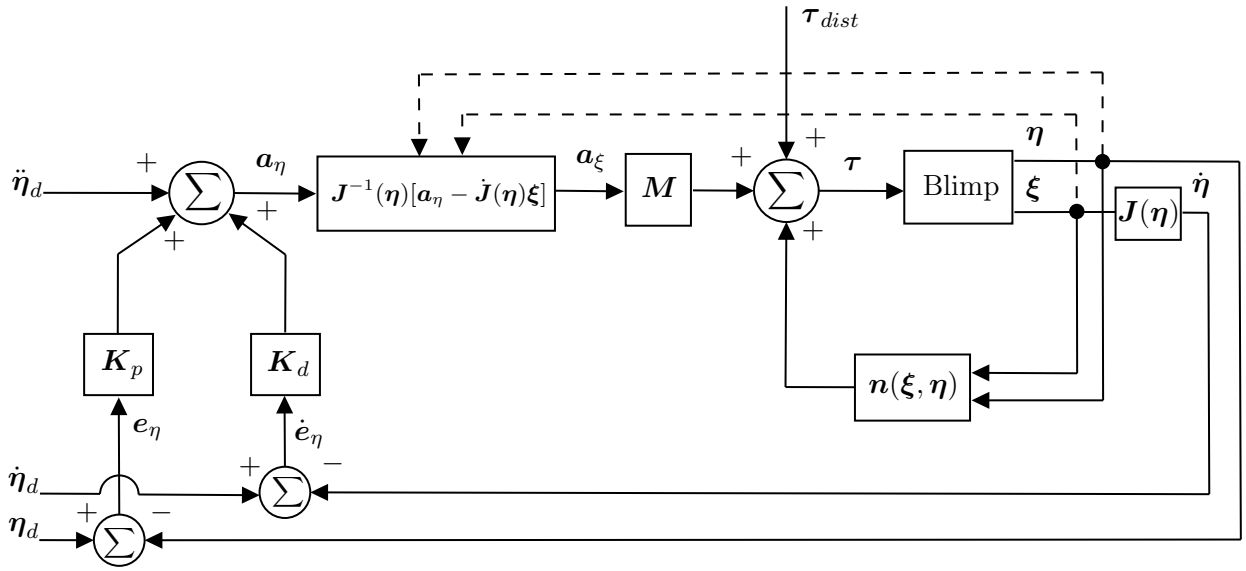

Figure C.4: Nonlinear trajectory-following controller for position and attitude of the blimp system.

C.4.3 Analysis and results

In this section we will show a simulation based on trajectory tracking using the feedback linearization technique in the earth-fixed reference frame. The simulation has been implemented in MATLAB and the control system is the one shown in the Figure C.4. The simulated trajectory was defined in the FCC reference frame that we have shown in section 4.2. The trajectory depicts the scenario in which the blimp takes off vertically, climbs up reaching a certain altitude and then continues longitudinally along the entire length of the detector, finally it descends to the ground on the opposite side. The reference trajectory was constructed with the method of linear functions with parabolic blends as reported in section 4.4. The via points in the FCC frame are given as follow:

$$\boldsymbol{\eta}_1^{FCC} = \begin{bmatrix} 0 \\ -10 \\ -40 \end{bmatrix} m \quad \boldsymbol{\eta}_2^{FCC} = \begin{bmatrix} 0 \\ 10 \\ -40 \end{bmatrix} m \quad \boldsymbol{\eta}_3^{FCC} = \begin{bmatrix} 0 \\ 10 \\ 40 \end{bmatrix} m \quad \boldsymbol{\eta}_4^{FCC} = \begin{bmatrix} 0 \\ -10 \\ 40 \end{bmatrix} m$$

The time interval in which the blimp flies is formed by the initial and final time defined as

$$t_0 = 0\ s \qquad t_f = 120\ s$$

The trajectory update rate has been set at $f = 10$ Hz, i.e. with a time interval of $dt = 0.1$ s. The duration of the distance between path points are

$$t_{d12} = 30\ s \qquad t_{d23} = 60\ s \qquad t_{d34} = 30\ s$$

while the duration of blend regions are

$$t_1 = 5\ s \qquad t_2 = 10\ s \qquad t_3 = 10\ s \qquad t_4 = 5\ s$$

In Figure C.5 we report the time sequences of the desired trajectory that has been defined in the FCC reference frame and we notice that we have imposed a change in the spatial coordinates

while the Euler angles representing the body's attitude remain null.

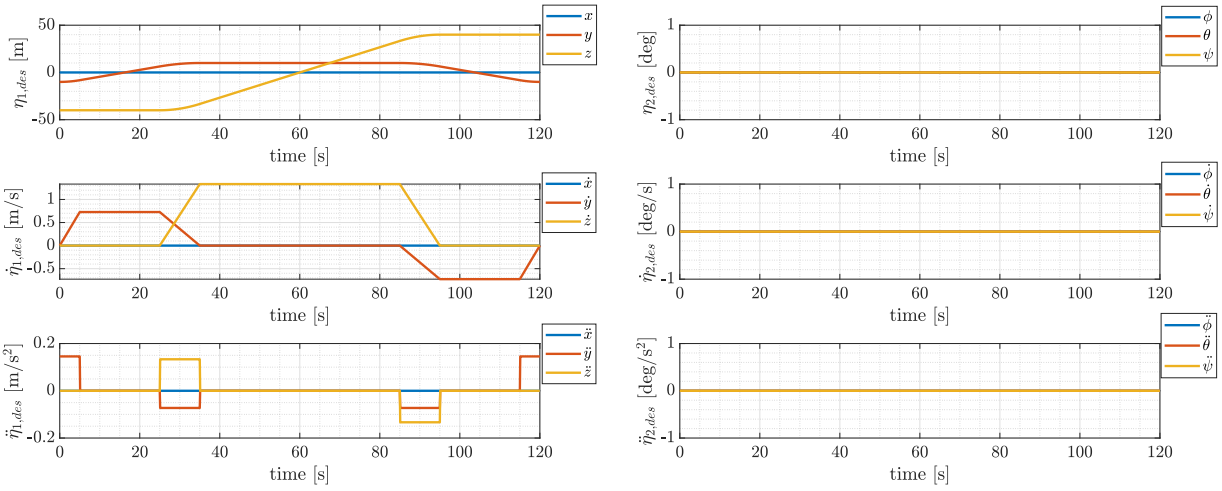

(a) **(b)**

Figure C.5: Time course of the desired linear position, velocity and accelerations (a) and desired angular position, velocity and accelerations (b) in the *FCC* reference frame for the CTC method.

The initial conditions for the integration of the equations were chosen as an initial error added in the x, y and z position and in the yaw angle ψ starting from the definition of the first via point $\boldsymbol{\eta}_1^n$ expressed in the inertial frame.

$$\boldsymbol{\eta}^n(0) = \boldsymbol{\eta}_1^n + \begin{bmatrix} 1\,\text{m} \\ 1\,\text{m} \\ 1\,\text{m} \\ 0 \\ 0 \\ 2\,\text{deg} \end{bmatrix} \qquad \dot{\boldsymbol{\eta}}^n = 0 \qquad \boldsymbol{\xi}^b = 0 \qquad \dot{\boldsymbol{\xi}}^b = 0$$

The gain matrices $\boldsymbol{K}_p$ and $\boldsymbol{K}_d$ were chosen diagonal with $k_p = 60$ and $k_d = 2\sqrt{k_p}$ on the main diagonal respectively. Furthermore, the magnetic disturbance acting along the current trajectory was also considered. The algorithm reported in section 5.7 was used to calculate the magnetic disturbance at each step. In this case to compensate for this disturbance, the function of the model-based control law $\boldsymbol{n}(\boldsymbol{\xi}, \boldsymbol{\eta})$ which cancels the nonlinearities of the system also takes into account the magnetic disturbance which is considered as a non-linear term to be canceled. When applying the magnetic field algorithm it was decided that the blimp had the following associated magnetic moment:

$$\boldsymbol{m}^b = \begin{bmatrix} 2 & 2 & 2 \end{bmatrix}^T \text{ Am}^2$$

The simulation results are shown below.

Figure C.6a shows the servo errors calculated during the application of the CTC method for blimp nonlinear control in the earth-fixed reference. It can be seen that these tend to zero quickly and this means that the system maintains and follows the desired state in terms of linear and angular positions and velocities which are shown in Figure C.5. Figure C.6b, on the other hand,

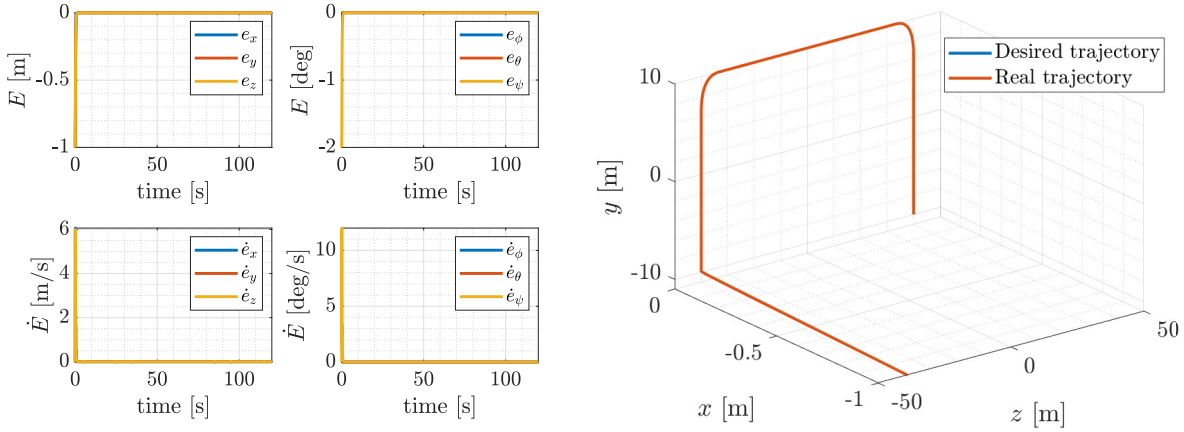

(a) **(b)**

Figure C.6: Time course of the linear and angular position and velocity errors calculated for the 6 DOF with the CTC method (a). Comparison between the desired and the real trajectory for the CTC method reported in the *FCC* frame (b).

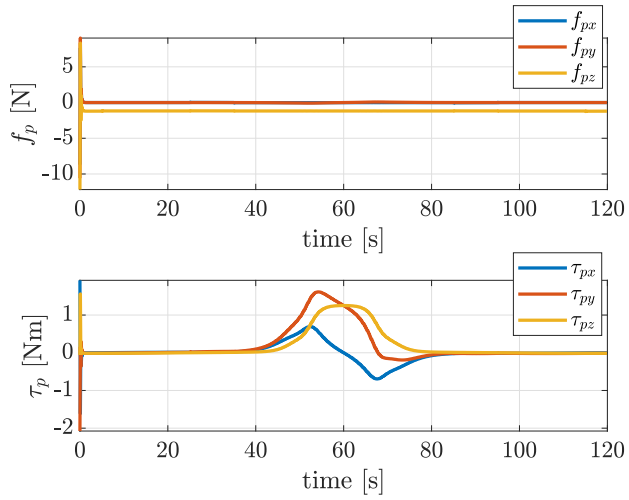

Figure C.7: Components of the propulsive forces and torques $\boldsymbol{\tau}^b$ provided by the CTC method for trajectory tracking and the disturbances rejection.

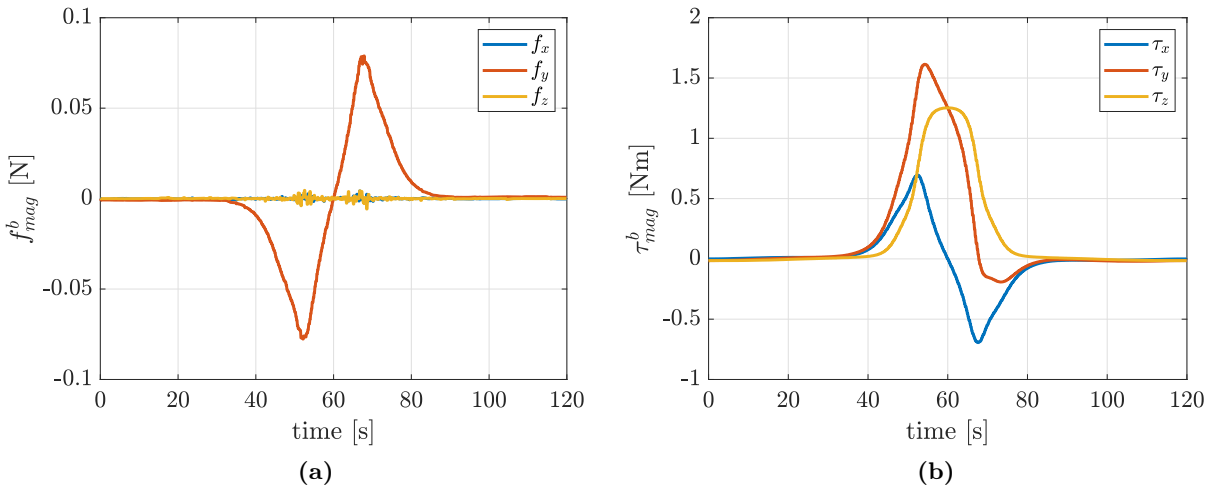

Figure C.8: Components of the magnetic forces (a) and magnetic torques (b) acting on the blimp on its current trajectory.

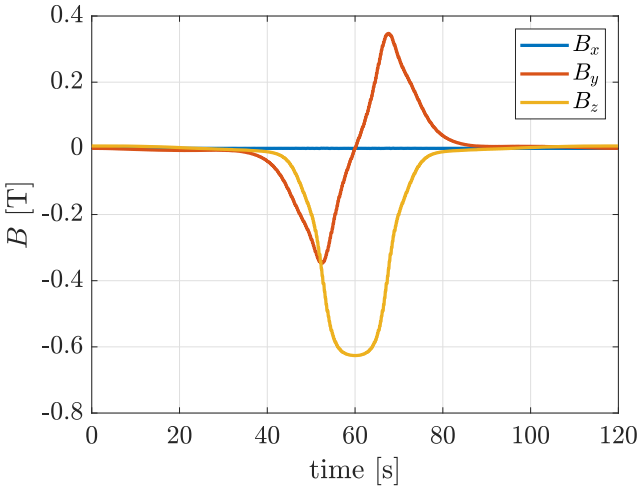

Figure C.9: Components of the magnetic field acting on the blimp during its current trajectory.

represents the comparison between the desired trajectory and the real one which is obtained from the integration of the equations of motion downstream of the application of the partitioned control law (C.22). From the comparison of the two it can be seen that the blimp faithfully follows the desired trajectory during motion and in the initial instant it cancels its wrong position.

Figure C.7 shows the time course of the propulsive forces and torques consequent to the control law that the blimp must exercise during its motion in order to follow the desired trajectory and simultaneously cancel the magnetic disturbance. It can be seen from the trend of the propulsive torque that in passing over the detector, the blimp must be able to exercise control torques of the order of 1 Nm in order to counteract the magnetic torques that act on it due to the presence of its electric motors that interact with the magnetic field. We remind that in this simulation we have not taken into account the configuration of the motors but we are considering that the system is able to somehow provide these forces and torques for all six of its degrees of freedom.

Figure C.8 (a) and (b) shows the magnetic disturbances in terms of forces and torques respectively. These interactions were calculated through the disturbance estimation algorithm reported in section 5.7. In this scenario, a certain magnetic moment defined in the body-fixed reference was considered with values on all three body axes equal to 2 Am^2. From this simulation we can see that in passing over the detector the system is subjected to a force in the y direction that would tend to make it deviate from the reference trajectory and this is a sobering result as the real Blimpduino system is not equipped with an actuator capable of providing a force in that direction. Also with regard to the magnetic torques that act on the system, the blimp if controlled with this technique must guarantee an ability to exercise torques around all three body axes.

Finally, Figure C.9 shows the temporal trend of the components of the magnetic field generated by the FCC-hh detector which are the ones that the blimp receive as it travels its current trajectory.